Thèse n° 4263

THÈSE

présentée à

L'UNIVERSITÉ BORDEAUX 1

par Sébastien ROUJOL

pour obtenir le grade de

DOCTEUR

Spécialité: Informatique

MR-guided thermotherapies of mobile organs: Advances in real time correction of motion and MR-thermometry

Dirigée par:

Mme. Jenny Benois-Pineau, Professeure Bordeaux 1

M. Chrit Moonen, Directeur de Recherche CNRS

Soutenue le: 25 Mai 2011

Devant la commision d'examen formée de:

M. Christian Barillot, Directeur de Recherche CNRS	Rapporteur
M. Christian Roux, Directeur de Recherche INSERM	Rapporteur
Mme. Jenny Benois-Pineau, Professeure Bordeaux 1	Examinateur
M. Chrit Moonen, Directeur de Recherche CNRS	Examinateur
M. Philippe Ciuciu , Charg de recherche CEA	Examinateur
Nicolas Grenier , PUPH Bordeaux2	Examinateur

Laboratory for Molecular and Functional Imaging:
From Physiology to Therapy
FRE 3313/University of Bordeaux 2
146, rue Lo Saignat
Case 117
33076 Bordeaux Cedex
France

Acknowledgments

I would like to start this thesis with a presentation of all the people that helped me in this adventure of 3 years, or I should say of 5 years. This thesis started actually in my mind more than three years ago and I would like to thank all the people that help me to find my way ...

I discovered 5 years ago the field of medical imaging with an internship of 4 months at the IMF lab. This was an amazing experience and this was mainly due to Chrit Moonen that first accepted me in his lab and Baudouin Denis de Senneville for all the time he spent to take me from scratch in the domain and learned me so many things that I finished to write a report almost as long as this thesis !

After this awesome 4 months, I was sure that I wanted to embark on the adventure of a PhD ! Then, I spent 6 months at NIH in the lab of Jeff Duyn under the supervision of Jacco de Zwart and Peter Van Gelderen. I had a second very nice experience in the MRI field with again very talented people that were also very nice guys. So I would like to thank the entire dutch mafia and all post docs that made my stay oversea fantastic and especially Marta and his husband Miguel just for sharing so many good times with me.

After this, back in my home country, I started my PhD in the IMF lab. So I would like to thank again Chrit that accepted me a second time in his lab and Jenny Benois-Pineau that accepted to be my PhD supervisor. They were always available for discussion even if their schedule was more than busy ! I also had the chance to go on several conferences, so thank you both for giving me these opportunities.

Then, this thesis would not have been possible without the help of the pillars of the lab: Baudouin Denis de Senneville, Mario Ries and Bruno Quesson. In addition to be talented scientist, they are very nice guys. I would like to thank Bruno for all the help he gave me during this thesis and all the discussions we had, especially about the cardiac studies, but also about the famous history of hula dance, mahalo ! Then, I would like to thank Baudouin for all scientific discussion we had that were very stimulating for me, and all the time we spent together around the orn Chtounck subjects and the classical "atlas". He was the driving force of this thesis together with Mario. So I would also like to specially thank Mario, that was during this time more than a mentor, his scientific and human vision were very precious, thank you again.

Then I would like to thank all the crazy people, that were engaged with a PhD program at some point, for sharing with me the same enthusiasm and the same passion for this work (and even if English is not my native language, after 3 years I really think the word "engaged with" perfectly describes this curious program). So, thanks to PYF, Silke, Charles, Greg, Roel, Luis, Julius, Coco, Mathieu, Cyril, Marc, Pierrot, Delphine, KaKa.

I also would like to thank especially Marie France and Colette for being always present to organize our administrative and social life at the lab. Well, for the social life, I have to mention the great help of my friend PYF with who we formed the most dynamic tandem for night life organization (my apologies to the veterans of the lab (Greg, Luis, Roel)... but we were self-proclaimed best animation team of the lab). So thanks to PYFROU !

I also would like to thank all the guys around that help me to survive to these 3 years. In addition to the already mentioned people, I would like to first thank Marianne for all

she gave me during this time and all my friends, my little Yas, Pierra, Johan, Mathieu, Nico, Fadi, Sab, Sabrina, Mariam, Aurélie, Polo, Judi and my ex roomates, Flo, Fatim, Mariama, Lenny, PtiCha and all the people that went at some point in this wonderful "Spanish Apartment". I will also miss the week end in San Sebastian with the birth of the famous "La poutre" in front of the so amazing song called "call on me" !

Finally, I would like to thank my family, my father, my mother for always being here when I need it and for being a model for me. I love you.

Contents

Glossary

MR: Magnetic resonance
MRI: Magnetic resonance imaging
US: Ultrasound
$HIFU$: High intensity focused ultrasound
GPU: Graphics processing unit
RF: Radio frequence
FOV: Field of view
TR: Repetition time
TE: Echo time
EPI: Echo planar imaging
PRF: Proton resonance frequency
B_0: Magnetic field strength
T_1: Longitudinal relaxation time
T_2: Transversal relaxation time
ECG: Electrocardiogram
TD: Thermal dose
SNR: Signal to noise ratio
ROI: Region of interset
MSE: Mean square error
TSD: Temperature standard deviation
$OFCE$: Optical flow constraint equation
$BHTE$: Bio heat transfer equation
EKF: Extended Kalman filter
$AEKF$: Auto-calibrated extended Kalman filter
∇: Gradient operator
$\partial x/\partial t$: Partial derivative of x with respect to t
$\bar{x}$: Mean of x
$\sigma(x)$: Standard deviation of x
I: MR-magnitude image
φ: MR-phase image
$I(x, y)$: Image intensity at pixel coordinates of (x, y)
$I(x, y, t)$: Image intensity at pixel coordinates of (x, y) and time t
$I(P)$: Image intensity in the pixel P
I_α: Partial derivative of I with respect to α
I_{ref}: MR-magnitude reference image
FIR: Finite impulse response
IIR: Infinite impulse response

Preface

Thermal ablation is already a clinically accepted routine to treat certain types of cancer and atrial fibrillation. These interventions generally employ a mini or non invasive heating device that induces localized hyperthermia in order to destroy pathological tissues. However, the lack of control during the intervention may lead to insufficient or excessive heating. In the first case, this may lead to disease reappearance and in the second case this can lead to the destruction of adjacent healthy tissue. As an example, 30% of the thermal ablations for atrial fibrillation treatment result in therapeutic failure. At present, the tissue temperature is not controlled during the intervention. Therefore, a control during the intervention may be highly advantageous. MRI, that has been largely employed for diagnostic purposes since the eighties, shows a great potential for guidance of such interventional therapeutic procedure. Modern MRI scanners allow rapid acquisition of high spatial resolution images with good tissue contrast. Moreover, in addition to anatomical information, MRI also provides temperature information that contributes to make this imaging modality very attractive for online ablation monitoring. However, MR-thermometry in mobile organ remains challenging.

This thesis focuses on new developments for MR-guided thermal ablations of mobile organs such as the liver, the kidney and the heart. The manuscript is structured as follows:

- A first part presents the clinical issues and the potential of MR-guided thermal ablations for the treatment of cancer and atrial fibrillation (see chapter 1). Then, chapter 2 describes the state-of-the-art and the challenges of MR-guided thermal ablations of mobile organs.

- In the second part, the feasibility of real time control of the intervention is shown, together with an interventional pipeline, which takes advantage of GPGPU programming. Developments for the feasibility in real time of MR-image reconstruction, MR-thermometry and MR-dosimetry are presented in chapters 4 and 5. In-vivo validations in both abdominal organs and in the heart are presented and further extensions of these methods are shown for the special case of HIFU ablation (see chapter 6).

- In a last part, methodological developments are presented, where several limits of existing methods are addressed. In particular, chapter 7 presents advances for the problem of motion estimation in presence of structures appearing transiently in the images (which can be encountered with reduced field of view imaging or with the presence of out-of-plane motion). Chapter 8 proposes a robust approach to address the problem of motion estimation with high intensity variations, which can occur during hyperthermia. In chapter 9, a criterion to assess the quality of the motion estimation process is proposed and its application for the autocalibration of a motion estimation algorithm is presented. The correction of motion induced magnetic susceptibility variation is also improved for the specific case of spontaneous motion and is presented in chapter 10. Finally, the management of temperature noise

is addressed in chapter 11 where a novel temporal filter is introduced that allows improving the precision while controlling the resulting temperature accuracy.

Part I

Introduction

Chapter 1

Problem description

1.1 Localized hyperthermia in medicine

1.1.1 Therapeutic applications

1.1.1.1 Treatment of cancer

Cancer can be seen as an uncontrolled growth of cells into healthy tissues. The resulting cells can create a tumor or spread to other locations in the body to form metastasis. Several treatments exist such as surgery (to remove the cancerous tissue), chemotherapy, radiotherapy, etc. A combination of these approaches are often used [1]. Surgery aims to remove the cancerous tissue but is not always a viable therapeutic option, depending on the location of the tumor. Chemotherapy uses drugs that aim to impair mitosis (cell division) or to cause cell death by apoptosis (programmed cell death). These drugs show generally also a high toxicity for healthy tissue and are thus limited in the therapeutic dose. A number of side effects are generally induced such as depression of the immune system, fatigue, gastrointestinal problem, hair loss, etc. Radiotherapy uses ionizing radiations that induces DNA damage which in turns leads to apoptosis. Similarly, the side effects of the absorbed radiation usually limit the therapeutic possibilities for this modality.

As a consequence, ongoing research in oncology continuously aims to improve efficiency of the treatment, decrease associated side effects, and accelerate patient recovery. A variety of novel strategies have been proposed in the recent years. Among them, thermotherapy appears to be a very promising candidate. Several approaches of thermotherapy have been suggested, such as direct tissue ablation through hyperthermia [2, 3, 4] or local delivery of therapeutic agents with localized mild hyperthermia as the triggering mechanism [5]. For direct tissue ablation a temperature elevation of typically 50-80°C is applied during a short amount of time in order to achieve the lethal dose leading to cell death of the tumorous tissues [6]. In the case of hyperthermia triggered local drug delivery, which is under active investigation, the therapeutic agent is encapsulated in thermosensitive nanocarriers and released in the target area by mild hyperthermia (typically few degrees of temperature increase). This approach opens great perspectives to increase the drug concentration with an effect limited to the tumorous area.

Direct tissue ablation through local hyperthermia can be achieved using different heating modalities such as laser [2], radio frequency [3] or high intensity focused ultrasound [4] ablators. The clinical potential of all three treatment modalities are under investigation for the ablation of cancer in various organs such as the breast [7, 8, 9, 10], in the prostate [11], in abdominal organs (the kidney or the liver) [12], and the brain [13]. The possibility to achieve a localized lesion in a mini- or non-invasive way makes these approaches very attractive. However, the success of these therapeutic processes require a precise monitoring and control in real time of the delivered energy. Magnetic resonance imaging (MRI)

has been suggested as a promising candidate for this role. MR-guided ablation has been evaluated for laser heating [14, 15], radio frequency (RF) heating [16, 17] and high intensity focused ultrasound (HIFU) heating [18, 19, 20, 21, 22, 23]. Since HIFU allows a non invasive treatment, this ablation modality appears particularly attractive. HIFU based ablation therapy has already matured into clinical routine for a variety of tumor types such as uterine leiomyoma [24, 25]. MR-guided HIFU ablation is also under investigation and shows promising results for prostate cancer [26], palliative treatment of bone metastases [27] or treatment of brain tumor / cerebral glioma [28] and in abdominal organs such as the kidney and the liver [22, 23].

1.1.1.2 Treatment of heart arrhythmia and atrial fibrillation

Another clinical application of localized hyperthermia concerns the treatment of heart arrhythmia such as atrial fibrillation. Heart arrhythmia refers to abnormal electrical stimulation of the heart muscle leading to ineffective contraction. Normally, the heart beat is triggered by an electrical impulse produced by a small area in the right atrium of the heart called the sinus node. The signal "travels" from one side of the heart (right atrium) to the other (ventricle) where it stops (see figure 1.1.a). A disturbance of the propagation speed of this signal can lead to bradycardia (a slow signal from this sinus node) or tachycardia (a high rhythm that is not necessary an arrhythmia since this effect is the normal response to physical exercises or emotional stress). Abnormal electrical activity of the heart can also be caused by the electrical impulse generated from a group of fibers outside the sinus node. This effect can lead to chaotic electrical impulses in the heart generating irregular and fast heart beats (see figure 1.1.b). The generalization of this phenomenon to an entire chamber is referred to as fibrillation. This can affect the atrium (atrial fibrillation (AF)) and the ventricle (ventricular fibrillation). Atrial fibrillation usually generates a number of symptoms such as palpitations, higher fatigability, shortness of breath and can results in long term to heart failure.

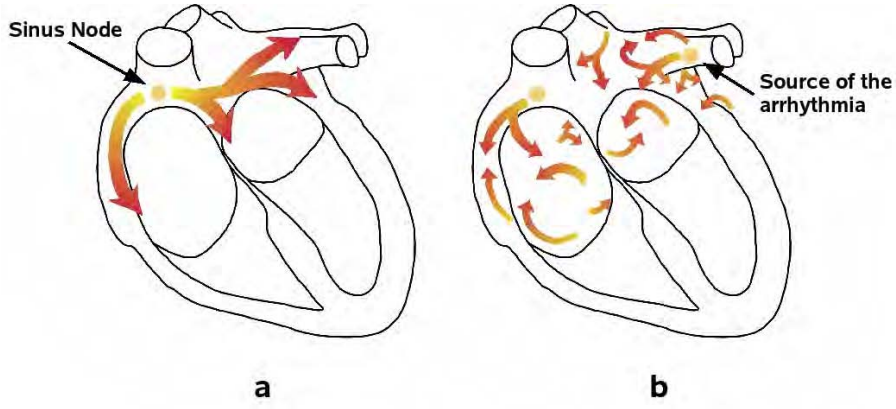

Figure 1.1: Electrical activity of the heart: (a) normal electrical activity, (b) electrical activity in presence of arrhythmia.

The two main therapeutic approaches to treat atrial fibrillation are the use of antiarrhythmic drugs and cardioversion. Antiarrhythmic drugs aim to restore a normal rhythm but are often accompanied by serious side effects. Cardioversion consists in administering an electrical discharge to the heart wall to change the electrical impedance of the tissue and thus to remove the cause of the fibrillation. Cardioversion allows to return to normal sinus rhythm immediately after the procedure in 86% of the cases and the success rate increases to 94% when antiarrhythmic medications are given before cardioversion. However, the long term therapeutic success is for 77% of the treated cases limited to the first year

and additional treatment may be needed [29]. Therefore, clinical research in the field of cardiology aims to develop new therapeutic approaches to improve the success rate of atrial fibrillation treatment. One of the most promising strategies is based on tissue ablation in order to change the electrical impedance of the problematic tissue of the heart [30, 31]. The intervention is usually accomplished with a catheter that applies radio frequency in the desired area. This induces a necrosis that renders the tissue electrically inactive and thus incapable to conduct the electrical impulse. This treatment is already in clinical routine [32, 33, 34, 35] but a therapeutic failure rate of 30 % is observed likely due to insufficient or excessive temperature exposure. In this thesis, the potential of MR-guided catheter ablation is investigated in order to monitor and control delivered energy during the intervention.

1.1.2 Heating devices

Hyperthermia can generally be generated by several devices such as laser, microwave, radio frequency or high intensity focused ultrasound. In this thesis, we focus on both radio frequency and HIFU ablation.

1.1.2.1 Radio frequency

Radio frequency ablation (RFA) is a mini invasive approach that uses high frequency electrical current through a needle electrode to induce resistive heating in the target region which leads either to direct cauterization or apoptosis.

1.1.2.2 High Intensity Focused Ultrasound

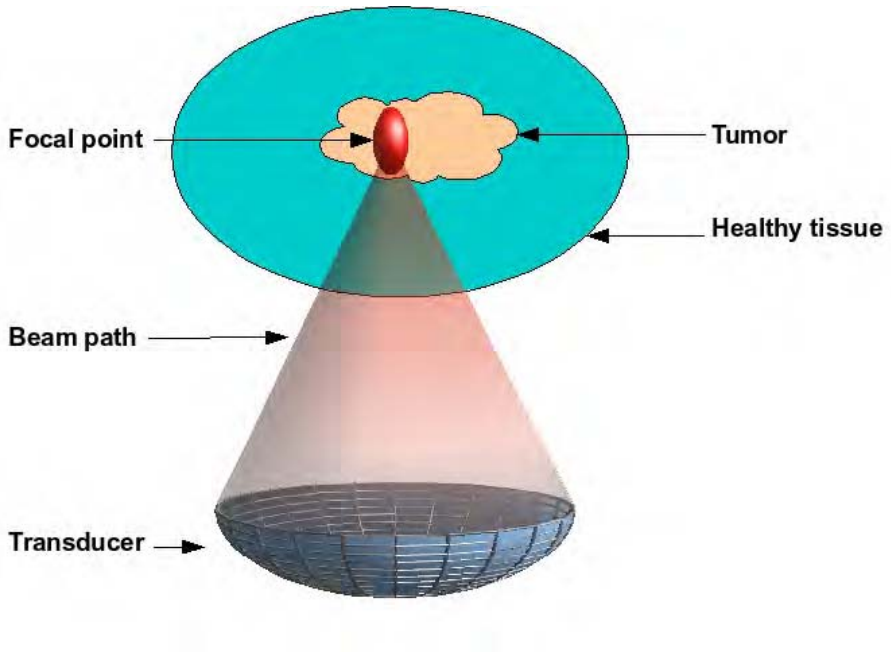

Figure 1.2: Principle of HIFU ablation

Ultrasound is an acoustic sound wave with a frequency beyond the audible spectrum of the human ear (typically greater than 20 kHz). As the acoustic waves propagate through the tissue, part of it is absorbed and converted to heat. In order to obtain a localized ablation, transducers composed of several ultrasound elements can be used to achieve a focused beam onto the ablation area in a non-invasive way. By adjusting the relative

phases of each element, converging wavefronts are created, which add their energy in the beam focus due to constructive interference (see figure 1.2). Each sonication treats a precisely defined portion of the targeted tissue. The entire therapeutic target is treated by successively focusing at several locations.

1.2 MR-guided thermal ablation

A variety of imaging modalities are available for medical imaging purposes. In the last decades, several 3D imaging techniques have been employed such as computed tomography (CT), magnetic resonance imaging (MRI) and ultrasound (US) imaging. Recently, the potential of these techniques for planning, monitoring and controlling a surgical intervention has been extensively investigated in the research community. In this thesis, we focus on MRI as the imaging modality of choice.

1.2.1 Introduction to MRI

A brief introduction to the mechanism of MR-acquisition and MR-reconstruction is presented in appendix A from the signal theory point of view. MR-scanners acquire complex data and store the digitized signal in k-space (see appendix A.1), which is a matrix of spatial frequencies that can be seen as an extension of the Fourier domain. The reconstructed image in the spatial domain is calculated using an inverse Fourier transform. The reconstructed data is a complex-value image (see figure 1.3) where its module corresponds to anatomical information (such as position and composition of the tissues) and the phase is directly proportional to the local proton resonance frequency.

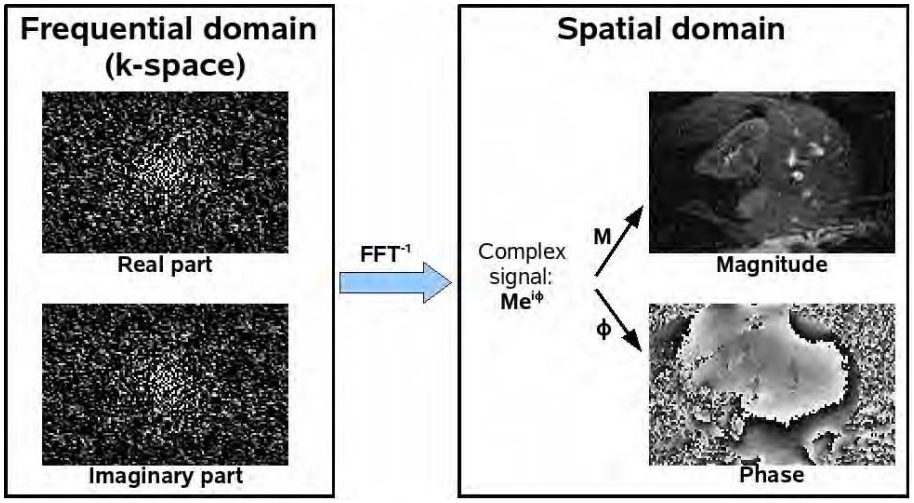

Figure 1.3: Image reconstruction from k-space data

1.2.2 MR-thermometry

MRI can be used to obtain temperature information since several tissue magnetic properties are temperature dependent. The tissue specific longitudinal relaxation time T_1 and the transversal relaxation time T_2^* as well as the resonance frequency of water proton are directly dependent on the tissue temperature [36]. In this thesis, all MR-thermometry experiments are based on the dependence of resonance frequency of water proton which is referred as proton resonance frequency (PRF) shift technique [37]. The PRF equation describes the temperature variation ΔT as being proportional to a phase variation $\Delta\varphi$ in gradient echo pulse sequence as follows:

$$\Delta T = \frac{\Delta \varphi}{\gamma \cdot \alpha \cdot B_0 \cdot TE} \tag{1.1}$$

where $C = \gamma \cdot \alpha \cdot B_0 \cdot TE$ is often called the PRF constant, with γ the gyromagnetic ratio, α the temperature dependent water chemical shift, B_0 the static magnetic field strength and TE the echo time.

This technique allows to obtain temperature information on each individual pixel.

1.2.3 MR-dosimetry: the thermal dose concept

Temperature elevation induces cell death but the relationship between the required temperature elevation and the time exposure regards to cell death is not straightforward. For these reasons, Sapareto et al. [38] have introduced the concept of thermal dose (TD) which can be formulated mathematically as follows:

$$TD = \begin{cases} \int_0^t 2^{T(t)-43} dt, \text{ if } T < 43°C \\ \int_0^t 4^{T(t)-43} dt, \text{ if } T > 43°C \end{cases} \tag{1.2}$$

The tissue destruction is achieved when the equivalent thermal dose exceeds the lethal thermal dose. The lethal thermal dose related to cell death is achieved for a temperature elevation of 43°C during 240 mn. The thermal dose thus represents a good way to determine the therapy endpoint.

Chapter 2

Challenges of MR-guided ablation of mobile organs

This chapter presents the main limitations and challenges of MR-guided ablation on mobile organs and a brief state of the art is given for each of them in order to clarify the contribution of this thesis.

2.1 Organ motion

2.1.1 Introduction to motion estimation

To understand the challenge introduced by organ motion, a first description of encountered motion is given that is followed by a presentation of the associated effects on the interventional process. Then, a brief overview of existing methods to handle and correct organ motion artifacts is detailed.

2.1.1.1 Characterization of organ motion

In our applications, three different organs are targeted: the kidney, the liver and the heart. Each of these organs has specific 3D displacement properties that are now described.

The kidney

The displacement of this organ is mainly subject to the influence of the respiration. The kidney is rather rigid and its motion can be roughly represented by a 2D periodic linear displacement.

The liver

The liver motion is also mainly influenced by the respiration and is thus periodic. Therefore, the main contribution of the motion is a linear displacement. However, some elastic deformation can be observed, especially in the upper part of the organ.

The heart

The heart displacement is subject to a more complex motion induced by the respiratory and the cardiac activities. The respiration induces a large linear displacement and the cardiac activity generates an elastic deformation. Note that these two physiological activities and their associated motion are asynchronous.

In top of of these periodic physiological mechanisms such as the respiration and the cardiac activity, a second potential source of motion is related to spontaneous motion. It corresponds to the displacement of the patient into the scanner. This type of event are unpredictable and by definition not periodic.

2.1.1.2 Effects of organ motion

Organ motion leads to several types of artifacts on MR-images that can be separated into

- a direct effect that corresponds to the displacement of the target in the image and is detailed in this section.
- indirect effects such as the modification of the local magnetic susceptibility or heating of undesirable area. These effects are presented in the sections 2.2.0.4 and 2.6.1, respectively.

The effect of the organ motion can be categorized into two parts which are generally referred to as intra-scan motion and inter-scan motion.

Intra-scan motion Intra-scan motion, corresponds to motion occurring during the MR-acquisition itself. This generally leads to image motion artifacts such as blurring and ghosting on images (see figure 2.1.c).

Several strategies have been suggested to avoid intra-scan motion artifacts: Respiratory (or cardiac) gated sequence monitor physiological activity with external sensors (such as respiratory bellows, or electrocardiogram) and synchronize the data acquisitions. Although this is efficient to cope with motion artifacts, this reduces the temporal resolution of the acquisition which, depending on the heating modality, might be insufficient to follow temperature elevation.

Optical camera can also be integrated into the MR-scanner to identify patient motion [39]. This system was first designed for functional MRI to cope with patient head motion and correct imaging plane position in real time. Although this approach is very attractive for functional MRI to remove intra-scan motion (since long acquisition schemes are often used), this is not suitable to estimate organ motion since only patient surface motion can be recorded.

Therefore, for MR-thermometry on mobile organs, fast MR-acquisition schemes are generally preferred to minimize intra-scan motion. In addition, for the particular case of MR-guided HIFU ablation, a very fast adjustment of the focal position is required in order to follow the organ motion. The combination of high frame-rate MRI with fast MR-acquisition schemes appear desirable in this case. Consequently, 3D MR-acquisition on mobile organs is hard to achieve due to the inherent problem of intra-scan motion. For these reasons, 2D acquisition or multislice acquisition (with a small amount of slices) are generally preferred where only 2D in-plane motion estimation is feasible.

Inter-scan motion Motion occurring between two acquisitions (see figure 2.1.a,2.1.b), generally referred to as inter-scan motion, is composed by an inplane component and out-of-plane component leading to a mis-alignment of MR-images and to strong artifacts on temperature and thermal dose measurement.

Out-of-plane motion yields structures that appear transient in the temporal series of MR-images. This effect is caused by organ motion in the third dimension perpendicular to imaging plane. Even with a perfect co-registration of inplane motion, this leads to the observation of different tissues over time. Therefore, the temperature and thermal dose information will be strongly artifacted. Although a 3D MR-acquisition would help to resolve this issue, another approaches have to be considered since 2D MR-acquisitions have

to be employed to get rid of intra-scan motion. Since for abdominal organs, respiratory induced motion causes predominantly a linear displacement in head-foot direction and to a lesser extend in anterior-posterior direction, a coronal or sagittal orientation of the slice positioning can help to minimize through-plane motion and reduce the problem to a 2D in-plane motion. Alternatively, tracking of the slice position can be employed for this purpose and can be achieved using a pencil beam navigator echo [40] or ultrasound images [41]. This also allows to reduce the 3D motion to a 2D in plane motion. A detailed description of available techniques to handle and correct inplane motion on MR-images is now presented.

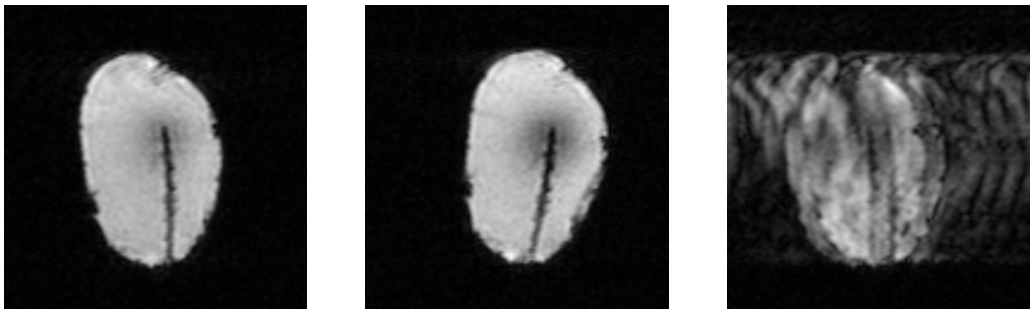

(a) (b) (c)

Figure 2.1: Illustration of motion artifact: (a) reference image, (b) image acquired at different positions of the object, (c) image acquired with a longer acquisition (intra-scan motion) leading to blurring and ghosting.

2.1.2 In-plane motion estimation

The term of in-plane motion estimation can be defined as the estimation of the displacement and of the deformation of image structures from one image to another. For this, a variety of methods have been suggested [42]. To summarize the main methods or class of methods, several classifications using various criteria have been proposed in the past. Here, we use the criteria proposed by Maintz and Viergever [42] that was specifically designed for the classification of medical image registration methods. This classification was recently took up by Markelj et al. [43] for a review of 2D and 3D registration methods designed for image-guided interventions. The classification relied on nine criteria:

- Dimensionality
- Nature of registration basis
- Nature of transformation
- Domain of transformation
- Interaction
- Optimization procedure
- Modalities involved
- Subject
- Object

We now present the constraint imposed by our application on these criteria.

2.1.2.1 Dimensionality

As previously stated, we focus in this section on 2D motion estimation since the motion in the third dimension is generally addressed using a slice tracking technique.

2.1.2.2 Nature of registration basis

This defines the type of information employed for the motion estimation process. Three types of information can be used for this purpose.

Non image based information

Navigator echoes can be used for motion estimation purpose. It corresponds to the acquisition of one or several lines crossing the k-space center which are Fourier transformed to obtain a 1D projection of the 2D image [44]. Each of these projected profiles can then be used to estimate the translational motion of the object along one direction. The acquisition of this information is very fast (few milliseconds) and thus not prone to intra-scan motion. However, only one dimensional translation displacement can be obtained. Several navigator echoes can then be positioned in the three dimensions to obtain translational displacement in the three dimensions. Although this approach may be useful for organ describing very simple displacement, this is not sufficient for the motion estimation of organ with complex deformation such as abdominal organs or the heart.

Ultrasonic echoes can also be employed to estimate the displacement of a target. It corresponds to the emission of a sound wave on a reflecting target and to the measure of the reflected ultrasound wave. An object will reflect a certain amount of the sound wave and a signal peak will be recorded along the time by the transducer. The amount of time necessary for the wave to go from the object to the transducer can then be calculated. Finally, the distance between the transducer and the object can be computed multiplying this time by the speed of the sound [45]. The acquisition of this information is very fast but suffer from the same limits that those presented for navigator echoes. Only one dimensional translational information is available. Even if the estimation can be performed in 3D using also three perpendicular transducer, the result will be insufficient to cope with the complexity of the deformation of our targeted organs. However, the acquisition of an ultrasonic echo is not synchronized with the MR-acquisition and can thus be realized in parallel to regular MR-acquisition which is a substantial advantage compared to navigator echoes.

Extrinsic information

Extrinsic information such as invasive or non invasive markers can be employed for motion estimation purpose [46, 47, 48]. However, the implantation of invasive markers appears undesirable for clinical routine since the presented therapeutic procedure are mini- or non-invasive. However, in the specific case of RF ablation, the presence of the catheter can be used for motion estimation. This approach consists of integrating an active tracking coil into a mini invasive heating device (here the catheter). The position of the active tracking coil is then detected with a receiver coil. This allows to obtain a 3D information of the displacement of a single point (corresponding to the heated tissue) [49].

Non invasive markers has gained a great interest for motion detection of the bulk (with markers directly positioned on the patient skin) but appears highly limited for mobile organ motion estimation. However, MR-imaging can be used to artificially generate non invasive markers such as tagged imaging, where images have horizontal and vertical black lines that deform along the time with the target motion. This was initially proposed for cardiac imaging in order to study the contractile function of the heart. However, temperature information cannot be estimated in area where the signal has been canceled

(i.e. on the black lines) which is limiting for monitoring and control of the whole heated area.

Intrinsic information

It corresponds to either feature based, segmentation based or voxel based motion estimation algorithms.

Feature based methods [50], often referred to as indirect approaches, try to estimate correspondences of specific areas or pixels and are then used to obtain the parameters of a motion model. Manual selection of feature points has been suggested but is not adapted to a real time therapeutic application. Therefore, feature detection algorithms are required in order to extract feature points. A large number of automatic solutions have been proposed in the literature for this purpose where a comparison can be found in [51]. One of the most famous are the Harris's points [52] or the SIFT algorithm [53]. Once estimated in both the reference image and the image to register, a matching process is required to pair each detected feature point. In order to remove outlier in the matching process, several approach have been proposed such as RANSAC [54]. After the matching process, the parameter estimation of a transformation model (generally rigid or affine model) that map each matched point is performed (since this problem is over-determined, a singular value decomposition is generally employed). This type of approach directly depends on the ability to identify anatomical structures, and thus on segmentation performance. However, segmentation is often complicated in interventional imaging on moving organs where images are generally hampered by low SNRs.

Segmentation based methods [55] extract anatomical structures on both the reference image and the image to register and try to match/fit them in order to detect the motion between both images. Segmentation algorithms generally require a priori knowledge of targeted organ such as its structure, its intensity, the surrounding tissues or the presence of fat, which are variant over the patients and thus might be limiting for a robust clinical routine. In addition, since segmentation methods are also usually hampered by low SNR, which is inherent to the employed fast MR-imaging sequences, we did not investigate so far the potential of such approaches.

Voxel-based methods [56, 57] directly rely on the voxel intensities over the whole image and several criteria has been proposed to estimate the motion such as the minimization of the squared intensity difference, the maximization of the cross correlation, the maximization of the mutual information, the Fourier domain based cross correlation, etc. These approaches are under active investigation and the main types of algorithms are presented in section 2.1.3.

2.1.2.3 Nature of transformation

A transformation model has to be defined in order to characterize the targeted organ motion or in other words to relate the image to register to the reference image. Therefore, the choice of the transformation model has to be realized in accordance with the organ motion characteristics. A transformation model is usually defined by a limited number of parameters which depends on the type of the transformation. The most popular transformation models are the translation model (two translation parameters), the rigid model (two translation and one rotation parameters), the affine model (two translations, one rotation, two scaling and one shear parameters) or more sophisticated models as shown in Figure 2.2.

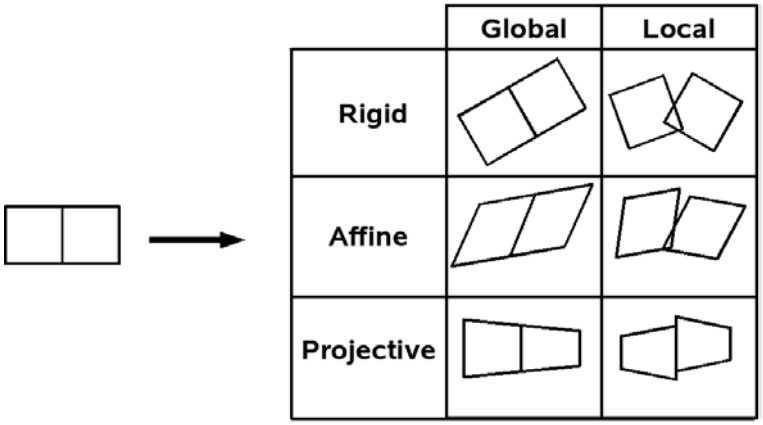

Figure 2.2: Examples of transformations

2.1.2.4 Domain of transformation

The transformation model can be global (over the whole image or a part of an image), at block level (group of pixels) or even at pixel level. For motion estimation on mobile organs, it was shown that a global model (affine) can be employed to retrieve the global motion of the target, followed by a voxel-based model (translational) to refine the solution [58].

2.1.2.5 Interaction

User interaction has to be minimized in order to make the procedure suitable for use in clinical routine. Nevertheless, small interactions such as a prior masking of the targeted organ in a reference image (that only requires few seconds) are often proposed in current works.

2.1.2.6 Optimization procedure

The search method of the transformation parameters is generally determined by motion estimation problem formulation. Further refinement and acceleration of parameter search can also be obtained using a coarse-to-fine strategy (based on estimation at lower resolution). Sub-sampled images have a better SNR with smaller displacement than native resolution images. The parameter of the transformation model are first estimated at the lower resolution and used as initialization for superior resolution. This process is repeated for each resolution level toward the native resolution [59].

2.1.2.7 Modalities involved

Multimodal imaging is under active research for motion estimation purpose [60, 61]. However, only MR-scanner was available in our laboratory, therefore this thesis focused on monomodal motion estimation based on MRI.

2.1.2.8 Subject

The motion estimation and compensation is fulfilled individually for each patient which is called intra-subject registration.

2.1.2.9 Object

The targeted organ (the kidney, the liver and the heart) and their characteristic motion have been presented in the introduction of this chapter (see section 2.1.1.1).

2.1.3 Voxel-based motion estimation using intrinsic image information

2.1.3.1 Global transformation model estimation

Non spatial domain based methods

Based on the properties of the Fourier transform (Fourier shift theorem, Fourier rotation theorem or Fourier scale property), several estimation methods conduct the motion estimation in the frequency domain [62, 63].

The Fourier shift theorem states that a translation displacement in the spatial domain corresponds to a phase shift in the frequency domain. If we consider an image to register that is translated from a vector x_0, y_0 from the reference image, then the inverse Fourier transform of the cross power spectrum will be a Dirac delta function centered in (x_0, y_0). This method is often referred to as phase correlation technique [62].

If images differ from translation, rotation, a more sophisticated strategy is required. The Fourier rotation theorem states that a rotation in the spatial domain corresponds to a rotation in the frequency domain. Therefore, by taking polar coordinates of the image in the Fourier domain, the rotation will be transformed into a translation. Then the phase correlation technique is used to get the rotation parameter. Once rotation has been removed, translational parameters can be estimated using the same phase correlation technique [63].

In case where images differ with respect to translation, rotation and scale, the process is even more complex. The rotation and scaling are first estimated using the modulus of the Fourier transform in logarithmic-polar representation (where a rotation is always a translation in polar coordinate and a scaling is a translation in logarithmic representation). Both translations are then estimated using the phase correlation technique and corrected. Finally, the translational parameters are estimated using the direct phase correlation technique [63].

Note that several alternatives data representation have been suggested for motion estimation purposes such as the wavelet transform [64] or the Hough transform [65, 66, 67].

Intensity based methods

Here, the motion model is defined as a geometric transformation T over a whole image I or a part of an image. This type of model generally has a limited number of parameters θ (translation, rotation, scaling, shears, etc) compared to the number of pixel where the model is expected to be valid. This leads to an over-determined system that is generally resolved using minimization approaches S such as gradient descent, Gauss Newton, Marquardt-Levenberg, etc. The associated cost function F to minimize is often based on image intensity criterion such as mean square error, correlation coefficient, inter-correlation coefficient, or mutual information, etc. The optimal transformation parameters $\theta_{optimal}$ can thus be obtained as follows:

$$\theta_{optimal} = \underset{\theta \in T|S}{\operatorname{argmax}} F(I_{ref}, T(I, \theta)) \tag{2.1}$$

with I_{ref} the reference image.

2.1.3.2 Local transformation model estimation

Pel-recursive methods

Pel-recursive methods are based on the hypothesis of intensity conservation of a point along its trajectory, which is expressed by the following expression:

$$DFD(x, y, t) = I(x + dx, y + dy, t + dt) - I(x, y, t) = 0 \tag{2.2}$$

where DFD stands for displacement frame difference. Here, the problem of motion estimation is ill posed since only one equation is provided, but with two unknowns (dx and dy). Pel-recursive algorithm predicts recursively the displacement of each pixel from its neighbor pixels. This approach relies on estimators of the iterative form:

$$d_{k+1}(x, y, t) = d_k(x, y, t) + up(x, y, t) \tag{2.3}$$

where $d_k(x, y, t)$ is one dimensional estimation motion vector at the location (x, y) and time t at the k^{th} iteration and $up(x, y, t)$ is the update term. The first Pel-recursive algorithm was proposed by Netravali-Robbins [68] that aims to minimize iteratively the DFD^2 using the steepest descent technique. A modified version was proposed by Cafforio-Rocca [69] to obtain an adaptive gain as a function of the gradient amplitude (i.e. a high gradient value generates a small step factor).

Variational techniques

Variational techniques, often referred in the literature to as "optical flow techniques", also rely on the hypothesis of intensity conservation of a point along its trajectory. The minimization of the DFD^2 (see equation (2.2)) is here derived from the following Taylor approximation of the image signal:

$$I(x + dx, y + dy, t + dt) = I(x, y, t) + I_x dx + I_y dy + I_t dt + ... \tag{2.4}$$

with $(I_x, I_y, I_t) = (\frac{\partial I}{\partial x}, \frac{\partial I}{\partial y}, \frac{\partial I}{\partial t})$.

By ignoring high order derivative terms of the Taylor approximation in equation (2.4), the DFD is then reduced to:

$$DFD = I_x dx + I_y dy + I_t dt = 0 \tag{2.5}$$

leading to the famous optical flow constraint equation:

$$I_x u + I_y v + I_t = 0 \tag{2.6}$$

where $(u, v) = (dx/dt, dy/dt)$ represents the displacement vector

The motion estimation problem is then reduced to the minimization of the functional:

$$E = \iint_{xy} \left[I_x u + I_y v + I_t\right]^2 dxdy \tag{2.7}$$

However, the existence of a solution cannot be guaranteed (especially if $\nabla I = 0$). Moreover,the uniqueness of the solution cannot be ensured since we only have one equation with two unknowns (referred to as the aperture problem). To overcome these limitations, additional constraints are required and a variety of algorithms has been proposed in the literature and are now presented.

Initial approach

The first approach was presented by Horn & Schunck [70]. An additional regularization term was proposed in order to impose the motion field to be locally smooth expressed by the following minimization:

$$E_{reg} = \iint_{xy} (\|\nabla u\|_2^2 + \|\nabla v\|_2^2) dxdy \tag{2.8}$$

where $\|\nabla u\|_2^2 = u_x^2 + u_y^2$ and $\|\nabla v\|_2^2 = v_x^2 + v_y^2$, with ($u_x = \partial u/\partial x$, $u_y = \partial u/\partial y$, $v_x = \partial v/\partial x$, $v_y = \partial v/\partial y$)

Therefore, the general minimization problem proposed by Horn & Schunck is described with the following function:

$$E_{hs} = \iint_{xy} \left([I_x u + I_y v + I_t]^2 + \alpha^2 \left[\|\nabla u\|_2^2 + \|\nabla v\|_2^2 \right] \right) dxdy \tag{2.9}$$

where α^2 is a weighting factor designed to link the two individual metrics (intensity variation and motion regularity).

This functional is then minimized solving the system provided by the calculus of variations and the Gauss Seidel method that provides the following iterative scheme:

$$\begin{cases} u^{n+1} = \overline{u}^n - I_x \dfrac{\overline{u}^n I_x + \overline{v}^n I_y + i_t}{(I_x^2 + I_y^2) + \alpha^2} \\ \\ v^{n+1} = \overline{v}^n - I_y \dfrac{\overline{u}^n I_x + \overline{v}^n I_y + i_t}{(I_x^2 + I_y^2) + \alpha^2} \end{cases} \tag{2.10}$$

with $\overline{u}$ and $\overline{v}$ the mean values of the velocity field on the neighborhood of each estimated point. Details of the derivation of the numerical scheme are included in Appendix C.

Intensity variations modeling

Since the main idea of optical flow technique relies on the assumption of intensity conservation, some approaches tried to relax this constraint, integrating into the variational framework a model of the intensity variation. The first proposition was presented by Cornelius and Kanade [71] where the intensity variation was modeled as a constant variation as follows

$$I(x + dx, y + dy, t + dt) = I(x, y, t) + c(x, y, t) \tag{2.11}$$

They also imposed c to be locally smooth since an intensity variation is usually spatially smooth. The minimization problem became:

$$E_{ck} = \iint_{xy} \left([I_x u + I_y v + I_t - c]^2 + \alpha^2 \left[\|\nabla u\|_2^2 + \|\nabla v\|_2^2 \right] + \beta^2 \|\nabla c\|_2^2 \right) dxdy \tag{2.12}$$

where u, v and c were the three unknown parameters to be estimated. The minimization problem was reduced to an iterative scheme using the same strategy as for Horn & Schunck approach.

Another method was proposed by Gennert and Negahdaripour [72] and modeled the intensity variation in a linear way such as

$$I(x + dx, y + dy, t + dt) = m(x, y, t) I(x, y, t) + c(x, y, t) \tag{2.13}$$

where $m(x, y, t)$ is the linear coefficient. The solution can also be computed using the variation calculus and the Gauss Seidel approach.

Oriented smoothness approach

Discontinuities in optical flow at object boundary can occur and are hard to estimate with the previous formulations since the smoothness of the motion field is imposed in the whole image. To overcome this limitation Nagel proposed a novel formulation that proposed an oriented-smoothness constraint on the motion field [73]. In its proposition, motion field smoothness is not imposed across high intensity gradients. This work was proposed in order to model occlusions. The variational framework was as follows:

$$E_n = \iint_{xy} \Big([I_x u + I_y v + I_t]^2 + \frac{\alpha^2 \left[(u_x I_y - u_y I_x)^2 + (v_x I_y - v_y I_x)^2 + \delta \left(\|\nabla u\|_2^2 + \left[\|\nabla v\|_2^2 \right] \right) \right]}{\|\nabla I\|_2^2 + 2\delta} \Big) dxdy \tag{2.14}$$

with δ a constant.

Robust optical flow estimation

In the presented variational framework, the estimation tries to fit a model using data hampered by noise. However, the influence of pixels depicting high intensity variation due to the noise (that can be considered as outlier) may deteriorate the model fitting process. In robust statistics, a robust estimator is designed to give less importance to outliers. As demonstrated by Hampel et al. [74], the influence function, that characterizes the bias that a measurement has on the solution, can be determined by the derivative of the estimator function. For example a quadratic function, which is used in all previously presented model, $\rho(x) = x^2$ has a derivative $\Sigma(x) = 2x$ that means that outliers influence increases linearly with their distance to the true value. In order to decrease outlier influence, an estimator must give less importance to values far from the true value. For these reasons, several propositions were made such as the Lorentzian estimator (represented in Figure 2.3) defined as

$$\rho_\sigma(x) = log(1 + \frac{1}{2}(\frac{x}{\sigma})^2) \tag{2.15}$$

and its derivative as

$$\Sigma_{\sigma(x)} = (\frac{2x}{2\sigma^2 + x^2}). \tag{2.16}$$

Note that the derivative of the Lorentzian tends to 0 for infinity values.

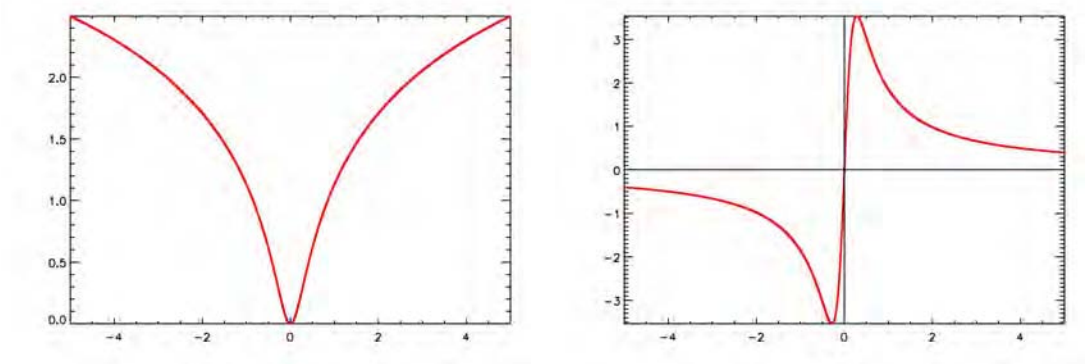

Figure 2.3: Illustration of the Lorentzian estimator: (a) Lorentzian function (with σ=0.2), (d) derivative of the Lorentzian function (with σ=0.2).

Using this robust estimator, Black and Anandan proposed a robust estimator for optical flow estimation [75]. Assuming that the motion is constant in a region, they proposed the following minimization:

$$E_{ba} = \iint_{xy} \rho\left([I_x u + I_y v + I_t]\right) dxdy \tag{2.17}$$

where all the previously presented regularization terms could have been added.

Other algorithms

A large number of optical flow approaches has been proposed in the last three decades. Combinations of the different ideas has also been intensively investigated as for example robustness principle and intensity variation (Kim et al. [76]).

2.1.3.3 Discussion

To register time series of MR-images to a reference position, two approaches can be employed using either absolute motion estimation (where the motion in each frame is estimated to a common reference frame) or additive relative motion estimation (by summing estimated motion on each successive frame). A relative estimation takes benefits of the small displacement present between two successive frames (under fast MR-acquisition scheme). However, the summation of each estimated motion, required to register each frame to a common position, also implies the error/uncertainty summation of each estimation. Therefore, absolute motion estimation is generally privileged.

For the specific application on mobile organs, it was shown that a good solution was the combination of two direct methods using a global motion estimation (estimating a global affine model) combined with a local motion estimation (based on optical flow approach) [58]. However, these algorithms suffer from their high computation time for real time applications. Recently, Denis de Senneville et al. [77] have shown that GPU implementation can substantially reduce this time offering new opportunities to real time applications. Another limit is the number of free parameters present in the different models that represents an open question for clinical use of these methods where a manual calibration of the parameters in function of the type of images (SNR, resolution, organ, etc) is hardly feasible.

2.2 Correction of motion induced B_0 variation

2.2.0.4 Introduction to motion induced magnetic field variation

An indirect consequence of organ motion concerns the induction of magnetic field susceptibility variation (see figure 2.4). The magnetic susceptibility is a property of an object to generate a magnetic field when positioned into an exterior magnetic field. In such a case, the global magnetic field is modified. As the temperature variation, this effect generates a local additional shifts on MR-phase images. Although this effect is negligible on assumed static target, with mobile target it induces an apparent temperature modification, which can bias or even completely mask the true temperature evolution induced by the energy deposition.

Therefore, the determination of the reference phase image (ϕ_{ref}, from equation (1.1)) for PRF-based MR-thermometry is not straightforward and would require a precise modeling of the inhomogeneous magnetic field. Although this is hard to achieve under real time conditions, several alternative strategies have been proposed to correct motion related errors in PRF-based MR thermometry.

(a) (b)

Figure 2.4: Illustration of motion induced phase variation: (a) and (b) are two images acquired at two different time points in the respiratory cycle.

2.2.1 Multi-baseline based correction

Multi-baseline approaches are based on a learning step (prior to heating) where the relation between motion and phase variation is "learned".

2.2.1.1 Atlas-based approach

In atlas-based approach (see figure 2.5) [58, 78], a set of N images are acquired before hyperthermia. Magnitude together with co-registered phase images are stored in a look-up table. During hyperthermia, a reference phase image is obtained for each new acquired image using this reference collection dataset. For this purpose, the current magnitude image is compared to each magnitude image of the collection by computing the list of inter-correlation coefficients. Finally, the phase image associated to the magnitude of the collection with the maximal inter-correlation value is selected and used as the reference phase for PRF-thermometry computation.

This approach is designed to correct MR-thermometry artifacts on organs that are subject to a periodic displacement due to the respiratory cycle. Since phase variations are "learned" in a preceding learning step and subsequently applied to correct the MR-thermometry during the intervention, the method can intrinsically not correct for MR-thermometry artifacts associated with spontaneous motion. If during hyperthermia new positions are observed, a recalibration of the phase correction data is required. This task can be completed in the relatively short time of two to five respiratory cycles because of the high imaging frame-rate. However, for the case of low frame-rate imaging a complete re-calibration leads to long interruptions of the temperature measurements and thus to potentially unacceptable interruptions of the intervention. Finally, this method allows an accurate correction of susceptibility related phase changes even in regions with complex susceptibility distributions or signal discontinuities such as organ boundaries.

2.2.1.2 Linear fit modeling approach

An extension of the atlas-based approach has been proposed that aims to model before hyperthermia a linear relation between phase variations and motion variations in a pixel by pixel basis (see figure 2.6 [79, 80]. For this, a set of N images are acquired before hyperthermia where magnitude, registered phase images and estimated motion descriptors are stored in a look-up table.

Temporal phase unwrapping A temporal unwrapping is performed on phase images to prevent jump of 2π due to the periodicity of the phase. For this, phase images are first

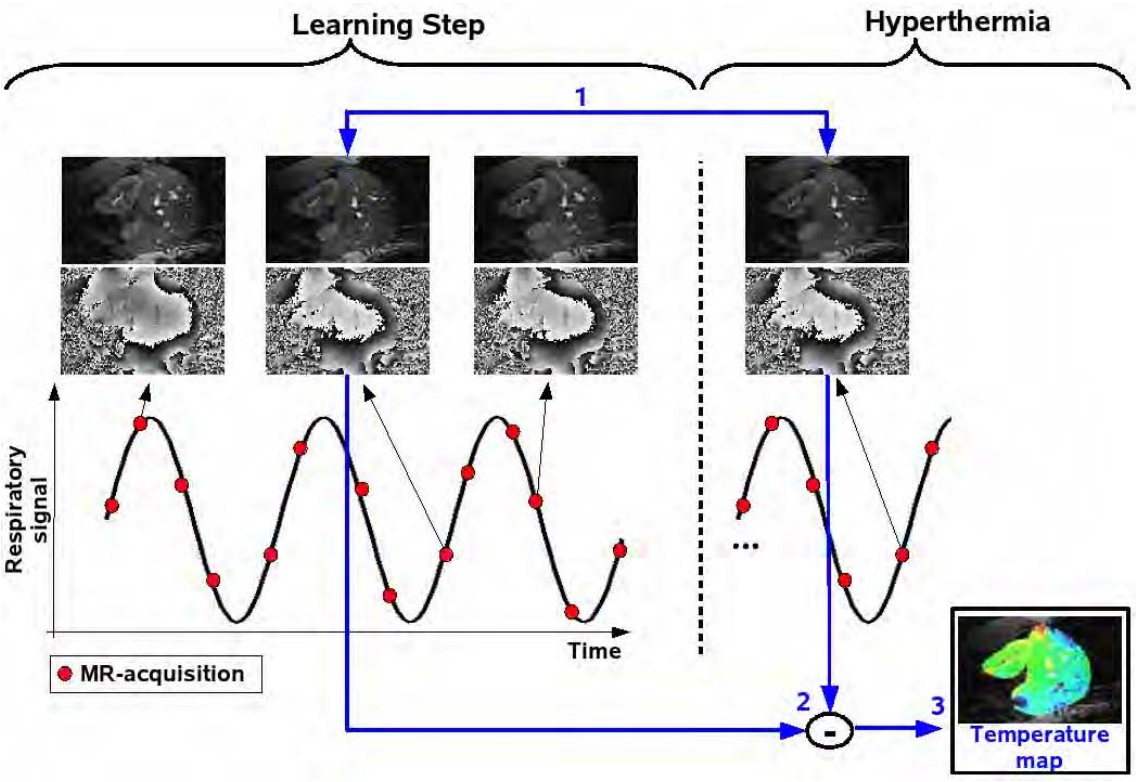

Figure 2.5: General scheme of the atlas-based approach.

reordered over time in function of their corresponding displacement vector amplitude and subsequently phase unwrapped.

Motion descriptor extraction Motion descriptors T^t are generally associated with a motion representation basis. For example, motion estimation algorithm based on parametric model decomposes the motion into M different components. In the case of an affine model, $M = 6$ components are estimated (two translations, one rotation, two scale, one shear). In this case, motion descriptors could be represented by these 6 components. However, this type of representation basis is limited to global motion representation. To obtain a more refined and optimal decomposition, a principal component analysis (PCA) can be applied to the N motion fields (estimated with any motion estimation algorithm). This allows to decompose any series of N motion fields into an optimal basis of M motion fields (with $M \ll N$). Consequently, each motion field can be decomposed as a linear combination of each basis element and the M linear coefficients can be used as motion descriptors.

Linear model estimation For each individual voxel, a system of N equations expressing the unwrapped registered phase (ϕ_t) as a linear combination of the M motion descriptors (noted T_i^t, $0 \leq i < M$ is the index of the basis component, and $0 \leq t < N$ is the index of each image of the pre-treatment step) is given by:

$$\phi_t(x, y) = \sum_{i=0}^{M-1} T_i^t P_i(x, y) + P_M(x, y), \forall t, 0 \leq t \leq N - 1 \tag{2.18}$$

where (x, y) denotes pixel coordinates, P_i, $(0 \leq i < M)$ are the unknowns and can be intuitively seen as a parameterized magnetic field model. This results in an overdetermined system resolved using a Singular Value Decomposition (SVD) .

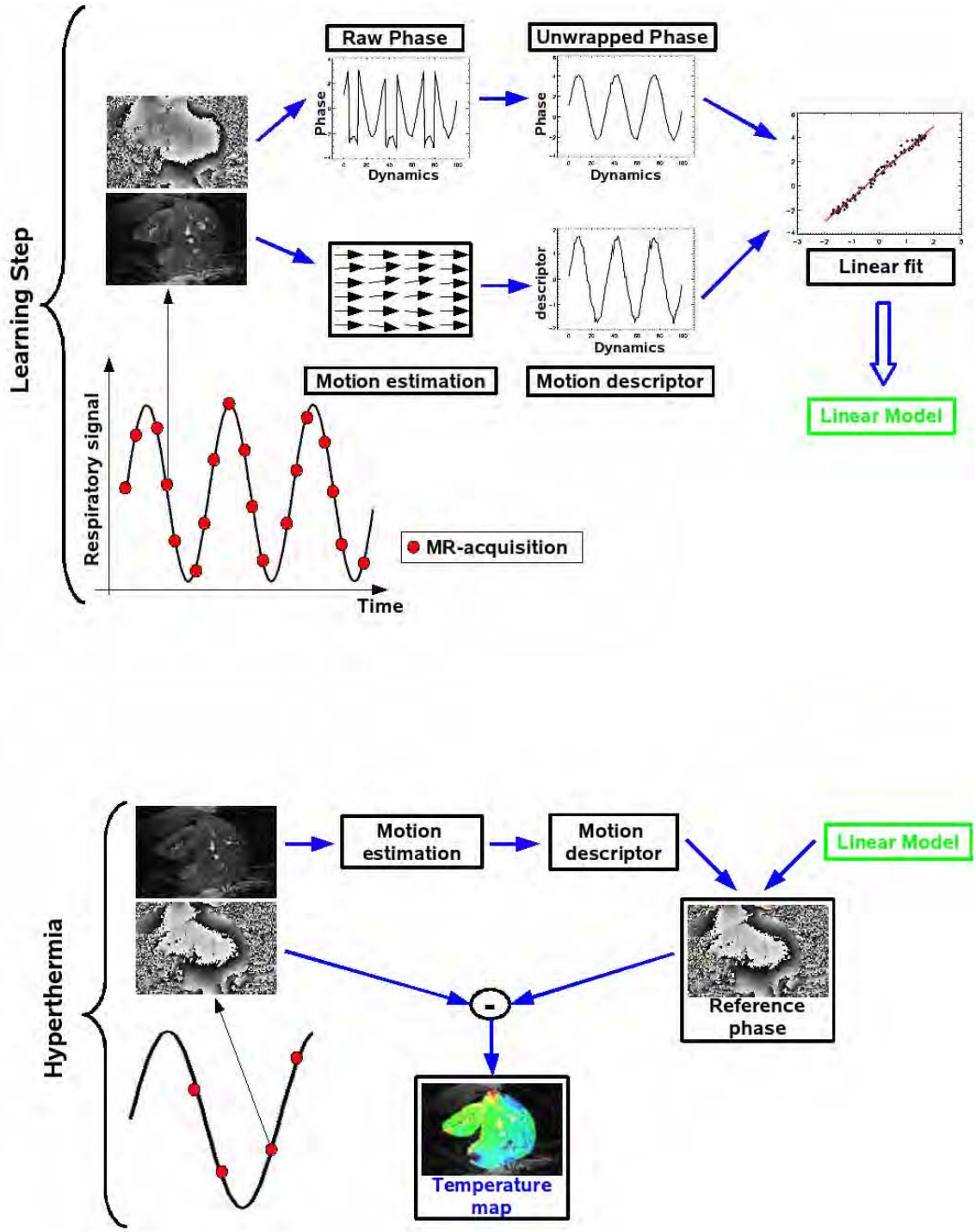

Figure 2.6: General scheme of the linear model approach.

Determination of the reference phase image during hyperthermia For each image acquired during the learning phase, the motion descriptors are calculated and used with the P_i (calculated from equation (2.18)) to compute a synthetic reference phase map (ϕ_{ref}) as follows:

$$\phi_{ref}(x,y) = \sum_{i=0}^{M-1} T_i^t P_i(x,y) + P_M(x,y),\ \forall t, 0 \leq t \leq N-1 \tag{2.19}$$

This reference phase map is then used with the current acquired registered phase image for PRF-thermometry computation.

The linear fit modeling approach extends the atlas based approach and allows to improve the results with respect to the three following aspects. First, the correction is not constrained to positions present in the collection, but can also be interpolated to intermediate positions, which significantly reduces discretization errors and the required number of images in the correction data set. Second, while the atlas based correction can intrinsically not correct for motion amplitudes higher than the ones observed in the learning phase, the phase model allows extrapolation and can still provide an estimate of the reference phase. Finally, since the reduced set of P_i coefficients is derived from the resolution of an overdetermined system of 50-100 reference images, noise will be reduced on the synthetic reference phase images. Ideally, the noise contribution on temperature uncertainty can thus be reduced by a factor of 2 (as optimally $\sigma(\phi_{ref})$=0).

On the other hand, the linear fit modeling approach introduces several new problems compared to the atlas based approach: The magnetic field perturbation is estimated assuming a simple linear magnetic field variation with organ displacement. Although this assumption holds in general for small displacements, the precision of this simple model must be carefully evaluated in regions displaying large motion amplitudes or large susceptibility variations, such as in the vicinity of the digestive tubes, or at the lung/liver/heart interface. This can in practice be achieved by simply mapping, during the learning step, the fitting error ε(x,y), which can be obtained by subtracting the measured phase from the reference image computed from the linear model. This also allows to discard regions where low signal levels in conjunction with large susceptibility variations that may prevent a successful temporal phase unwrapping that is required to adjust the linear model to the phase data.

2.2.2 Referenceless based correction

In this approach, a reference phase image is obtained by fitting a polynomial function from a region of interest (ROI) outside the heated area of the measured phase image (see figure 2.7) [81]. In order to avoid fitting problems due to spatial phase wraps, phase-unwrapping is applied in the ROI before fitting. The appropriate size and location of the ROI as well as the optimal polynomial order for the phase fit are determined before heating.

This correction is only based on the current image and do not require any learning phase. Therefore, this method can correct susceptibility related phase changes induced by any type of motion (even non-periodic such as spontaneous motion).

This approach requires an a priori choice of a ROI to estimate a polynomial fit of the phase in order to derive the reference phase. The performance of this approach depends largely on optimal ROI placement, size, and shape. Ideally, the fitting ROI should encompass the ablation area and should be sufficiently close to allow a precise estimation of the background phase in the target area. On the other hand, the fitting ROI should also be sufficiently far to avoid contamination of the fit due to heat diffusion/conduction, and should not encompass areas displaying strong local susceptibility variations.

The limitations of this approach become evident when application scenarios do not permit to fulfill all four conditions simultaneously, such as minimally invasive ablation, or interventions at the boundary of organs:

- In the first case of minimally invasive ablation, strong local B_0 variations are typically present in the ablation area when invasive ablation devices such as RF-electrodes,

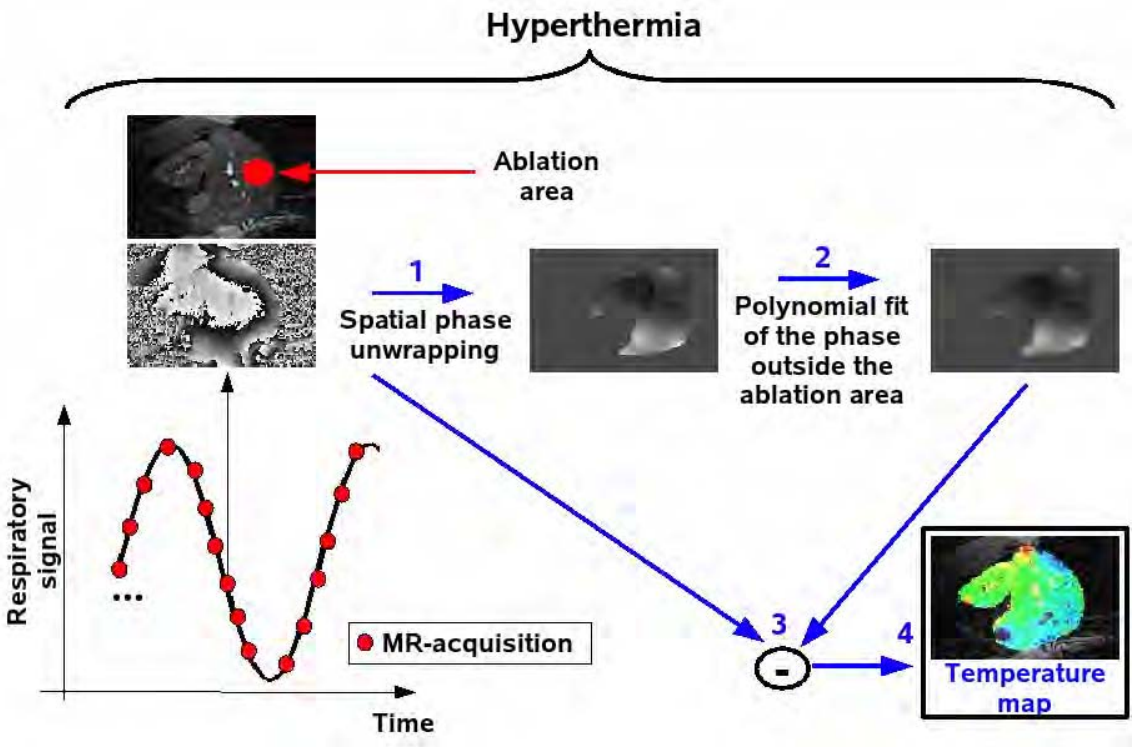

Figure 2.7: General scheme of the referenceless approach.

laser-fibers or cryo-ablators are employed. These local variations cannot be modeled by a polynomial fit based on far field data. This in turn leads to incorrect estimates of the background phase and consequently to temperature offsets in the vicinity of the device. Therefore, due to the exponential dependence of the thermal dose on the temperature, these systematic offsets have a large impact on the accuracy of the time estimate when the necrosis occurred.

- Another limit of the method appears when the ablation area is in the vicinity of an organ boundary and does not allow the fitting ROI to encompass the ablation area. In this case, the polynomial fit can not be used to interpolate the background phase, but to perform an extrapolation. This leads to reduced precision of the fit, in particular since the susceptibility variations on the organ boundaries lead to large B_0 fluctuations.

2.3 Temporal drift of the magnetic field

Although recent MRI designs have excellent spatial magnetic field homogeneity, their field is not entirely stable over time when sustained high frame-rate imaging is applied. Sustained high frame-rate imaging may lead to spatio-temporal fluctuations of the external magnetic field. These fluctuations have been observed due to frequency drifts of the exciter/receiver system, or by temperature changes in the shimming material of the scanner due to the high load on the gradient coils. Therefore, temporal drift of phase images can be observed and the subtraction of phase images acquired at different times can be affected with a different bias for each pixel [82, 83]. This effect has to be removed prior to temperature estimation.

2.4 Image noise and temperature precision

Noise mainly comes from two sources: thermal noise (coming from patient body and its thermal motion) and different scanner elements (coils, electronics, wire, etc). Noise can be quantified using the signal to noise ratio (SNR) defined as follows:

$$SNR = \frac{\bar{I_S}}{\sigma(I_N)} \tag{2.20}$$

where $\bar{I_S}$ denotes the average of the signal in the target area and $\sigma(I_N)$ is the standard deviation of the signal in the noise. To manage the SNR, a lot of MR-parameters can be modulated such as the voxel size (the higher the voxel signal, the higher the SNR), signal averaging (repetition of the acquisition to average the signal), etc. Noise can also be reduced in post processing using imaging processing techniques such as spatial or temporal filtering. Note that the theoretical minimal temperature precision (T_{theo}) achievable for a given SNR is given by the following equation [84]:

$$T_{theo} = \frac{\sqrt{2}}{SNR.\gamma.\alpha.B_0.TE} \tag{2.21}$$

where $C = \gamma.\alpha.B_0.TE$ defines the PRF constant described in 1.2.2.

2.5 The rib obstacle

In the case of HIFU heating, the beam path goes through a number of different tissues. In particular, one of the main limiting factors of an HIFU experiment in an organ such as the liver, arises from the rib obstacle. Here, the HIFU beam has to go through the ribs in order to reach the liver. However, ribs have the propriety to heat more or less 7 times faster than a regular tissues. Therefore, a strategy to decrease rib heating is required. For this, elements of the transducer responsible for undesired heating are either switched off or modulated in their amplitude or phase [22, 85, 86].

2.6 Spatio-temporal control of delivered power

The control of the intensity and the location of the applied power is an important issue for HIFU ablation. With an insufficient heating, abnormal cells will survive leading to disease reappearing. On the other hand, an uncontrolled heating may lead to the destruction of healthy tissue. In the case of mobile organs, the spatio-temporal control of the HIFU beam may be required in order to

- follow the organ motion to prevent heating of undesired area.
- perform volumetric heating strategy to treat larger volume.

2.6.1 Beam steering for motion compensation

Previous studies on MR-target tracking of abdominal organs in the field of radiation therapy [87, 88] and HIFU-beam steering [58] have been realized. In this study, the aggregated time of the MR-image acquisition, the data transport, the image analysis and the final beam correction was in the order of 150-250 ms. Nevertheless, the kidney of a healthy adult volunteer moves under free-breathing conditions at rest with a period of 3-5 s and a motion amplitude of 10-20 mm. Assuming an ideal sinusoidal motion pattern this allows the peak velocity to be estimated between 6 and 20 mm/s. Therefore, a tracking error of more than 5 mm is expected due to the latency of the calculation. Since such an error margin

is for therapeutic purposes in general not acceptable, sophisticated algorithms for trajectory prediction have to be employed to compensate for this latency. Since most of these algorithms rely on the periodicity of the respiratory cycle, they require stable breathing patterns of several seconds of adaptation before they can provide robust predictions. This condition is generally well full-filled for the case of mechanically assisted ventilation for patients undergoing an intervention under general anesthesia. However, currently most HIFU-interventions are carried out under free-breathing conditions. For free-breathing patients the respiratory cycle is subject to variations in frequency and amplitude and to spontaneous fluctuation/deviations due to non-nutritive swallowing or coughing. Since such events are intrinsically hard to predict, they firstly can lead to large short-term tracking errors and secondly to a destabilization of the prediction algorithm. Therefore, the minimization of the latency is one the main concern to improve the robustness of beam steering.

2.6.2 Beam steering for volumetric heating strategy

Several works attempted to control the energy deposition in space and in time. The feasibility of an automatic control of the temperature based on an automatic proportional, integral, and derivative (PID) temperature feedback loop has been first demonstrated [89, 90] without MRI. The help of fast MR-thermometry for temperature control have been then demonstrated in a single point [91] and for several points [92]. A spatio-temporal control over a predefined volume was then proposed by Mougenot et al. [93] where the strategy was to heat the voxel depicting the larger difference from the desired target temperature.

2.7 Clinical aspects and feasibility of the intervention

To make the therapy suitable for clinical use, a number of technical challenge have to be addressed.

Real time feasibility

This interventional procedure can be seen as a real time system. Therefore, a common constraint to all presented challenges is the real time feasibility of the proposed solution. This aspect is developed in part II.

Security control / Patient safety

The patient safety is part of the main concerns of the intervention. The minimization of the risk for the patient is mandatory. Therefore, prior modeling of the intervention [94, 95, 96, 97, 98], automatic control during the intervention [22, 93] and physician supervision appear necessary for clinical use of the system.

Simple and automated process

The part of user interaction is a tedious problem. For example, many signal processing methods use a set of free parameters that has to be tuned prior the execution. In this case, a highly user dependent system makes it sensible to user error and may increase the intervention duration. On the other hand, a fully automated system has to be highly robust and repeatable in order to be run independently but makes the system much more simple to use. Generally, a good trend can be to use a highly automated system combined with a user supervision to correct for possible error on the automated system.

Fast intervention

The intervention duration is also critical from a cost point of view and resource/material access. For these reasons, the duration of the intervention has to be minimized.

Conclusion

In this part, an introduction to the targeted medical applications together with the associated challenges were presented. Although several methodological solutions have been proposed to perform MR-guided thermal ablation of mobile organs, their applications in a real case still require further developments to guarantee the patient safety and the efficiency of the therapeutic intervention. In particular, the current frequency of 1 Hz used to observe organ motion and temperature evolution has to be increased to improve the performance of HIFU beam steering applications and volumetric ablation strategies. Therefore, in the next part of this thesis, solutions to address these limitations are proposed using very fast MRI combined with computationally efficient strategies for the reconstruction of MR-images and the correction of temperature artifacts (induced by motion, magnetic field drift, noise, etc).

Part II

Feasibility of real time MR-guidance of thermal ablation of mobile organs

Chapter 3

Introduction to real time computing

3.1 The time constraint of a real-time system

The time constraint of a real-time system corresponds to the available time to compute a given task. For MR-guided thermal ablation on mobile organs, two different systems have to be considered:

- Update of the heating device power, which is based on previous thermometry and dosimetry information. Note that this system is also in charge to detect the therapy endpoint.
- Update of the HIFU beam position, which is based on organ motion displacement.

As mentioned in the introduction, both of these systems are updated based on MR-images. Therefore, the time constraint is defined by a processing framerate above the framerate of the MR-acquisition associated with a low overall processing latency in order to guarantee the service quality of the feedback control. If this constraint is not respected, congestion is expected in the process introducing additional latency of the output which can possibly lead to life threatening effects such as heating of an undesired area, etc.

To give a rough idea of the time constraint, a first presentation of the system timing is given. Then, solutions to handle real time computing are presented.

3.2 Required computation time for MR-guided ablation

The choice of the imaging framerate depends on the observed system variation speed and the required precision of the feedback controller. Therefore, to better understand the choice of the imaging framerate, it is important to clearly identify the mechanism of each feedback controller and their characteristics.

3.2.1 Retro control systems and choice of the imaging framerate

Here, we present the constraints of each system.

- Update of the heating device power: This system is a closed loop feedback controller, therefore the stability of the system has to be considered. For this the analysis of the close loop transfer function of the controller allows to define the condition of stability and convergence. The required precision is in the range of a degree Celsius, and temperature variations of a degree Celsius are approximatively observed over a

period of a range of a second. In this context, assuming no latency in the temperature estimation process, a system update every second appears sufficient to keep the temperature estimation below an error of one degree.

- Update of the HIFU beam position: This system is an open-loop feedback controller. Therefore, this system does not have stability issue. The information of motion is used to update the beam position of the HIFU transducer. Previous study showed the impact of latency on tracking error [58]. The free breathing period at rest in generally in the range of 3-5 s on a healthy adult and an organ such as the kidney depict a motion amplitude of 10-20 mm. This result in a peak velocity of 6-20 $mm.s^{-1}$ if we assume the motion pattern as an ideal sinusoid. In this condition, it was shown that a latency of more than 150-250 ms can induce a tracking error of more than 5 mm [58] which is not acceptable for a therapeutic process. Recently, it was shown that a framerate of 10 Hz combined with a short latency inferior to 114 ms was demonstrated to allow the deposition of more than 90% of the delivered energy in the target area [99].

3.2.2 Latency effect

In addition to the system update frequency, this is important to investigate the latency effect of each update. Latency of a process corresponds to the interval of time between an event and the response to this event. In our case, the event is the acquisition of new data. After this, the response can be the data reconstruction, the thermometry or dosimetry computation or even the update of heating device (position or power). For these reasons, several latencies are defined in this thesis, as shown in Fig 3.1.

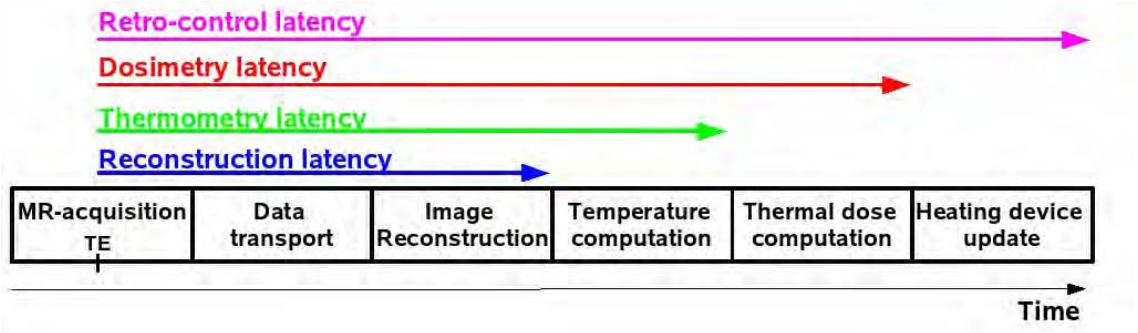

Figure 3.1: Latency of the main interventional steps

As mentioned in section 2.6.1, the latency introduces an additional error in the update process and has thus to be minimized. The effect of latency can also be compensated using a prediction algorithm. However, the performance of prediction algorithms generally decreases for long time prediction, showing the need to minimize latencies and thus computation times. In addition, they cannot anticipate spontaneous events.

3.3 Choice of adapted hardware for efficient parallel computing

3.3.1 Choice of an adapted parallel computing hardware

At the beginning of this thesis, the employed solution in the laboratory for parallel computing was based on symmetric multiprocessor (SMP). This type of hardware contains multiple identical processors that use a shared memory and are connected via a bus.

SMPs generally have a limited number of coprocessors in order to avoid bus contention which thus appears limited for massive parallel computing. In our algorithm, a lot of processing steps are realized independently in a pixel by pixel basis making a parallelization level to the pixel level desirable. In such condition, alternatives to SMP were investigated in order to improve the number of parallel running threads.

One of the main requirement was to guarantee a high framerate processing to satisfy the time constraint of the real time system and also to ensure a short latency. Therefore, all the hardwares that connect a group of computers via a network communication interface, such as grid computing or cluster computing were not suitable since the overhead imposed by the distribution of the data at the beginning and the collection of the data at the end will introduce substantial latency.

Another requirement for the choice of hardware was the possibility to exploit several level of parallelization that we referred in the scope of this thesis as: inter processing task level (to execute several tasks in parallel) and intra processing task level (to parallelize a given task). Based on all presented conditions, specialized parallel computer such as Field-programmable gate array (FPGA) or General-purpose computing on graphics processing units (GPGPU) were considered. A FPGA is a computer chip that can rewire itself for a given task and can be programmed using hardware description languages. A GPU can be seen as a massive parallel coprocessor capable of executing a very high number of threads in parallel. The recent GPUs contain 128-480 basic arithmetic processing units and are pretty cheap (few hundreds of dollars). Parallel computing architecture have been developed by GPU manufacturers to make GPU programming easier based on a well known programming model. For example, ATI stream, Chronos group with OpenCL or NVIDIA with CUDA proposed C-style languages and do not require hardware knowledge as for a FPGA. For these reasons, GPGPU appeared as an interesting solution for a real time implementation of the interventional process. Principles of GPGPU are now presented.

3.4 GPGPU principles

A GPU is constituted by a large number of basic arithmetic processing units that are organized into groups of multi-processors containing fast shared on-chip memory and a slower global memory shared across multiprocessors.

The GPU allows running a batch of threads to execute the same program (called kernel) independently on different data (see figure 3.2). Each kernel is organized into a grid of N_{block} blocks. Each block contains a set of N_{thread} threads executed in parallel by one multiprocessor.

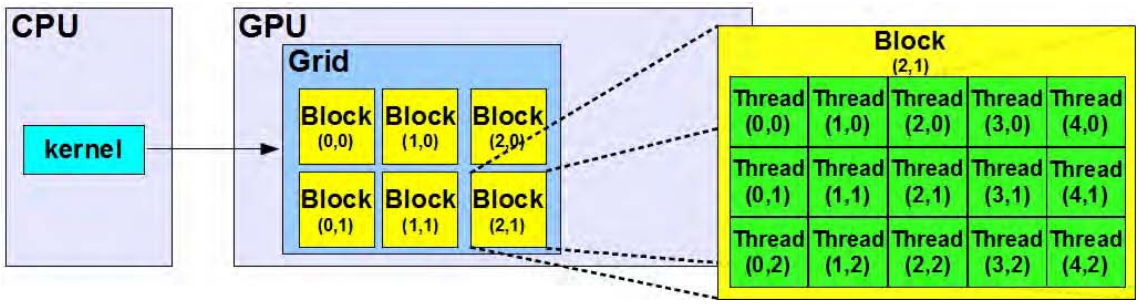

Figure 3.2:

Threads of the same block can share information (via the shared memory) (see Figure 3.3). Synchronization barriers also exist at the block level (for the threads of one block).

Data is exchanged between the dynamic random access memory (DRAM) of the GPU

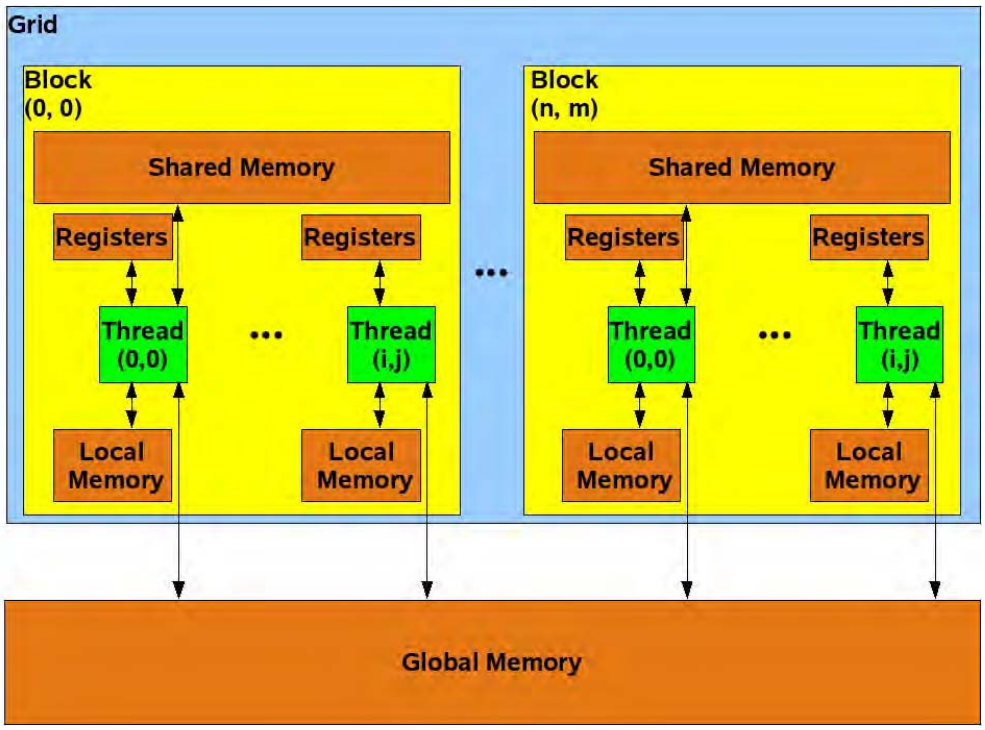

Figure 3.3:

and the RAM of the hosting computer via direct memory access (DMA) of the PCI-express bus, which is bandwidth limited to 3-4 GB/s. In addition the GPU DRAM memory access has a high latency (400-600 clock cycles). Therefore, in order to obtain a maximal processing performance on this particular GPU architecture, implementations have to conform the following guidelines:

- Excessive exchange of data between the RAM of the hosting computer and the GPU has to be avoided.
- The large memory latency of the global GPU DRAM can be hidden by designing the kernels to solve the mathematical problems with a high density of arithmetic operations per memory access and designing the execution configuration to exploit the dimensionality of the given problem to maximize N_{block} and N_{thread}.
- Memory intensive processing has to be implemented so that cooperation takes place between threads within the same block and not between different blocks.
- Multi-dimensional data in the DRAM should be organized so that memory access from the individual threads results in contiguous memory access by the memory controller.

3.5 Discussion and conclusion

In this chapter, a definition of the time constraint imposed by our real-time system was given. However, this time constraint can be seen as an upper bound of the time available to compute all necessary processing steps. It is important to note that further improvements of computation times below this upper bound, would allow to reduce the overall latency and thus to improve the quality of the output information / decision. As mentionned in the previous section, GPGPU appeared simple to use and to program, cheap and well

suited for our application. Therefore, in this thesis the potential of GPGPU, as a solution for a real time implementation of the interventional process, was evaluated.

Chapter 4

Real-time MR-reconstruction

4.1 Fast MR-acquisition

As seen in section 2.1.1.2, organ motion occurring during the MR-acquisition process (referred to as intra-scan motion) causes blurring and ghosting artifacts. Optimized fast MR-acquisition schemes represent an established way to minimize this effect, before more sophisticated correction schemes have to be employed. The data acquisition has to be rapid enough to resolve physiological motion such as respiratory or cardiac motion, and the signal changes from the interventional process itself. In addition, the employed data acquisition and reconstruction schemes must not introduce long image latencies, since this degrades the value of the image data for feedback control.

4.1.1 Parallel imaging methods

Parallel MRI allows to increase the speed of the MR-acquisition by skipping a number of phase-encoding lines in k-space during the acquisition (see figure 4.1). However, as defined in appendix A (section A.2.2), the field of view is directly proportional to the samples density in k-space. Therefore, as detailed in appendix A.3, the reduction of the number of k-space lines leads to a reduction of the FOV in the corresponding direction, and thus to aliasing artifacts on reconstructed images (as illustrated again in figure 4.1b).

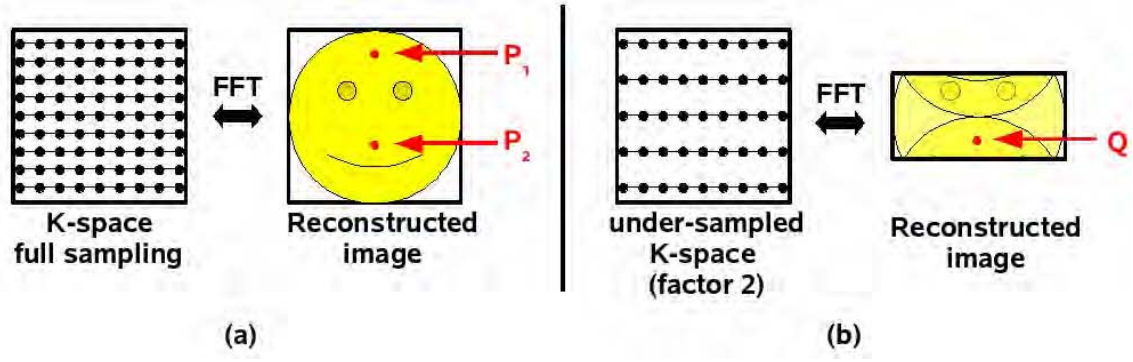

Figure 4.1: Effect of k-space undersampling: (a) is a image obtained with a full k-space sampling, (b) is an image from a two-fold undersampled k-space in up-down direction.

In this example, only every other line in phase encoding direction were acquired. Therefore, the two pixels P_1 and P_2 appear superimposed in the position Q of the reconstructed aliased image. In this case:

$$I_{aliased}(Q) = S(P_1) * I(P_1) + S(P_2) * I(P_2) \tag{4.1}$$

where $I(P)$ and $I_{aliased}(P)$ denotes respectively the intensity of pixel P in the unaliased and aliased image and $S(P)$ is the sensitivity of the receiver coil in the real space at the spatial position which corresponds to the position P in the image. Equation (4.1) denotes the relation of pixels intensities for a sampling reduction of a factor 2. In the general case, the relation becomes

$$I_{aliased}(Q) = \sum_{i=1}^{n} S(P_i) * I(P_i) \tag{4.2}$$

where n denotes the number of superimposed pixels P_i in the pixel Q.

The principle of parallel imaging relies on the simultaneous acquisition of the signal with several different receiver coils with different spatial sensitivities (see figure 4.2). The signal acquired by a specific coil is weighted by the coil sensitivity. Reconstruction methods exploit the difference of the spatial sensitivity of each coil to compensate for the effect of the undersampled k-space.

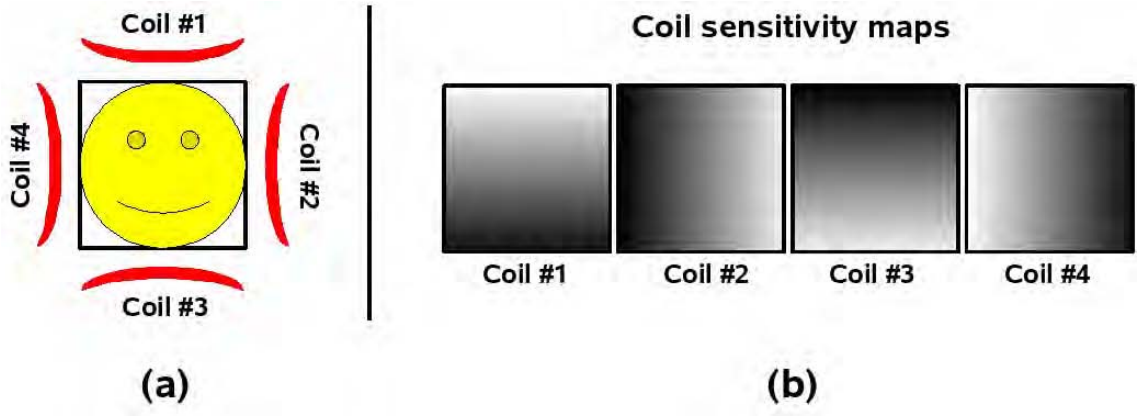

Figure 4.2: Illustration of parallel imaging: (a) acquisition of the MR-signal with several receiver coils (4 in this example), (b) coil sensitivity maps of each coil used to reconstruct the final image.

Several parallel imaging methods have been proposed in the last decade among those SMASH [100], GRAPPA [101] or SENSE [102]. A rapid overview of the mechanism of one of these methods (SENSE) is now presented.

4.1.2 SENSE reconstruction

Since, each receiver coil has it own sensitivity, equation (4.2) can be formulated for each coil leading to the following system of equations:

$$\begin{cases} I_{aliased,c_1}(Q) = \sum_{i=1}^{n} S_{c_1}(P_i) * I(P_i) \\ I_{aliased,c_2}(Q) = \sum_{i=1}^{n} S_{c_2}(P_i) * I(P_i) \\ \quad\quad\quad\quad ... \\ I_{aliased,c_m}(Q) = \sum_{i=1}^{n} S_{c_m}(P_i) * I(P_i) \end{cases} \tag{4.3}$$

where m is the number of coil, $I_{aliased,c_j}(Q)$ denotes the reconstructed aliased signal from the j^{th} coil in the pixel Q and $S_{c_j}(P_i)$ is the sensitivity of the j^{th} coil in the pixel P_i. The undersampling factor is often referred as the SENSE factor. In the case of an integer value, n is uniformly equal to the SENSE factor for each voxel. In the case of a real value, n will be equal to either $Ent(SENSE_{factor})$ or $Ent(SENSE_{factor})+1$ for each voxel with $Ent(x)$ a function that rounds x down to the nearest integer. Note that this system has a unique solution as long as the number of coil m exceeds the SENSE factor.

This system can be rewritten using linear form as follows:

$$I_{aliased} = SI \tag{4.4}$$

The solution can be found by inverting S as follows:

$$I = (S^T S)^{-1} S^T I_{aliased} \tag{4.5}$$

Therefore, the SENSE reconstruction requires coil sensitivity data as prior knowledge, which depends on the coil type and position. However, since the SNR of a receiver coil improves with the loading factor, optimized coil-arrays for abdominal imaging are generally designed as flexible surface coils, which are directly placed on/around the patient body. As a consequence, during the long acquisition times of interventional imaging procedures, displacements of the coils are frequently encountered. This leads to increased image artifacts over time rendering this approach unsuitable. Therefore, methods such as TSENSE [103] have been proposed to overcome this problem.

4.1.3 TSENSE reconstruction

TSENSE reconstruction collects high-resolution calibration data in order to update coil sensitivity data during the acquisition.

However, the additional computational overhead leads to reconstruction times that often exceed the MR-acquisition time, in particular if large coil arrays are used, and are therefore in practice hard to exploit for real-time therapy guidance.

Guttman et al. demonstrated the feasibility of a real-time reconstruction for adaptive TSENSE on a four channel receiver system with an image latency of 0.3 s [104]. Hansen et al. [105] showed that a Cartesian SENSE reconstruction can be significantly accelerated - by up to two orders of magnitude - if the massively parallel architecture of commodity graphics hardware (GPU) is used [106].

Here, both approaches are combined to demonstrate the ability to reconstruct adaptive TSENSE data in real-time with low image latencies on affordable commodity hardware [107, 108]. For this, a detailed performance comparison of the TSENSE reconstruction steps for the GPU and CPU implementation is presented and the image latency and throughput of the full reconstruction under different typical interventional work-loads are benchmarked. Finally, the benefit of the proposed online reconstruction for therapy guidance is demonstrated with two in-vivo imaging experiments imitating typical conditions for MR-guided thermotherapy on abdominal regions and cardiovascular catheterization under real-time MRI guidance.

4.2 Real time TSENSE reconstruction

4.2.1 Reconstruction implementation

The detailed overview of the implementation of a reconstruction pipeline is shown in figure 4.3. The acquisition system streams raw k-space data of dynamic image n to a communication thread (CPU-thread #1) on the reconstructor, which feeds - over a buffer queue - a second preparatory reconstruction thread. Here k-space ordering and Fourier-reconstruction in readout-direction are carried out and the resulting mixed image/k-space data is buffered to a shared-memory, which is accessible by all further reconstruction processes. The shared-memory is implemented as a round-robin to allow CPU-threads #3 and #4 to complete the reconstruction of dynamic image n, while threads #1 and #2 are immediately ready to receive and process new incoming data of the subsequent image n+1. Since for high frame-rate imaging occasional data backlog can not be fully excluded,

this mechanism also allows to detect a violation of the real-time condition and to provide the option to either buffer or to discard new incoming data.

The main image reconstruction is carried out by CPU-thread #3 which applies a 1D EPI-phase correction, which is based on a non phase-encoded reference scan [109], and the Fourier transformation of the image data in phase encoding direction.

For non-SENSE encoded images the image reconstruction would be complete at this point. SENSE encoded images require an additional unfolding step. Furthermore, adaptive TSENSE requires a continuous recalculation of the sensitivity maps and subsequently the SENSE matrix, which in itself is very time consuming. As Hansen et al. have shown, the highly linear nature of the reconstruction steps required for SENSE are well-suited for GPU offloading [105]. The presented architecture takes advantage of the linearity by offloading all adaptive TSENSE calculations to a GPU. For this, the CPU-thread #4 sends a copy of the undersampled k-space to the GPU. Subsequently, the GPU Fourier-transforms this data, applies a temporal low pass filter, calculates the corresponding sensitivity maps and recalculates the SENSE matrix as described by Kellman et al. [103].

Simultaneously, the CPU-thread #3 finalizes the Fourier-reconstruction of the folded image and sends the result to the GPU for the final SENSE reconstruction step. Finally, an optional temporal filter used for residual artifact suppression can be applied. Upon completion of the reconstruction, the image is taken over by a CPU-thread #5 which dispatches the images to one (or several) viewing station(s).

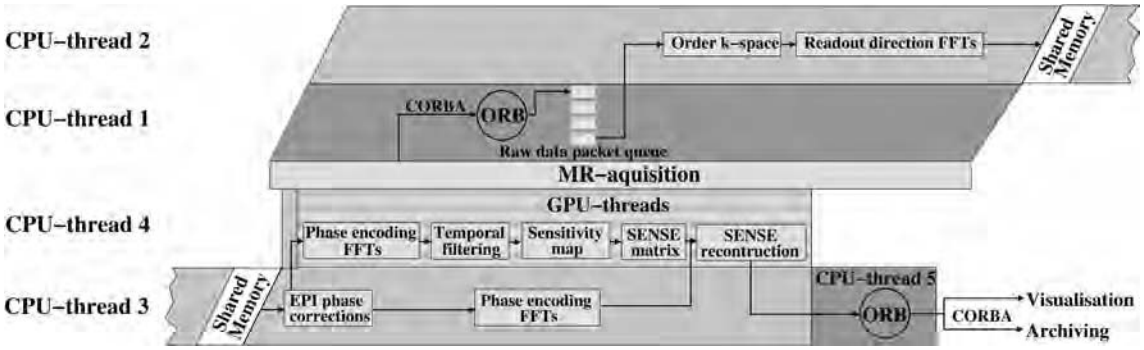

Figure 4.3: Overview of the thread architecture of the reconstruction pipeline. In order to achieve high throughput and short image latencies, as many independent data handling/reconstruction steps as possible are carried out in parallel: CPU-threads one and two handle/reconstruct k-space data from the dynamic image n+1, while CPU-threads three and four finalize simultaneously the reconstruction of dynamic image n. The time-consuming processing steps for the adaptive TSENSE reconstruction are offloaded to GPU-hardware which in itself uses up to 128 threads in parallel. A separate thread for dispatching the data to a visualization and an archiving system is used.

The reconstructor was a dual processor (INTEL 3.1 GHz Penryn, four cores) workstation with 8 GB of RAM and dual 1 Gb/s network interface cards. The GPU was a NVIDIA 8800GTX card with 768 MB of DRAM connected over a PCIe x16 link. For the data transport from the MR-acquisition system to the reconstructor and from the reconstructor to the viewing station(s) a real-time implementation of the common object request broker architecture (CORBA) known as The Ace Orb (TAO) [110, 111] was used. For Fourier reconstruction and all linear algebra operations on the CPU, the ACML math package [112] was employed. The package contains linear algebra packages BLAS [113] and LAPACK [114]. The GPU implementation of the adaptive TSENSE method was realized using CUDA ([106]), with in-house developed linear algebra routines based on methods presented in Numerical Recipes in C++ [115].

4.2.2 Detailed GPU implementation

Since the potential of GPU-hardware for SENSE reconstruction has been evaluated by Hansen et al. [105], the description of GPU implementation is limited in this thesis to the minimum required to understand the presented TSENSE implementation.

Since the storage order of the MR-data is reorganized during the reconstruction (in order to obtain contiguous memory access from the individual threads and thus to speed up DRAM memory access), the following reconstruction-related denotations apply within the scope of this chapter: The MR-signal S is referred to as $S(r, p, s, c)$. The order of the indices reflects the ordering of the data in the computer memory, r being the fastest varying component (r the index in read-out direction, p the index in phase direction, s the slice index and c the coil index). Let N_r, N_p, N_{psense}, N_s and N_c define the number of elements in the read-out direction, the number of phase encoding steps, the number of phase encoding steps reduced by SENSE acceleration, the number of slices and the number of coils, respectively.

4.2.2.1 Fourier Reconstruction in phase encoding direction

Since for the most of the GPU reconstruction steps $N_{block} = N_r N_c N_s$, and N_{thread}=N_p, the data is first reordered from data organization $S(r, p, c, s)$ to $S(p, r, c, s)$ to allow coalesced memory access by the threads (N_{thread}=16×16 in our implementation, N_{block}=$N_r N_p N_c N_s / N_{thread}$). This step also prepares the Fast Fourier Transformations (FFTs) in phase encoding direction by applying the required frequency shifts. Subsequently, the CUDA programming API [106] provided FFT is applied in the p-dimension (using N_{thread}=N_p, N_{block}=$N_r N_c N_s$), resulting in an unaliased image for each receiver coil and slice.

4.2.2.2 Temporal Filtering

All coil images $I_{aliased,c_i} (\forall 0 \leq i < N_c)$ have periodic aliasing with a frequency equal to $1/SENSE_{factor}$. Therefore, in order to suppress this artifact, all coil images $I_{aliased,c_i}$ are temporally low pass filtered with an infinite impulse response filter (IIR) using a SENSE factor dependent bandwidth of $1/SENSE_{factor}$ as described in details by Maclair et al. [116]. The resulting unaliased coil images $I_{unaliased,c_i}$ are thus obtained as follows:

$$I_{unaliased,c_i}(t) = \sum_{k=0}^{T} a_k \cdot I_{aliased,c_i}(t-k) - \sum_{j=l}^{T} b_j \cdot I_{unaliased,c_i}(t-j) \tag{4.6}$$

where a_k and b_l are the filter coefficients and T is the temporal window size of the filter. The principle of this type of filter is described in detail in appendix F.1. The GPU implementation of this filter employed the following configuration: N_{thread}=N_p, $N_{block} = N_r N_c N_s$.

4.2.2.3 Sensitivity Map Update

First, the calculation of the synthetic reference I_{ref} image is performed. This can be, for the case of TSENSE, provided by the Sum-of-Square of the coil images as follows:

$$I_{ref} = \sqrt{\sum_{k=1}^{m} I^2_{unaliased,c_k}} \tag{4.7}$$

using the following GPU settings:$N_{thread} = N_p$, $N_{block} = N_r N_s$. Subsequently, the coil sensitivities are calculated ($N_{thread} = N_p$, $N_{block} = N_r N_s$) and a receiver coil noise decorrelation step [117] is performed. For the decorrelation step, the first N_c threads load each

one element of the pre-calculated matrix $L^{-1} \bigotimes I_d$, where L is derived from the receiver noise matrix (ψ_{noise}) using a Cholesky decomposition $LL^H = \psi_{noise}$ (with L^H the conjugate transpose of L) and I_d is the identity matrix. After a mutual barrier point each thread loads the reference image value for the position associated with the thread and calculates the spatial coil sensitivity map S_{c_i} for all coils as follows:

$$S_{c_i} = \frac{I_{unaliased,c_i}}{I_{ref}} \tag{4.8}$$

Then, the noise decorrelated sensitivity maps $S_{decorr_{c_i}}$ are obtained as follows:

$$S_{decorr,c_i} = (L^{-1} \times I_d) S_{c_i} \tag{4.9}$$

The result is stored in $S(c, p, r, s)$ order to prepare the SENSE-matrix recalculation.

4.2.2.4 SENSE-matrix Recalculation

The unfolding matrix U is calculated for each slice position (using N_{thread}=N_r, N_{block}=$N_{psense}N_s$) as follows:

$$U = (S^H_{decorr} S_{decorr} + R^{-1})^{-1} S^H_{decorr} \tag{4.10}$$

where R is a diagonal matrix with the regularization term along the diagonal [118]. Each thread calculates the matrix inversion for one pixel using an adapted version of the Cholesky decomposition algorithm [119].

4.2.2.5 SENSE-Reconstruction

This step (performed using N_{thread}=N_{psense}, N_{block}=$N_r N_s$) begins with a noise-decorrelation of folded image ($I_{aliased_{decorr}} = (L^{-1} \bigotimes I_d) I_{aliased}$, where $I_{aliased}$ and $I_{aliased_{decorr}}$ are the aliased and the noise decorrelated aliased image, respectively). Then, the unfolding process is performed as follows:

$$I_{unaliased} = U I_{aliased_{decorr}} \tag{4.11}$$

where $I_{unaliased}$ is the unaliased image. Note that superimposed voxel indices are precalculated in both data organizations $S(r, p, c, s)$ and $S(p, r, c, s)$ to speed up this step. In our implementation, $I_{aliased}$ is computed on the CPU in parallel with the SENSE-matrix recalculation step explained above.

4.3 Evaluation experiments

4.3.1 In-vivo applications

All in-vivo experiments were performed on a Philips Achieva 3.0 T X-series scanner equipped with a Philips 16-channel torso coil. The wrap-around coil consists of an anterior and a posterior segment with two lateral ladder-shaped arrangements of four elements, respectively. The following acquisition parameters were used:

4.3.1.1 Abdominal thermometry imaging

A gradient-echo EPI (GE-EPI) sequence, using an echo-train of 67 echoes (33 for two-fold and 17 for four-fold acceleration, respectively), a fixed TE of 15 ms and TR of 50 ms for all acceleration factors, a flip angle of 35°, a bandwidth in phase-encoding direction of 4.1 kHz (1.5 kHz for two-fold and 0.7 kHz for four-fold acceleration), was used to acquire a single slice placed on the right kidney of a healthy volunteer. The resulting image resolution was 3.13×3.13×5 mm^3. Fat suppression with spectral pre-saturation with inversion recovery (SPIR) was used (one excitation per TR cycle, bandwidth 135Hz).

4.3.1.2 Cardiac imaging

A single short axis view of the heart of a healthy volunteer was acquired using a balanced steady-state free precession (TrueFISP) [120] sequence (TR = 4.0 ms, TE = 2.0 ms, flip angle = 41°) with an image matrix of 128×88 (128×44 for SENSE 2; 128×30 for SENSE 3) and a dynamic scan time of 800 ms (427 ms for SENSE 2; 300 ms for SENSE 3) leading to an image resolution of 2.8×2.8×7 mm^3.

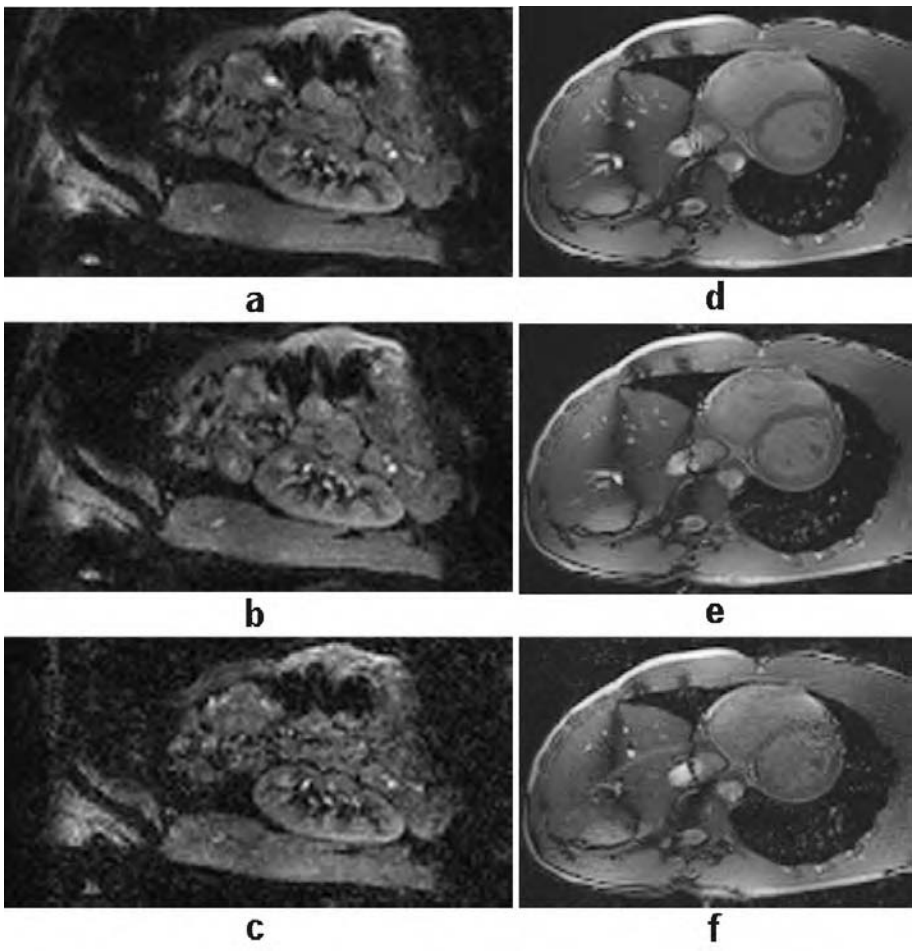

Figure 4.4: Real-time reconstructed MR-images using a combined CPU/GPU reconstruction (left-right: foot-head, up-down: anterior-posterior direction): (a-c) : Fully sampled gradient recalled EPI image centered on the kidney (a) and TSENSE accelerated by factor of 2 (b) and 3 (c). (d-f) : short axis view obtained with balanced SSFP, with full sampling (d) and with a TSENSE acceleration factor of 2 (e) and 3 (f).

Figures 4.4 shows a fully sampled (4.4a), two-fold accelerated (4.4b) and three-fold accelerated (4.4c) abdominal image of the right kidney of a healthy volunteer obtained under free-breathing conditions. An imaging frame-rate of 20 images/s was maintained online for 300 seconds of MR-imaging. The center of the image depicting the kidney was artifact-free over the entire imaging duration and is hence suitable for continuous MR-thermometry. Similarly, figures 4.4.d, 4.4.e, and 4.4.f show a T2/T1-weighted short axis view of a healthy volunteer obtained under free-breathing conditions.

4.3.2 Real-time benchmarking and latency

The GE-EPI sequence used for real-time benchmarking was similar to the sequence used for "abdominal imaging" but used no SPIR preparation and the shortest TE/MR-acquisition

time achievable (reported in Table 2).

Table 4.1 compares the computation time for each TSENSE reconstruction step for a two-fold accelerated image (resolution 128×128, six and sixteen receiver channels) between the implementation using the CPU only and the CPU/GPU implementation. The two most time consuming tasks, the temporal filtering of coil images and the SENSE matrix recalculation, were accelerated by a factor of 14.7 and 16.3, respectively and lead to an overall eight-fold increase of the reconstruction speed despite the additional data transfer to the GPU.

Table 4.1: Computation time in ms for all TSENSE reconstruction steps for a single slice of resolution 128×128 pixels with an acceleration factor of 2 using a six receiver coils and a sixteen one.

Treatment	6 receiver coils		16 receiver coils	
	CPU	GPU	CPU	GPU
k-space data transfer from CPU to GPU	-	0.37	-	0.83
Phase encode FFTs	1.83	0.52	5.77	1.35
Temporal low-pass filtering	17.24	1.04	53.24	2.68
Sum of squares	0.23	0.15	1.05	0.49
Sensitivity maps update	1	0.23	2.14	0.56
SENSE matrix recalculation	10.61	0.62	11.53	1.54
Folded image transfer from CPU to GPU	-	0.37	-	0.83
SENSE reconstruction	0.57	0.22	2.11	0.59
Optional temporal low-pass filtering	1.7	0.4	1.7	0.4
Unfolded data transfer from GPU to CPU	-	0.13	-	0.13
Total	**33.18**	**4.05**	**77.54**	**9.4**

Figure 4.5 compares the computation time measured for various TSENSE acceleration factors (2, 3 and 4) and different image resolutions (128×128, 256×256 and 512×512 pixels) using the CPU/GPU approach (4.5a) and using the CPU only (4.5b).

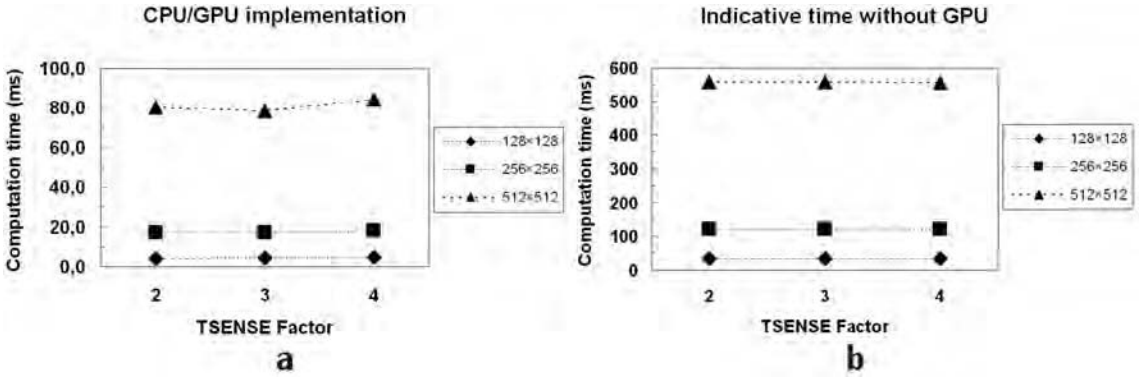

Figure 4.5: Computation time measured for various TSENSE acceleration factors (2, 3 and 4) and different image resolutions (128 ×128, 256×256 and 512×512 pixels) using the CPU/GPU approach (a) and using the CPU only (b). Acceleration factors around 7-8 were measured with the proposed CPU/GPU approach for each tested resolution. Computation times remain identical using the proposed CPU/GPU approach for each tested TSENSE acceleration factor.

Table 4.2 reports the data transfer time, the reconstruction time and the resulting image latency (as defined in figure 3.1) under real-time conditions for coil setups with 4,

6, 8, and 16 elements, and TSENSE acceleration factors of 2, 3, and 4 (resolution 128×128, two-fold read-out oversampling). Since computation times for multi-slice acquisitions are almost linear with the slice number, only results measured with a single slice are reported.

Table 4.2: Reconstruction time and image latency in ms with TSENSE factor 2 (a), 3 (b), 4 (c) for a single slice reconstruction of resolution 128×128 for 4, 6, 8, 16 coil channels. With the proposed CPU/GPU implementation, total computation times are far below the TR on all tests demonstrating that real-time reconstruction is feasible.

TSENSE factor		2			
MR-acquisition time		44			
TE		22			
Channel number		4	6	8	16
Data transport time		31	31	76	76
CPU only	Reconstruction	23.4	33.2	42.3	82.2
	Latency	54.4	64.2	118.3	158.2
CPU/GPU	Reconstruction	3	4.1	5.2	9.8
	Latency	34.0	35.1	81.2	85.8

(a)

TSENSE factor		3			
MR-acquisition time		31			
TE		15			
Channel number		4	6	8	16
Data transport time		19	24	44	59
CPU only	Reconstruction	23.7	33.6	42.5	83
	Latency	42.7	57.6	86.5	142.0
CPU/GPU	Reconstruction	3.1	4.2	5.4	10.2
	Latency	22.1	28.2	49.4	69.2

(b)

TSENSE factor		4			
MR-acquisition time		23			
TE		11			
Channel number		4	6	8	16
Data transport time		17	22	27	47
CPU only	Reconstruction	22.4	33.9	42.7	83.2
	Latency	39.4	55.9	69.7	130.2
CPU/GPU	Reconstruction	3.3	4.5	5.7	10.7
	Latency	20.3	26.5	32.7	57.7

(c)

Data transport varies between 17 ms (four-fold accelerated, four channels, ∼135 kB per image) to 76 ms (two-fold accelerated, 16 channels, ∼1 MB per image) depending on the data size. The reconstruction itself has a theoretical peak performance between 75 images/s (SENSE 4, 16-channels) to 330 images/s (SENSE 2, 4-channels). However, in practice the achievable peak data-throughput was found to be limited by the I/O subsystem of the acquisition system to ∼2.1 MB/s, which corresponds to an image frame-rate of 20 images/s for a two-fold TSENSE accelerated data set (128×128, two-fold read-out oversampling, 16 receiver channels) with an overall image latency of 90 ms, or 40 images/s and an image latency of 60 ms for a four-fold acceleration.

4.4 Discussion and conclusion

The usefulness of a reconstruction pipeline for real-time MR-guidance of interventional procedures can be characterized by the reconstruction speed and the achievable image latency. Fundamentally, the reconstruction time of the pipeline has to be comparable to, or preferably shorter as, the acquisition time of the MR-system, in order to maintain the real-time condition for sustained imaging. Table 4.2 shows that a purely CPU-based reconstruction limits MR-acquisition to only 4-6 coils elements and SENSE acceleration factor to 2-3. Since the proposed CPU/GPU implementation of the TSENSE reconstruction achieves in average an eight-fold acceleration, these limits are virtually removed. In practice, this means that imaging speed is now limited by the boundaries imposed by the MR-sequence, the specific absorption rate, the desired signal-to-noise ratio and the I/O-bandwidth of the acquisition system.

For the case of MR-guided surgical interventions, large image latencies introduce a significant lag between the action and its observable consequence and thus limit the accuracy and speed of the procedure. The proposed CPU/GPU reconstruction achieves image latencies from 20 to 90 ms for all coil configurations and acceleration factors, and is thus well-suited for manual feedback.

Depending on the application, potential data backlog can either be discarded to prevent a sustained desynchronization between acquired and reconstructed images, or be buffered to preserve the temporal continuity of the image data.

The presented work shows that a reconstruction pipeline for real-time reconstructed adaptive TSENSE imaging, which is suitable for interventional MR-guidance, is realizable on affordable commodity hardware. However, multiple channel coil are required to use such reconstruction method. The Philips Sonnalleve HIFU platform already has an integrated multiple channel coil composed of three coils. However, in our experiment, two of the three channels usually provided very poor signal quality which is highly limiting for parallel imaging. For these reasons, the construction of a multiple channel coil with a higher number of channel was planned in the laboratory and by Philips. This project is still in work and progress, therefore, the TSENSE reconstruction was not employed in the following studies presented in this thesis.

Chapter 5

Real time feasibility of MR-thermometry and dosimetry on mobile organs

5.1 Introduction

As described in the introduction, a number of challenges has to be addressed in order to achieve MR-thermometry and MR-dosimetry on mobile organs (see section 2). For this, we proposed in this chapter a whole processing pipeline extending the work of Denis de Senneville et al. [58] where the frequency of the MR-thermometry was limited to 1 Hz. In our contribution, a very fast (10-15 Hz) strategy for motion compensated MR-thermometry and dosimetry of mobile organs is proposed. Here, fast MR-acquisition schemes have been employed to minimize intra-scan motion together with an efficient processing pipeline for MR-thermometry and dosimetry calculations [121, 122]. In this processing pipeline, the problem of motion (including motion estimation and the correction of motion related susceptibility variation) is addressed with algorithms presented in [58]. Therefore, since all temperature maps are registered to a common reference position, a temporal filtering is proposed to reduce the noise of the MR-thermometry measures. Finally, to remain compatible with the time constraint of the real time system and to ensure a short latency, a GPU implementation of all computational intensive calculations (especially the motion estimation process) was added.

The potential of the real-time pipeline to remove MR-thermometry artifacts dynamically is evaluated in-vivo on the abdomen of 11 healthy volunteers under free-breathing conditions and in the heart of 9 healthy volunteers under free-breathing conditions.

5.2 A real time correction pipeline

The general scheme of the correction pipeline employed for the calculation of MR-thermometry and dosimetry is presented in figure 5.1. The intervention is separated into a pre-treatment step and a hyperthermia step. The pre-treatment step is performed prior to the intervention to calibrate the multi-baseline method addressing the problem of motion related phase variations (see section 2.2.1). During the subsequent hyperthermia step, all incoming images are first co-registered to the common position of the reference image [123]. For this, the motion estimation process is composed by two step process where the principal displacement component (PDC, see global motion estimation in section 2.1.3.1) is first estimated and followed by an optical flow registration algorithm (see section 2.1.3.2). Subsequently, the phase image is corrected for motion related phase variations based on

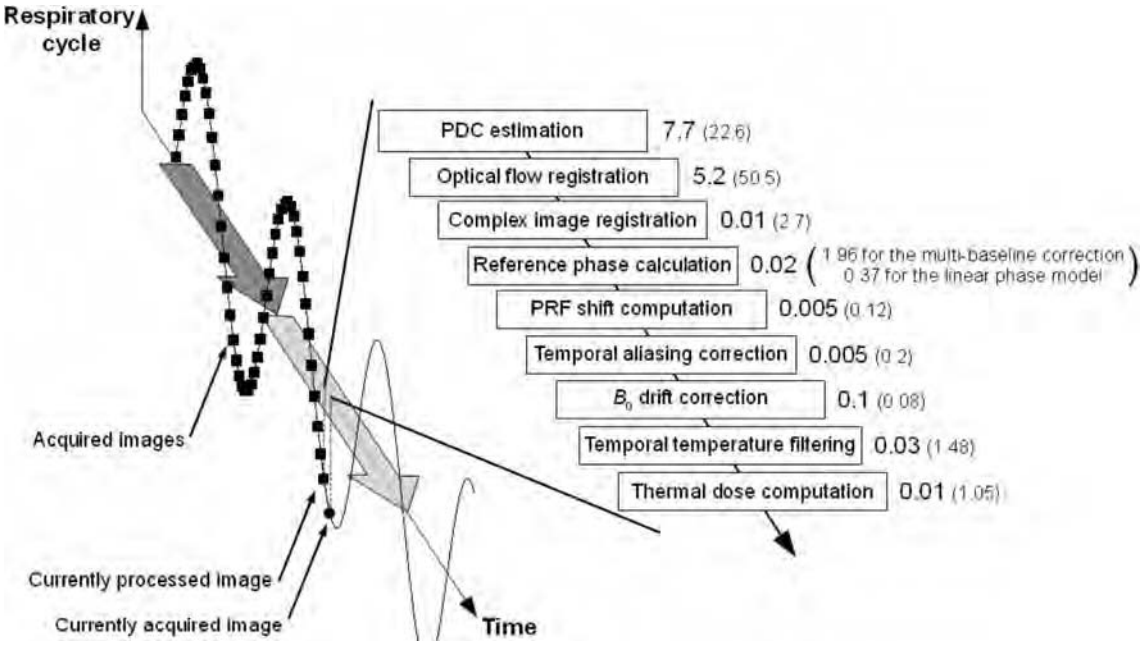

Figure 5.1: Data processing sequence. The intervention is separated into a pre-treatment step (dark grey arrow) and a hyperthermia step (light grey arrow). Computation times for a single image (resolution 128×128) are reported in milliseconds for each processing step with the CPU/GPU implementation (bold) and CPU only implementation (brackets). The most time consuming task, the image registration, was accelerated by a factor of 3 for the global motion estimation estimation and a factor of 10 for the local motion estimation using the CPU/GPU implementation. All others tasks, being in the range of a millisecond, have been substantially reduced below 0.1 ms.

the multi-baseline strategy and the temperature is calculated. A drift correction is applied to remove temperature artifact caused by magnetic field drift. Then, temporal filtering based on an infinite impulse-response (IIR) filter [124] is applied to the temperature maps to increase the Signal-To-Noise ratio (SNR) and finally the thermal dose is calculated.

The proposed approach takes benefit of a combined CPU/GPU architecture by offloading computational intensive calculations to the GPU and thus freeing the CPU for pipeline management and data preparation. The parallelization level was always set to the pixel level and in this case N_{block} was equal to the image pixel number divided by N_{thread} with N_{thread}=16×16.

5.2.1 Organ displacement estimation

In the presented work, a global motion estimation is initially performed on the magnitude images. This method serves also for preconditioning the more complex local motion estimation. Note that all corrections are estimated on the magnitude images but applied to the complex MR-images to avoid interpolation problems with spatial phase wraps.

Global motion estimation: An affine transformation model (see section 2.1.3.1) is used where the free parameters are estimated using a differential Gauss-Newton approach [125]. The model is defined as follows:

$$\begin{pmatrix} dx \\ dy \end{pmatrix} = \begin{pmatrix} t_x \\ t_y \end{pmatrix} + \begin{pmatrix} a_1 & a_2 \\ a_3 & a_4 \end{pmatrix} \begin{pmatrix} x - x_g \\ y - y_g \end{pmatrix} \tag{5.1}$$

where (dx, dy) are the horizontal and vertical components of the estimated displacement in the pixel of coordinates (x, y). $\theta = (a_1, a_2, a_3, a_4, t_x, t_y)$ is the affine model parameter vector, x_g, y_g are the pixel coordinates of the point used as reference for the transformation estimation (e.g. the rotation center). This reference point is chosen as the gravity center of the ROI in our case.

Since the complexity of the estimated deformation is limited, the algorithm is unsuitable to cope with fold-over MR-artifacts, mixtures of static/dynamic parts of the entire field-of-view and complex motion patterns. Therefore it is restricted to a region of interest (ROI), which is manually set at the beginning of the intervention containing the full path of the targeted organ. Here, the transformation model is global, therefore the GPU implementation is not straightforward. Only steps that relied on pixel by pixel basis were thus offloaded to the GPU. The others steps remained on the CPU.

Local motion estimation: An optical flow approach (see section 2.1.3.2) using the variational framework proposed by Cornelius and Kanade [71] was implemented. This algorithm estimates the motion on a pixel by pixel basis using an iterative numerical scheme (similarly to the Horn & Schunck algorithm described in appendix D). The final iterative numerical scheme can be obtained from different resolution approaches such as the Gauss Seidel method or the Jacobi method (see appendix E). The resulting iterative scheme for one pixel requires the knowledge of neighboor pixel intensities. Using the Jacobi method, only neighboor pixel intensities from the previous iteration are required (contrary to the Gauss Seidel method; for details, see appendix E.1 and E.2). Therefore, the Jacobi method was employed and the parallelization was set to the pixel level. In order to optimize the computation time and to stabilize the convergence of the algorithm, a multi-resolution scheme was used [59] that iterates the registration algorithm from a four-fold down-sampled image step-by-step to the full image resolution.

5.2.2 Correction of motion related phase variations

Precise modeling of the inhomogeneous magnetic field in-vivo and under real-time conditions is difficult to achieve and thus several alternative simplified strategies have been proposed to allow to correct motion related errors in PRF-based MR thermometry (see section 2.2.0.4). In this study, both multi-baseline approaches, the atlas based approach and the linear model approach, presented in section 2.2.1, have been implemented. A training step of N dynamic acquisitions (typically N=100) was acquired prior to MR-thermometry for both methods.

During hyperthermia, the atlas based approach compares each incoming magnitude image with each magnitude image present in the collection in order to find the most similar one (using an intercorrelation coefficient as criterion) and to return the associated phase image. This step was not offloaded to the GPU since this can be done in parallel with the motion estimation process. Therefore this step remained on the CPU (run by an independent thread) in order to take interest of a parallelization level between CPU and GPU.

For the linear model approach, this is different since the method needs the transformation model parameter as input. Therefore, since the computation of equation (2.19) is done independently on each pixel, this method was implemented on the GPU.

5.2.3 Correcting for local temperature aliasing

Since the 2π periodicity of the image phase can lead to aliasing artifacts in the temperature maps, a temporal phase unwrapping on a pixel-by-pixel basis is applied. This process

is valid under the condition that the temperature variation between two successive acquisitions does not create a phase variation greater than 2π. Note that on mobile targets, each phase image is registered to a common reference position and subsequently phase corrected, before temporal unwrapping is performed. Therefore, background-phase changes do not contribute to this limitation. This step was also implemented on the GPU.

5.2.4 Correcting for magnetic field drift

As described in the introduction of this thesis (see section 2.3), magnetic field of recent MRI scanners are not entirely stable over time when sustained high frame-rate imaging is applied. This may introduce a temporal drift of the magnetic field leading to a temporal drift of phase images. Therefore, subtraction of phase images acquired at different times (as realized with the multi-baseline approach) can be affected with a different bias for each pixel [82, 83], resulting in undesired temperature offsets on temperature maps. In this study, this perturbation is corrected by subtracting a global temperature offset (a magnitude-weighted average is used to give less importance in poor signal area) obtained from a region of interest, which is chosen in the moving organ, adjacent to the ablation area. The calculation of the global temperature offset was realized on the CPU since this step requires a summation over a small amount of pixels that do not takes advantage of a GPU implementation. On the other hand, the subtraction of the global temperature offset from each pixel of the temperature map can be easily parallelized at the pixel level and was offloaded to the GPU.

5.2.5 Temporal filtering of the temperature

Since the temperature maps are registered to a reference position, a temporal filter was applied to reduce the measurement noise of the thermometry. An infinite impulse-response (IIR) low-pass filter of 5^{th} order was used. It employed an elliptic approximation in the denominator of the transfer function (also referred to as a Cauer filter), which offers steeper rolloff characteristics than others IIR designs such as Butterworth or Chebyshev filters [126]. An IIR filter relies on the combination of past and current measured signal with past filtered signal, and has been already presented in section 4.2.2.2 (note that a detailed description of IIR filtering can be found in appendix F.1). Output of this type of temporal filter often contain a delay that can be considered as an additional latency of the temperature information. With this filter, the introduced latency is directly proportional to the period of time between two successive dynamics. Therefore, high frame rate imaging appears much more appropriate to minimize this latency effect.

The filter coefficients were designed using the signal processing toolbox of MATLAB with the following characteristics: $f_{pass-band}$=1.5 Hz to 8 Hz, $f_{stop-band}$=4.5 Hz to 8.5 Hz, ripple pass-band: 3 dB, ripple stop-band: 50 dB. Pass-band and stop-band were adjusted depending on the dynamic scan-time of the employed sequence to result in an overall temporal resolution of 2 Hz.

Since this filter is computed on a pixel by pixel basis, its was implemented on the GPU as well.

5.3 Real time benchmarking and latency

Figure 5.1 details the computation time of each processing step of the two proposed pipelines for an image resolution of 128×128 pixels between the CPU only and the CPU/GPU implementation. The most time consuming task, the image registration, was accelerated by a factor of 3 for the PDC estimation and a factor of 10 for the optical flow computation. The resulting overall latency for the entire pipeline (including 13 ms for data transport

and 1.2 ms for image reconstruction) was reduced from 95 ms (CPU only) to 27.3 ms (CPU/GPU).

5.4 Experimental validation of the MR-thermometry pipeline

The temperature stability achieved with the presented pipeline is presented in both abdominal organs and the heart of healthy volunteers under free breathing condition (without heating). For this, the temporal standard deviation of the temperature, referred to as TSD in the scope of this thesis, was computed for each pixel and for each volunteer and serves as a measure of the achieved temperature precision.

5.4.1 Temperature stability study on abdominal organs

A first study was conducted to evaluate the performance of the processing pipeline in the abdomen of healthy volunteers [121, 122].

5.4.1.1 Experimental set up

Dynamic MRI was performed under free-breathing conditions on the abdomen of 11 healthy volunteers under real-time conditions. An imaging frame-rate of 10 images/s was maintained for 300 seconds of MR-imaging while MR-Thermometry was performed in real-time. The MR sequence employed the following parameters: 3000 dynamic sagittal images, one slice, TR=100 ms, TE=26 ms, bandwidth in readout direction=2085 Hz, flip angle=35°, FOV=256×168 mm^2, slice thickness=6 mm, matrix=128×84, using a four element phased array body coil. Statistical evaluation of the temperature stability was performed on the kidney and the liver of each volunteer individually by averaging the TSD over a ROI, which was manually set in an area with maximal SNR and avoiding areas showing a complex susceptibility distribution (such as organ boundaries or major vessels).

5.4.1.2 Experimental results

Figure 5.2 details the precision improvement of each separate phase correction step for kidney and liver. Over the 11 human volunteers, the SNR was evaluated to 9.64 ± 2.4 (min=7.2, max=14.3) in the kidney and 7.5 ± 3.1 (min=4.5, max=14.3) in the liver.

On average over all volunteers, the TSD is improved from an initial value of over 8 °C to 2.12 °C (kidney) and 2.66 °C (liver) using the atlas based approach, and to 1.5 °C (kidney) and 2.16 °C (liver), when the linear phase model is used. This precision can be furthermore improved by over 20 % if a drift correction is applied: While a TSD of 1.51 °C (kidney) and 2.07 °C (liver) were obtained with the atlas based correction, the correction based on a linear phase model achieves a further reduction to 1.26 °C (kidney) and 1.77 °C (liver). Additional temporal filtering results in a final precision of 0.86 °C (atlas based), 0.79 °C (linear model) in the kidney and 1.05 °C, 0.98 °C in the liver.

Figure 5.3 shows as an example the least precise result of the examined volunteer group. Even in this case, both correction strategies ensured 2 °C of temperature stability in 70 % of all pixels of both the kidney and the liver.

5.4.1.3 Discussion

The proposed approach for 2D motion compensated MR-thermometry and dosimetry addresses both, inter-scan and intra-scan motion artifacts on abdominal organs, by applying high framerate MRI coupled with real-time image registration and multi-baseline phase

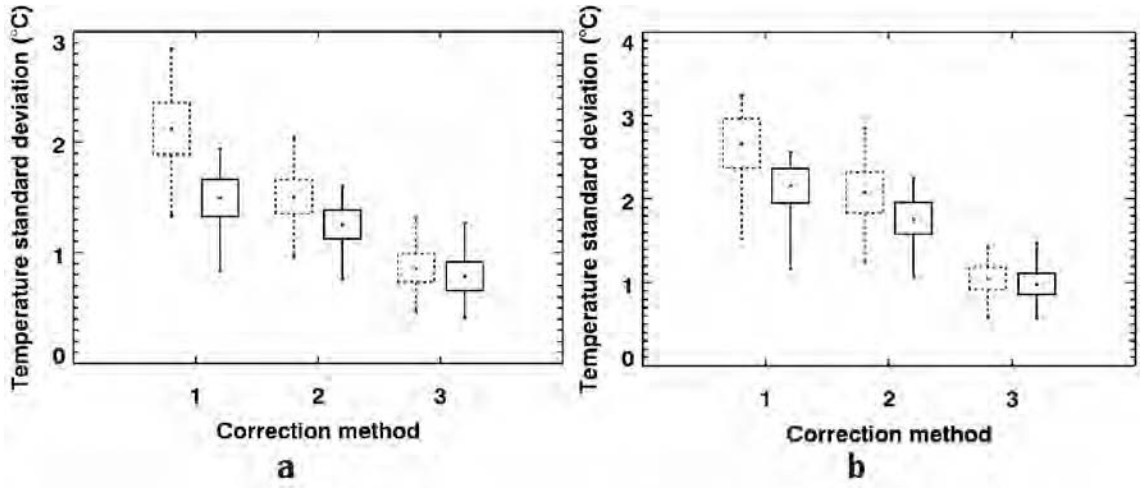

Figure 5.2: Box-and-Whisker plot of the group analysis of the temperature precision over the 11 volunteers obtained in the kidney (a) and the liver (b), with the multi-baseline approach (dash line) and with linear phase modeling approach (solid line). Plotted values correspond to the minimum (lowest point), the average (cross), the maximum (highest point) and the standard deviation (box height) values across the group, before drift correction (1), after drift correction (2) and after temporal filtering (3).

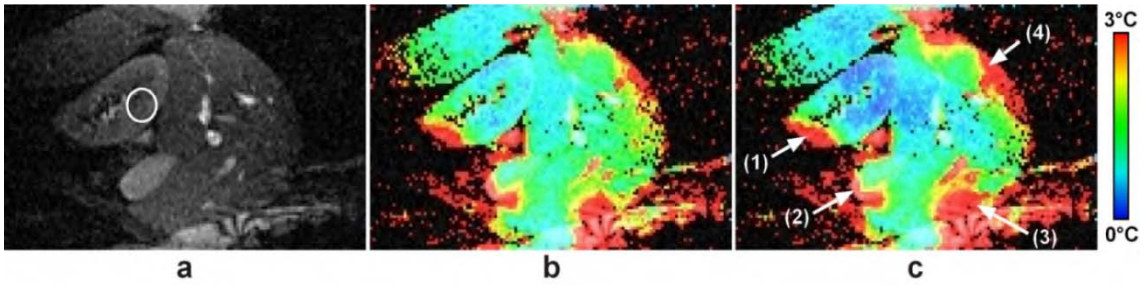

Figure 5.3: Temperature stability obtained in the abdomen of a healthy volunteer with each proposed correction method: (a) anatomical image depicting the ROI used for drift correction, (b) the TSD map obtained with the multi-baseline method, (c) the TSD map corrected with the linear phase model. White arrows indicate regions where large susceptibility variations render the temperature correction difficult: vicinity of the digestive tube (1), vicinity of the quadratus lumborum muscle (2), vicinity of the vertebral column (3) and upper part of the liver (4).

correction of all incoming MR-images. This, in conjunction with the use of parallel processing on affordable commodity graphics hardware, allows to achieve a sub-second temporal resolution with very short image latencies over sustained imaging periods of several minutes that is purely limited by the constraints of the MR-acquisition.

The temperature artifacts related to the periodic respiratory motion of the abdominal organs were reduced to the boundary imposed by the SNR of the employed sequence in both, kidney and liver. Additional temporal filtering of the temperature maps allows to freely readjust the balance between temporal resolution and additional precision of MR-Thermometry.

5.4.2 Temperature stability study in the heart

The processing correction pipeline has then be evaluated in the heart of healthy volunteers [127, 128].

5.4.2.1 Experimental set up

Healthy volunteers (N=9) were positioned head first in supine position in a 1.5 Tesla scanner (Philips Achieva/Intera). A 5 elements cardiac coil was used for image acquisition, with three rigid elements located in the bottom part and 2 flexible elements positioned on the top of the thorax, near the heart. The electrocardiogram was recorded continuously using MR-compatible electrodes provided by the MR manufacturer. After the initial planscan (see Figure 5.4), the short axis of the heart was localized on true-fisp images. This geometry was used to investigate the precision of the thermometry in the left ventricle of the cardiac muscle. The acquisition sequence for MR thermometry was triggered on the cardiac signal to acquire one data set per cycle. Six contiguous adjacent slices were acquired sequentially to cover a volume of interest within a single heart beat with the following parameters: 250×166 mm^2 rectangular field of view, 96×96 matrix (resulting in an in-plane resolution of 2.6 mm for an acquisition time per slice of 37 ms), slice thickness=7 mm, TE=20 ms, TR equals to the period of the cardiac cycle, single shot EPI (echo train of 43 echoes), parallel imaging with SENSE acceleration factor of 1.6. Saturation slabs were positioned on each side of the imaging stack to reduce the intensity of the blood signal on the MR images [129]. The slice location was dynamically adjusted using a pencil-beam navigator positioned at the liver/lung interface (slice tracking technique [40]) in order to compensate for respiratory related out-of-plane motion induced by breathing. The triggering delay was adjusted to acquire the last slice in the mid or end diastole. No arrhythmia rejection criteria nor slice tracking limits were applied to ensure a systematic acquisition of a complete stack independently of potential jitter in the period of the cardiac cycle and/or variations of the respiratory amplitude. For each volunteer, the volume was continuously acquired 200 times to cover a period of time of 3 to 5 minutes (depending on the period of the volunteer cardiac cycle).

5.4.2.2 Experimental results

The respiratory and cardiac cycles durations on the 9 volunteers ranged between 6-8 s and 0.8-1.5 s, respectively. Representative MR images of the thermometry sequence at two extreme positions in the respiratory cycle are displayed in Figure 5.5. The SNR of the magnitude image on the left myocardium (19.8 ± 6, min=14, max=32) was sufficient on all volunteers to apply the motion correction algorithm. The local phase variations associated with respiratory induced susceptibility changes were observed during respiratory cycle (see figure 5.5c and 5.5.d).

TSD maps obtained without and with the multi-baseline correction (atlas based correction) in the worst case are reported in figure 5.6a and 5.6b, respectively. The temperature evolution in a single pixel located in the septum displayed periodic oscillations associated with the respiration, with a maximal amplitude without correction of 50°C (Figure 5.6c). After correction, the oscillations were reduced leading to a TSD lower than 5°C in 75% of the pixels included in a ROI covering the left ventricle.

The TSD was first evaluated on the myocardium (blue area in figure 5.5a) of the 9 volunteers. The TSD reached a value up to 20°C in absence of specific corrections. The use of the multi-baseline correction methods resulted in reduction of the TSD for all cases. Over the 9 volunteers, the TSD on the left ventricle was $3.6°C \pm 0.94$ (min=2.48, max= 5.44) with the atlas based correction and $3.67°C \pm 1.03$ (min=2.66, max=5.58) with the linear phase model approach. No magnetic field drift has been observed, thus the magnetic

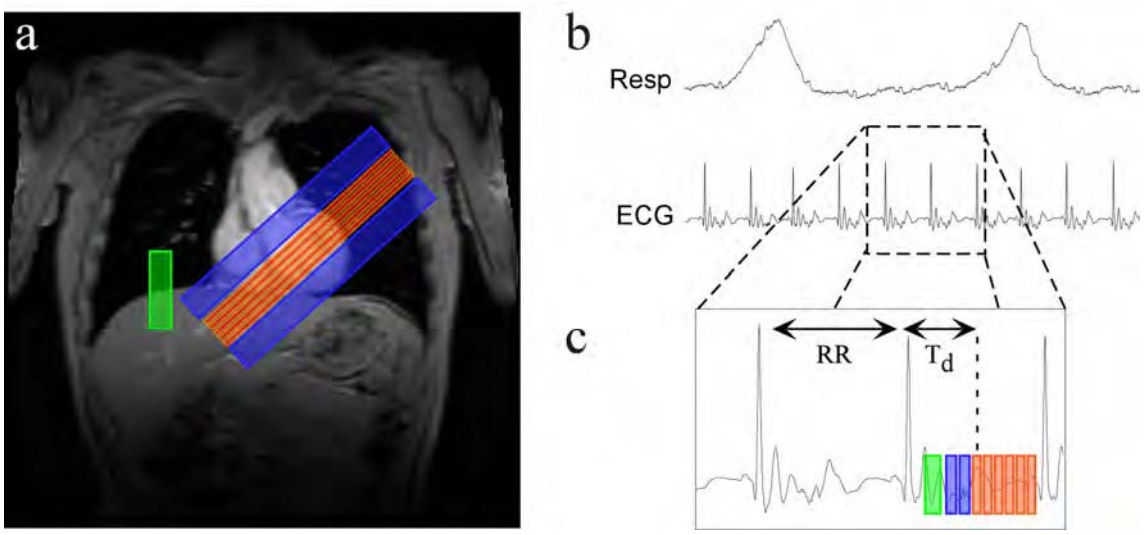

Figure 5.4: Experimental setup used for MR temperature imaging of the short axis on the left ventricle. a: MR anatomical image obtained in a coronal plan. Slices used for temperature imaging are reported in red. Slice position is adjusted on-line using a navigator positioned on the liver/lung interface (reported in green). Saturation slabs positioned on each side of the imaging stack are reported in blue. b: Respiratory and electro-cardiogram signal recorded on-line. c: The complete stack is acquired in the mid or end diastole cardiac phase. The volume was acquired to cover a period of time of at least 2 minutes in order to evaluate the precision and the stability of the thermometry sequence.

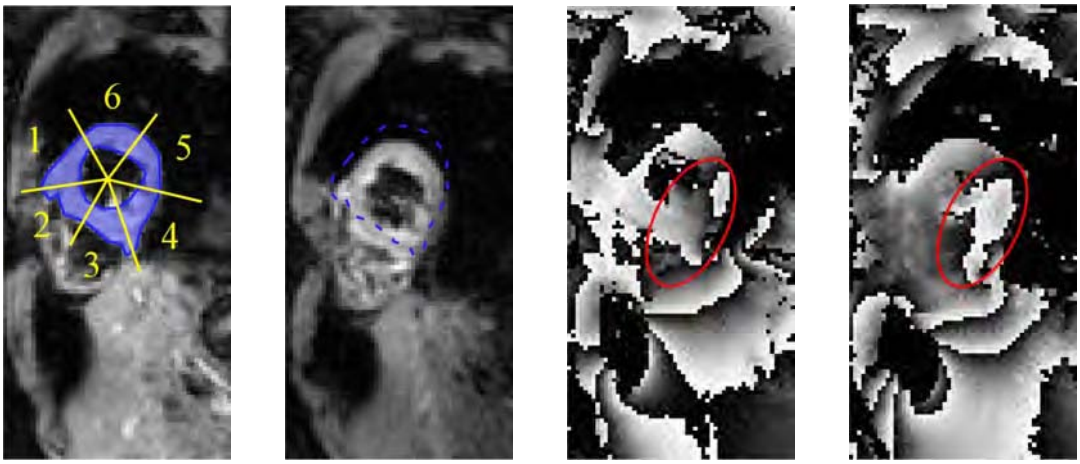

(a) (b) (c) (d)

Figure 5.5: Example of MR images obtained in the short axis of the heart at two different instants of the respiration process. a, b: anatomical images. The six segments defined by the standardized myocardial segmentation and nomenclature are reported in a [130]. The region of interest manually set on the myocardium for the temperature stability study is reported in blue. This region of interest is reported in dash line in b to show the motion of the ventricle. c, d: corresponding phase images. Large phase changes induced by local susceptibility variations related to lung volume modifications and liver displacements are observable especially at the heart/lung interface (red ellipse).

field correction was not employed in the presented results. In this experiment, no temporal filtering was used since the dynamic scan time is equal to the period of the cardiac cycle

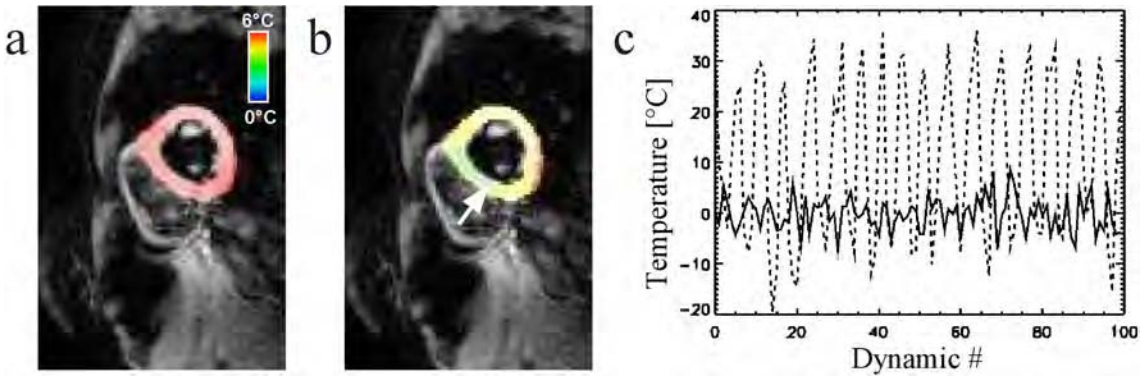

Figure 5.6: Worst temperature stability obtained on the left ventricle of the examined volunteer group (volunteer 6 in Figure 4). a: the TSD map obtained without motion correction, b: the TSD map obtained with motion correction, c: the temperature temporal evolution in a pixel located in the septum (white arrow on (b)) without (dashed line, SD=15.4 C) and with motion correction (dot line, SD=3.3 C).

and would introduce substantial latency of several seconds.

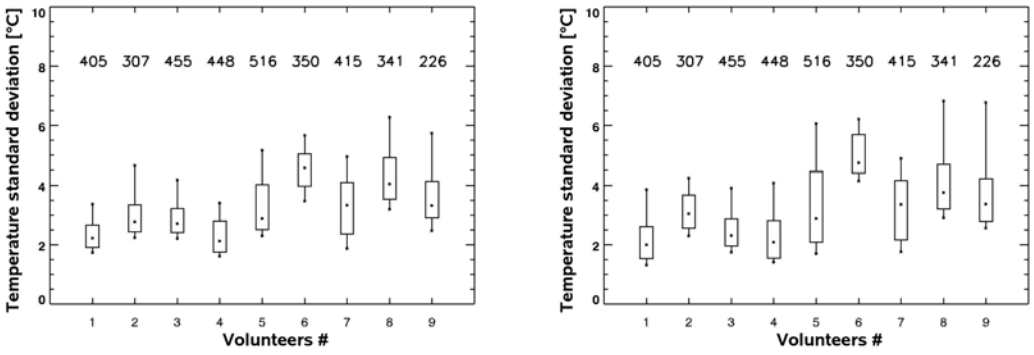

Figure 5.7: Temperature stability for each volunteer obtained with the atlas based approach (a) and linear phase model approach (b). Box and Whisker plot of the TSD for each tested volunteer in the myocardium of the left ventricle. Temperature level values corresponding to 10% (lowest point), first quartile (lower box limit), median (cross), third quartile (higher box limit) and 90% (highest point) of the distribution of TSD are plotted for each volunteer. Pixel number in the region of interest is also reported.

Figure 5.8 shows a Box and Whiskers graphical representation of the TSD for each segment of the left ventricle, defined by the standardized myocardial segmentation and nomenclature [130] (see figure 5.5). In this representation, 5 temperature levels were reported, corresponding to first decile (T10) of the distribution of the TSD values, the first quartile (T25), the median value (T50), the third quartile (T75) and the last decile (T90), respectively. For both multibaseline corrections, all the volunteers revealed similar distributions for segments #1, #2, #3 and #6, with T50 values around 3°C and T75 below 3.5°C (see Figure 5.8a,b). Segments #4 and #5 showed a T50 of approximately 4°C, and T75 ranging between 4.3°C and 5.5°C.

5.4.2.3 Discussion

MR thermometry of the human heart was shown feasible with an accuracy of 3.6°C±0.88 (min=2.48, max= 5.44) and at an update rate of 5 images/cardiac cycle. Stability was

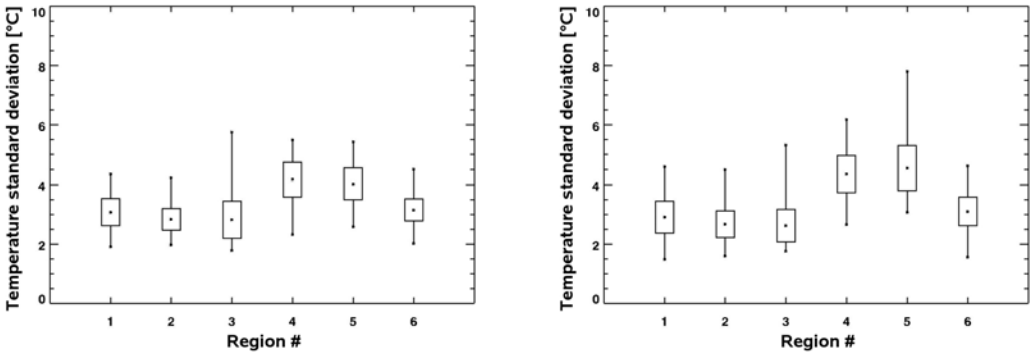

(a) (b)

Figure 5.8: Temperature stability obtained in each segment with the atlas based approach (a) and linear phase model approach (b). Box and Whisker plot of the TSD evaluated for each region of the standardized myocardial segmentation and nomenclature. Temperature levels values corresponding to T10(lowest point), T25(lower box bound), T50(cross), T75(upper box bound), T90(highest point) of TSD distribution over all volunteers are plotted.

better in the septum (region #2 and #3) and in the regions #1 and #6. The two regions (#4 and #5) depicting a higher temperature standard deviation were much more prone to susceptibility artifacts since they are at the liver/heart/lung interface and thus suffer from important spatial and temporal susceptibility variations. Since the lower precision boundary of PRF-based MR-thermometry on static targets is directly proportional to the inverse of the SNR of the employed sequence, it is possible to evaluate the effectiveness of the correction strategies for dynamic phase artifacts by a direct comparison. On the 9 human volunteers the SNR study leads to a minimal achievable temperature standard deviation of 1.06°C±0.27 (min=0.64, max=1.39). The experimental study converge toward those theoretical values when the multi-baseline correction was used. However, remaining residual motion artifacts and image distortions inherent to EPI acquisitions prevented to reach those theoretical values experimentally. The resulting TSD in each analyzed region on the volunteers was approximately 50% higher than those reported by [131] on animals under mechanical ventilation, but remained acceptable for efficient monitoring of the temperature evolution in the myocardium and at an update rate at least 10 times higher. Major advance as compared to recently published results [131] is the improved temporal resolution and volume coverage, since 5-6 slices were acquired at each heart beat (∼1 sec) instead of a single slice every 10 to 20 sec. Typical RF ablation duration remains in the range of 1 min, and therefore, acquiring only 3 to 6 temperature images during the ablation process may appear insufficient to characterize the temperature evolution and render the evaluation of the thermal dose difficult. To overcome this major limitation, we proposed to accelerate the acquisition sequence using EPI in combination with ECG triggering, navigator based slice tracking and image processing for compensation of motion related susceptibility artifacts. This method reduces the 3D complex motion of the heart to a 2D in-plane motion, for which in-plane image registration algorithms can be applied. The resulting standard deviation of the temperature was acceptable in view of local temperature increases achieved during cardiac catheter ablation.

5.5 Discussion & conclusion

In this chapter, an efficient processing pipeline has been presented for very fast MR-thermometry and dosimetry. The different steps of this processing pipeline are now dis-

cussed.

5.5.1 Real time feasibility of the correction

MR-acquisition times of typically 100 ms per slice or less are required to avoid intra-scan artifacts. Combined with high frame rate such as in abdominal experiments, it places severe restriction on the available processing time for image reconstruction, image registration and all MR-thermometry related calculations in order to maintain sustained real-time MR-thermometry.

Figure 5.1 shows that the motion estimation step remains the most time consuming step. GPU based implementation allows to reduce the computation time for all image processing steps below the used MR-acquisition time. This provides a theoretical achievable image processing frame-rate of 30 images/s maintaining the real-time condition. This renders the method purely limited by the MR-acquisition time.

The proposed correction pipeline ensures a latency of 27.3 ms (image matrix of 128×128), which is suitable for interventional MR-guidance and is realizable on affordable commodity hardware.

5.5.2 Organ displacement estimation

5.5.2.1 Global motion estimation

A global motion estimation using an affine image registration was found to be well suited for targets that show only little plastic deformation during the respiratory cycle, such as the kidney. However, since such targets are in general in the vicinity of either elastic soft-tissue, such as digestive tubes or liver, or static tissue, such as the quadratus lumborum muscle or the vertebral column, the algorithm needs to be confined to a ROI encompassing only the full path of the selected target and excluding such problematic areas. For targets that display a complex spatially variant deformation such as the liver, this approach was unsuitable since a global adaptation of only six free transformation parameters leads to a poor representation of the complex deformation. The main advantages of this approach are the short computation times and its robustness against noise and local intensity variations.

5.5.2.2 Local motion estimation

This technique allows to estimate complex organ deformations with sub-pixel precision on a voxel-by-voxel basis. Furthermore, the underlaying regularity constraint [70] that assumes a continuous differentiable motion field was found well suited for elastic targets that display local deformations during the respiratory cycle such as the liver or the heart.

However, these algorithms require a prior calibration of few parameters which makes the method performance dependent on the calibration and thus on the data. In clinical context, this imposes an additional manual calibration step that complicates and extends the intervention. In order to make this type of approach suitable for clinical use, an autocalibration approach of local motion estimation algorithms is proposed in chapter 9.

The Cornelius and Kanade approach [71], relaxing the global regularity constraint suggested by Horn and Schunck [125], limits mis-registration caused by small contrast changes. However, this condition can still be violated during hyperthermia as several MR relevant tissue properties, such as T_1 and T_2 relaxation times, can change during heating process, leading to strong local signal intensity variations in the heated region. The impact of this mis-registration effect on large ablation areas, which may be used for advanced ablation strategies such as spatial volumetric temperature feedback [93], requires further investigation and a novel approach to improve robustness of local motion estimation in presence of T_1 and T_2 variations, which is presented in chapter 8.

For heart experiments, it should also be noticed that the presence of saturation slabs positioned on each side of the imaging stack (see Figure 1) may induce appearance and disappearance of surrounding tissue in the image field of view which may disturb the registration process based on conservation of local image intensities [129]. This impact on mis-registration is studied in chapter 7 and a novel approach is proposed to remain robust against appearance and disappearance of tissue surrounding our target.

5.5.3 Susceptibility related phase changes with motion

Organ motion in MR-images is reduced to the influence of the breathing activity in both the heart (due to ECG triggering) and abdominal organs. The proposed multi-baseline correction for susceptibility related phase changes is designed to correct MR-thermometry artifacts on organs subject to a periodic displacement, which is caused by the respiratory cycle. Since phase variations are "learned" in a preceding learning step and subsequently applied to correct the MR-thermometry during the intervention, the method can intrinsically not correct for MR-thermometry artifacts associated with spontaneous motion. If during hyperthermia new positions are observed, a recalibration of the phase correction data is required. In abdominal organs, the employed high imaging frame-rate allows to complete this task in the relatively short time of two to five respiratory cycles. However, this represents a disadvantage compared to other correction approaches such as referenceless correction approaches [81]. For the heart, a recalibration requires much more time since the frame rate is equal to the cardiac frequency. Alternative strategies such as hybrid methods between multibaseline and referenceless approaches as proposed by Grissom et al. in [132] may be of interest.

However, compared to the latter, the proposed multi-baseline correction allows an accurate correction of susceptibility related phase changes even in regions with complex susceptibility distributions or signal discontinuities such as organ boundaries (for example at the heart/liver interface (region 4 and 5 of the heart)), since it requires neither a uniform susceptibility distribution in the target nor time-consuming 2D spatial phase-unwrapping steps [133].

To take advantages of both strategies, a hybrid approach is proposed and presented in chapter 2.2.

5.5.4 Noise consideration and subsequent temporal filtering

Commonly, MR-thermometry is considered to be limited by the precision penalty imposed by the associated low SNRs on the temperature measurements. Since all MR temperature images in the time series are registered to the same reference position, temporal filtering using a low pass filter can be applied to improve temperature accuracy prior to thermal dose calculation. This, in turn, allows to choose a balance between temporal resolution and the precision of the MR-thermometry that can be freely adjusted according to the employed interventional modality and the available SNR of the target area. Theoretically, a perfect co-registration allows to double the SNR, and thus the precision of the temperature measurements, by reducing the bandwidth by a factor of 4. In the volunteer study of the abdominal experiments, a filter with a transition band between 0.15 and 0.45 resulted in an improvement of the precision of MR-thermometry by a factor 1.85 which corresponds well to the expected theoretical result. Although this type of filter allows to improve the thermometry precision, the resulting thermometry accuracy may be biased by the introduced latency of the filter. However, the quantification of the introduced accuracy bias is hard to achieve. Although the temperature accuracy can be evaluated using temperature probe on ex-vivo experiment, only sparse true temperature information is available. In addition, the quantification for in vivo experiment appears limited by the invasiveness of

the method. However, the control of both the accuracy and the precision appears necessary for a temporal filter employed for clinical use. Therefore, a study on accuracy and precision of spatio-temporal filter has been conducted and had lead to the proposition of a novel filtering method that aims to improve the MR thermometry precision while guarantying its accuracy. This study is presented in the chapter 11.

Chapter 6

Real time MR-guided thermal ablation of mobile organs

In this chapter, a presentation of applications of MR-guided thermal ablation of mobile organs using the presented MR thermometry and dosimetry processing pipeline is given in both abdominal organs and the heart. All experiments in this chapter were performed on a 1.5 T Achieva MR-scanner (Philips Healthcare, Best, the Netherlands).

6.1 MR-guided HIFU ablation of mobile organs

For all presented HIFU experiments, ablations have been realized using the Philips Sonnalleve HIFU platform containing a 256-element phased array ultrasound transducer. MR-signal was recorded using the integrated multiple channel coil of the HIFU platform.

6.1.1 Fix point ablation

The presented MR-thermometry and dosimetry pipeline has been directly evaluated in vivo on a porcine kidney under general anesthesia during MRI guided HIFU ablation [121, 122]. This experiment was part of a joint study with Dr. Mario Ries and Dr. Baudouin Denis de Senneville as the principle investigators.

6.1.1.1 Experimental set up

In this first experiment, no focal point position adjustment with respect to target displacements was performed. The MR sequence employed the following parameters: 1500 dynamic sagittal images, one slice, TR=100 ms, TE=41 ms, bandwidth in readout direction=2085 Hz, flip angle=35°, FOV=320×140 mm^2, slice thickness=6 mm, matrix=128×56. The data processing sequence designed for the linear phase modeling approach was used to perform the MR-thermometry and dosimetry in real-time.

6.1.1.2 Experimental results

The overall temperature accuracy over the whole kidney was 0.65 °C ± 0.11 (min=0.4, max=0.99) with a measured SNR of 6 (although a SNR of 6 provides a theoretical temperature standard deviation of 1.47 °C, the temporal filtering reduces the initial temporal resolution of 10 Hz down to 2 Hz improving the temperature precision by a factor of $\sqrt{5}$). Figure 6.1a shows the temperature image after 39 seconds of sonication corrected with the linear phase model approach. The evolution of the temperature at the focal point position is reported on figure 6.1b. An hyperthermia of 12 °C was reached, which leads to a final thermal dose of 10 % of the lethal dose as shown in figure 6.1c.

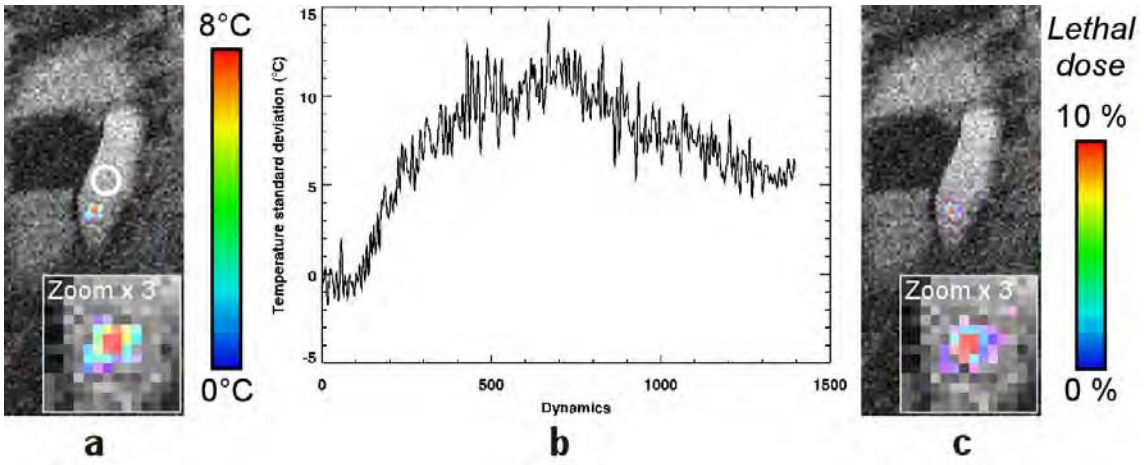

Figure 6.1: MR-Thermometry results obtained on a porcine kidney during HIFU heating, corrected using the linear phase model: (a) the temperature distribution obtained after 39 seconds of heating and the ROI used for drift correction overlayed on the anatomical image, (b) the temporal evolution of the temperature at the focal point position (note that the baseline precision of 0.65 °C decreases during hyperthermia due to a change of the T1 relaxation [84]), (c) the thermal dose map obtained at the end of the experiment.

6.1.1.3 Discussion

The method was found robust and artifact free in all examined cases and well able to follow the temperature evolution of an in-vivo HIFU ablation. This renders the method well suited for the MR-guidance of hyperthermia ablation in abdominal organs under free-breathing conditions and as the basis for more advanced automatic spatial and temporal temperature control algorithms used in conjunction with dynamic ultrasound beam-steering.

6.1.2 Beam steering ablation

A further joint project with Dr. Mario Ries and Dr. Baudouin Denis de Senneville as principal investigators, evaluated the potential of the combination of a real time MR-thermometry pipeline with a dynamic ultrasound beam-steering [134, 40, 99]. In this study, my contribution was on the development of real time methods for 2D in-plane displacement estimation and 2D thermometry calculation (which are presented in chapter 5).

The aim of this work was to explore the possibility to have a 2D MR-thermometry information and to track the target in 3D space in order to adapt the beam position with a sufficiently high temporal resolution and a sufficiently low tracking latency so that sophisticated modeling of the target trajectory is not required.

6.1.2.1 Method description

In the presented work, MRI is used for two tasks: Target tracking and MR-thermometry. Since both tasks do not require the same temporal resolution, the following strategy is employed to optimize the tracking accuracy as well as the precision of MR-thermometry.

3D Target tracking This is achieved by tracking the target position in the image plane with 2D motion estimation algorithm (see section 5.2.1), while out-of-plane motion is estimated based on 2D selective navigator data positioned in the direction perpendicular

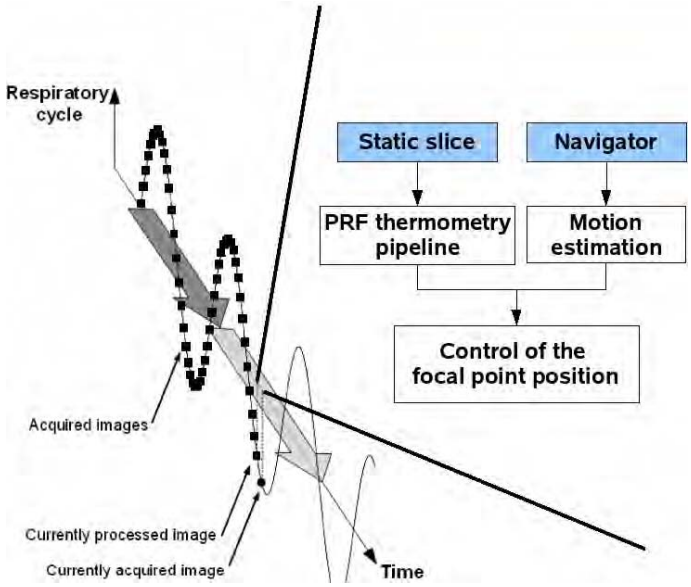

Figure 6.2: Scheme of the data processing pipeline: The tracked slice is used to detect 2D in plane motion and extract thermometry information while the navigator allows to obtain the motion information in the third dimension. Finally, based on the 3D motion information, the beam position can be adjusted.

to the imaging plane as originally suggested by Hardy et al. [135] and refined by Nehrke et al. [136]. The 3D target location is obtained by combining the current 2D in-plane displacement vector field with the current slice position obtained by the pencil beam navigator.

The latency arising from the image transport and the data processing is compensated by using the linear predictor of an Kalman filter employing a physical model of the motion (see appendix F.2 for a detailed description of the Kalman filtering formalism). This motion model A is given by the linear equation of motion in absence of external forces and is then defined as:

$$A = \begin{pmatrix} 1 & 0 & 0 & \Delta t_i & 0 & 0 \\ 0 & 1 & 0 & 0 & \Delta t_i & 0 \\ 0 & 0 & 1 & 0 & 0 & \Delta t_n \\ 0 & 0 & 0 & 1 & 0 & 0 \\ 0 & 0 & 0 & 0 & 1 & 0 \\ 0 & 0 & 0 & 0 & 0 & 1 \end{pmatrix} \tag{6.1}$$

where Δt_i and Δt_n are the latencies for the image based measurement and the navigator based latency, respectively. The state variable of the Kalman filter is then defined as $x_k = (x_1, x_2, x_3, \partial x_1/\partial t, \partial x_2/\partial t, \partial x_3/\partial t)^T$ expressed in the coordinates of the HIFU-system, where (x_1,x_2,x_3) denote the 3D target location and ($\partial x_1/\partial t$, $\partial x_2/\partial t$, $\partial x_3/\partial t$) is the velocity. The anticipated future target state which is sent to the HIFU-generator is thus $x_{t+1} = Ax_t$.

2D MR-thermometry 2D MR-thermometry is achieved using an extension of the processing pipeline presented in chapter 5. The slice position is hereby continuously adjusted to the current target location using fast pencil beam navigator echoes. Therefore, the multi-baseline approach was extended to use both navigator information and magnitude image for the research in the look up table. The first order matching criteria is the slice position obtained from the pencil beam navigator. Subsequently, magnitude image match-

ing is used on the non-realigned magnitude images to find the correction with the most similar in-plane position.

6.1.2.2 Experimental validation

Beam steering on a moving phantom A physiological phantom with relaxation times matched to the human kidney was mounted on a motorized platform to simulate an abdominal organ (displacement 15 mm peak-to-peak, motion period 5 s to match the human respiratory cycle). Data acquisition was performed using a gradient recalled single shot echo-planar sequence with the following parameters: TE=46 ms, image matrix=128×84, flip angle=35°, voxel size=2×2×5 mm^3. The following repetition times were used: 66 ms, 92 ms, 150 ms, 300 ms, 600 ms, whereby the experiment with 66 ms used a reduced matrix size of 128×64 with a TE of 32 ms. The Kalman filter was calibrated as follows: The measurement noise covariance R was set to the nominal MR-resolution and the process noise covariance Q was directly determined from the harmonic motion pattern to a value of 0.2 mm.

Figure 6.3 shows the temperature map after 60 s of sonication overlayed over the corresponding magnitude image. Figure 6.3a shows the effect of a sonication using a static beam position on the moving phantom. In this case the beam energy is spread over the entire trajectory of the target, whereby the majority of the energy is deposited in the two turning points of the oscillatory motion, where the target speed is lowest. The fully motion compensated HIFU experiment shows that the beam energy is deposited at the predefined location (see figure 6.3b). Similar results can be achieved if the acquisition slice is rotated by 90° (see figure 6.3c). In this case in-plane and through-plane motion are compensated.

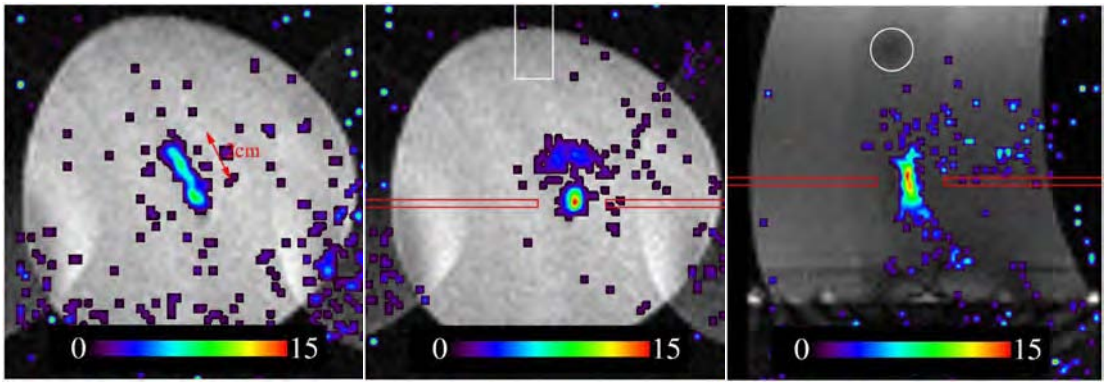

(a) (b) (c)

Figure 6.3: Temperature distribution obtained after 60 s of a HIFU application on a phantom subjected to periodical motion. The temperature distribution of (a): non-compensated HIFU application, (b): The fully motion compensated HIFU experiment and (c): fully motion compensated HIFU experiment with an acquisition slice is rotated by 90°.

Beam steering on invivo experiments A total of three pigs were anesthetized by an initial intramuscular injection of propofol (10 ml) and subsequent administration of propofol (1 ml/min) through a dorsal ear vein. The volume and the frequency of the mechanical ventilation (45 to 100 % O2, respirator paraPac, ResMed SA, France) was adjusted so that the motion of the kidney induced by the respiratory cycle was found to be between 8 mm and 12 mm with a period of 6 s. The animals were placed in right lateral decubitus position so that the right kidney was accessible through an unobstructed beam-path

directly below the rib-cage. One single slice was acquired using a gradient recalled single shot echo-planar sequence with the following parameters: TE=46 ms, TR=92 ms, image matrix=128×84, flip angle=35 °, water-selective binomial 121 excitation pulse, 1.5 kHz readout bandwidth, voxel size=2.3×2.3×5 mm^3. After completion of the experiments the animals were euthanized by intravenous injection of Pentobarbital. The animal experiments were conducted in agreement with the French law on animal experimentation and in compliance with institution's rules for animal care and use.

Motion compensated MR-thermometry was performed for a duration of two minutes on the right kidney. After an initial baseline sampling of 30 s, a HIFU sonication of 80 W acoustic power and 60 s duration was performed on the first animal. In the subsequent two animals experiments, 30 s of sonication with and acoustic power of 100 W were used. The experiments were repeated on each animal two times, first with dynamic beam-steering enabled and then with a fixed beam for comparison.

The Kalman filter was calibrated as follows: Since a direct measurement of R and Q is hard to achieve in-vivo, both have been optimized empirically based on preparatory image data obtained under the same experimental conditions. A value of 0.1 mm was found to be a good compromise for the process noise covariance Q and the nominal MR-resolution of 2.3 mm was used as an upper bound for the measurement noise covariance R.

Representative for the results obtained in all three animals, figure 6.4 shows an overlay of the temperature map after 30 s of sonication with 100 W acoustic power for both, the uncompensated and the motion compensated experiment. Since the kidney has a very high perfusion rate, a "line" effect similar to the results from the uncompensated phantom experiments was not observable in any of the in-vivo experiments. However, the uncompensated experiments reached in all three experiments a lower final temperature than the experiments performed with full motion compensation (compensated: 25.3 °C, 10.1 °C and 8.8 °C; non-compensated: 19.3 °C, 7.2 °C and 8.1 °C for animal 1,2 and 3, respectively) and shows fluctuations in the temperature rise which correlate the recorded displacement of the target area.

6.1.2.3 Discussion and conclusion

The aim of the presented study was to demonstrate the feasibility of real-time HIFU beam steering on moving targets. The presented study shows that it is possible to perform 3D Real-Time MRI guidance of a HIFU intervention on abdominal organs in vivo over sustained periods of several minutes. During the intervention both, the target location and the target temperature are continuously available with a high temporal resolution and precision. This allows HIFU interventions using a high duty cycle while minimizing undesired tissue damage and presents therefore a step towards clinical non-invasive HIFU therapies of kidney and liver tumors under free-breathing conditions.

The suggested Kalman-predictor evaluates the velocity of a Kalman filtered target trajectory to anticipate the future target position. The predictor is robust against noise and changes of the respiratory cycle and stabilizes rapidly after typically 2-3 datapoints, even if fluctuation/deviations in the respiratory cycle have occurred. However, the predictor is not suitable for parts of the motion pattern which are subject to high accelerations, since it will produce overshoots and deviations from the true trajectory. However, due to the high frame-rate and the low latency, the predictor is only required to anticipate the target position over short epochs of 50-100 ms before newly measured data is available, which limits the impact of such events.

Furthermore, since the target temperature and the thermal dose are continuously updated, it open the possibility to combine beam steering for both 3D target motion compensation and efficient volumetric heating strategy.

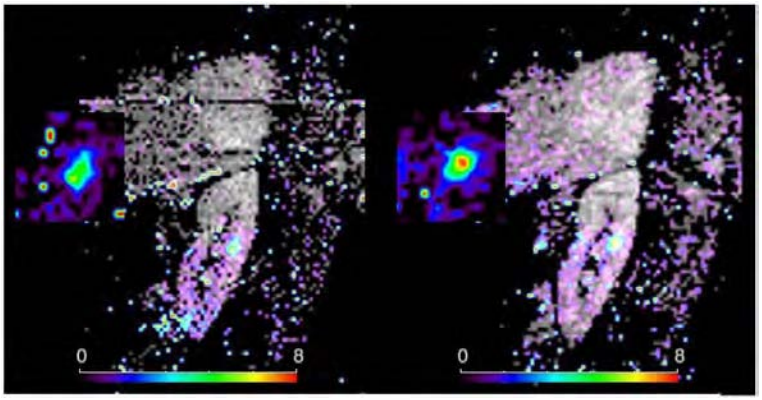

(a)

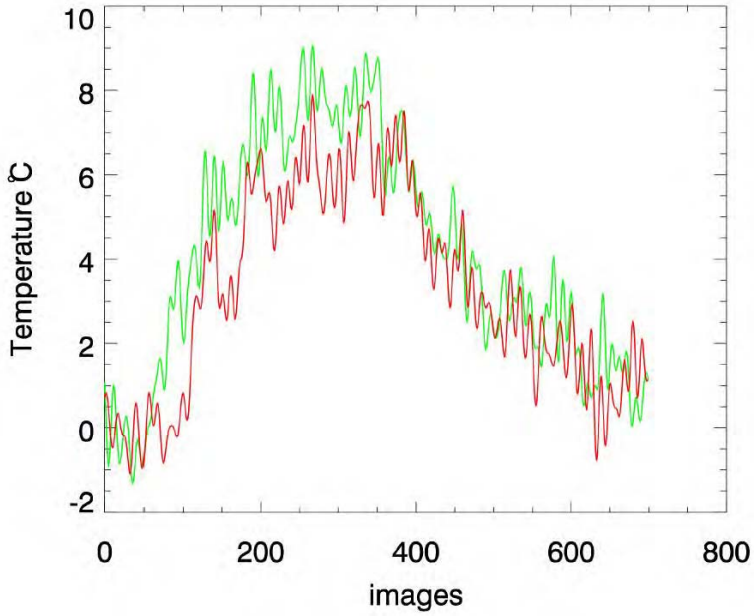

(b)

Figure 6.4: Magnitude images of the kidney of the uncompensated (a, right) and the motion compensated HIFU-ablation experiment (a, left), overlayed with the temperature maps obtained after 30 s of sonication of the third animal experiment. The inlay shows a four-fold zoom of the temperature map of the target area. The temperature evolution of the voxel with the maximal temperature rise with the uncompensated (red line) and the motion compensated (green line) HIFU-ablation experiment are plotted in (b).

6.1.3 Volumetric control strategies

As treatment volumes are generally larger than the focal point size, strategies for volumetric sonication are required. In this work, the method proposed by Mougenot et al. [93] was further developed to include thermal dose control using a proportional controller based on real time MR-thermometry and dosimetry information. Then, this information is combined with the 3D motion of the target in order to dynamically control the focal point position.

This study was realized as a joint project with Dr. Silke Hey and Dr. Mario Ries as the principal investigators and my contribution was on the real time implementation of the employed processing pipeline.

The feasibility of the proposed method was tested experimentally ex vivo under conditions simulating respiratory motion of abdominal organs.

6.1.3.1 Method description

3D volume coverage In order to ensure sufficient volume coverage while maintaining a high temporal resolution, the acquisition of a static image slice for 2D motion estimation was combined with a sweep of a second slice covering the target area. For this purpose, one slice was translated by Δs for every image acquisition, thus covering a total range of $S_z = n\Delta s$ in the slice encoding direction for a slice sweep comprising n slice positions (Fig. 6.5). While the static slice was updated for every image acquisition and served for 2D motion estimation, an update of the entire image volume took $n.t_{\mathrm{dyn}}$ where t_{dyn} is the dynamic scan time of the acquisition. In general, arbitrary displacement schemes are possible, allowing for example to oversample a certain spatial position. For the implementation presented here, however, the slice was continuously translated from $-S_z/2$ to $S_z/2$ with Δs equal to the sequence slice thickness.

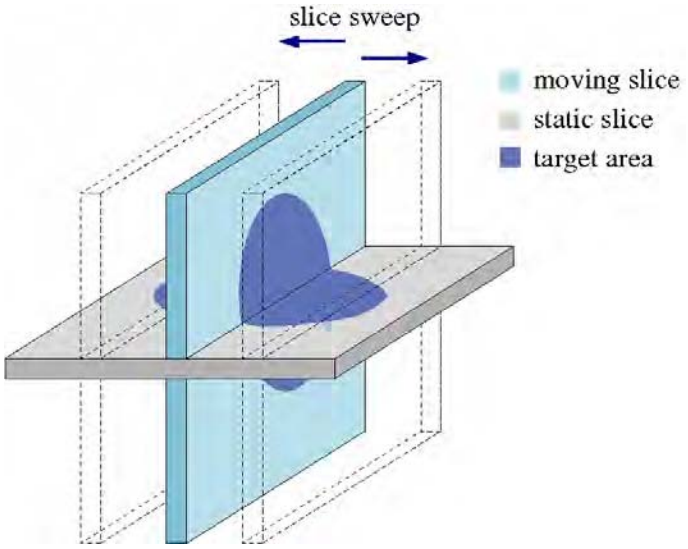

Figure 6.5: Principle of the slice sweep to increase the volume coverage. While one slice remains static, the second slice is moving continuously to cover the whole target area.

Image processing pipeline For 2D motion compensation in combination with the described trajectory optimization, a dedicated image processing pipeline has been developed (Fig. 6.6). My contribution in this pipeline was the development of the real time implementation of both the motion estimation and the PRF-thermometry pipeline steps. Motion estimation for the adaptation of the focal point position was carried out on the static slice only (left side in Fig. 6.6) in order to reduce the latency. For this a two step approach based on a global motion estimation followed by a local motion estimation was employed as described in detail in section 5.2.1. The retrieved position updates were directly forwarded to a dedicated thread controlling the ultrasound transducer. In a second independent pipeline, both acquired slices were motion compensated and temperature and thermal dose were calculated using the MR-thermometry and dosimetry pipeline presented in chapter 5. Subsequently, the calculated 2D temperature and thermal dose maps were gridded into an imaging volume aligned with the physical axis of the ultrasound transducer. Trajectory optimization was carried out on the 3D temperature and thermal dose maps and the resulting position updates of the trajectory were forwarded to the transducer control thread. This implementation allowed the treatment of a slice sweep covering n=11 slice positions which were gridded into a 3D volume of $96 \times 96 \times 30$ with isotropic resolution of $2.5\,\mathrm{mm}^3$ within a total dynamic scan time of 140 ms for both slices.

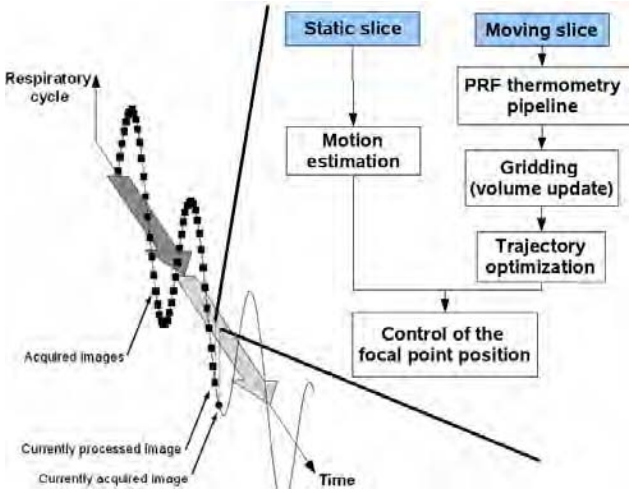

Figure 6.6: Scheme of the data processing pipeline. The static slice is directly processed in a separate thread (left) which calculates the displacement with respect to the transducer in order to adapt the focal point position accordingly. The sweep slice on the other hand is used to calculate 3D motion compensated temperature and thermal dose maps which are then used to optimize the trajectory of sonication points.

6.1.3.2 Evaluation experiments

Imaging protocol PRF MR-thermometry was performed based an a RF-spoiled single shot gradient recalled EPI sequence(TR=125 ms, TE=41 ms, matrix= 128 × 75, voxel size= 2.5 × 2.5 × 5 mm^3, 2 image stacks (both coronal), bandwidth in readout direction= 1561 Hz). Experiments were carried out on an agarose phantom. A trajectory of 5 sonication points was optimized and the sonication duration for each point was set to 25 ms and 60 W electronic power were applied. For 2D control, the volume sweep covered 5 different slice positions with a displacement of 5 mm. For 3D control, in order to achieve a higher volume coverage, the slice thickness was increased to 6 mm and the volume sweep was extended to cover 11 slice positions with a displacement of 6 mm.

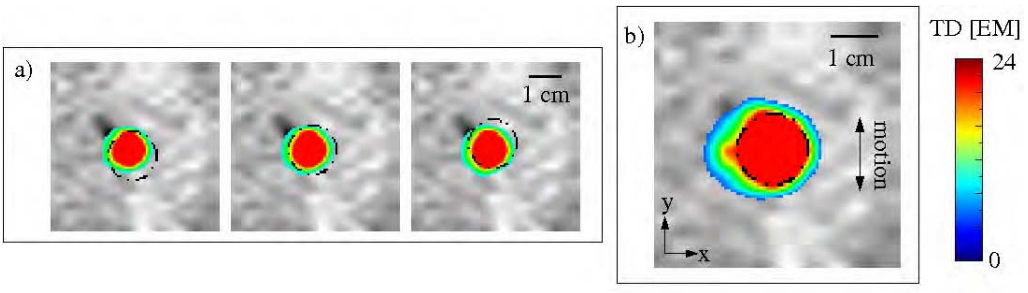

Figure 6.7: 2D thermal dose control experiment with target thermal dose of $TD_T = 24\,\mathrm{EM}$ (10% of the lethal thermal dose) and a circular target area of 15 mm diameter. a) Overlays of the thermal dose maps for different points in the motion cycle. The theoretical position of the target area without motion compensation is depicted by the dashed-dotted black circle. b) Thermal dose map at the end of the treatment. The target area is depicted by a black dashed-dotted circle.

Two-dimensional thermal dose control with motion One dimensional physiological motion was simulated (peak-to-peak amplitude of 4.5 mm with a period of 3 s) by a motorized MR-compatible platform which was attached to the agarose platform to create periodical displacements during the treatment. A circular target area of 15 mm diameter was chosen with a target thermal dose of $TD_T = 24\,\mathrm{EM}$. Figure 6.7a shows the achieved thermal dose map at the end of the treatment. The resulting thermal dose distribution shows good correspondence with the target area without any motion related effects. All voxels within the target area received a thermal dose $TD \geq TD_T$. Only one voxel outside the target area was heated to that extent ($TD = 41.6\,\mathrm{EM}$). The overall heating duration was 88 s.

Three-dimensional thermal dose control An ellipsoidal target volume (short axis 7.5 mm, long axis 15 mm along the beam axis, 123 voxels) was chosen for thermal dose control with a target value of $TD_T = 24\,\mathrm{EM}$. Figure 6.8 shows the thermal dose profiles in the three orthogonal planes for four different time points as well as the thermal dose profile at the end of the treatment for the three directions. In order to reduce overheating due to the near-field effect, heating starts in the areas with the largest distance from the transducer surface with a preference of the central voxels of the target ellipsoid. In the radial view (xy), good agreement between the final thermal dose distribution and the target area is visible. Parallel to the beam axis, overheating in adjacent voxels occurred. This is also visible in the thermal dose profile in z which indicates overheating along the beam axis. As a result, 124 voxels outside the target area received a thermal dose above the target value ($TD = 25.2 - 600.7\,\mathrm{EM}$).

6.1.3.3 Discussion

Volume coverage and 3D control The implementation of a slice sweep made it possible to combine volume coverage with frame rates compatible with the real time constraints of motion compensation and temperature control. As the slice positions covered by the slice sweep can be chosen for each application, volumetric temperature and thermal dose information can be used to monitor the near field or critical areas in the beam path in order to prevent extensive heating. Alternatively, a 3D imaging volume can be constructed using the integrated gridding algorithm. By choosing the displacement Δs inferior to the slice thickness, the principle of superresolution [137] can be used to increase the spatial resolution in the sweep direction. An example of the feasibility of static 3D control using such 3D volume has been presented and evaluated. It is possible to achieve a pre-defined thermal dose within the 3D target area, but the control precision is reduced compared to 2D control. Deviations are mainly visible along the beam axis as a result of the elongated focal point and the near-field heating which increases with treatment time.

Motion compensation and latency In the presence of periodical displacements comparable to physiological motion, similar precisions for the thermal dose algorithm were found with no evidence of motion-induced broadening of the heated area. The separation of image processing necessary for real-time beam tracking and the calculations required for temperature monitoring and trajectory optimization led to a lower latency in the adaptation of the beam position. For the current implementation, a refresh-rate of 125 ms was sufficient to reliably follow the periodic motion with period 3 s. A further latency reduction is mainly limited by signal considerations as minimum two slices have to be acquired. The latency for the trajectory optimization mainly depends on the number of slice positions covered by the slice sweep. For 2D control, this delay could be reduced by applying a sweep pattern which oversamples the slice containing the area to be heated with the other slices serving as safety control to prevent overheating in adjacent voxels.

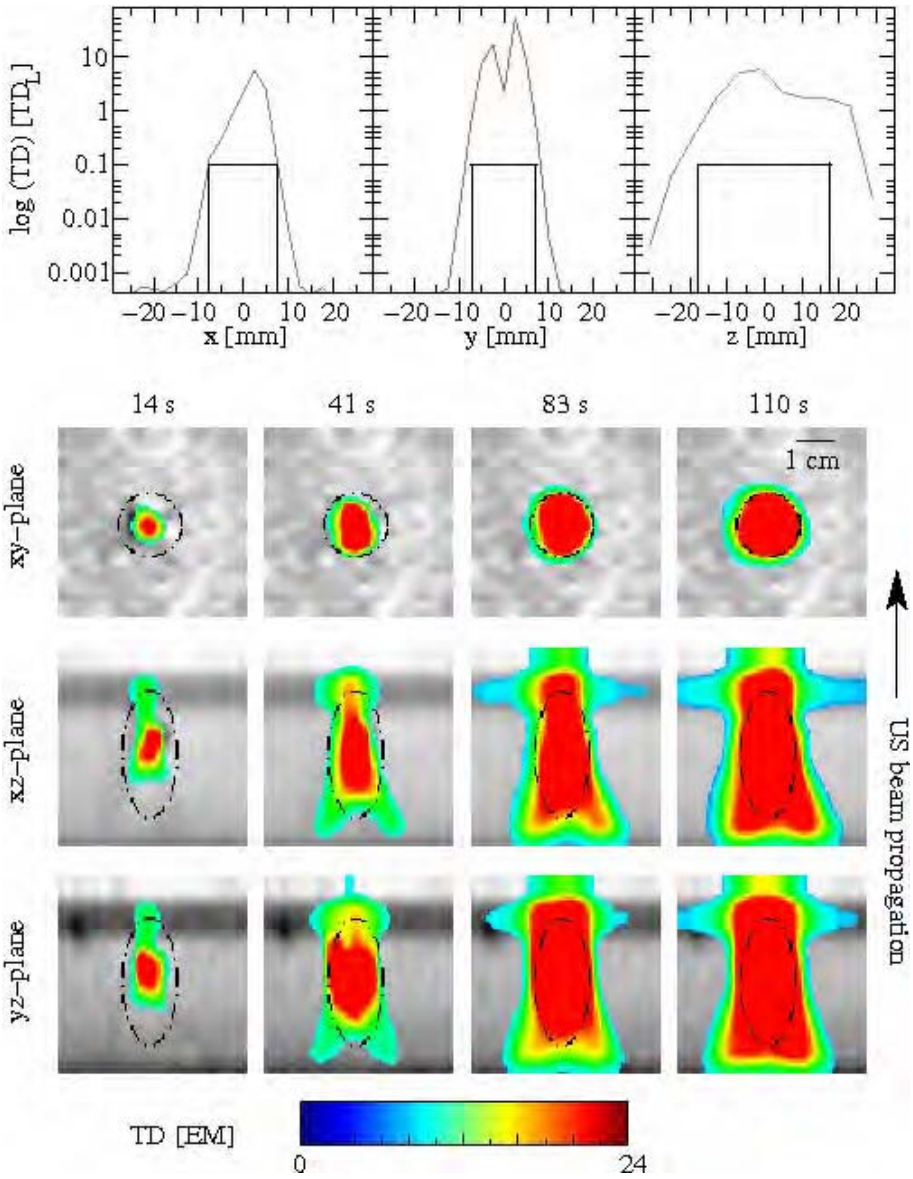

Figure 6.8: 3D thermal dose control experiment with target thermal dose $TD_T = 24\,\mathrm{EM}$ (10% of the lethal thermal dose) and an ellipsoidal target area of $7.5 \times 7.5 \times 15$ mm^3. Top: Thermal dose profiles along x (blue line), y (red line), and z (green line) through the center of the target volume. The target thermal dose TD_T is depicted by a black solid line. Bottom: Color overlay of the thermal dose for different time steps and the xy-plane (first row), xz-plane (second row), and the yz-plane (third row). The borders of the target area are visualized by a black dashed-dotted line.

The spherical phased-array transducer used in this work offered only limited possibilities in terms of electronic displacement of the focal point position ($\pm 1.2\,\mathrm{cm}$ in x/y and $+1.5/-2.5\,\mathrm{cm}$ along z) coupled to a comparably large focal point size of $\approx 1.2 \times 1.2 \times 8\,\mathrm{mm}$. For the treatment of larger target volumes, a transducer with a higher ratio of focal length to the size of the single elements may allow to benefit more from the possibilities of volumetric control.

6.2 MR-guided RF ablation in the heart

6.2.1 Ablation in the heart of a sheep

The MR-thermometry and dosimetry pipeline has also been evaluated in vivo on the ventricle of the heart of a sheep under general anesthesia during MRI guided RF ablation [128, 138]. Although atrial fibrillation treatment requires the ablation in the atrium, this experiment was a first test to demonstrate the feasibility of MR-guided RF ablation in the heart. This experiment was part of a joint study with Dr. Pierre Jaïs and Dr. Bruno Quesson as the principle investigators.

6.2.1.1 Experimental set up

The experimental protocol was in compliance with the rules for animal care of the institution and with the French law on animal experimentation. Each animal (N=2) weighing 55kg± 4 was sedated by intramuscular injection of 0.1mg/kg of acepromazine (Calmivet, Vetoquinol, Lure, France) and anesthetized by IV injection of 0.1mL/kg of pentobarbital (Ceva sant animale, Libourne, France) before being instrumented in an XRay room. The animal was ventilated with a 40 % humidified oxygen via a tracheostomy and general anesthesia was maintained using continuous IV perfusion of sodium pentobarbial (6mg/kg/h). The right femoral artery was cannulated with an 8 FR sheath. The MRI compatible RF ablation catheter was advanced into the left ventricle with a retro aortic approach. The animal was then moved to the MR Lab for MR temperature imaging of the RF ablation. After completion of the experiment, the animal received a lethal IV injection of Dolethal.

MRI guided RF-heating was performed in vivo in the left ventricle of a sheep under general anesthesia (see above for details in animal preparation). Real-time MR thermometry was performed during RF ablation with a similar acquisition protocol as for the volunteer study, by acquiring 400 dynamic images in the short axis orientation. The acquisition was ECG triggered and respiratory compensated with navigator based slice tracking, using 5 slices, TR/TE=650/16ms, bandwidth in readout direction=2085Hz, flip angle=35°, FOV=320×140mm^2, slice thickness=6mm, matrix=128×56.

6.2.1.2 Experimental results

The cardiac cycle duration was approximately 650 ms. The SNR on the magnitude image was 20 and a TSD (evaluated on the 50 dynamics prior to RF ablation) of 1°C was measured on the whole myocardium. This value rose to 2°C at the tissue electrode interface (figure 6.9c and 6.9f). MR-guided RF ablation of the left myocardium showed consistent evolution of the tissue temperature, with a progressive increase near the catheter tip during 60 sec energy delivery, followed by spontaneous tissue cooling by heat conduction and perfusion. Temperature images acquired at the end of the RF energy delivery showed a larger heated area for a heating performed at 10W RF power than for a heating performed at 5 W (figure 6.9a and 6.9d). The maximum increase of temperature in the pixel at the contact with the catheter tip for 5 W/10 W RF power were 9°C (figure 6.9b) and 16°C (figure 6.9e), respectively. No heating was observed in the adjacent slices. Temperature elevation higher than 5°C were achieved in ellipsoidal regions of dimension 7×17 mm^2 (5W RF) and 10×20 mm^2 (10 W RF).

6.2.1.3 Discussion and conclusion

The precision of the temperature estimate on animal during catheter RF ablation was better than those observed on healthy volunteers (approximately a factor of 2). This could be attributed to the well controlled breathing conditions due to mechanical ventilation of

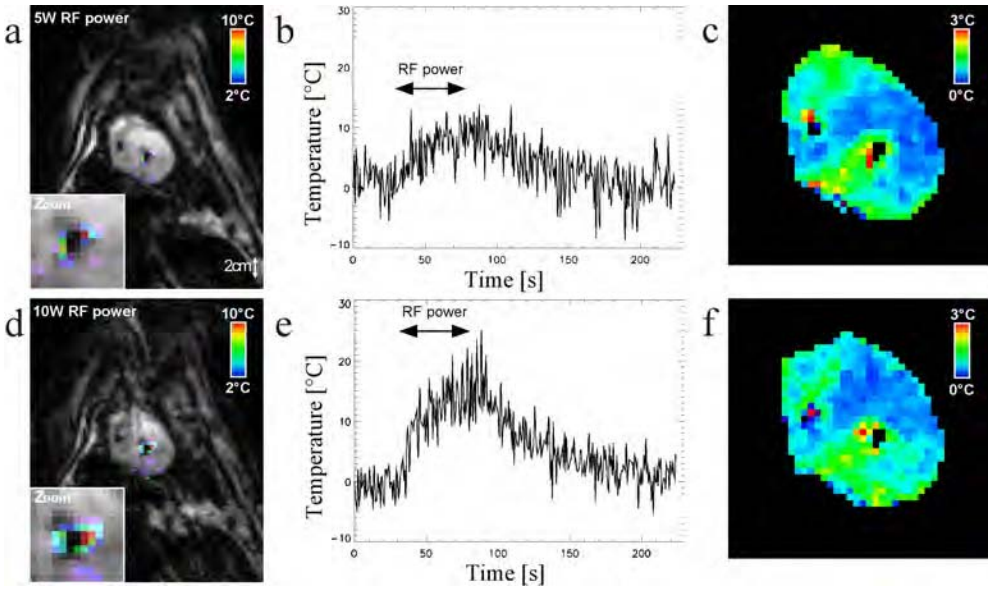

Figure 6.9: MR-Thermometry results obtained on the left ventricle of a sheep heart during RF-heating. a: the temperature distribution obtained after one minute of 5W RF heating overlayed on the anatomical image, b: corresponding temporal evolution of the temperature at the extremity of the catheter (up to 8°C of temperature evolution were measured), c: corresponding TSD map obtained before hyperthermia, d: the temperature distribution obtained after one minute of 10W power heating overlayed on the anatomical image, e: corresponding temporal evolution of the temperature at the extremity of the catheter (up to 16°C of temperature evolution were measured), f: corresponding TSD map obtained before hyperthermia.

the animal, which lowered both the amplitude and speed of heart displacement along the feet-head axis, reducing the risks of uncompensated out-of plane motion associated to imperfect slice tracking. The use of fast and motion compensated thermometry allowed for visualization of the temperature evolution with a temporal resolution lower than 1 sec. Minimal artifact of the catheter on temperature images was observed and the increase in temperature was consistent with the RF energy deposition. These results demonstrate the feasibility of online cardiac tissue temperature monitoring during RF ablation with a MRI compatible catheter.

6.2.2 Discussion and conclusion

In this chapter, several applications and extensions of the MR-thermometry and dosimetry processing pipeline, proposed in chapter 5, have been presented. The feasibility of real time MR-guidance of a thermal ablation has been shown in-vivo in both the abdomen (using HIFU heating) and the heart (using RF-heating) of animals. Methodological extensions have been successfully proposed for HIFU ablations, especially to optimize the energy deposition using 3D HIFU beam steering for target tracking and 3D volumetric control of the delivered energy. However, several methodological challenges still remained to be developed, as discussed in chapter 5, in order to improve the robustness of the interventional procedure and thus the patient safety. Therefore, based on this analysis, novel methods have been developed and are presented in the next part of this thesis.

Conclusion

In this part, very fast MRI (using frame-rate in the order of 10 Hz) has been employed for MR-guided HIFU ablations. Real time implementations of an efficient MR-reconstruction method and a MR-thermometry and dosimetry pipeline have been proposed. These methods have been demonstrated to ensure the time constraint imposed by our real time system and have been validated in typical clinical scenarios. The MR-thermometry and dosimetry processing pipeline has been successfully employed for in-vivo MR-guided HIFU experiments. This method has been extended in further studies where for example the feasibility of very fast MR-thermometry and HIFU beam steering was demonstrated.

This processing pipeline has also been evaluated in the heart and promising results were obtained. The feasibility of real time MR-guided RF-ablation has also been shown in-vivo.

However, as presented in section 5.5, several artifacts may still be encountered during the intervention, which could hamper the reliability of the therapeutic process and thus the patient safety. Therefore, several methodological developments have been carried out in this thesis to improve the robustness of the existing pipeline. These works are now presented in the next part of this manuscript.

Part III

Advances in methodological development for MR-guided thermal ablation

Chapter 7

Motion estimation with structures appearing transients

7.1 Introduction

As we have seen in chapter 5 and 6, interventional procedures are usually restricted to a part of the organ/tissue under study. In these conditions, the acquisition of large field of view is time consuming and thus not always necessary. Therefore, reduced field of view imaging may be useful to restrain the imaged area around the target and accelerate the MR-acquisition. The gain in time may thus be invested for the improvement of the spatial and / or temporal resolution in order to decrease partial volume effects (undesirable for quantitative analysis) and increase imaging framerate (required to observe rapid phenomena).

Several strategies have been proposed to achieve a reduction of the field of view such as saturation slabs, which can be set around the imaging targeted area. Alternatively, outer volume suppression [139] can be used or more recently, the transmit SENSE technology [140] would also allow the acquisition of reduced FOV. For the particular application of cardiac function analysis and guidance of interventional procedures, Schaeffter et al. [141] also proposed a strategy for interactive reduced FOV imaging.

Although a reduced FOV may improve spatial or temporal resolution, it introduces a new challenge for the target motion estimation. Indeed, structures close to the target that would appear similar in all images using full FOV imaging (since FOV is usually centered on the target), may appear transient in the case of reduced FOV due to the respiratory motion and the limited spatial coverage. This effect is illustrated in figure 7.1.

(a) (b)

Figure 7.1: Illustration of structures appearing transient in the field of view: in this case, the upper part of the liver is present in a first image (a) and totally disappeared in a second image (b) acquired at a different time points of the respiratory cycle.

In such a case, an optical flow algorithm might be expected to fail locally to recover the real motion since the assumption of energy conservation is violated. In detail, if a structure is only present in the reference image, the algorithm might try to take signal from the target (in the image to register) to regenerate the structure. Alternatively, if a structure only appears on the image to register, the algorithm might try to register the structure inside the target. In addition, this effect is expected to be higher if intensity levels of both target and structure are comparable. Note that a similar problem can also occur in the case of out of plane motion produced near the target (that can occur in both full FOV and reduced FOV imaging). To improve robustness of the algorithm against this effect, one can increase α^2 value to decrease the influence of intensity gradient. However, this will also decrease the ability of the algorithm to estimate complex motion since it gives more importance to the motion field smoothness.

To overcome this limitation, Loncaric et al. [142] proposed to constrain the iterative scheme of the Horn & Schunck algorithm (described in chapter 2, section 2.1.3.2) by introducing constraint points. However, their algorithm was designed to obtain a final motion field that exactly fits, for each constraint point j, its initial estimated displacement (u_j, v_j). They proposed to directly modify the iterative scheme of the Horn & Schunck functional (see equation (2.10)) as follows:

$$\begin{cases} u^{n+1} = \beta u_{hs}^{n+1} + (1-\beta) u_{if} \\ \\ v^{n+1} = \beta v_{hs}^{n+1} + (1-\beta) v_{if} \end{cases} \tag{7.1}$$

with

$$u_{if} = \frac{\sum_{j \in F} \frac{u_j}{d(i,j)^2}}{\sum_{j \in F} \frac{1}{d(i,j)^2}} \quad v_{if} = \frac{\sum_{j \in F} \frac{v_j}{d(i,j)^2}}{\sum_{j \in F} \frac{1}{d(i,j)^2}} \tag{7.2}$$

where u_{hs} and v_{hs} corresponds to the iterative scheme of the Horn & Schunck approach, F denotes the region of influence of each constraint point and $d(i,j)$ is the distance between the pixel i and the pixel j. β is a weighting factor designed to balance the influence of each constraint point in its neighborhood (β=0 at constraint point location and rises to 1 for pixels outside the neighborhood constraint region). This method requires the a priori exact knowledge of each constraint point displacement. An attempt to integrate feature points into the optical flow formulation was proposed by Becciu et al. [143] for cardiac contraction analysis using tagged MRI. In their work, feature points were extracted from the tags. However, MR tagged images are generally unsuitable for interventional or diagnostic MRI, since images are tagged by regular lines where the signal has been removed. Recently, a variational approach, integrating segmented region motion, was proposed for large displacement estimation [144]. This method uses a linearized OFCE deviation together with regularization terms which include the correspondence of region displacements in the image plane. Despite the interest of such an approach in general purpose of video sequences, its application to MRI sequences is not straightforward due to the inherent difficulties of segmentation of frames into spatially coherent regions.

In our approach, a global motion compensation was first employed as described in chapter 5 (see section 5.2.1), to overcome the problem of large displacement estimation which is mainly due to respiratory motion. Hence only residual optical flow has to be estimated as precisely as possible. To do this, we integrate additional displacement information of feature points (referred to as constraint point in the scope of this thesis) into the formulation of optical flow Horn & Schunck functional. Furthermore, to fulfill the real time condition and ensure short latency, all computationally intensive calculations were off-loaded to a dedicated graphics processing unit (GPU). The proposed algorithm [145, 146] (referred to as constrained motion estimation (CME), in the scope of this thesis)

was compared with the Horn & Schunck approach on both synthetic data and cardiac & kidney MR-images.

7.2 Motion estimation with constraint point regularization

The proposed CME algorithm is a two-step procedure (see Fig. 7.2). During a preparation step, constraint points are selected (step 1 in Fig. 7.2). For this, a mask manually set around the target (heart or kidney in our case) on the reference image is drawn and its edge is extracted and sampled. To refine the positioning of each sample point, a feature point detection is realized on the reference image. Then, the closest feature point for each sample point is selected. In a second step (lower block in Fig 7.2), the motion is estimated for each image as follows: A global translational motion estimation is performed and used to initialize a local estimation of the displacement of constraint points. Non physiological constraint point displacements are identified and corresponding constraint points are discarded. The displacements of the constraint points are then integrated into the constrained optical flow algorithm (using the global estimated motion as preconditioning) to obtain the final motion field. As mentioned in chapter 5 isotropic 3D images on mobile organs are hard to achieve due to technical limitations of fast MR acquisition sequences. The proposed technique has thus been evaluated in 2D case.

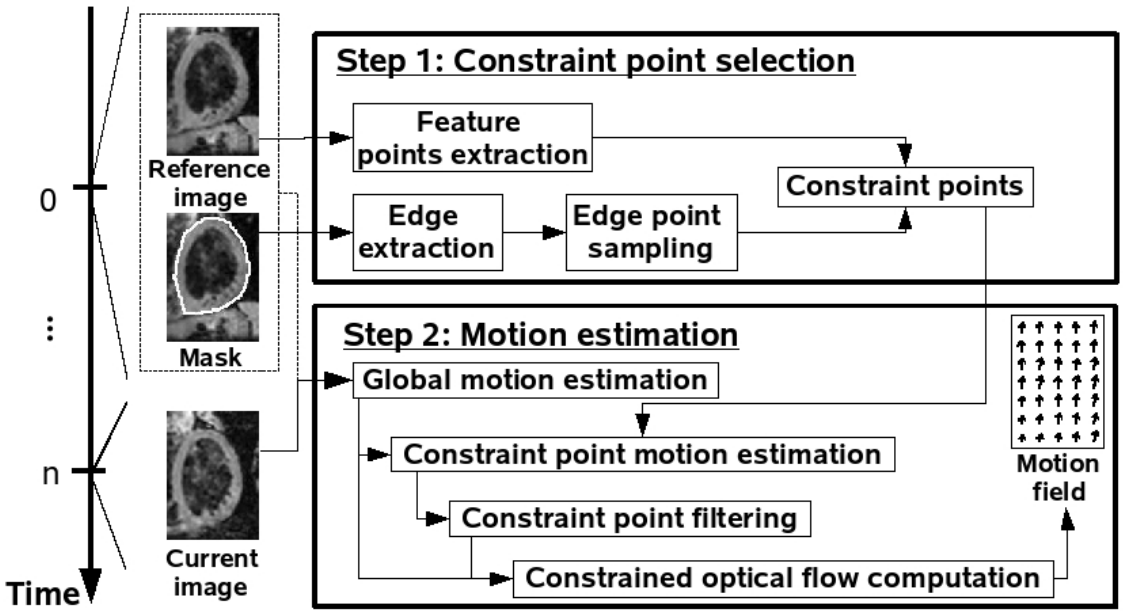

Figure 7.2: General scheme of the algorithm. Prior to the intervention, constraint points are automatically extracted from a reference image and its associated mask (step 1). Then, during the procedure, the motion field is estimated for each frame (step 2).

7.2.1 Step 1: Constraint point selection

Anatomical points are localized and tracked over the time in order to guide and constrain the motion estimation of the target. For this, anatomical structures such as organ boundaries, which remain present during the acquisition and follow the target, represent good candidates for this role. Although a precise automatic segmentation of the target is achievable [147], these methods are typically hampered for rapid MRI by low SNR (typically from 5 to 20). Instead, we use a region of interest (ROI) manually set around the target

of the reference image. The edge of the ROI is first extracted and then regularly spaced sampled to obtain a set of N points surrounding the target.

Nevertheless, if considering the future application of the method as an interactive tool to be used by a staff physician, it is mandatory to allow a certain degree of freedom on the ROI drawing. Hence the regularly spaced sampled constraint points could not and surely will not be very precise. We therefore propose to "move" them to the nearest feature point computed on the reference image. Typically a small neighborhood of regularly spaced sampled points is chosen to search for a closest feature point (e.g. 3×3 pixels neighborhood). Due to the abundance of works in stereo matching and image retrieval, a large amount of feature point detectors has been tested and reported in literature [51]. The critical point is the stability of these methods with respect to affine transformations of image plane, lightening and scale variations and noise. In the case of MR images, the noise and deformable motion are the main factors. According to the evaluation in [51], the Harris-Stephens detector [52] appeared to provide a good compromise between robustness and computation time. The feature point detection is based on the following response function:

$$R(x,y) = Det(M_{x,y}) - k \cdot Tr(M_{x,y})^2 \tag{7.3}$$

with

$$M_{x,y} = \sum_{i,j \in S} w_{i,j} \begin{pmatrix} I_x^2 & I_x I_y \\ I_x I_y & I_y^2 \end{pmatrix}_{i,j} \tag{7.4}$$

where (x, y) denotes the space coordinates, Det denotes the determinant of a matrix, Tr is the trace of a matrix, w is a weighting factor (Gaussian kernel over a region S) and k is a sensitivity parameter set to 0.04 in our study. The response is positive in a corner region, negative in an edge region and close to zero in a flat region.

7.2.2 Step 2: motion estimation algorithm

An optical flow based algorithm is more efficient when it is initialized near the global optimum solution. Therefore, to initialize it, a global motion estimation is first performed with a simple translational model, as described in section 5.2.1 by setting a_1, a_2, a_3, a_4 (defined in equation (5.1)) to 0. The translation parameters (horizontal and vertical) are estimated using a sign-gradient-descent with fixed step inspired by Netravali-Robbins method [148]. The estimation is restricted to a ROI defined in section 7.2.1.

Then, constraint point displacements are individually estimated (two translation parameters) using the global estimated displacement as initial estimate. This estimation is restricted to a small patch centered on each constraint point intersected with the initial ROI to allow a local refinement of the global displacement. The estimation is resolved by a simple region matching using an inter-correlation coefficient as the cost function F (as described in equation (2.1)) for the registration quality assessment. We experimentally found that a patch size of 10×10 pixels is satisfactory. To remove occasional non physiological estimates, a simple outliers rejection was added. The displacement vector $(d_x, d_y)^T$ of a constraint point was supposed to follow bivariate Gaussian distribution with independence of d_x and d_y coordinates. A constraint point is rejected if at least one of its coordinates violates the marginal 3-sigma rule.

The idea of the presented approach is to constrain the Horn & Schunck formulation by locally estimated displacements of feature points. Hence, we propose the following extension of the Horn & Schunck formulation with an additional regularization term:

$$E_c(u,v) = \iint \Big([I_x u + I_y v + I_t]^2 + \alpha^2 \left(\left[\|\nabla u\|_2^2 + \|\nabla v\|_2^2 \right] \right) + \lambda^2 \sum_{i=0}^{N} \Big(\rho(d_i, R) \left[(u-u_i)^2 + (v-v_i)^2 \right] \Big) \Big) \, dxdy \tag{7.5}$$

where (u_i, v_i) are the horizontal and vertical components of the displacement estimated for the i^{th} constraint point. λ^2 is the regularization parameter that allows balancing between the initial behavior of the Horn & Schunck algorithm and the constraint influence. ρ is a distance function, defined as

$$\rho(d_i, R) = \exp\left(-d_i^2 / R^2\right) \tag{7.6}$$

where d_i represents the Euclidean distance between the pixel of coordinates (x, y) and the i^{th} constraint point, R is a bandwidth parameter. Obviously, the quality of the estimated motion of the constraint points and the bandwidth influence the resulting optical flow. These settings will be discussed in the experimental part of this study.

The minimization of $E_c(u, v)$ is obtained based on the resolution of the associated Euler Lagrange equations and the Gauss Seidel method and is detailed in appendix D.2. This resulted in the following iterative scheme:

$$\begin{cases} u^{n+1} = \frac{\alpha^2\left(I_y^2+\alpha^2+\lambda^2 S\right)\bar{u}^n - \alpha^2 I_x I_y \bar{v}^n - \alpha^2 I_x I_t + \lambda^2\left(\left(I_y^2+\alpha^2+S\right)S_{u_i} - I_x I_y S_{v_i} - I_x I_t S\right)}{\left(\alpha^2+\lambda^2 S\right)\left(I_x^2+I_y^2+\alpha^2+\lambda^2 S\right)} \\ v^{n+1} = \frac{\alpha^2\left(I_x^2+\alpha^2+\lambda^2 S\right)\bar{v}^n - \alpha^2 I_x I_y \bar{u}^n - \alpha^2 I_y I_t + \lambda^2\left(\left(I_x^2+\alpha^2+S\right)S_{v_i} - I_x I_y S_{u_i} - I_y I_t S\right)}{\left(\alpha^2+\lambda^2 S\right)\left(I_x^2+I_y^2+\alpha^2+\lambda^2 S\right)} \end{cases} \tag{7.7}$$

with $S = \sum_{i=0}^{N} (\rho(d_i, R))$, $S_{u_i} = \sum_{i=0}^{N} (\rho(d_i, R) \cdot u_i)$ and $S_{v_i} = \sum_{i=0}^{N} (\rho(d_i, R) \cdot v_i)$

Note that with a zero λ^2, the iterative scheme is identical to the initial one proposed by Horn & Schunck.

7.2.3 Implementation

As described in chapter 5 (section 5.2.1), a multi-resolution approach [59] was added to both the Horn & Schunck and the CME implementations, which iterates the motion estimation algorithm from the 3^{rd} level of sub-resolution to the full resolution. Again, as also described in chapter 5, the most time consuming task, i.e. the iterative numerical scheme of the optical flow algorithms, was offloaded to a dedicated GPU.

The overall algorithm was implemented in C++ and evaluated on a dual processor (INTEL 3.1 GHz Penryn, two cores) workstation with 8 GB of RAM and dual 1 GB/s network interface cards. The GPU implementation was based on Compute Unified Device Architecture (CUDA) framework [106] using a NVIDIA GTX280 card with 1 GB of DRAM connected over a PCIe x16 link.

7.2.4 Experimental setup

The proposed algorithm was evaluated on both synthetic and in vivo datasets:

7.2.4.1 Simulated experiment

A sequence of $T(= 100)$ images was created. To simulate respiratory motion typically encountered on mobile organs, a "ground truth" periodic translational displacement field

$D_g t(t)$ (maximum amplitude=7 pixels, step size=1.5 pixels) was synthesized. The SNR of 20 was chosen to simulate a realistic acquisition. A rectangular structure appearing only for the three largest displacement amplitudes (thus present in half of the images) was added. The synthetic sequence is presented in figure 7.3a,b.

7.2.4.2 In vivo experiments

In vivo experiments were conducted on 13 healthy volunteers under free breathing conditions. Cardiac imaging was performed on the first six volunteers using saturation slabs and thus introducing problems typically encountered when zoom imaging is used (therefore the use of saturation slabs is referred to as zoom imaging conditions in the scope of this paper). The seventh volunteer underwent another cardiac experiment where the slice geometry was chosen so that out-of-plane motion was present. Finally, a study on the kidney was realized on the remaining 6 volunteers under zoom imaging conditions. For all of these experiments, the volunteer was positioned in head first in supine position in a 1.5 Tesla scanner (Philips Achieva/Intera).

In-vivo study on the heart under zoom imaging conditions: Dynamic MRI was performed under free-breathing conditions on the heart of six healthy volunteers. The acquisition sequence was ECG-gated (i.e. triggered on the cardiac signal) using a five element phased array cardiac coil. Five contiguous adjacent slices were acquired per cycle (200 cycles per experiment), in short axis view, in the mid or end diastole of each cardiac phase. A slice tracking technique [40] was used to compensate for respiratory motion in the third dimension perpendicular to the imaging plane and thus decrease related out-of-plane motion. Nevertheless, the residual in-plane respiratory motion still remains. Blood signal reduction was obtained using saturation slabs positioned on each side of the imaging stack. The single shot EPI sequence employed the following parameters: FOV=260×260 mm^2, acquisition matrix=96×96, reconstruction matrix=96×96, voxel size=$2.7 \times 2.7 \times 7$ mm^3, echo time=20 ms, repetition time=40 ms, SENSE acceleration factor=1.6 [102]. A saturation slab was positioned underneath the extreme position of the heart (corresponding to the position at maximum respiratory displacement) to simulate zoom imaging conditions.

In-vivo experiment on the heart, demonstrating out-of-plane motion: The same cardiac protocol was used in this experiment except the saturation slabs were removed to acquire a larger signal area.

In-vivo study on the kidney under zoom imaging conditions: A single coronal slice was acquired during 200 dynamics using a four element phased array body coil. A dual shot EPI sequence employed the following parameters: FOV=200×400 mm^2, acquisition matrix=84×118, reconstruction matrix=176×176, voxel size=$2.3 \times 2.3 \times 6$ mm^3, echo time=26 ms, repetition time=52 ms, flip angle=35°. Zoom imaging conditions were achieved using a saturation slab positioned on the top of the extreme position of the kidney. In such conditions, the typical amplitude of the heart and kidney motion is about 8 pixels in imaging plane between two extreme images in the respiratory cycle.

7.2.5 Assessment of motion estimation quality

Commonly, criteria based on the difference of motion compensated images are used to assess the accuracy of motion estimation [149]. However, these criteria are biased with "noise registration" and do not necessary reflect the accuracy of a motion field since they only rely on pixel intensities. Therefore, as demonstrated further in chapter 9, since our data are generally hampered by low SNRs, these criteria are not appropriate in our context.

To assess the quality of the estimated motion on synthetic images, a criterion based on the direct comparison between estimated motion field (D) and ground truth motion

field (D_{gt}) was evaluated as follows:

$$GSE = \frac{1}{T}\sum_{t=1}^{T}\left(\frac{1}{N}\sum_{(x,y)\in m}\|D(x,y,t) - D_{gt}(x,y,t)\|_2\right) \tag{7.8}$$

where t is the image index in the time series, m is a binary mask that allows to restrain the computation to a ROI and N the number of elements set to 1 in m. This criterion is referred to as gold standard error (GSE) in the scope of this paper.

To assess estimated motion in in vivo images, a manual segmentation of the target organ was realized on each registered image. The covering percentage (CP) between these ROI and the reference ROI was then analyzed and used as an in vivo motion estimation quality criterion.

$$CP(t) = \frac{ROI_{ref} \cap ROI_t}{ROI_{ref} \cup ROI_t} \tag{7.9}$$

where ROI_{ref} and ROI_t are respectively the ROI in the reference image and the ROI manually set around the target in the t^{th} registered image of the time series. A CP value of 1 denotes an ideal matching of the ROIs and thus a good registration. A CP value of 0 denotes no correspondence between the ROIs. We note that in manual segmentation of ROI for benchmarking purposes, a fine rotoscoping technique on a pixel-by-pixel basis was applied by a specialist. Obviously, some errors are possible because of aliasing effects, but we consider them negligible.

7.3 Results

7.3.1 Simulated experiment

The comparison between both algorithms was first realized on a synthetic dataset where the reference image and an example of image at a different position of the cycle are displayed respectively in Fig. 7.3a and b. The appearing rectangle, located at the bottom of Fig. 7.3b, is expected to hamper the motion estimation at the bottom of the object (in the red ROI displayed in Fig. 7.3a). Therefore, the gold standard error was computed for each dynamic, over this ROI and the results are plotted in Fig. 7.3c. The Horn & Schunck algorithm showed very poor performance on this area where the appearing rectangular structure biased the accuracy of the algorithm (three repetitive high values). On the other hand, the proposed CME approach remains stable over the time and provides a more accurate motion field.

7.3.2 In vivo experiments

Similar results were obtained in vivo on several experiments in both the heart and kidney of volunteers.

7.3.2.1 In-vivo study on the heart under zoom imaging conditions

The first analysis was realized on a short axis view of the heart of a healthy volunteer (SNR=12) (Fig. 7.4a). The area with low signal intensity in the lower part of the image corresponds to a saturation band that may allow reduction of the FOV without additional fold-over artifacts. This image was used as a reference for the in vivo sequence. A ROI was first manually set around the left ventricle (LV) (contour shown in Fig. 7.4b) and the constraint points were derived from the combination of a subsampled contour of this ROI

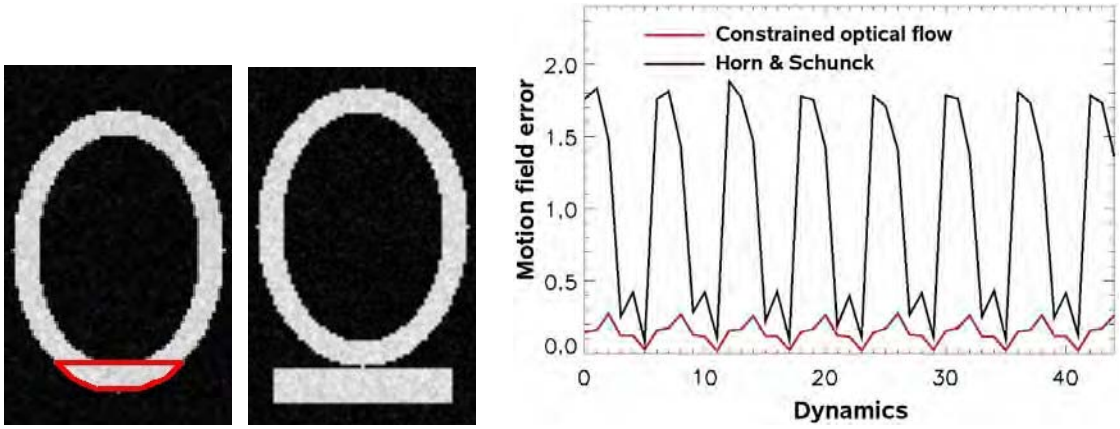

(a) (b) (c)

Figure 7.3: Gold Standard Error on a synthetic sequence, (a): reference image, (b): example of image to register, (c): motion field error calculated over the red ROI (shown in (a)) using both methods.

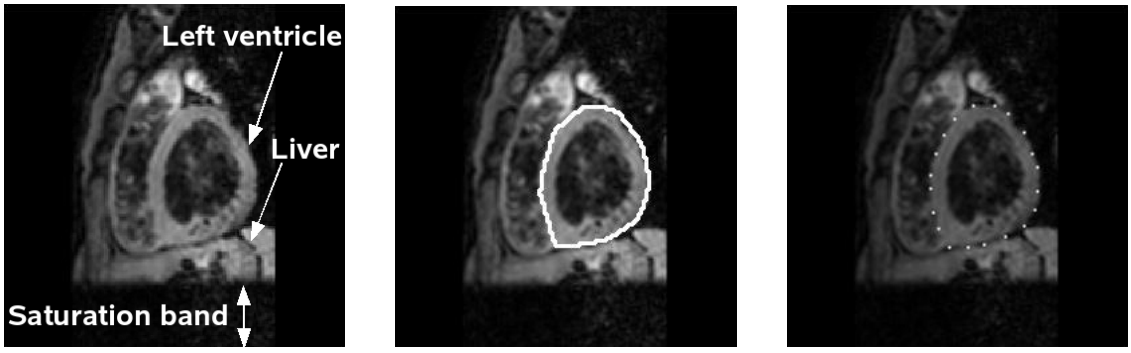

(a) (b) (c)

Figure 7.4: Constraint selection. (a): reference image, (b): reference image and the corresponding ROI manually set around the target, (c): constraint points.

and a feature detection (see Fig. 7.4c). These points precisely match the contour of the LV. The motion estimation algorithm was then evaluated on the time series images.

In order to accurately estimate the displacement of each constraint point, a global motion estimation step is used as initialization of the constraint point motion estimation. The interest of such combined approach is illustrated in figure 7.5. Here, the inter-correlation coefficients obtained over a region centered on a constraint point was computed before and after the global motion estimation step and after the constraint point motion estimation step. Although the global motion estimation step (red curve) clearly improved the initial intercorelation value (black curve), a further refinement of the solution was achieved with the constraint point motion estimation step (blue curve).

The overall performance of the CME is now presented. An example of an image from the same sequence acquired at a different position in the respiratory cycle is displayed in Fig. 7.6a. A large inferior displacement of the heart is observed compared to the reference position (Fig. 7.4a). The position of the liver (below the heart) is also very different and its signal almost disappeared in Fig. 7.6a, due to the displacement induced by the respiration.

The Horn & Schunck method (with α^2=0.1) resulted consequently in a poor motion estimate in the lower part of the LV (the white ellipse in Fig. 7.6b) where the myocardium

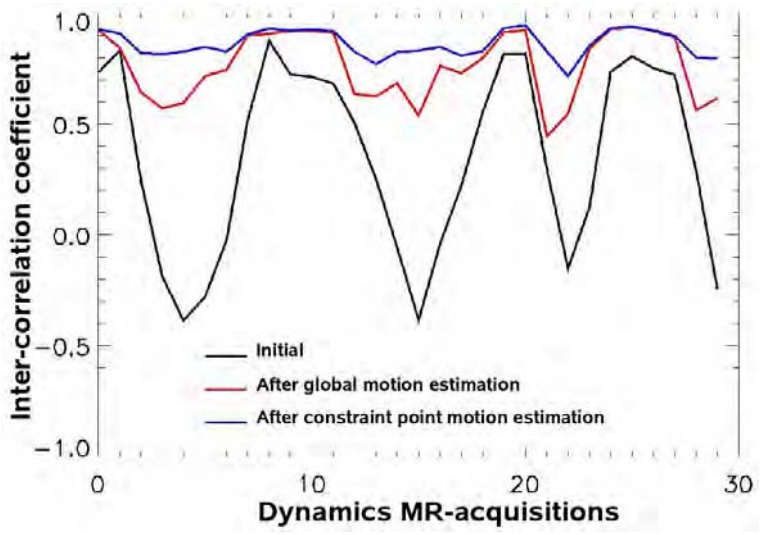

Figure 7.5: Typical time evolution of inter-correlation coefficients obtained over a region centered on a constraint point. Values obtained without correction (black curve), after global motion estimation (red curve) and after constraint point motion estimation (blue curve) are plotted.

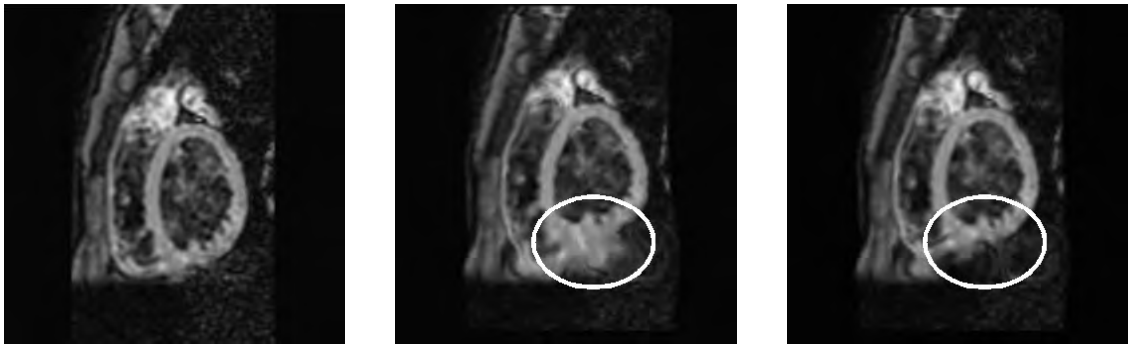

(a) (b) (c)

Figure 7.6: Registration results obtained with Horn & Schunck approach and the proposed one on volunteer #3 (a): image to register, (b): registered image using Horn & Schunck method, (c): registered image using the CME approach.

is deformed. In such a case, the algorithm takes pixels from the myocardium (in the image to register) to regenerate the transient structure present in the reference image and thus failed to recover the real motion. Using the proposed CME approach (with α^2=0.1, λ^2=0.05, R=$\sqrt{5}$, N=20), the LV (see Fig. 7.6c) visually matched the reference image. The algorithm was not disturbed by the disappearance of the liver. These findings are typical for the entire image sequence as shown in Fig. 7.7a where CP is plotted (see red and black curves). Due to the respiratory cycle, the transient structure present in the reference image appeared periodically on the time series. In these conditions, the Horn & Schunck approach periodically failed to register images that do not contain the non persistent structure. A reliable registration was achieved using the proposed CME which provided over time a stable CP value (around 0.92%) similar to the one obtained with the Horn & Schunck algorithm in images containing the transient structure.

The behavior of the proposed CME was also tested for the influence of the number of constraint points N and the bandwidth parameter R (see equation (7.6)). Exhaustive

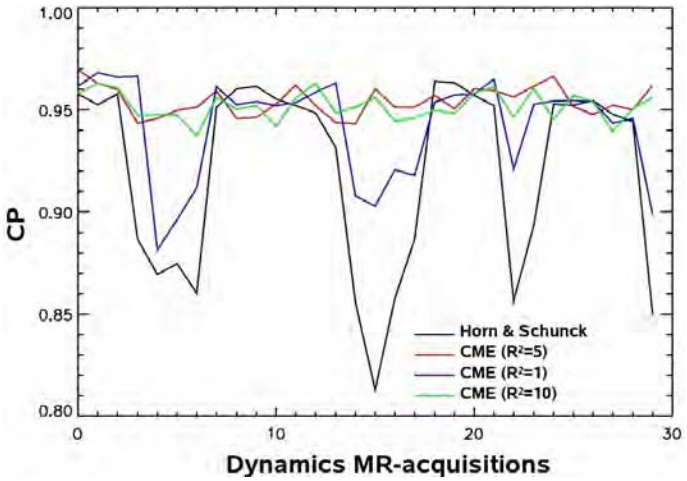

(a)

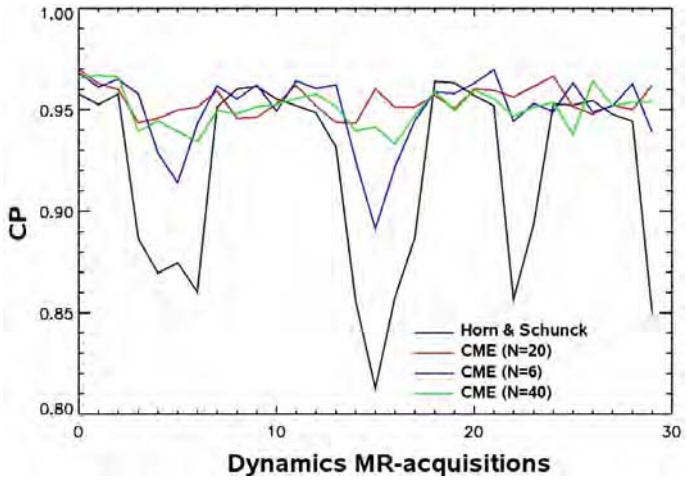

(b)

Figure 7.7: Behavior of the proposed CME using different configurations: for several values of R with N=20 (a) and several values of N with $R = \sqrt{5}$ (b).

assessment of the quality criterion is rather tedious as it requires manual tracking of ROI in all registered frames of the sequence. Hence, we sparsely sampled the N parameter space and R parameter space.

Furthermore, a precise evaluation of the quality criterion requires ideally set ROIs on the registered frames. Hence the manual error at this evaluation stage will bias the result. Furthermore, very low variations are expected with closed parameter values. Hence in Fig. 7.7, we plot the CP quality criterion for a limited number of parameter values (see Fig. 7.7a,b). As expected, a performance decrease is observed with a small bandwidth (when R=1) and with a small number of constraint points (when N=6).

Similar results were obtained in the study over six volunteers (see Fig. 7.8). The mean CP was found always better with the proposed CME. The plot shows that minimal CP values are very low for certain dynamics using Horn & Schunck approach, whereas the proposed CME allows to maintain reliable performance for all dynamics. This tendency is confirmed with the CP standard deviation values that are also significantly reduced with the proposed constrained optical flow.

Constraint point filtering allowed the rejection of constraint points with non physiological estimated displacement. A temporal average of less than 0.37 % of the constraint

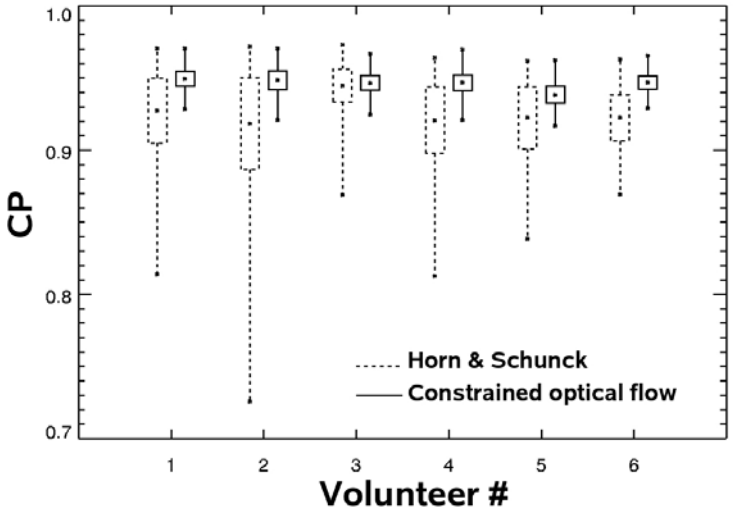

Figure 7.8: Analysis of motion estimation performance in the heart of six volunteers using Horn & Schunck approach and the CME approach. Box and Whisker plot of CP where displayed values correspond to the minimum (upper point) and maximum (lower point) CP values obtained on a dynamic, the averaged CP value (point inside the box) and the standard deviation of CP values (box size).

points were rejected with a maximum of two points for a dynamic.

7.3.2.2 In-vivo experiment on the heart demonstrating out-of-plane motion

Since out-of-plane motion is frequently encountered in MR-guidance application, this experiment investigated the potential of the method to this complex situation. In Fig. 7.9 the reference image and an image acquired at different positions in the respiratory cycle (13^{th} of the time series) are shown (see Fig. 7.9a and 7.9b respectively). It can be observed that a structure which was present on the reference image (indicated by a white arrow) had totally disappeared in the second image, due to out-of-plane motion. The registered images using both the Horn & Schunck and the CME approaches are displayed in Fig. 7.9c and 7.9d. The Horn & Schunck approach tries to regenerate this structure using the surrounding signal in the image, i.e. the signal of the myocardium of the LV (see the white ellipse in Fig. 7.9c). Using the CME, the registered image visually matches the reference image (see Fig. 7.9d). This observation is confirmed by the CP analysis in Fig. 7.9e. The Horn & Schunck approach periodically failed to register those images that do not contain the underneath structure, whereas the CME provided reliable registration for all images.

7.3.2.3 In-vivo study on the kidney under zoom imaging conditions

Since many intervention procedures are conducted on abdominal organs, a third experiment was realized on the kidney. Images obtained on a healthy volunteer (volunteer # 3) are displayed in Fig. 7.10. The reference image and an image acquired at a different position of the respiratory cycle are shown respectively in Fig. 7.10a and 7.10b. Two perturbations are observed in the top part of the kidney: The liver, on the top of the kidney, partially disappears in the second image and the intensity of the upper of the kidney depicts a high variation. As expected, the Horn & Schunck approach registered pixels with similar intensity and the upper part of the kidney was deformed (see Fig. 7.10c). Using the CME, the constraint allows to conserve the initial shape of the kidney (see Fig. 7.10d). The CP value variations over time shows that the CME provides a better stability

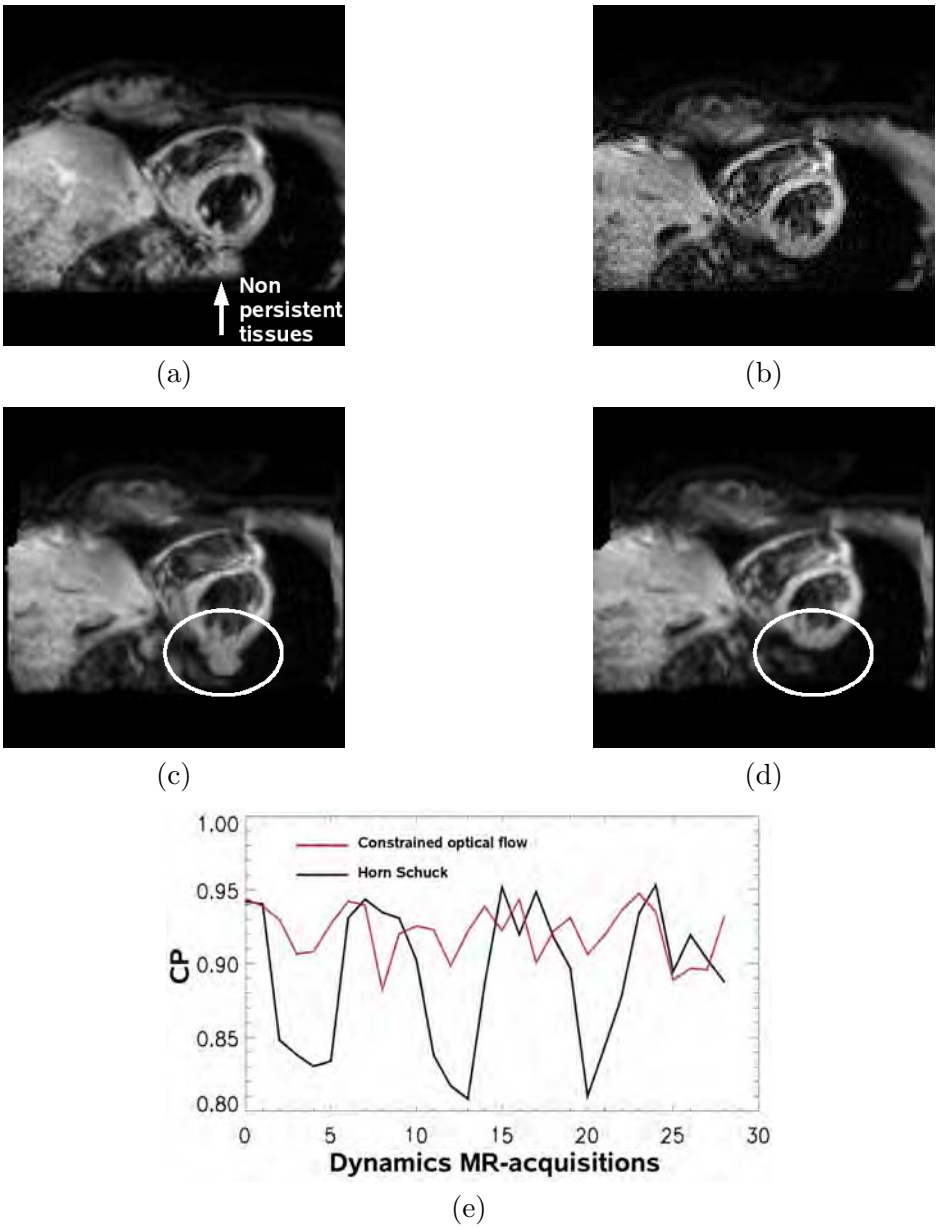

Figure 7.9: Analysis on experiment #2 (a): reference image, (b) image to register (13th of the time series), (c): registered image using the Horn & Schunck approach, (d): registered image using the CME approach, (e) CP comparison between both the CME and the Horn & Schunck approaches.

and a better performance than the Horn & Schunck method (see Fig.7.10e.

These results were representative for the registration quality obtained across the entire volunteer group. The performance of both algorithms was evaluated over six volunteers and is shown in Fig. 7.11. Temporally averaged CP values were always improved with the proposed CME approach except on volunteer #2 where both algorithms showed comparable performance. On this particular volunteer, the contrast between the kidney and the intrusive structure which is the boundary of the liver was very strong. Therefore, the Horn & Schunck method performed similar to the CME approach.

Performance of the constraint point filter were slightly different to the results obtained in the heart. A temporal average of less than 2.67 % of the constraint points were rejected

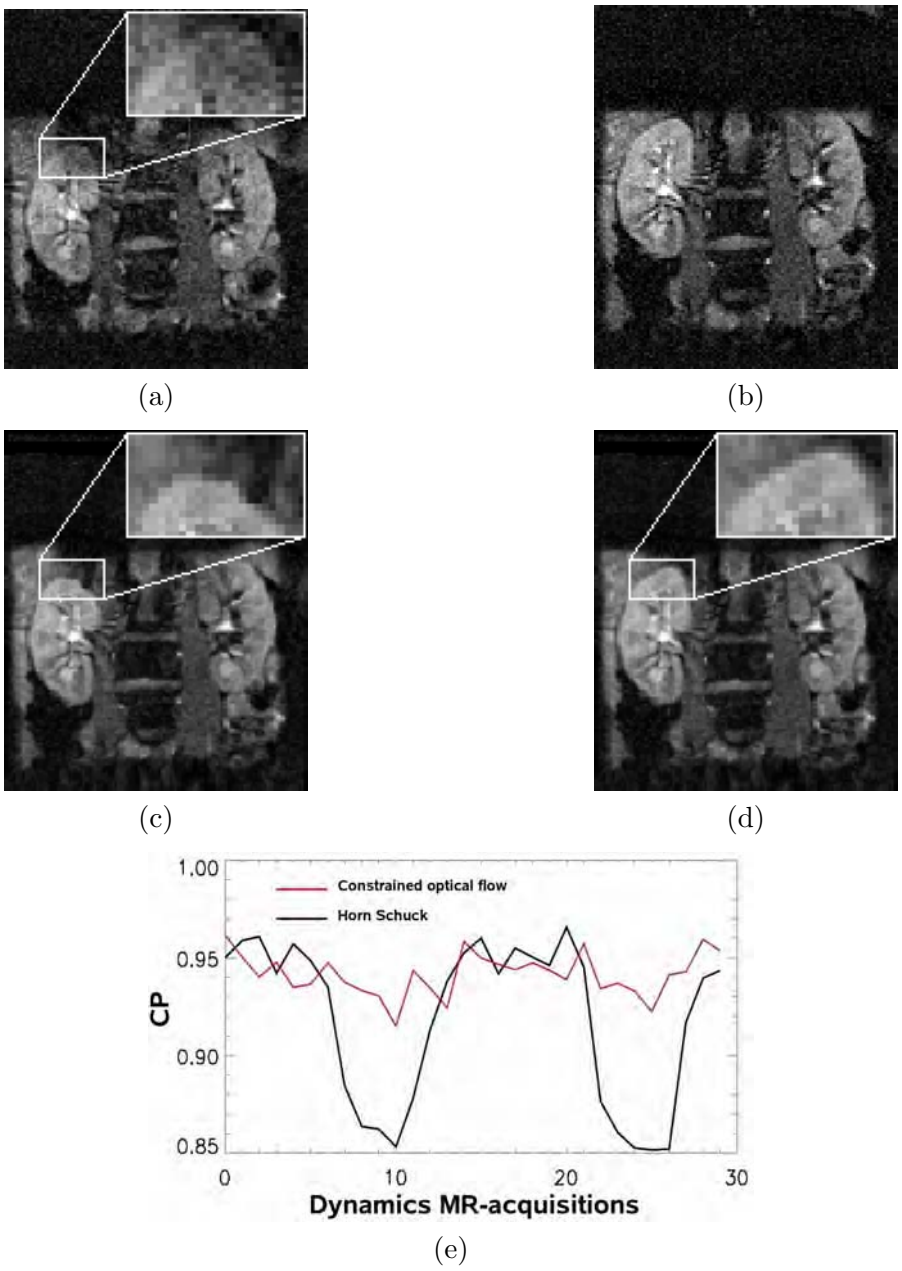

Figure 7.10: Analysis of experiment #3 (a): reference image, (b) image to register (10th of the time series), (c): registered image using the Horn & Schunck approach, (d): registered image using the CME approach, (e) CP comparison between both the CME and the Horn & Schunck approaches.

with a maximum of three points for a dynamic.

7.3.3 Real time benchmarking

The GPU based implementation allows a significant reduction of the whole computation time. Benchmarking was realized for each different processing steps for an image sequence of spatial resolution 128 × 128 (see Table 7.1). The computation time of the proposed approach was evaluated to 85 ms (CPU only implementation) and reduced to 22 ms using the CPU/GPU. A reduction factor of 10 was achieved for the computation time of the

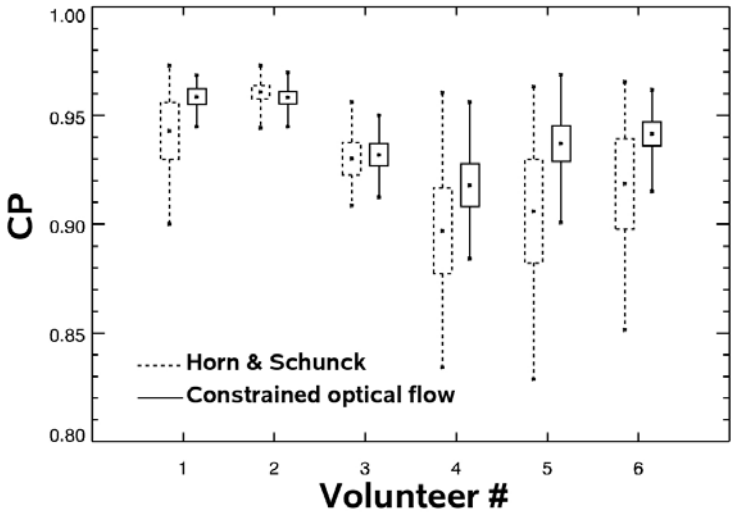

Figure 7.11: Analysis of motion estimation performance in the kidney of six volunteers using the Horn & Schunck approach and the CME approach. Box and Whisker plot of CP where displayed values correspond to the minimum (upper point) and maximum (lower point) CP values obtained on a dynamic, the averaged CP value (point inside the box) and the standard deviation of CP values (box size).

iterative numerical scheme of the optical flow algorithm (see equation (7.7)).

Algorithm steps	**Computation times**
Global motion estimation	5 ms
Motion estimation of constraint points	10 ms
Optical flow iterative scheme	7 ms (70 ms)
Total	22 ms (85 ms)

Table 7.1: Computation times of the different steps of the proposed algorithm for one image of resolution 128×128 pixels. Computation times obtained with CPU only implementation are presented in bracket.

7.4 Discussion and conclusions

7.4.1 Validation of the proposed method on synthetic dataset and in vivo experiments

The results of the proposed CME on a synthetic dataset showed a superior performance compared to the Horn & Schunck approach that failed to estimate the real motion.

Furthermore, the volunteer studies confirmed the feasibility of the CME in in vivo experiments in both the heart and the kidney. For almost all cases, the Horn & Schunck method was very disturbed by the intrusive structures, whereas the CME provided good performance for all dynamics. It is important to note that the CME and the Horn & Schunck approaches show comparable performance for images and regions not affected by non persistent structures.

The robustness of the proposed method against out-of-plane motion was also experimentally shown. Appearing and disappearing structures of surrounding tissues were found to biased the Horn & Schunck approach. For the same sequence, the CME performed well

for all dynamics and demonstrated its potential usefulness for broader types of image sequences.

7.4.2 Real time feasibility of the method

MR-guidance of interventional procedures relies on the instantaneous availability of the processed images. Therefore, this limits the available computation time. In addition, Denis de Senneville et al. demonstrated in [58] that large latencies have to be compensated with the help of accurate motion prediction. However, prediction algorithm performance greatly increases with short latencies. Recently, in the particular case of a HIFU ablation on mobile organs, it was demonstrated that a latency inferior to 100 ms was required for the adjustment of the beam position in order to ensure an energy deposition similar to a static experiment [134]. Here, the demonstrated CPU/GPU implementation allows the acceleration of the required processing time by a factor of four and thus facilitates to ensure real time conditions with low latency.

7.4.3 General discussion on the proposed method

Contrary to previous works using constraint points, a comprehensive formulation of the minimization problem was proposed. The confidence into the predetermined displacement of the selected constraint points can be freely adjusted with the regularization parameter λ^2. The quality of the obtained optical flow depends on the quality of initial constraint point vectors, the number of constraints and the ρ function parameters:

- For the motion estimation of the constraint points, only a translational model was considered as it was the most robust for small patch sizes surrounding constraint points. The optimal patch size in 128×128 MRI sequences was found to be 10×10 for our images.
- In order to control optical flow, the constraint points have to be placed near eventual occlusion (or problematic area). The manual choice of constraint points is not realistic during an interventional procedure, and we can only encourage the staff physician to approximately trace the contour of the ROI. Hence the subsampling has to be sufficient in order to get a good coverage of problematic area. On the other hand, a too large number of constraint points will slow down the computational process. Therefore, for the demonstrated application, N=20 was found to be a good compromise.
- The bandwidth of the ρ function regulates the influence of remote points. The large bandwidth yields a quasi interpolation of constraint point displacements over the whole image. An optimal experimental value was $R=\sqrt{5}$.
- Outliers rejection for constraint point vectors was found particularly useful for small patch sizes where estimations are more sensible to out-of-plane motion, noise, etc.

7.4.4 Conclusion

In this chapter a new regularization constraint of the energy functional of the Horn & Schunck method was presented. This extension renders optical flow well suited to provide motion estimation for interventional MRI on mobile organs. This approach represents a flexible solution to integrate constraint point displacement into the optical flow estimation. It opens great perspectives to integrate other motion information such as navigator echoes or ultrasonic echoes. Although the proposed method was validated in vivo in both the

heart and the kidney, its feasibility on other organs such as the liver should be investigated in future study.

Although the Horn & Schunck approach is a popular method for motion estimation, several extensions, such as [73, 71, 72] have been proposed in the past. Here, the proposed formulation can be extended to any of these methods and should be investigated in future studies. We think, that using our method in conjunction with more sophisticated global motion initialization such as in [150] could also improve the overall performance. We intend to investigate it in the future as well.

Finally, the use of parallel processing on affordable commodity graphics hardware demonstrates the feasibility of the algorithm in real time with very short latency required for interventional procedures.

Chapter 8

Motion estimation during hyperthermia

8.1 Introduction

Local hyperthermia introduces tissue modifications that lead to a variation of the local T_1 and T_2 relaxation time and thus to local intensity modifications on magnitude images, as illustrated in figure 8.3. Consequently, the condition of energy conservation of the OFCE (equation (2.6)) is locally violated and might thus lead to incorrect motion estimates.

As presented in section 2.1.3.2, one way to cope with the problem of intensity changes was first suggested by Cornelius and Kanade [71] for the registration of images obtained under a varying illumination. They proposed to model the illumination variation, individually for each pixel, as a constant variation. A further refinement was proposed by Gennert and Negahdaripour [72] which models the illumination variation as a linear function of brightness values (see section 2.1.3.2). However, these approaches may be limited to model strong intensity variations typically encountered in our case. Another solution was proposed by Maclair et al. [151] that imposed severe restrictions on the periodicity of the organ motion which is thus limited by potential spontaneous motion.

Alternatively, here the physical cause of the intensity perturbation, the local temperature change, is integrated in the motion estimation algorithm [152]. This is achieved by using the temperature map of the most recently acquired data set to adapt the local weights of confidence in the intensity conservation (left part of equation (D.1)) of the subsequently acquired new image.

8.2 Motion estimation with temperature regularization

Since for a motion estimation during a hyperthermia procedure, all images have to be registered to a common reference position, the proposed approach is divided into two steps: First, the heated area is identified using registered temperature maps obtained from the previous dynamics. Then, a new optical flow algorithm is used where the assumption of energy conservation is locally relaxed in the heated area. For this, temperature information is introduced into a modified formulation of the Horn & Schunck's formulation. Although temperature maps can be computed in real time [122], this information is only available after the image registration process is terminated. Therefore, in order to integrate temperature information into the registration process of the most recent image, it is necessary to use the temperature maps obtained from the preceding image. In principle this approach would limit the permissible temperature variations between two successive acquisitions, however, for rapid subsecond MR-sequences and typical power output of clinically used ablation devices, this is generally not the case.

8.2.1 Proposed optical flow formulation

Since the assumption of energy conservation, as proposed originally by Horn & Schunck, is locally violated for imaging hyperthermia, a temperature dependent weighting function (called $\beta(x, y)$ in the scope of this paper) is introduced. This function allows to attribute for each pixel at the coordinate (x, y) a level of confidence in equation (2.6) (a value of 1 denotes a high confidence and 0 denotes no confidence). The resulting new formulation of the optical flow constraint equation can be written as:

$$E_{tr} = \iint \left(\beta(x,y) \left[I_x u + I_y v + I_t \right]^2 + \alpha^2 \left[\|\nabla u\|_2^2 + \|\nabla v\|_2^2 \right] \right) dxdy \tag{8.1}$$

This functional is minimized based on the resolution of the Euler Lagrange equations and the Gauss Seidel method. A detailed description of the derivation of the solution is given in appendix D.3 and provides the following iterative scheme:

$$\begin{cases} u^{n+1} = \overline{u}^n - \beta(x,y) I_x \dfrac{\overline{u}^n I_x + \overline{v}^n I_y + i_t}{\beta(x,y)(I_x^2 + I_y^2) + \alpha^2} \\ \\ v^{n+1} = \overline{v}^n - \beta(x,y) I_y \dfrac{\overline{u}^n I_x + \overline{v}^n I_y + i_t}{\beta(x,y)(I_x^2 + I_y^2) + \alpha^2} \end{cases} \tag{8.2}$$

To cope with large displacement, a multi-resolution approach was used which iterates the registration algorithm from a four-fold down-sampled image step-by-step to the full image resolution.

8.2.2 Heated area identification

The region prone to high local intensity variations is updated in real time during the hyperthermia procedure. The weighting function β is directly derived from the temperature maps $T(x, y)$ using a temperature threshold $T_{threshold}$ to classify pixels (x, y) inside the heated area ($T(x, y) > T_{threshold}$) and outside the heated area ($T(x, y) < T_{threshold}$). To decrease instabilities of the numerical scheme, the β function was designed as a continuous function as follows:

$$\beta(x,y) = \begin{cases} 1 & \text{, if } T < T_{threshold} \\ \exp \frac{-(T - T_{threshold})^2}{k^2} & \text{, if } T \geq T_{threshold} \end{cases} \tag{8.3}$$

where k^2 allows to define the speed of convergence to 0 for the weighting function β. k^2 and α^2 were empirically set to 5 and 0.3, respectively. Note that $T_{threshold}$ has to be small enough, since intensity variations can arise with low temperature variations, depending on the employed sequence. On the other hand, $T_{threshold}$ has to be higher than the temperature measurement noise to prevent instabilities and undesired effects on the weighting function β. Therefore, a value of two times the standard deviation of the temperature (measured prior hyperthermia) was employed.

8.2.3 Implementation

Implementation was realized in C++ and evaluated on a dual processor (INTEL 3.1 GHz Penryn, two cores) workstation with 8 GB of RAM. Since a high framerate is required, the registration process was off loaded to a GPU, using the Compute Unified Device Architecture (CUDA) framework [106]. For this, a NVIDIA GTX280 card with 1 GB of DRAM was employed.

8.2.4 Experimental setup

The proposed algorithm was evaluated on a synthetic dataset and in an ex vivo heating experiment. Although a temperature variation induces a phase variation, additional effects, such as local magnetic susceptibility variations induced by motion, can create additional unwanted shifts on phase images. These position dependent effects on the phase have been removed prior to the temperature computation using a multi-baseline phase correction as described in detail in [122].

Simulated experiment: An ellipsoidal object was simulated for N=200 frames. In order to evaluate the ability of our algorithm to estimate complex deformations in presence of strong intensity variations, a complex vertical displacement d was empirically created for each frame i, as follows:

$$d_i(x,y) = imod3 + 2 * sin((2 * \pi * y/Y_{RESOL}) + (imod3) * \pi) \tag{8.4}$$

where Y_{RESOL} was the image resolution in the vertical dimension. Local signal loss was simulated by reducing the initial overall signal-to-noise ratio (SNR) of 13 for the last 100 images in a small area (size: 5 × 5 pixels) to zero (100 % signal loss in the center area and 70 % in the periphery). Since for this simulation no actual temperature change was present, an artificial β function with a value of 0 in the signal decrease area and 1 elsewhere was used.

Heating experiment: Dynamic MR temperature imaging was performed on a Philips Achieva 1.5 T MRI-system (Philips Healthcare, Best, The Netherlands) using a dual-shot, gradient recalled echo-planar acquisition sequence. $N = 3000$ images were acquired with the following parameters: Image dimension=128 × 58, echo time=15 ms, repetition time=30 ms, flip angle= 20°, field of view=256 × 104 × 5 mm^3. A porcine muscle was positioned on a motorized platform, which generated a periodic displacement. For an independent assessment of the object displacement, an additional navigator echo (0.5 mm precision) was positioned parallel to the displacement on the apex of the muscle in order to get the reference displacement. Since a navigator echo only provides a one dimensional displacement information, the created displacement was purely translational (amplitude=10 pixels and frequency=0.5 Hz). RF heating was performed using a clinical MR-compatible RF device (Radionics, Burlington, MA) with 8 W of RF-power during 75 seconds.

8.2.5 Assessment of motion estimation accuracy

The proposed algorithm is compared to the Horn & Schunck's algorithm (setting uniformly $\beta(x,y) = 1, \forall(x,y)$). To assess the motion estimation accuracy, the gold standard error (GSE), as defined in chapter 7 (see equation (7.8)), was employed. This criterion corresponds to the spatial average of the Euclidean distance between the estimated motion and the true motion (the created displacement for synthetic dataset experiment and the navigator value for the heating experiment). The GSE was computed in our case over a mask m positioned around the heated region.

8.3 Experimental validation

8.3.1 Simulated experiment

Synthetic images are displayed in Fig. 8.1. The reference image is shown in Fig. 8.1a. The last image of the time series, depicting a local signal variation, with its associated true displacement, are shown in Fig. 8.1b. The corresponding registered images and estimated motion fields (in the area with simulated signal decrease) obtained with the

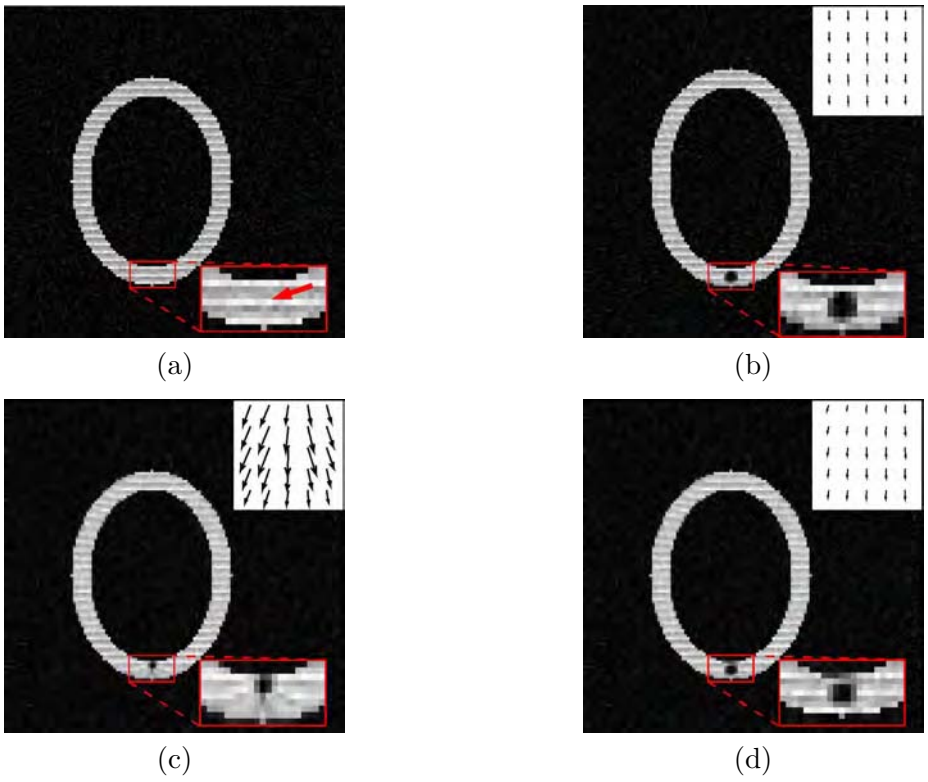

Figure 8.1: Results obtained on synthetic datasets: (a) reference image (b) last image of the time series with the real input displacement. Registered images and corresponding motion field (of the area with the simulated signal decrease) obtained with the Horn & Schunck's approach (c) and the proposed approach (d).

original Horn & Schunck's approach and the proposed method, are respectively shown in Fig. 8.1c and 8.1d. The motion field obtained with the Horn & Schunck's algorithm does not represent the true displacement as shown in Fig. 8.1b, and the area containing the simulated signal decrease was significantly reduced on the corresponding registered image. With the proposed approach, the estimated motion field (see Fig. 8.1d) corresponds to the simulated displacement and intensities are well conserved in the area with the simulated signal decrease.

To confirm these results over the entire sequence, a temporal analysis of the motion accuracy (Fig. 8.2a) and the registered image intensity conservation (Fig. 8.2b) was performed in a pixel (indicated by a red arrow in Fig. 8.1a) located in an area subject to signal variations. Both algorithms provide the same results for the first 100 dynamics since no signal decrease was present. However, on the last 100 dynamics, the Horn & Schunck's algorithm displays large errors on the estimated motion fields and the pixel intensity on the registered images was found biased. In comparison, the proposed approach provides an accurate motion field estimate throughout the entire image sequence and the resulting image intensity remained similar to the true intensity. Note that the precision of the estimated motion field appears also improved in areas with decreased signal.

8.3.2 Heating experiment

The results of the heating experiment are displayed in Fig. 8.3. The reference image is displayed in Fig. 8.3a, while an image after 50 seconds of sonication is shown in Fig. 8.3b. A strong signal decrease form the initial SNR of 18 is visible in the heated area (see enlarged areas in Fig. 8.3a and 8.3b). The corresponding registered images, motion

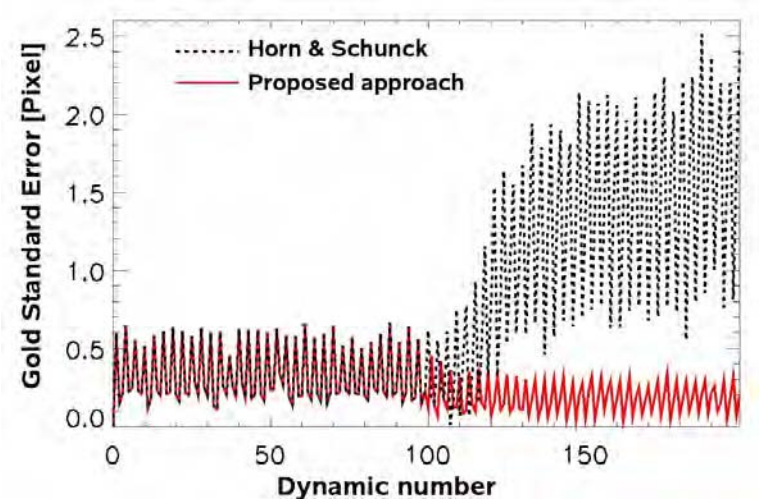

(a)

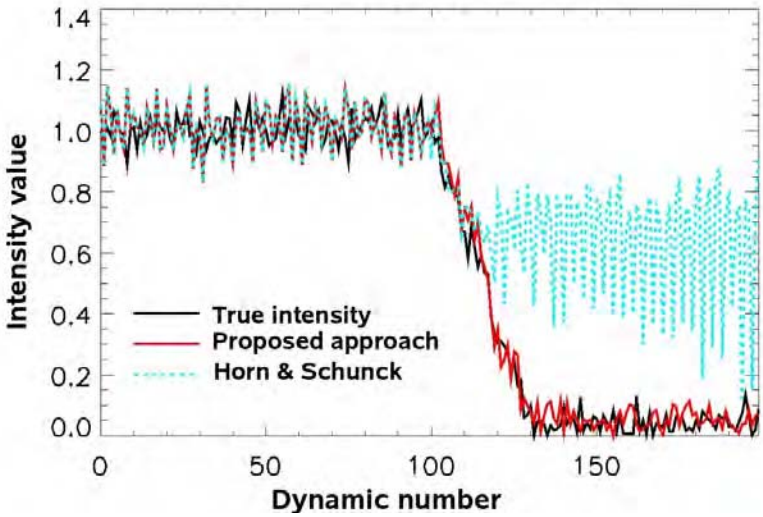

(b)

Figure 8.2: Analysis of registration accuracy in a point subject to large intensity variations (shown by the arrow in Fig. 8.1a): (a) GSE, (b) intensity evolution on registered image.

fields and temperature maps which are obtained using the navigator based registration, the Horn & Schunck's algorithm and the proposed modified optical flow are shown in Fig 8.3c, 8.3d and 8.3e. The estimated motion field and the temperature map of the Horn & Schunck's algorithm (Fig. 8.3d) show significant differences to the results obtained with the navigator based image registration, which served as the reference result (Fig. 8.3c). The proposed modified optical flow image registration provides motion fields and a temperature maps (Fig. 8.3e) which are similar to the reference results. To confirm the robustness of the presented method, an analysis over the temporal evolution of the estimated motion field accuracy is presented in Fig. 8.4a. Here, the gold standard error is computed in a pixel located in the heated area (indicated by the red arrow in Fig. 8.3a). The Horn & Schunck's approach provides poor results as soon as the hyperthermia procedure starts while the proposed method remains stable and accurate over the time. Fig. 8.4b shows the resulting temperature evolution obtained for each method. Contrary to the Horn & Schunck's approach, the temperature evolution obtained with the proposed method is close to the reference results.

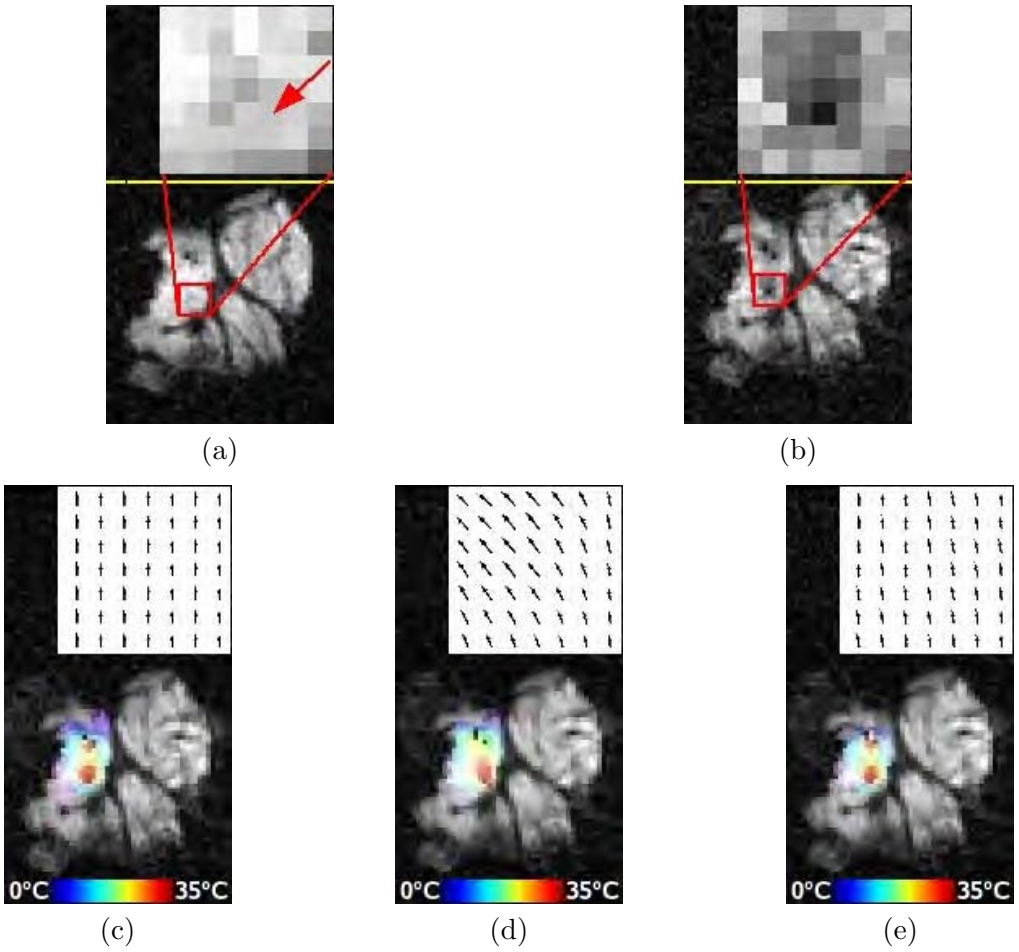

(a) (b) (c) (d) (e)

Figure 8.3: Results obtained on the heating experiment: (a) reference image, (b) image obtained after 50 seconds of sonication, corresponding registered image, temperature and estimated motion field using: (c) navigator based registration, (d) Horn & Schunck's approach, (e) the proposed approach.

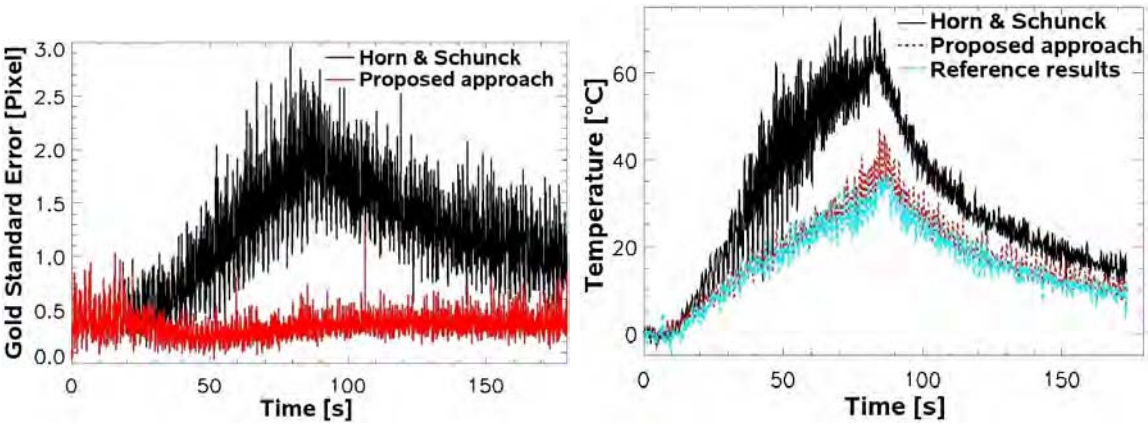

(a) (b)

Figure 8.4: Temporal analysis of the registration accuracy in a pixel located in the heated area (red arrow in figure 8.3.a) of the gold standard error of the estimated motion field (f) and the corresponding temperature evolution (g).

The GPU based implementation allows reduction of the computation time for an image of 128 $\times$ 128 pixel of 60 ms (CPU only) to 5 ms. Therefore, the computation time is compatible with the required framerate (10-15 Hz) for real time MR-guidance of hyperthermia.

8.4 Discussion and conclusions

Motion compensated MR-guidance of hyperthermia requires a robust and precise image registration throughout the entire intervention. The original Horn & Schunck's algorithm was found to be very susceptible to intensity variations due to the heating process. An estimation error of up to 2-3 pixels ($\equiv$ 4-6 mm) of mis-registration was observed. This limits the usefulness of the algorithm for applications where the image and temperature data is used for retroactive control of the interventional device. In comparison, the proposed approach, which integrates a priori knowledge of temperature and thus intensity variations directly in the registration process, resulted in a much improved performance: The accuracy of estimated displacement corresponds well to the true displacement throughout the entire intervention. Since for this approach the spatio-temporal shape of the weighting function β, and in particular the temperature threshold, have a large influence on the displacement estimation, an automatic calibration appears advisable. Furthermore, the estimated motion field in the heated area is only computed from surrounding pixels using a diffusion process. As a result, the precision of the estimated motion appears improved. However, complex deformation in the heated area might be not well represented. The processing time was found below 5 ms for an image of 128 $\times$ 128 pixels, which demonstrates the ability to perform this algorithm in real time while maintaining short latency.

Since for MR-guidance of hyperthermia the method was found well suited to cope with strong signal decrease due to the heating process, it can potentially be applied to other application scenarios of dynamic MR-image data which contain problematic areas such as arteries with blood pulsation, bolus passage, or minimally invasive devices such as a catheters or laser guides.

Chapter 9

Autocalibration of a motion estimation algorithm using a physical motion model

9.1 Introduction

Motion estimation algorithm generally employs a set of free parameters. In general, their optimal calibration depends on several factors (such as the target motion amplitude, noise, the complexity of the deformation, the image resolution, ...) and thus depends on the application (targeted organ, location of the tumor, slice orientation, ...). However, a manual calibration where the physician would have to select the best set of parameters appears infeasible for two reasons:

- It would be user controlled. The parameter tuning would be based on apparent registration quality and not on the accuracy of the estimated motion field. Therefore, only regions with geometric structures would be evaluated by the physician. In this case the estimated motion field of flat area will not be considered.
- It would be time consuming. For each set of parameters, the physician would have to control the quality of the registration for different images corresponding to different positions in the respiratory cycle. It would require several dozens of minutes and severely increase the cost and thus the feasibility of the intervention.

For these reasons, an autocalibration of the motion estimation algorithm appears necessary. Then, this requires to define an optimization strategy to converge to the optimal set of parameters and a motion estimation quality criterion for the optimization function.

In this chapter, an autocalibration method for a motion estimation algorithm is proposed. For this, a cost function, which relates the quality of the registration, is required. Here, we show that existing magnitude based criteria are highly limited with low SNR and a novel criterion based on MR-phase images is proposed. Then, this criterion is used to assess, for a set of positions observed before the interventional procedure, the optimal configuration of the registration algorithm. Since for most therapeutic applications within the human body, motion is caused by the respiratory or the cardiac cycle and is thus periodic, this optimal configuration can be used during the interventional procedure. To demonstrate the usefulness of this criteria, an optical flow based image registration algorithm (derived from the Horn and Schunck algorithm) is optimized using both existing criteria and the proposed criteria for abdominal organs subjected to respiratory motion.

The potential of the method was evaluated in a phantom experiment. Results of the optimal image registration were compared with gold standard positions given by an

external sensor. Then, the method was demonstrated in-vivo in the abdomen of twelve volunteers under free breathing, with conditions similar to a thermo-ablation. Results of the optimal image registration were compared with manually defined gold standard positions.

9.2 Image registration quality criteria

9.2.1 Existing criteria

The strategy to assess the performance of a motion estimation algorithm, depends on the availability of the real motion knowledge. For the case where the real motion (M_{real}) is known, several criteria such as the angular error or the absolute error can be used. The angular error represents the angle between the real motion flow and the estimated motion flow (M_{est}) [153]. However, this criterion penalizes much more errors in small flows that errors in large flows. Therefore, in this thesis, we employed the absolute error (see chapter 7 and 8) which is defined as the spatio-temporal average of the Euclidean distance between M_{est} and M_{real}. This criterion is referred to as Gold standard error (GSE) in the scope of this chapter.

However, the knowledge of the true motion is generally limited for in vivo imaging. Navigator echoes or ultrasonic can provide independent measure of the displacement but cannot represent elastic deformations. A manual registration of a given set of landmark points can be realized and used as true motion in each specific landmark point but is not feasible for real time applications.

Alternatively, the video coding area has proposed several solutions. However, motion estimation objectives for video coding and MR-guidance are slightly different. While MR-guided thermal ablations require the estimation of the true motion, video coding tries to find the best pixel match from one frame to another in order to minimize the differences between the reference frame and the registered current frame. One of the most famous proposed criterion employed in the video coding area is the mean squared error between the registered image and the reference image. As mentioned in chapter 7, this criterion may be disturbed with low SNRs since the motion estimation and the assessment of the registration quality rely on the same magnitude information. Unfortunately, as described in chapter 2 (see section 2.1.1.2) and chapter 5, real-time MRI of mobile organs is frequently hampered by low SNR values, generated by fast MR-acquisition schemes employed to minimize intra-scan motion. Therefore, motion estimation assessment could be improved if the criterion could be based on additional information which is independent of the information used for motion estimation.

9.2.2 Proposed quality criterion on image registration

9.2.2.1 Physical background

A promising way to provide this information is to exploit the phase information of the MR-image (here it is proposed to exploit the phase component of the complex magnetization vector associated with each voxel in the image domain, not the phase associated with the Fourier representation of the anatomical image (see section 2.1.3.1). While the magnitude of an MR-image reflects the underlaying anatomy, the MR-phase φ in gradient recalled echo images is mainly determined by the local susceptibility distribution χ and the local magnetic field strength H:

$$\varphi\left(\vec{r}\right) \propto \gamma\mu_0\left(1-\sigma\left(T\left(\vec{r}\right)\right)\right)\left(1+\chi\left(\vec{r}\right)\right)H\left(\vec{r}\right) \tag{9.1}$$

whereby the gyromagnetic ratio γ and the magnetic constant μ_0 represent material constants, $\vec{r}$ the spatial position and σ the temperature (T) dependent screening constant of the water protons. Since the susceptibility of biological tissue varies little, it is mainly the magnetic field strength H which determines the spatial variation of φ. Furthermore, since modern MR-systems achieve a good homogeneity of the magnetic field strength H across the field-of-view, φ is a spatially slowly varying function which is differentiable within homogeneous tissue. These characteristics appear advantageous for a basis of tissue displacement detection. Therefore, a new criterion to quantify the quality of the registration of MR-images based on the MR-phase image similarity (PIS) is presented [154, 155].

9.2.2.2 Principle of the proposed criteria

As shown in equation (9.1) the phase of the MR-signal represents the susceptibility distribution and the magnetic field variation in the magnet. Since both change due to organ motion, we propose to use this physical information to assess the accuracy of an estimated motion field. However, as presented in chapter 2, two main factors, related to organ displacement, may disturb the similarity between two phase images [156]:

1. The spatial mismatch due to the displacement, which leads to a spatial mismatch of the respective magnetic susceptibility distribution $\chi(\vec{r})$.

2. Additional phase shifts generated by a modified local demagnetization field, which is caused by a modified magnetic susceptibility distribution[156] [157] [158]. To account for these phase shifts, a precise modeling of the inhomogeneous magnetic field in-vivo is required. For that purpose, the recently suggested linear phase model approach (see section 2.2.1.2), assuming a simple linear relation between magnetic field variation (phase variations) and the target displacement, can be employed.

Each variation of the object position leads thus to a unique phase image. If phase variations with motion have been modeled, a synthetic phase map (φ_{reco}) can be constructed, as presented in chapter 2 (see section 2.2). In this study, the linear model, described in detail in figure 2.6, was employed. This model requires the estimation of its parameters before hyperthermia. Then, the model is employed during hyperthermia to provide synthetic phase maps (from a motion descriptors) which are subtracted to the current phase images to get the temperature information. In this study, the model is employed to generate synthetic phase maps before hyperthermia, which are then compared to the corresponding registered MR-phase images to quantify registration errors.

The only required intervention of the user is to define before hyperthermia, on the reference image, a region of interest encompassing the area where the registration must be optimized (we note m the associated binary mask). A reference data set was created to sample the susceptibility perturbations with motion. For most therapeutic applications, motion is caused by the respiratory or the cardiac cycle and is thus periodic. Thus, a set of K images ($K = 50$ was chosen in the scope of this study) covering several motion cycles of the target with a sufficient sampling density to avoid discretization errors (5-10 images per second) was acquired. A collection of registered phase images, encoding local magnetic susceptibility variations and noted φ_r, was built and used to assess the quality of the registration. For that purpose, all phase images were registered to a common reference position on a pixel by pixel basis using the implemented registration algorithm applied on the anatomical (i.e. magnitude) image information. Registration errors were quantified by evaluating the phase similarity between any new acquisition (φ_r) and a synthetic one (φ_{reco}). This synthetic phase map was computed assuming a linear relation between phase

variation and motion. Since the 2π periodicity of the phase would lead to a severe bias of the similarity measure, a temporal phase unwrapping on a pixel-by-pixel basis was applied between φ_r and φ_{reco}. A temporal analysis was performed to reflect the accuracy of the registration algorithm with various amplitudes and deformations likely to be encountered. For that reason, the accuracy of each estimated motion was quantified for each image of the reference dataset, and averaged to obtain the PIS criterion, defined as:

$$PIS = \frac{1}{K}\sum_{k=1}^{K}\left(\frac{1}{N}\sum_{(x,y)\in m}\left(\varphi_r(x,y,k) - \varphi_{reco}(x,y,k)\right)^2\right) \tag{9.2}$$

Where (x, y) denotes pixel coordinates, k the image index in the time series, and N the number of pixels set to 1 in the binary mask m. φ_{reco} was evaluated for each individual pixel assuming a linear phase variation along the target displacement D as follows:

$$\varphi_{reco}(x,y,k) = a(x,y).D(x,y,k) + b(x,y) \tag{9.3}$$

where $D(x, y, k)$ is a scalar relating the displacement amplitude and orientation along the principal axis of the estimated target motion computed as follow:

$$D(x,y,k) = \Delta X(x,y,k).V_1 + \Delta Y(x,y,k).V_2 \tag{9.4}$$

where ΔX and ΔY denotes horizontal and vertical components of the estimated displacement, and $\vec{V} = (V_1, V_2)$ is the eigen vector associated with the highest eigen value of the matrix μ defined as follows:

$$\mu = \begin{pmatrix} \cdot & \cdot \\ \cdot & \cdot \\ \cdot & \cdot \\ \overline{\Delta X}(k-1) & \overline{\Delta Y}(k-1) \\ \overline{\Delta X}(k) & \overline{\Delta Y}(k) \\ \cdot & \cdot \\ \cdot & \cdot \\ \cdot & \cdot \end{pmatrix} \tag{9.5}$$

where $\overline{\Delta X}(k)$ and $\overline{\Delta Y}(k)$ denote the displacement vector averaged over the mask m.

a and b are the slope and the intercept of the simple linear regression between the registered phase value φ_{reg} and the target displacement D computed as follow:

$$\begin{cases} a(x,y) = \dfrac{\overline{D(x,y).\varphi_{reg}(x,y)} - \overline{D(x,y)}.\overline{\varphi_{reg}(x,y)}}{\overline{D(x,y)^2}.\overline{D(x,y)}^2} \\ b(x,y) = \overline{\varphi_{reg}(x,y)} - a(x,y).\overline{D(x,y)} \end{cases} \tag{9.6}$$

9.3 Automatic calibration of the registration

The PIS criterion was used to autocalibrate the Horn & Schunck algorithm. This method has a free parameter α^2, a weighting factor designed to link the two individual metrics (intensity variation and motion regularity): while low α^2 values allow estimation of large motion amplitude, high α^2 values increase robustness against noise or possible local intensity variations not attributed to motion. Therefore, α^2 value optimization was performed in a preparative calibration step. For that purpose, an exhaustive enumeration of α^2 were performed (30 α^2 values were tested between 0 and 0.75) and the value minimizing the PIS criterion was selected as the optimal parameter.

9.3.1 Implemented image registration algorithm

The Horn and Schunck algorithm (presented in chapter 2) was thus applied to anatomical (i.e. magnitude) images [70]. In order to stabilize the convergence of the algorithm, a multi-resolution scheme was used [59] which iterates the registration algorithm from a 4-fold downsampled image (where displacements are small and the SNR is increased by the low-pass filtering inherent to the down-sampling process) step-by-step to the full image resolution, as realized in chapter 5, 7 and 8.

The optical-flow algorithm, applied on magnitude images, provides a motion field with a sub-pixel precision and an interpolation was required to obtain registered phase images. Due to the 2π periodicity of the phase, the spatial transformation could not be directly applied on phase images. Although this problem could be circumvented by employing a 2D phase-unwrapping step to the phase images, this remains a computationally intensive processing step which is often unstable in areas with signal discontinuities and strong susceptibility changes frequently encountered in abdominal imaging. Therefore, we applied the estimated motion to the complex MR images, to obtain registered phase images, avoiding spatial phase wraps problems.

As previously mentioned (see chapter 5), it is difficult to acquire on-line 3D isotropic images because of the technical limitations, spatial and temporal resolution trade-offs, and low SNR associated with fast 3D acquisition sequences. Therefore, the method was thus evaluated in 2D.

All computationally intensive calculations were offloaded to a dedicated graphics processing unit.

9.3.2 Experimental setup

The potential of the method to calibrate optical flow based image registration algorithms was first evaluated on a phantom experiment. Subsequently, the improved performance for the on-line estimation of organ displacements is demonstrated in-vivo on abdominal imaging of twelve volunteers. Dynamic MR imaging was performed on a clinical Philips Achieva 1.5 T MR-system (Philips Healthcare, Best, The Netherlands). All calculations were performed on a dual processor (3.1 GHz Penryn; four cores, INTEL Santa Clara, CA, USA) workstation with 8 GB of RAM. The GPU was a NVIDIA GTX280 card with 1 GB of DRAM. The GPU implementation was realized using CUDA.

9.3.2.1 Criterion comparison

The PIS criterion was compared with the following criteria:

Magnitude image similarity (MIS) The temporal average of the mean square error between each registered magnitude image (M_r) acquired during the second step and the reference one (M_{ref}) was computed as follows:

$$MIS = \frac{1}{K}\sum_{k=1}^{K}\left(\frac{1}{N}\sum_{(x,y)\in m}\left(M_r(x,y,k) - M_{ref}(x,y,k)\right)^2\right) \tag{9.7}$$

Gold standard error (GSE) The spatio-temporal average of the Euclidean distance between the estimated motion field and a gold standard motion information was evaluated. Since in the phantom experiment, the target undergoes a translational motion, the motion was fully characterized using a navigator echo [44]. For the in-vivo study, validation of the alignment was based on 10 landmark points, which were manually positioned and tracked over the K images in the targeted region by a staff scientist with the precision of a pixel.

9.3.2.2 Phantom study

A physiological sample with relaxation times matched to the human kidney was mounted on a motorized platform to simulate an abdominal organ moving due to respiration. The applied motion pattern consisted of a periodic sinusoidal translational displacement of 20 mm of amplitude with a period of 2 s. The object displacement was monitored by an independent measure obtained by a navigator echo (0.5 mm precision), positioned parallel to the displacement, in order to get the reference displacement for the evaluation of the GSE criterion. Dynamic MR imaging was performed with a dual shot gradient recalled echo-planar sequence, which employed the following parameters (TR=30 ms, TE=15 ms, voxel size= $2\times2\times5$ mm^3, FOV=$256\times104\times5$ mm^3, echo train length=25, echo spacing=1.1 ms, flip angle=20°, bandwidth in readout direction per pixel=1777 Hz). The study was investigated for different noise levels by adding an additional Gaussian noise to the initial complex data in a separate post processing step, in order to achieve series of images with an SNR of 5 to 15.

9.3.2.3 In-vivo study

Dynamic MRI was performed under free breathing conditions on the abdomen of 12 healthy volunteers under real-time conditions. The single shot gradient recalled echo-planar (EPI) sequence employed the following parameters: 3000 dynamic sagittal images acquired with an imaging frame-rate of 10 images/s, single slice, TR=100 ms, TE=26 ms, voxel size $2.3\times3.1\times6$ mm^3, FOV=$300\times197\times6$ mm^3, echo train length=63, echo spacing=0.8 ms, flip angle=35°, bandwidth in readout direction per pixel=2085 Hz, using a four element phased array body coil. The proposed calibration method was evaluated both in the kidney and the liver individually.

9.3.2.4 Statistical Analysis

The significance between the optimal α^2 values obtained with the MIS, the PIS and the GSE for a variety of noise input has been evaluated for the ex-vivo experiment using an ANOVA (Analysis of Variances) in form of a F-test with significance threshold p=0.05. If the test was found significant, additional paired t-tests were applied to the data of all pairs of criteria. A significance of p=0.05 was used and corrected with the Bonferroni method.

The same statistical study was performed to assess the significance between GSE obtained with the MIS and the PIS criteria for both phantom and in-vivo experiments.

9.4 Experimental validation

9.4.1 Phantom study

Magnitude and phase images obtained for two different phantom positions are displayed in Fig. 9.1. It can be observed in 9.1c and 9.1d that, contrary to magnitude images, phase images are not only shifted with the target displacement (shown by the red dashed lines), but also prone to an additional perturbation generated by a modified local susceptibility distribution (see red arrows in Fig 9.1c and 9.1d).

Figure 9.2 depicts the quality of the registration evaluated for each α^2 value with the MIS (Fig. 9.2a) and the PIS (Fig. 9.2b) criteria. The GSE criterion is reported in dashed lines for comparison. Although the units are not the same, curve shapes can be compared. With both criteria it can be observed that the quality of the registration turned to be very poor for extreme α^2 values (close to 0 or to 1 in this example). An optimal configuration of the implemented registration algorithm was found with both criteria: the minimum of the MIS criterion was obtained for α^2=0.175, and the minimum of the PIS criterion was

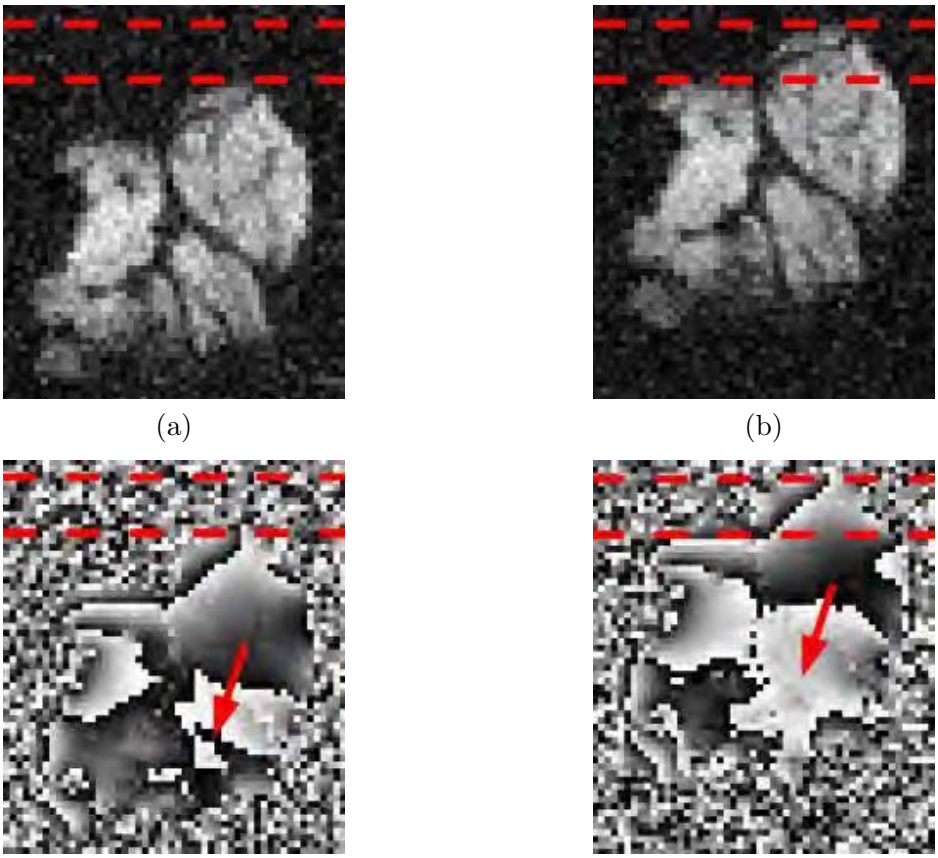

Figure 9.1: Magnitude (a,b) and phase (c,d) images obtained for two different positions of the phantom with a SNR of 10. Note that the phase is a smooth function in space and the visible phase wraps are due to the 2π periodicity of the arctan function.

obtained for α^2=0.475. However, while the error of the estimated displacement was 1.16 millimeters for α^2=0.175, this value was 0.65 millimeters for α^2=0.475.

Motion fields estimated with α^2=0.175 and α^2=0.475 are reported in Fig. 9.3b and 9.3c, respectively. Only the motion field estimated with an optimal α^2 value evaluated using our PIS criterion matched visually the real target motion measured with the transmission line (see Fig. 9.3a).

Results observed in Fig. 9.2 were confirmed for all tested SNR levels. Optimal α^2 values obtained using each tested criteria are displayed in Fig. 9.4a. Those results were confirmed for all tested SNR levels. α^2 values optimizing each criteria, are displayed for all tested SNR in Fig. 9.4a. A statistically significant difference of the optimal α^2 values obtained with the MIS, the PIS and the GSE for a variety of noise input could be observed ($p<0.05$). However, only the α^2 optimized with the PIS did not show a significant difference with the GSE optimization ($p>0.05$). As observed in Fig. 9.2, the MIS criterion provided lower α^2 values compared to the PIS criterion for each tested SNR. α^2 values optimizing our criterion and the GSE were similar and was found to increase from 0.4 to 0.6 with the SNR.

The error of the estimated displacement obtained with an α^2 value optimized using the PIS, the MIS and the GSE criteria for several values of SNR, are reported in Fig. 9.4b. While the criteria based on anatomical image similarity led to a maximal error on the estimated displacement higher than one millimeter, the proposed PIS criterion reduced this value in the range of half a millimeter. The proposed PIS criterion provides

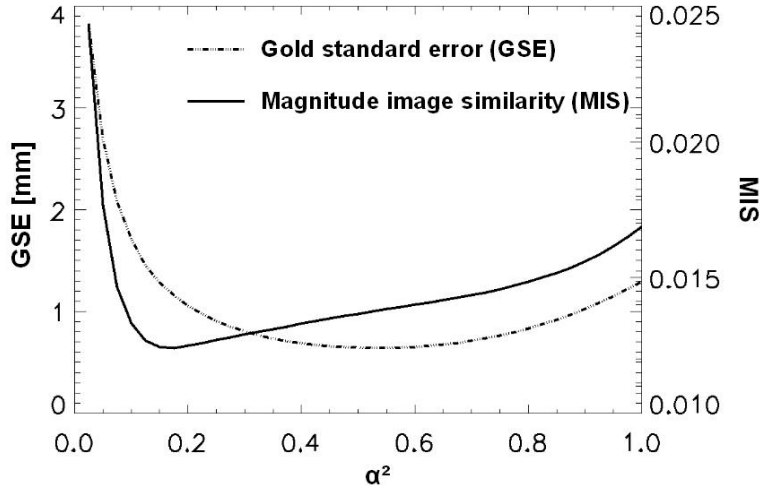

(a)

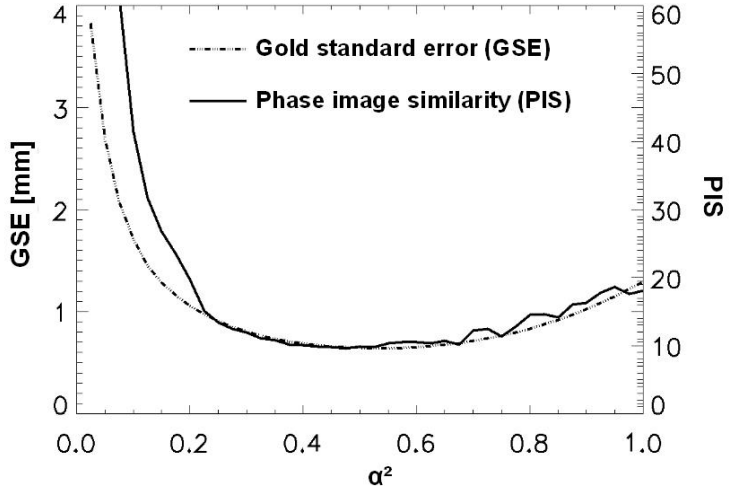

(b)

Figure 9.2: Automatic determination of the α^2 value for the phantom experiment (SNR was set to 10). The registration quality was assessed with the GSE (dashed line) and compared to the MIS (a) and the PIS criteria (b).

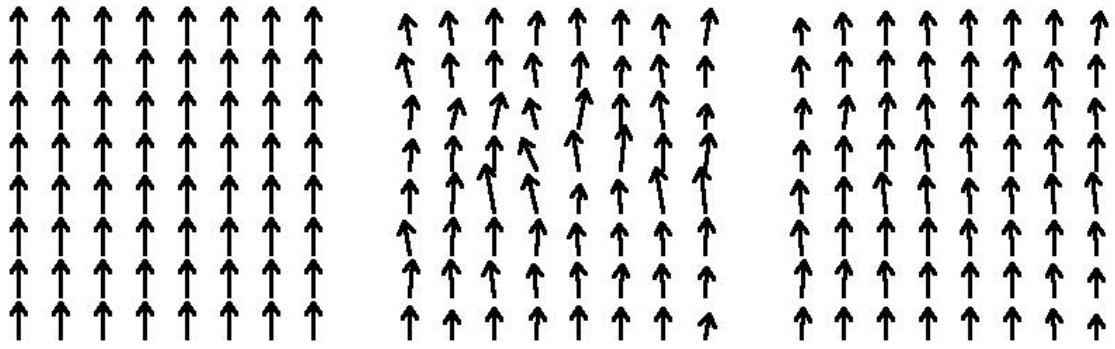

(a) (b) (c)

Figure 9.3: (a): Gold standard motion obtained from the transmission line, (b): motion field obtained with an α^2 value optimized by the MIS criterion ($\alpha^2 = 0.175$), (c): motion field obtained with an α^2 value optimized by the PIS criterion ($\alpha^2 = 0.475$).

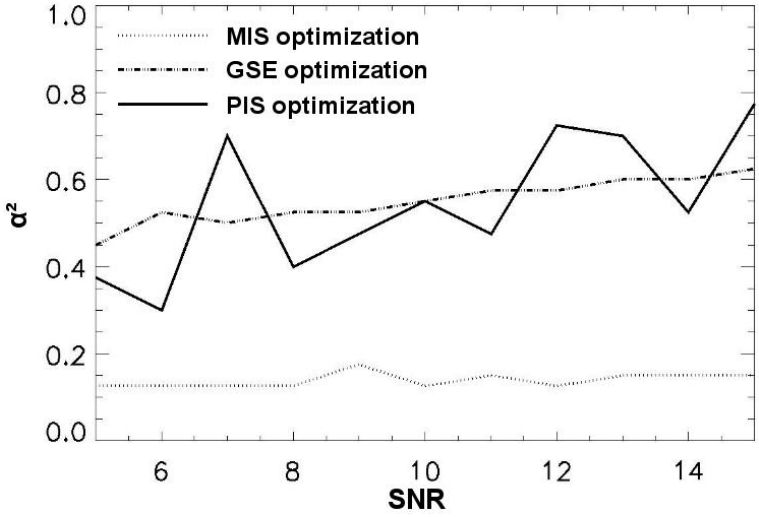

(a)

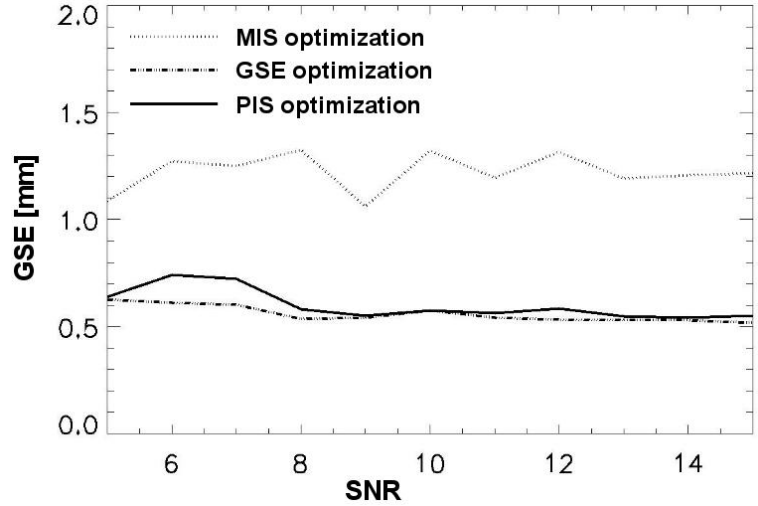

(b)

Figure 9.4: (a): α^2 values optimizing each criteria, for all tested SNR, (b): Gold standard errors obtained with optimal α^2 values obtained with each criteria.

an accurate motion field for all tested SNR levels. It can be observed that the motion field accuracy was identical when the α^2 value was optimized using the PIS or the GSE criterion.

9.4.2 In-vivo study

Over the 12 human volunteers, the motion amplitude peak-to-peak obtained from the landmark points was 10 mm ± 4.5 (min=4, max=18) in the kidney and 11 mm ± 4.5 (min=6, max=18) in the liver. The SNR was evaluated to 10 ± 2.5 (min=7, max=14) in the kidney and 7 ± 3 (min=4, max=14) in the liver.

Fig. 9.5 shows a subset of the results obtained from the in-vivo experiments. Figure 9.5a and 9.5b show the magnitude and the phase image of the liver and kidney in their reference position. The two manually chosen masks m on the kidney and the liver (indicated in Fig. 9.5a by the red and blue dashed lines, respectively) were used to restrict the calibration procedure to both organs. A second set of images show magnitude and phase at a different point of the respiratory cycle (9.5c and 9.5d), with the contours of

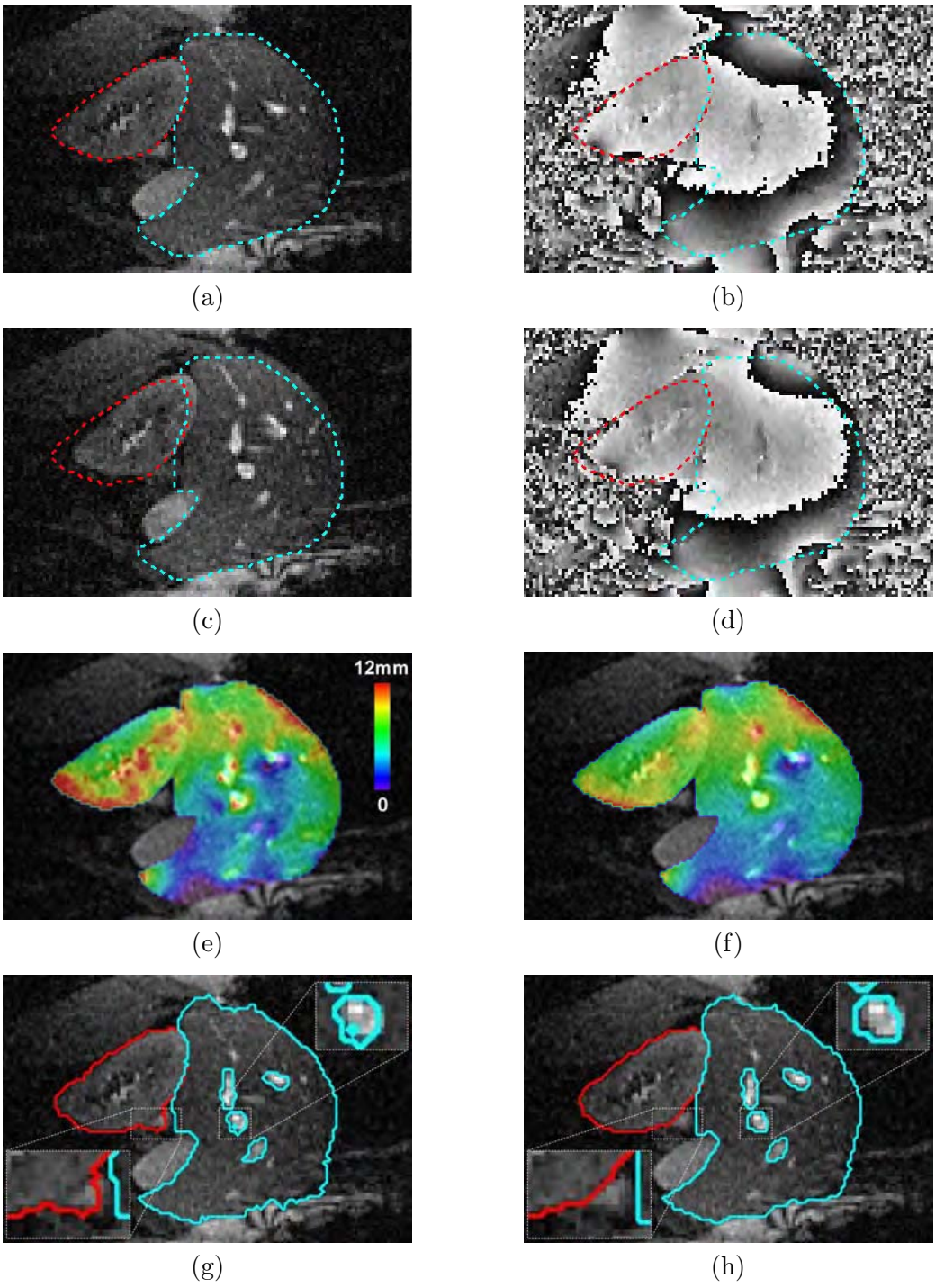

(a) (b) (c) (d) (e) (f) (g) (h)

Figure 9.5: Typical findings of the in-vivo study: The magnitude (a) and phase (b) image acquired at the reference position are displayed with the associated processing masks m (red and blue overlays for the kidney and the liver, respectively). The corresponding shifted/deformed magnitude and phase images taken at a different point of the respiratory cycle are shown in (c) and (d). Masks m at the reference position are added as dashed line to illustrate the displacement. The spatial distribution of the estimated displacement amplitude obtained with the MIS and the PIS are displayed in (e) and (f), respectively. Registration results for both calibration approaches are shown as registered masks of the shifted image overlayed to the reference image (solid lines in (g) and (h)).

the reference position indicated by a dashed contour line. The maximum displacement between both images sets is in this case 9 mm. This second set was registered to the reference position with both the MIS and the PIS calibrated registration process. The spatial distribution of the estimated displacement amplitude is reported for the MIS and the PIS criteria in Fig. 9.5e and 9.5f, respectively. As expected, larger displacements were observed in the upper part of the liver, close to the lung. A maximal error on the estimated displacement of 8 millimeters was measured on the landmark points with the MIS in the bottom and the center of the kidney and the upper part of the liver. This maximal error decreased to 4 mm when the proposed PIS criterion was used. Another convenient way to visualize the quality of the result is to subject the masks, manually set on Fig. 9.5c, which depicts the anatomical contours, to the same transformation. This is shown in figure 9.5e and 9.5f respectively, where the realigned masks are overlayed as a contours over the original reference image of 9.5a. Note, in the two zoomed regions, the registration errors arising from the low α values of the MIS-based calibration ($\approx$ 8 mm of mismatch were observed), which are absent when the PIS was used for the calibration.

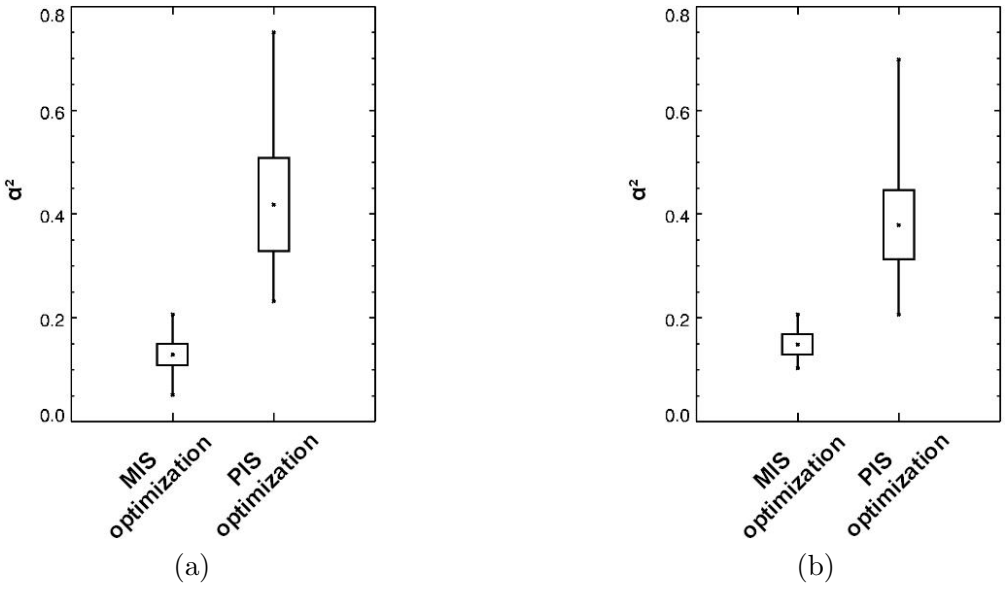

Figure 9.6: Box-and-whisker plot of α^2 values optimizing the MIS and the PIS criteria for each volunteer in the kidney (a) and the liver (b). Plotted values correspond to the minimum (lowest point), the average (cross), the maximum (highest point), and the standard deviation (box height) of the optimized α^2 values across the volunteers.

The statistical analysis over the tested volunteers of α^2 values optimizing each criteria is reported for the kidney and the liver in Fig. 9.6.a and 9.6.b, respectively. Similarly to the ex-vivo experiment, the MIS criterion provided lower α^2 values compared to the PIS. The error of the estimated displacement obtained with an α^2 value optimized using the PIS, the MIS and the GSE criteria are reported in Fig. 9.7.a (kidney) and Fig. 9.7.b (liver). For both kidney and liver, a statistically significant difference of the GSE could be observed for the MIS and PIS criteria in comparison with the acquisition without image registration ($p<0.05$). The PIS criterion performed significantly better than the MIS ($p<0.05$), as confirmed in the Box-and-Whisker plots in Fig. 9.7, which represents the GSE evaluation over all volunteers in both kidney (9.7.a) and liver (9.7.b).

While the criteria based on anatomical image similarity led in average to a maximal error on the estimated displacement higher than 4-5 mm, the proposed PIS criterion reduced this value below 2 mm. In both kidney and liver, the proposed criterion provided motion field accuracy in the range of the best achievable provided by the GSE criterion

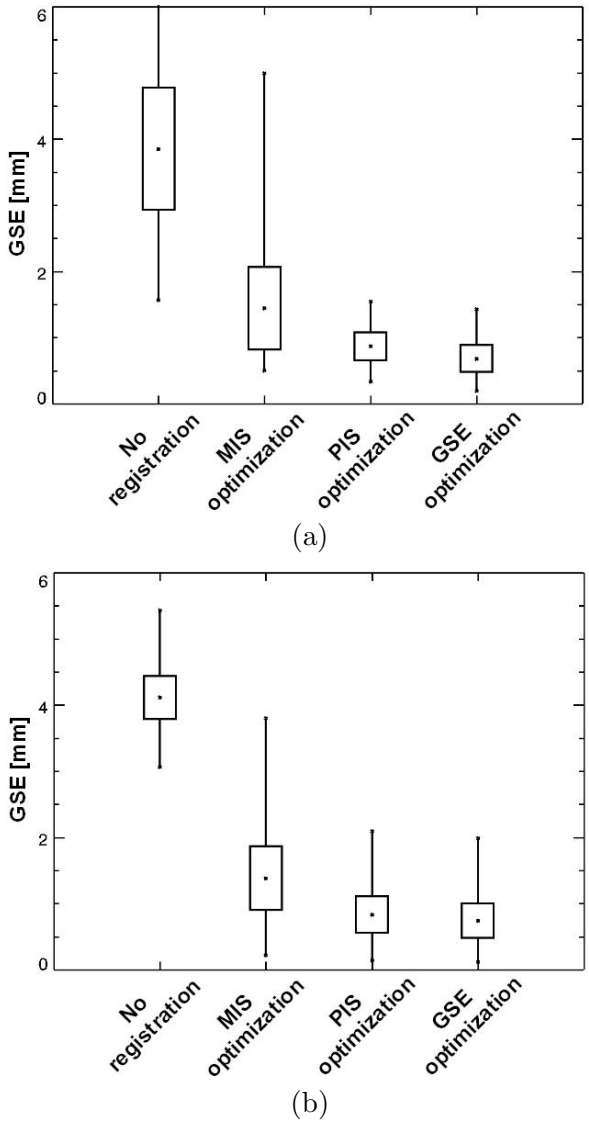

Figure 9.7: Box-and-whisker plot of the gold standard errors (averaged over the K images) obtained with α^2 values optimizing each criteria over the 12 volunteers in the kidney (a) and the liver (b). Plotted values correspond to the minimum (lowest point), the average (cross), the maximum (highest point), and the standard deviation (box height) values across the 12 volunteers.

(≈ 0.8 mm).

9.5 Discussion and conclusions

Using the implemented Horn and Schunck algorithm, a poor estimation of the displacement is performed when α^2 decreased toward 0, due to instabilities of the numerical scheme. Identically, for α^2 increasing toward infinity, tested criteria indicated a poor estimation of the displacement, as the smoothness of motion constrains the velocity amplitude estimation. The GSE criterion, as a function of α^2, reflected these properties, as reported on Fig. 9.2a and 9.2b. It depicted a global minima, corresponding to an optimal registration calibration. Only the PIS matched properly this curve (see Fig. 9.2b).

The criterion based on anatomical image similarity was shown to be inefficient to evaluate the quality of the non-rigid registration, since up to several millimeters of dis-

placement error were found in both ex-vivo and in-vivo experiments. With the proposed PIS criterion, the metric used for motion estimation (magnitude signal) and the metric used to evaluate the registration accuracy (phase signal) are independent. In the ex-vivo study, the optimal α^2 value was systematically lower with the MIS criterion compared to the PIS criterion (see Fig. 9.4a). This is explained by the fact that registration of the noise on magnitude images improved the MIS criterion. Although this may not be a limitation for video encoding in which SNR is generally very high, this can be problematic in the case of fast MRI sequences which show generally a lower SNR, in particular for high framerates. On the other hand, the proposed PIS criterion was demonstrated to provide an optimal estimated motion similar to the best achievable one given by the GSE for all tested SNR levels in the ex-vivo study (see Fig. 9.4) and in both kidney and liver on the in-vivo study (see Fig. 9.7a and 9.7b).

Similarly, it can be observed for the in-vivo study that the optimal α^2 value was as well systematically lower with the MIS criterion compared to the PIS criterion (see Fig. 9.6a and 9.6b). Several application dependent factors require an accurate calibration of the registration. With the implemented registration model, high α^2 values increased robustness against noise or possible local intensity variations not attributed to motion, but limited estimation of strong motion amplitude. In practice, the SNR was found to vary a lot between volunteers due to different coil positioning. α^2 value optimizing both the PIS and the GSE criterion decreased for low SNR values (see Fig. 9.4a), since less importance had to be given to grey level intensity variations in equation (D.1). Identically, in the in-vivo study, more importance was given to the displacement field regularity constraint in equation (D.1) for small target motion amplitudes: while α^2 values higher than 0.7 were systematically found for displacement amplitudes lower than 6 mm (2 kidneys and 1 liver were concerned), α^2 values lower than 0.25 were required for displacement amplitudes higher than 15 mm (2 kidneys and 3 livers were concerned).

It is interesting to observe in Fig. 9.2 that both the PIS and the GSE, as a function of α^2, exhibits a flat zone. A range of values for α^2 allowing an accurate registration could thus be determined. This interval was similar for both the PIS and the GSE. This opens great perspectives to adjust freely α^2 in this interval, depending on the interventional application: in the present study, we used the optimal configuration of the registration algorithm for positions observed during the calibration step. Although this should be a good solution for patient under artificial breathing or for a post-processing study, α^2 may be set to the lower bound of this range for patients under free breathing, in order to allow the registration of possible larger motion amplitudes than observed during the calibration step. However, in case of a huge decrease of the SNR or increase of the target displacement amplitude, this lower bound may still be too high. In such a case, the therapeutic process should be stopped and a recalibration is needed.

The implemented magnetic field perturbation model assumed a simple linear magnetic field variation with organ displacement. However, although this assumption holds in general for small displacements, the precision of this simple model showed several limitations in regions displaying large susceptibility variations, such as in the vicinity of the digestive tube or in the upper part of the liver. Those effects explains the small difference between the PIS and GSE curves in Fig. 9.2b and 9.4a. In addition, the linear model could be limited in the presence of through plane motion. In this case, the measured phase signal over time will not be consistent with a given tissue, and the linear relation may become inconsistent in such area. Therefore, the PIS computation may be biased in such area. However, the spatial distribution of the linear model relevance can in practice be achieved by simply mapping the fitting error $\epsilon(x, y)$ from equation (9.3). This also allows one to remove from the mask m regions where low signal levels in conjunction with complex susceptibility variations may prevent adjustment of the linear model to the phase data.

The proposed calibration method reduced the user intervention to the determination of the mask m encompassing the targeted region. The computation time required for one image registration was 5 ms with the used material. The calibration process required the observation of thirty α^2 values, and, for each, the registration of $K = 50$ images and the PIS computation with equation (9.2). As an indication, less than ten seconds were required before the intervention for the whole calibration process. The proposed method can thus be conveniently performed just before the hyperthermia procedure to optimize an optical-flow based registration algorithm.

The proposed criterion based on phase MRI images is based on a physical parameter (i.e. the magnetic field variation with displacement) and was demonstrated to allow automatic calibration of an image registration algorithm for real-time MR-intervention. Estimated displacement in the ex-vivo and in-vivo experiments was comparable to the real target displacement. Although the proposed criterion was tested with a simple registration algorithm derived from the Horn and Schunck approach, it should be possible to extend to more complex image registration algorithms such as [73] or [71]. Results obtained also open great perspectives for an evaluation of the method with different slice positioning and orientations, and other targeted organs such as in the heart.

Chapter 10

Correction of motion related magnetic susceptibility variation for spontaneous motion

The correction of motion related susceptibility variations are generally corrected by either a multi-baseline approach or a referenceless approach (see section 2.2.1). However, each of these methods shows substantial limits that are reported in section 5.5.3. For this reason, an hybrid approach is presented in this chapter that aims to take advantages of both methods [159, 160]. This hybrid correction is compared to existing methods and show significant improvement in presence of spontaneous motion. This study was mainly carried out by Baudouin Denis de Senneville and Mario Ries. My contribution was the development of real time algorithms for motion estimation and compensation and for multi-baseline based MR-thermometry.

10.1 An hybrid correction method

The hybrid approach employs initially the multi-baseline algorithm to continuously provide temperature maps across the entire field of view. In addition, these temperature maps are also used to dynamically update the preparation parameters of the referenceless algorithm:

1. The fitting ROI is continuously adjusted: For this, the multi-baseline temperature map is thresholded (all values above 2.0 °C are discarded) and subsequently eroded by one voxel.

2. This ROI is used to calculate a referenceless temperature estimate. The difference between the temperature maps obtained with multi-baseline and with referenceless is retained as an offset correction map.

Should a spontaneous movement occur during the intervention, for which no reference phase is pre-recorded, the processing pipeline switches dynamically from multi-baseline to referenceless MR-Thermometry using the most recent fitting ROI and offset correction map. The criteria used to detect spontaneous motion is based on the observed two translations and the rotation of the PDC-estimation: Any currently detected translation or rotation exceeding the value range observed during the preparation phase by more than 0.5 voxel (translation) or 0.5 ° (rotation) is considered as a spontaneous movement and leads to the algorithm transition.

10.2 Experimental validation

Experimental protocol

A calf liver was positioned on a motorized platform inside the MR-scanner to simulate physiological motion. A periodic purely in-plane displacement in read-out (frequency encoding) direction, of an amplitude of 22 mm and a period of 6 seconds, was simulated. To evaluate the influence of spontaneous motions, the experiment was repeated under periodical motion and a singular lateral displacement of 1 cm amplitude and 1 s duration was introduced after 50 s of MR-thermometry, whereby the sample did not return to its original position.

Dynamic MRI was performed with a gradient recalled EPI sequence using a 121-binomial water-selective excitation pulse. The following acquisition parameters were used: 3000 dynamic coronal images, single slice, TR=18 ms, TE=8.8 ms, 14 images/s, FOV=256×88×6 mm^3, matrix 128×44, multi-shot acquisition with 11 lines per excitation, Band-width per pixel=1.7 kHz. Three hundred images were acquired prior to hyperthermia to allow precise sampling of the periodical displacement for the multi-baseline method. Subsequently, the tissue was heated with 8 W of RF-power during 85 seconds using bipolar electrodes, placed 1.2 cm apart.

The accuracy of the MR thermometry was evaluated using the readings of a fiber optic probe as a gold standard. The fiber optic probe (Luxtron STB Medical, LumaSense, France) was placed between both electrodes, and its position identified by additional high-resolution spin-echo (SE) imaging. The precision of the MR thermometry was quantified during the cool-down period (time interval 120-250 s) using the standard deviation between MR measurements and a fitted exponential decay curve.

Experimental results

Contrary to both multi-baseline and referenceless corrections, the hybrid approach provided accurate temperature and thermal-dose estimates over the entire duration of the experiment (see figure 10.1). The transition between "multi-baseline mode" and "referenceless mode" was triggered by the automatic detection of the motion event and did not introduce any apparent degradation of MR-thermometry except a change in measurement precision, as shown in figure 10.1f.

10.3 Discussion and conclusion

Due to the fact that the main limitations of multi-baseline and referenceless MR-thermometry are largely complementary, the presented hybrid approach represents an attempt to overcome their limits by combining both approaches.

Although multi-baseline MR-thermometry is able to provide accurate temperature and thermal dose measurements in the presence of periodical motion over the entire field of view, its main limitation is its inability to cope with spontaneous motion. The hybrid approach compensates for this inability by switching automatically to a polynomial fit for background phase estimation when such an event is detected, which is similar to the approach used for the referenceless method. However, the two main disadvantages of the referenceless method, its dependence of the accuracy of the selection of the fitting ROI location and, in particular when mini-invasive interventions are considered, its inability to provide background phase estimates which include the effect of strong local susceptibility variations, are thereby avoided: The initial observation of the temperature evolution using multi-baseline MR-thermometry allows to continuously adapt the fitting ROI in order to avoid the inclusion of heated or unstable areas and to provide an offset correction

map which removes the effect of local susceptibility variations. Note that although the polynomial fit for the background phase estimation is similar to the referenceless method, the latter correction represents a phase reference (i.e. the hybrid approach is never truly "referenceless".

However, the proposed hybrid approach can not eliminate all the limitations of the multi-baseline and the referenceless methods. The hybrid still requires a lengthy initial acquisition of a phase correction dataset and inherits the accuracy limitations for long experiments of both methods, either due to a possible contamination of the fitting ROI due to heat diffusion, or due to an imperfect spatio-temporal B_0 drift correction, depending on the operation mode.

For the case of generic applications, where the presence of exclusion criteria of either method are a priori not entirely known, a pragmatic way forward to guarantee accurate and precise temperature and thermal dose estimates, is to tailor a suitable combination of multi-baseline and referenceless MR-thermometry. The presented hybrid approach represents one of several possible solutions for such a combination and demonstrates that it is possible to achieve accurate and precise PRF-thermometry during periodical displacement even in the presence of spontaneous motion and strong susceptibility variations in the target area.

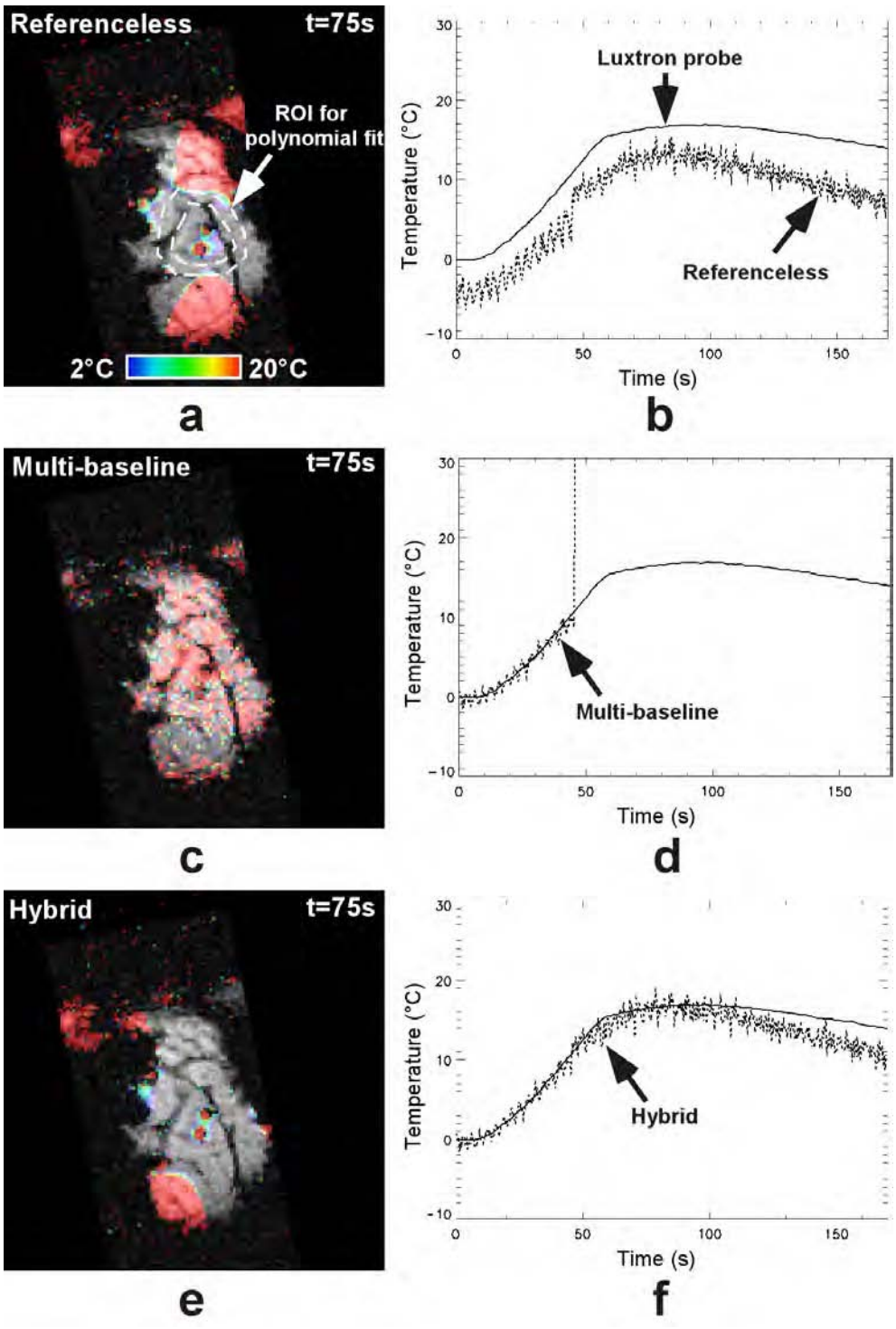

Figure 10.1: MR-Thermometry maps obtained 25 seconds after the occurrence of a spontaneous motion event (at $t = 50s$) of the referenceless (a), the multi-baseline (c) and the hybrid (e) approaches and the corresponding temporal evolution at the position of the Luxtron probe (b,d,f). The accuracy of the referenceless approach is limited by its ability to cope with the local magnetic field variations in the vicinity of the RF-electrodes which leads to an offset (b). Furthermore, the static ROI choice leads to a discontinuity at the point of the motion event. As the multi-baseline approach can not cope with this type of motion, it is not able to provide meaningful temperature readings after the event (artifact >50°C). Note that the hybrid approach follows closely the true temperature evolution.

Chapter 11

Temporal temperature filtering

11.1 Introduction

The precision of real time MR-thermometry is generally limited by both the available SNR [84] and the influence of physiological motion as described in the introduction of this thesis (see section 2.4). Consequently, algorithms used for retroactive control are liable to be biased or rendered unstable by the presence of noise in the temperature maps. Furthermore, the accuracy of the calculation of the thermal dose used for necrosis estimation deteriorates for low SNRs due to its exponential dependence on the temperature (see equation (1.2)). To overcome these problems, as described in chapter 5 (section 5.2.5), temporal filtering has been proposed as a solution to improve the precision of the temperature maps using an infinite impulse response (IIR) filter [122]. However, the use of this type of low-pass filters, or alternative designs such as finite impulse response (FIR) filters, introduces in general additional latency, leading to a reduced accuracy and limits the achievable temporal resolution of the observation process.

This can be alleviated by using more complex filter designs, which include physical knowledge of the observed system, such as Kalman filters [161]. Kalman filtering is based on the combination of both measured data and data derived from a forecast based on a physical model. Potocki & Tharp [162] proposed the bio heat transfer equation (BHTE) model [163] for this purpose. In their experiment, temperature information was only available at four different locations (obtained from optical fibers). The filter was essentially not designed for noise removal (since only four measurement points were available) but to estimate both blood perfusion and temperature information at unmeasured locations (spatial extrapolation). More recently, Ye et al. [164] employed Kalman filtering for improved model-based ultrasound temperature visualization. The predictor model was based on the construction of isothermal ellipsoids around the heated area. Although the precision of the resulting temperature maps was clearly improved (due to a high confidence placed in the model), the accuracy of the method was not evaluated.

Here, we propose a novel spatio-temporal filter based on Kalman filtering theory that aims to improve MR-thermometry precision while controlling its accuracy [165, 166]. For this, an extended Kalman filter is employed with the BHTE as a predictive model. However, the combination of the predicted data and the measured data is not a simple problem. A too large influence of the model would lead to a high noise reduction, but may introduce severe bias on the output accuracy if the model is not properly configured. With increasing emphasis on measured data, the noise removal will not be efficient, however the filter will tolerate imprecise calibration without giving rise to systematic error. Therefore, the filter has to be tuned as a function of the model accuracy which is a priori not known and may vary in time. For this, a dynamic evaluation of the model accuracy was added to the filtering process in order to adjust in real time the confidence in the model and thus the

balance between measured and predicted data. Finally, an outlier rejection was added to the filter to cope with strong temperature artifact. The proposed filter was evaluated on simulated datasets and its feasibility is demonstrated on MR-guided HIFU experiments on an agarose gel phantom and in-vivo on a porcine kidney. It showed significant improvement compared to non-adaptive temporal filter designs without giving rise to additional filtering latency.

11.2 An adaptive extended Kalman filtering for real time MR-thermometry

11.2.1 Temperature modeling using the Bio Heat Transfer Equation (BHTE) model

The BHTE model can be used to predict the temperature T from time $t-1$ to time t, based on the applied acoustic power P and a priori knowledge of the absorption rate (α), the heat diffusion coefficient (D) and the perfusion value (w) [163]. Note that this simplified model assumes these coefficients as spatially and temporally invariant. The BHTE in the voxel of coordinates $\overrightarrow{r} = (x, y, z)$ is defined as follows:

$$\frac{\partial}{\partial t} T_{(\overrightarrow{r},t)} = \alpha . P_{(\overrightarrow{r},t)} + D . \Delta T_{(\overrightarrow{r},t)} - w . T_{(\overrightarrow{r},t)} \tag{11.1}$$

where Δ denotes the Laplace operator. In the absence of large vessels, perfusion effects are often neglected and thus w is set to 0. The BHTE can be solved in the Fourier domain since the problem is turned into a linear differential equation as follows:

$$\frac{\partial}{\partial t} \widetilde{T}_{(\overrightarrow{k},t)} + (D.k^2 + w) . \widetilde{T}_{(\overrightarrow{k},t)} = \alpha . \widetilde{P}_{(\overrightarrow{k},t)} \tag{11.2}$$

where $\widetilde{T}, \widetilde{P}$ denotes the Fourier transform of T and P respectively, $\overrightarrow{k} = (k_x, k_y, k_z)$ denotes the frequency coordinates in the Fourier domain and $k^2 = k_x^2 + k_y^2 + k_z^2$. The solution is computed based on the variation of constants as follows:

$$\widetilde{T}_{(\overrightarrow{k},t)} = \widetilde{T}_{(\overrightarrow{k},t-1)} . e^{-(D.k^2+w)t} + \alpha . \widetilde{P}_{(\overrightarrow{k},t)} \frac{1 - e^{-(D.k^2+w)t}}{D.k^2 + w} \tag{11.3}$$

Since the BHTE models the physical processes of heat diffusion and absorption, it should be applied in 3D space in order to obtain unbiased results. Unfortunately, the available acquisition time is typically too limited in interventional imaging to obtain full 3D temperature imaging, especially if physiological motion has to be resolved. As a consequence, in practice the BHTE has often to be applied to 2D or severely undersampled 3D datasets. This leads to a systematic underestimation of heat evacuation and neglects potential heat inflow from adjacent slices, in particular for large prediction period. In order to evaluate the resulting bias on the filtered temperature data, the BHTE was implemented for both 2D and 3D temperature prediction and the results subsequently compared on simulated heating experiments.

Furthermore, although MR-thermometry provides coherent temperature information in areas of high signal (generally with a precision of few degrees), areas with very low signal level generally display temperature values with variations in the range of several tens of degrees. Since the BHTE model prediction is based on preceding filtered temperature maps represented in Fourier space, such areas have to be excluded by manual ROI-based masking to prevent a bias due to undesired high frequency noise.

11.2.2 BHTE based extended Kalman filtering

Since the discrete solution of the BHTE represents a non-linear model for data prediction, the original Kalman filtering theory, which requires a linear predictor, is not directly applicable. Non-linear predictors are addressed by the extended Kalman filtering (EKF) formalism. An EKF can be seen as a two step process. In a first pass, the filter computes a data prediction (at time t) based on the last filtered data point (obtained at time $t-1$). In a second pass, the algorithm optimally combines both predicted data and measured data to obtain the final filtered data corresponding to time t.

11.2.2.1 First pass: time update equations

The first pass of the filter is often referred to as time update equations. The temperature prediction T_t^- at time t and the a priori estimate error covariance P_t^- are computed as follows:

$$\begin{array}{rcl} T_t^- & = & f(T_{t-1}, u_{t-1}) \\ P_t^- & = & A_t P_{t-1} A_t^T + Q \end{array} \tag{11.4}$$

where T_{t-1} denotes the filtered temperature at time $t-1$, f represents the BHTE model and u_{t-1} is the control input parameter (the HIFU delivered power at time $t-1$ in our case). A_t is the Jacobian matrix of partial derivatives of f with respect to the temperature T at (T_{t-1}, u_{t-1}), A_t^T denotes the transpose of A_t, P_{t-1} is the a posteriori estimate error covariance at time $t-1$ and Q is the process noise covariance related to the model inaccuracy.

11.2.2.2 Second pass: measurement update equations

In a second pass, the Kalman filter combines both predicted T_t^- and measured T_t^m data to obtain the final filtered data T_t. The combination is weighted with a parameter K_t, often referred to as the Kalman gain, while the difference $T_t^m - HT_t^-$ is generally referred to as the innovation S_t. H relates the model state to the measurement (here H is the identity since the measurements are directly obtained in state space). During the second pass, K_t is first updated based on the new a priori estimate error covariance. Subsequently, the filtered temperature T_t can be computed from the weighted innovation S_t. The final step updates the a posteriori estimate error covariance P_t. The measurement update equations are summarized as follows:

$$\begin{array}{rcl} K_t & = & P_t^- H^T (H P_t^- H^T + R)^{-1} \\ T_t & = & T_t^- + K_t (T_t^m - H T_t^-) \\ P_t & = & (I - K_t H) P_t^- \end{array} \tag{11.5}$$

where R is the measurement noise covariance that relates to the MR-thermometry precision of the measure. Note that R can be obtained prior to hyperthermia by evaluating the standard deviation of the measured temperature.

11.2.3 Autocalibrated extended Kalman filtering (AEKF)

The EKF combines measured and predicted data via the Kalman gain K_t, that allows to optimally adjust the confidence between the employed model and the measured data. The Kalman gain is updated dynamically and predominantly influenced by two input parameters of the filter: The measurement noise covariance (R) and the process noise covariance (Q). While the measurement noise covariance can be determined from baseline data in absence of heating, the determination of Q is not straightforward. Q corresponds to the model accuracy and thus depends on the accurate knowledge of the physical parameters

of the tissue (absorption coefficient and heat diffusion), which are a priory not exactly known and thus in general only available as rough estimates.

In addition, heat absorption only occurs during the heating period when the HIFU system delivers acoustic energy, while heat diffusion is present during both heating and cooling. Therefore, the BHTE model may have a varying performance over time if not properly configured (for example using an incorrect absorption coefficient with the true diffusion coefficient). In such a case, Q would be better chosen as time variant.

This can be achieved using an adaptive EKF (AEKF), where Q is automatically adjusted over time based on a dynamic evaluation of the model accuracy for each new measurement. In the proposed implementation this is based on the assumption that temperature noise is white noise around the real value. The model is considered accurate at time t if ε_t, the spatio-temporal sum of the difference between predicted and measured data, is below a predefined error threshold $\varepsilon_{threshold}$, with

$$\varepsilon_t = \frac{1}{N * card(\varrho)} \| \sum_{i=t-N+1}^{t} \sum_{(x,y)\in\varrho} (T_i^-(x,y) - T_i^m(x,y)) \|. \tag{11.6}$$

Here, the model is evaluated over the temporal window size N and over a voxel perimeter ϱ around the focal point, which is referred to as the spatial window size M in the scope of this study. $\varepsilon_{threshold}$ is chosen as the maximum acceptable penalty of the filtering process on the measurement accuracy. Therefore, the autocalibration process selects the smaller Q value, providing an accuracy ε_t inferior to $\varepsilon_{threshold}$, using an optimization approach inspired by the gradient descent approach. Note that the research window for the optimal value of Q was empirically bounded to the interval $[0.0001, 1000]$ which is sufficient to represent the process noise covariance Q in our case.

11.2.4 Robust approach of AEKF

The computation of temperature maps requires an image processing pipeline, that can be rather complex especially in the case of MR-thermometry applied to mobile organs. Therefore, severe artifacts on temperature maps can be observed for a variety of reasons such as incorrect phase unwrapping or imperfect motion compensation. This type of error can have amplitudes much larger than the imprecision caused by low SNRs. Since the determination of the thermal dose corresponds to the integral over time of the temperature (see equation (1.2)), temperature artifacts introduce a non reversible error bias on the thermal dose calculation. In addition, due to the exponential dependence on the temperature, even temporally sparse occurrences of severe temperature artifacts lead frequently to an apparent thermal dose which is magnitudes off the true value. For HIFU interventions which use the thermal dose as a criterion for the determination of the therapy endpoint, this may affect the success of the intervention (overestimation) or patient safety (underestimation) and is thus highly undesirable. To detect such occurrences, an outlier rejection based on the Chauvenet's criterion [167] was applied to the difference between measured and predicted temperature, i.e. the innovation S_t. The outlier rejection considers an innovation S_t for rejection if the probability to obtain its deviation from the mean $\bar{S}_t$ is less than $1/(2 \cdot NS)$, NS being the number of measurement samples. Substituting $\bar{S}_t$ by ε_{t-1} as defined in equation (11.6), leads to the following robust formulation of the AEKF based on the Chauvenet's criterion:

$$T_t = \begin{cases} T_t^- & \text{, if } |S_t - \varepsilon_{t-1}| > \sigma(S_{t-1}) * e_{max} \\ T_t^- + K_t S_t & \text{, if } |S_t - \varepsilon_{t-1}| \leq \sigma(S_{t-1}) * e_{max} \end{cases} \tag{11.7}$$

where e_{max} is the ratio of the maximum acceptable deviation to precision [167] and $\sigma(S_{t-1})$ is the standard deviation of the innovation over the $N \times M$ sample points, excluding

the last innovation S_t. Note that a rejection of a measured temperature value T_t^m leads the filtered value T_t to depend only on the prediction T_t^-, which is equivalent to temporarily setting R=∞ in equation (11.5).

11.3 Experimental validation

11.3.1 Simulations

A 3D reference temperature dataset was simulated using the BHTE model (absorption=0.02 KJ^{-1}, diffusion=0.1 $mm^2.s^{-1}$, delivered power=100W (between the 20^{th} and the 70^{th} dynamic images), matrix=$32 \times 32 \times 16$, voxel size=$1 \times 1 \times 2$ mm^3, focal point size=$1.23 \times 1.23 \times 7.88$ mm^3, dynamic scan time=1 s). 100 datasets were derived with added Gaussian noise (σ=5°C). The proposed AEKF was evaluated using a 3D implementation of the filter. Since in practical cases, MR-temperature information is often available in 2D, the impact of a 2D implementation of the filter was also analyzed.

A matched Kaiser Bessel FIR filter was used for comparison and configured to retain 90% of the integrated power spectrum of the original noise free temperature simulation (pass band cutoff frequency=0.022 Hz, stop-band attenuation>21 Db, window size=15).

To quantify the performance of each filter, the mean square error (MSE) between filter output and reference data was used as quality criterion of the filter output accuracy.

11.3.1.1 Performance of EKF filtering

Figure 11.1 shows the filter performance on a simulated dataset. The FIR filter (figure 11.1a) introduces a latency inherent to its design, while the EKF (with a 3D implementation) avoids this effect (figure 11.1b,c,d). When configured with the exact physical parameters (figure 11.1b) the filter does not introduce any bias on accuracy and improves the output precision. An emphasis on the measured data (Q=10) leads to some smoothing of the temperature. On the contrary, a high confidence in the model (Q=0.1) provides an efficient noise removal in this case. Figure 11.1c shows the influence of an imperfect configuration of the model (in this case with an 50% underestimated absorption coefficient). Here, a bias on accuracy is observed, especially for Q values giving a large influence to the model. On the other hand, using small values of Q reduces the penalty on the accuracy but limits the filter ability to reduce measurement noise. Identically, a 2D implementation of the BHTE model introduces a bias that can be observed when a high confidence in the model is employed (Q=10). A lower Q value allows to improve the accuracy while decrease the precision of the resulting filtered temperature (see figure 11.1d).

These results confirms the necessity to adapt the value of Q in function of the bias of the input parameters (the absorption and diffusion coefficients) and the dimension of the employed implementation (2D or 3D). A quantification of EKF accuracy is now given for a mis-configured BHTE model using a 3D and 2D implementation of the BHTE model. The resulting improvements provided by the AEKF is showed for each case.

11.3.1.2 AEKF Filtering performance using the 3D implemented BHTE model with an approximative configuration

The error bias introduced by an approximative configuration of the BHTE based model was then investigated. With the employed absorption and diffusion coefficients and the chosen spatial resolution of the simulation, the choice of the absorption coefficient has a larger impact than the choice of the diffusion coefficient. An illustration of the bias introduced by an approximative configuration of the BHTE based model, obtained with several incorrect absorption values, is reported in figure 11.2. For this, the filter was

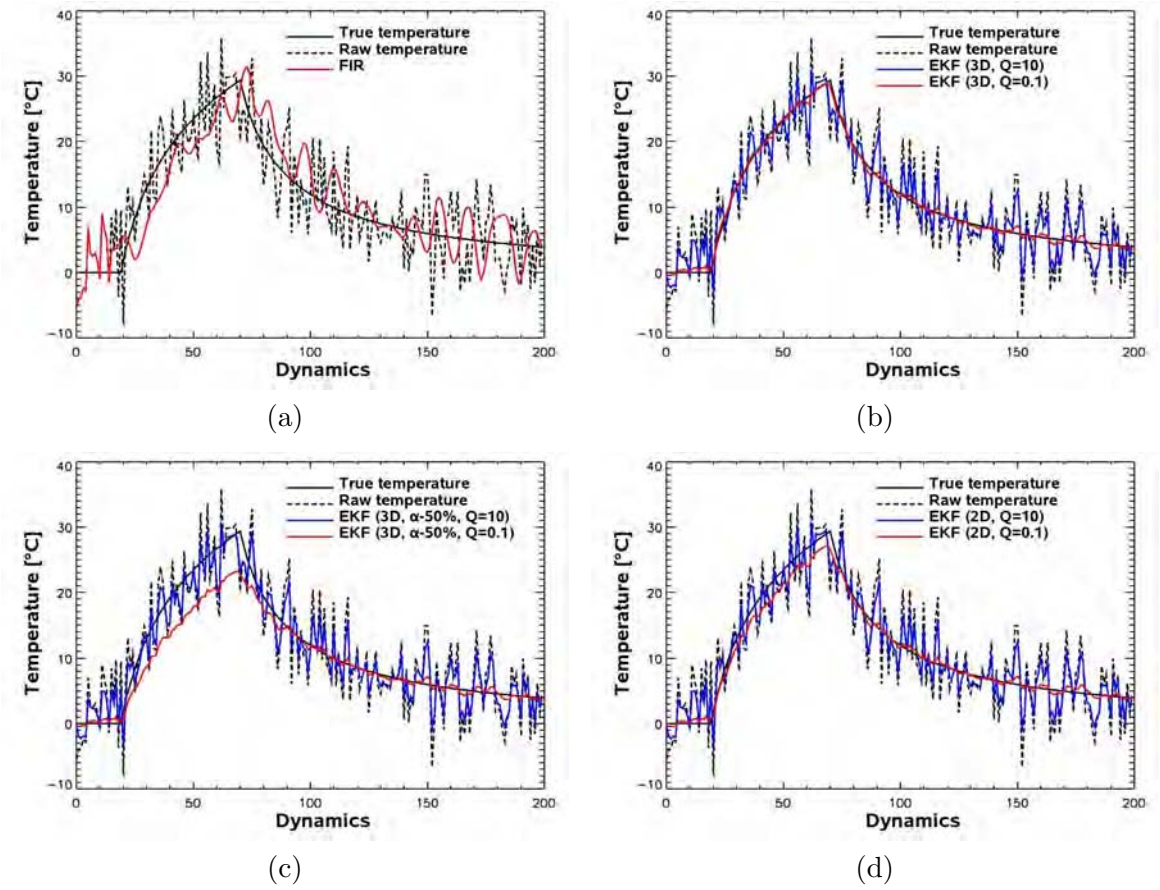

Figure 11.1: Examples of temporal filtering obtained in the focal point of the simulated dataset: results obtained using (a) a FIR filter (b) an EKF filter configured with the true absorption and diffusion values ($\alpha = 0.02$ KJ^{-1} and D =0.1 mm^2.s^{-1}), (c) an EKF filter badly configured (wrong absorption (α =0.01 KJ^{-1}) with true diffusion D =0.1 mm^2.s^{-1}), (d) an EKF filtering based on a 2D implementation of the filter. The measurement noise is significantly reduced with the FIR but leads to undesired latency of the temperature curve. While this effect is reduced with the EKF, note the strong influence of the process noise covariance Q on the EKF filtering performance.

tested using different Q values over all 100 datasets with an absorption coefficient varying over -50% to +50% of its true value. The evaluation of the error bias introduced by a mis-configuration of the absorption coefficient and the diffusion are plotted in figure 11.2a,b and 11.2c,d respectively. It can be observed that optimal Q values are different for the heating period (figure 11.2a,c) and for the cooling period (figure 11.2b,d) that illustrates the time varying accuracy of the BHTE model. However, for all configurations, even in the case of a mis-configuration of the BHTE model with a bias of $\pm$ 50 % of the input absorption coefficient, a good choice of the Q value can guarantee a better filter performance compared to the FIR filter. Therefore, an adaptive tuning of Q during the intervention appears mandatory and is now investigated.

The potential of the proposed AEKF to automatically adapt and optimize the value of Q was tested on the 100 datasets and the results are plotted in figure 11.3. The influence of a mis-configuration of both absorption (11.3a,b) and diffusion (11.3c,d) coefficients was evaluated during the heat-up (11.3a,c) and cool-down (11.3b,d) periods. The resulting accuracy obtained with the FIR filter was comparable to the accuracy without filtering, which is mainly due to the latency introduced by the filter and its inability to follow rapid

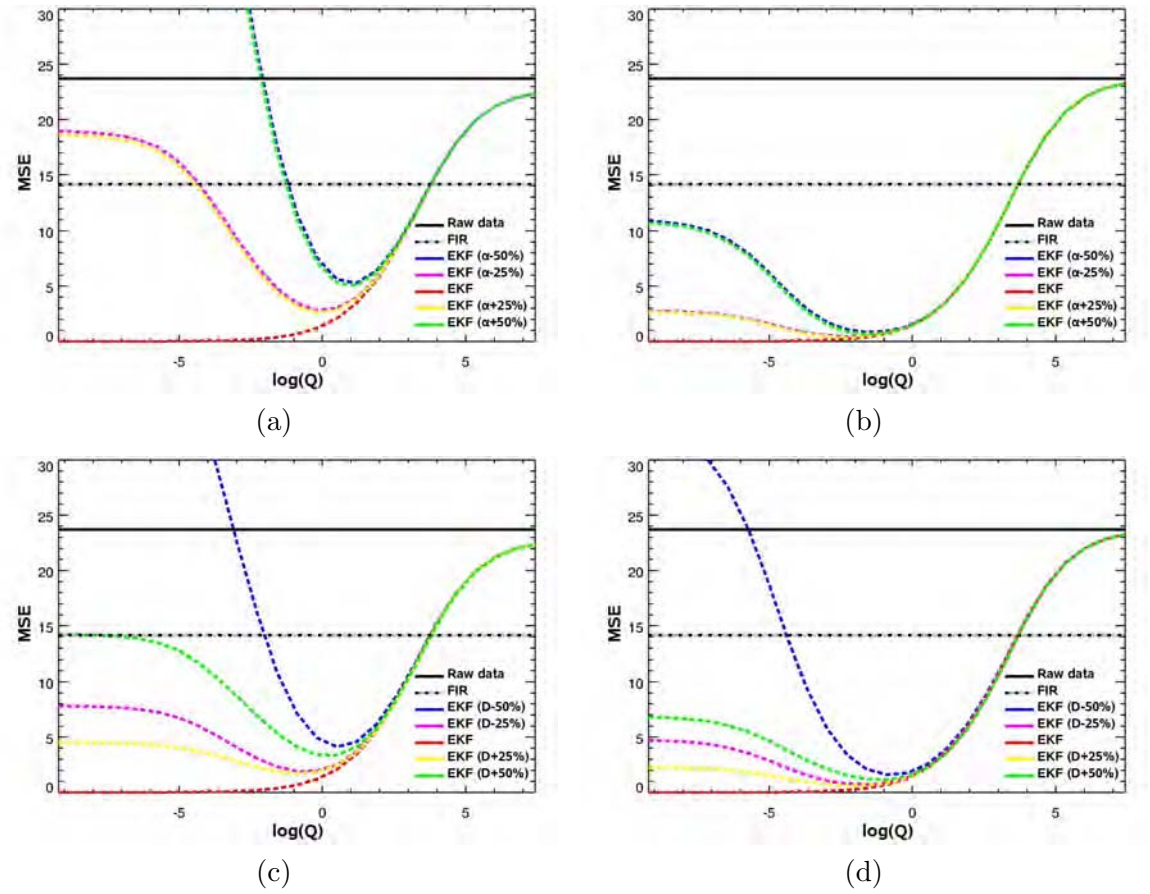

Figure 11.2: Mean squared error of the filtered signal obtained with a 3D implementation of the EKF filter in the focal point of the simulated dataset. Influence of absorption (a,b) and diffusion (c,d) on the mean square error (MSE) of the filtered temperature curve during heat-up (a,c) and cool-down (b,d) periods.

temperature variation. However, during the cool-down period, the FIR allows to improve the resulting accuracy by a factor of 3, due to the reduced temperature variation between two successive temperature points (compared to the heat-up period). Using the AEKF, the resulting accuracy was reduced in the worst tested case by factors 3 and 15 for the heat-up and cool-down periods respectively. Therefore, the AEKF outperforms the FIR even in the case of a mis-configuration of the BHTE model with a bias of ± 50 % of the input parameters.

11.3.1.3 Performance of the AEKF filtering using a 2D implementation of the BHTE model

Figure 11.4 investigates the error bias introduced by an approximative configuration of both absorption and diffusion coefficients in the BHTE model using a 2D implementation of the EKF. Identically to the 3D evaluation, the filter was tested using different Q values over all 100 datasets with each parameters varying for -50% to +50% of its true value. Evaluation of the error bias introduced by a mis-configuration of absorption (11.4a,b) and diffusion (11.4c,d) on the mean square error (MSE) of the filtered temperature curve during heat-up (11.4a,c) and cool-down (11.4b,d) is plotted. It can be observed that optimal Q values are different for the heating period and the cooling period and guarantee a better performance compared to the FIR filter even in the case of a mis-configuration of the BHTE model with a bias of ± 50 % of the input parameters.

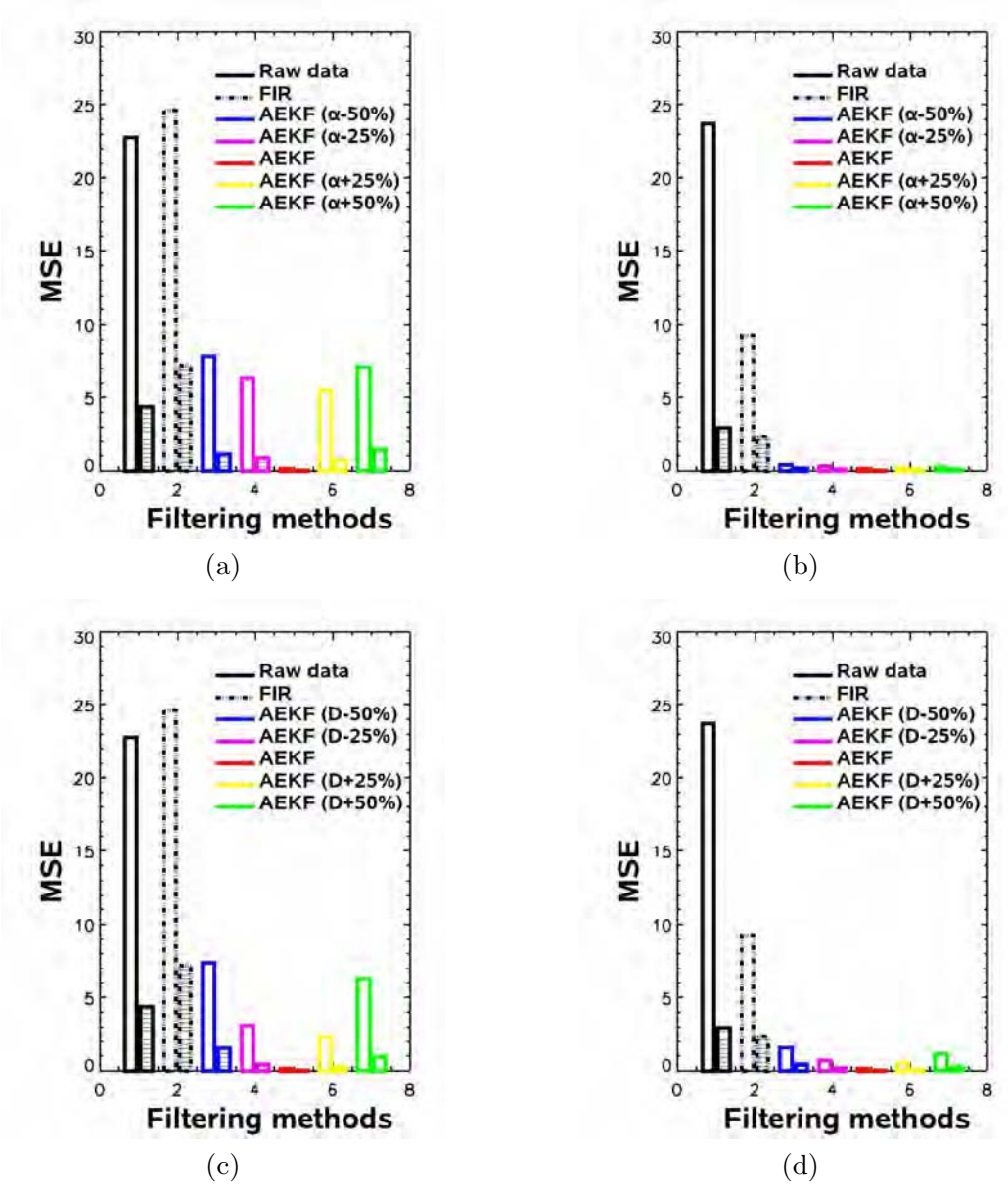

Figure 11.3: Temporal filtering performance obtained using several configurations of the model and a 3D implementation of the filter. Influence of absorption (a,b) and diffusion (c,d) on the mean square error (MSE) of the filtered temperature curve during heat-up (a,c) and cool-down (b,d) periods. The AEKF achieves a better filter performance than the FIR even if the tissue absorption α or the thermal diffusion are deliberately mis-configured by $\pm 50\%$. For each method, the MSE average and standard deviation over the 100 datasets are plotted in the empty box and the dashed box respectively.

The influence of a 2D implementation of the filter was then evaluated on the same simulated datasets. Figure 11.5 shows the impact of a mis-configuration of both absorption (11.5a,b) and diffusion (11.5c,d) coefficients during the heat-up (11.5a,c) and cool-down (11.5b,d) periods. The best performance of the AEKF is not achieved with the true configuration of the absorption and diffusion coefficients. Indeed, in this case, the focal point size in the third dimension is 7.88mm which is three times larger than the spatial resolution of the simulation in the third dimension. Under these conditions, all energy supposed to be delivered above and below the 2D single slice is not considered with this 2D

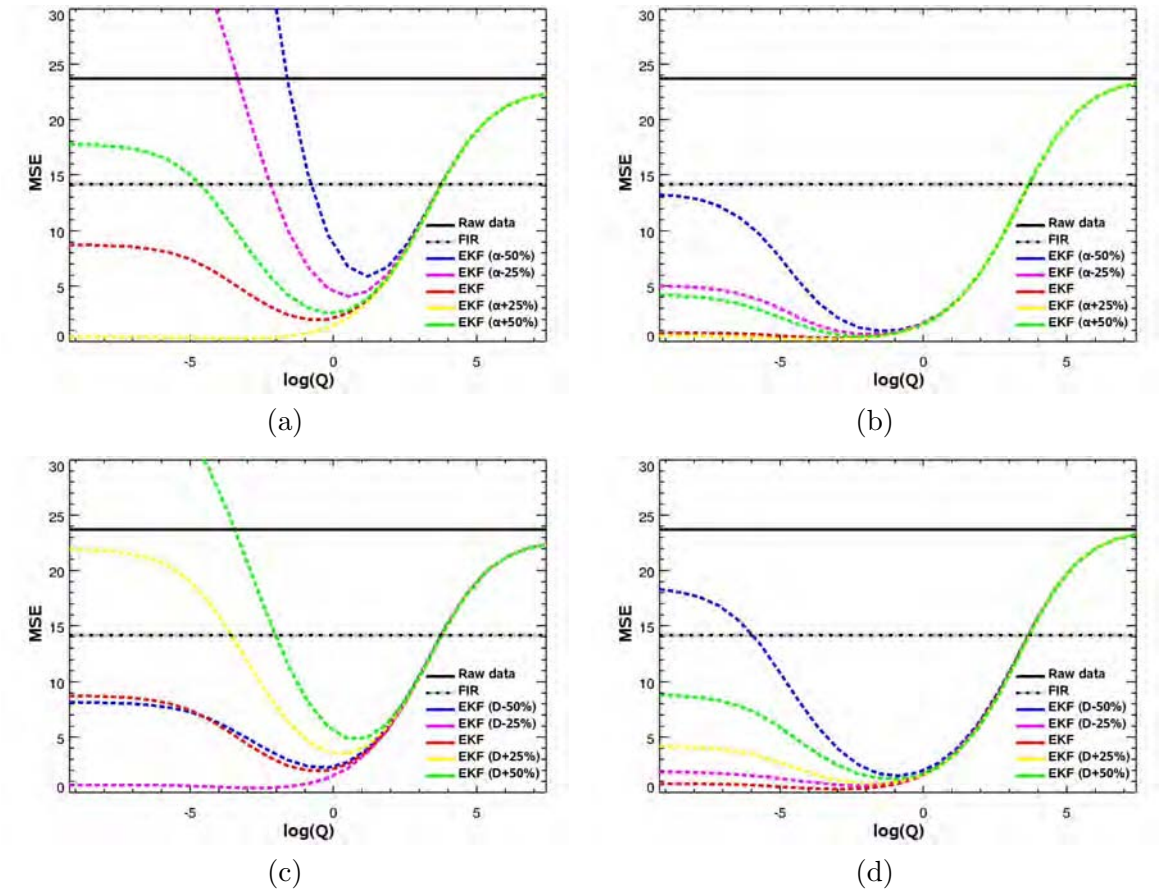

Figure 11.4: Mean squared error of the filtered signal obtained with a 2D implementation of the EKF filter in the focal point of the simulated dataset. Influence of absorption (a,b) and diffusion (c,d) on the mean square error (MSE) of the filtered temperature curve during heat-up (a,c) and cool-down (b,d).

implementation. Therefore, an AEKF with either an absorption coefficient overestimated by +25% of the true value or a diffusion coefficient underestimated by -25% of its true value allows to compensate for the lack of received energy and in this case outperform an AEKF with a true configuration. Similarly to the 3D AEKF evaluation, the resulting accuracy was reduced in the worst tested case by factors 3 and 15 for the heat-up and cool-down periods respectively. Therefore, with the employed conditions, the AEKF outperforms the FIR even with a 2D implementation and a mis-configuration of the BHTE model with a bias of ± 50 % of the input parameters.

11.3.1.4 Convergence of the optimized Q value

The performance of the presented adaptive EKF was then investigated and the obtained filtered temperature with the time optimized Q values are plotted in figure 11.6. Results obtained with a 3D implementation of the filter using an incorrect absorption coefficient of -50% of its true value and with the true diffusion coefficient are reported in figure 11.6a,b. This configuration is thus similar to the one employed in figure 11.1c and the results are thus directly comparable. The initial mean square errors of 22.7°C and 21.9°C during the heat-up and cool-down periods were reduced to 8.1°C and 0.5°C using the mis-configured AEKF (see figure 11.6a). The same configuration of the EKF led to a MSE of 26.9°C and 1.2°C with $Q = 0.1$ and 8.4°C and 8.5°C with $Q = 10$ (see figure 11.1c) for heating and cooling periods respectively. Therefore, AEKF performance is similar to EKF with

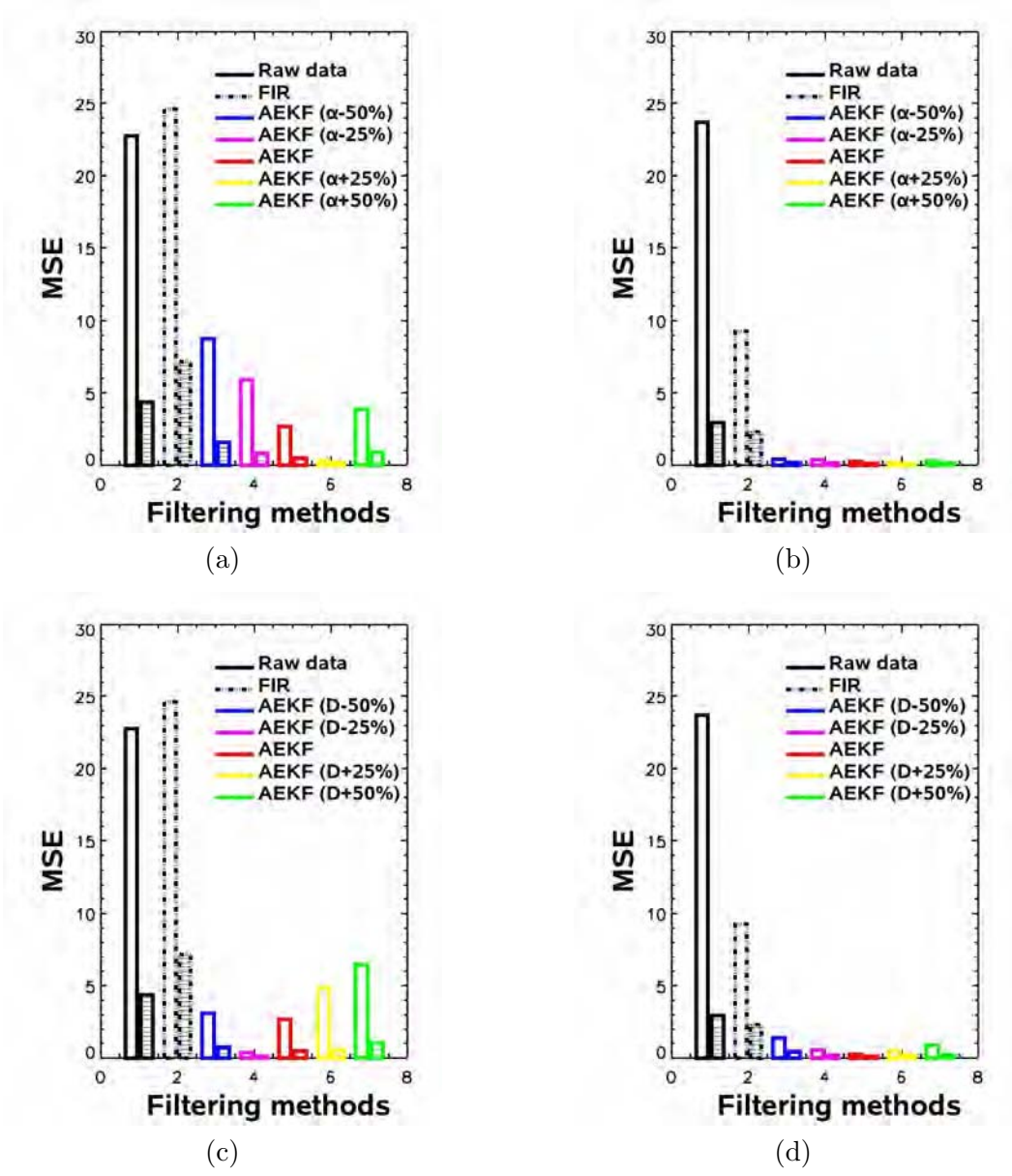

Figure 11.5: Influence of a 2D implementation of the filter: Similarly to figure 11.3 the impact of an incorrect choice of the absorption (a,b) or diffusion (c,d) coefficients was evaluated during both heat-up (a,c) and cool-down (b,d) periods. Again, the AEKF achieves a better performance than the FIR even using a 2D implementation of the filter with absorption or diffusion coefficients deliberately miss-configured by ±50%.

$Q = 10$ during heating and similar to EKF with $Q = 0.1$ during cooling confirming the benefit of an adaptation of the Q value. Finally, the AEKF clearly outperforms the FIR that provides a MSE of 18.3°C and 11.8°C for each of the two periods (see figure 11.1a). The BHTE based model was only incorrect during the heat-up period (since absorption is only relevant during power delivery). The time optimized Q values increased during this period in order to give more confidence in the measurements and converged into an interval of [log(0), log(2)] (figure 11.6b). This corresponds well to the optimum Q values (global minimum) obtained in figure 11.2a with the blue curve (-50%). Then, the model being true during the cooling down period, the optimized Q values decreased to improve the confidence in the model.

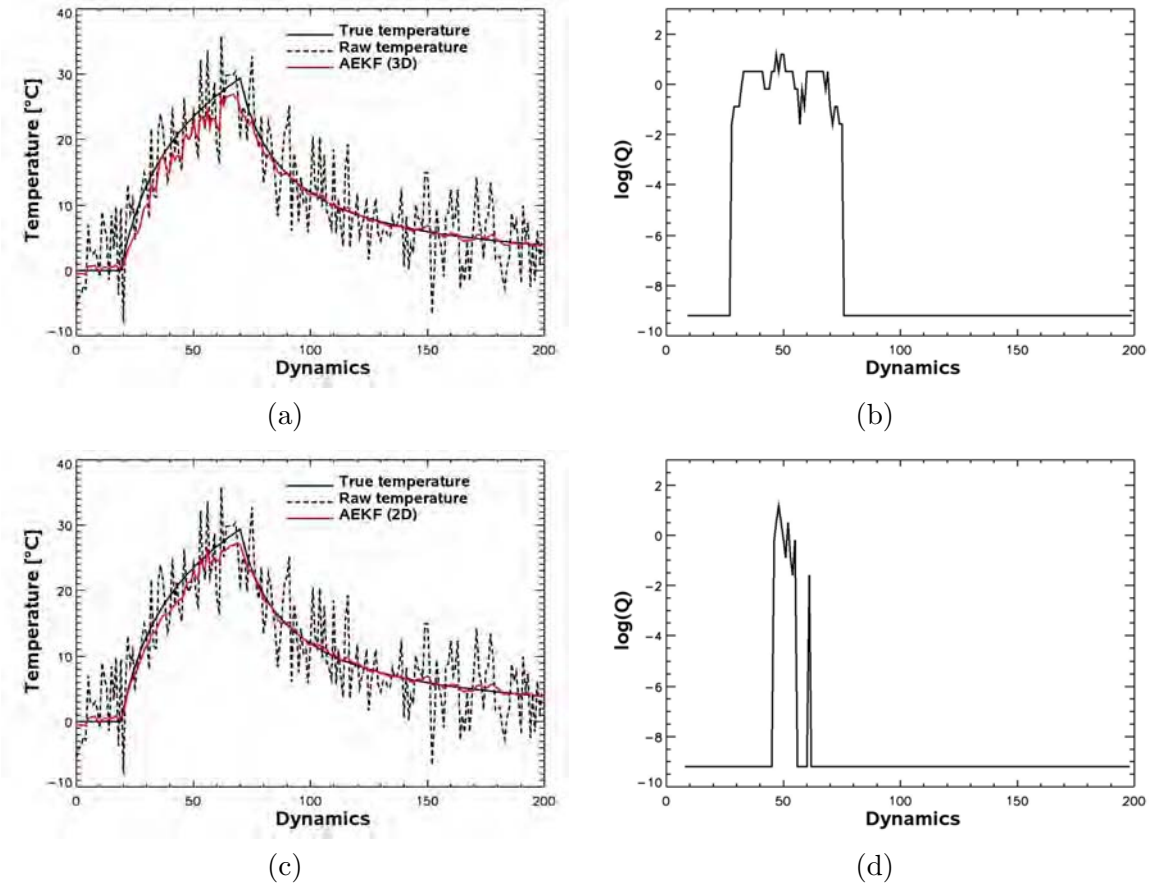

Figure 11.6: Effects of adaptive EKF using a 3D implementation of the BHTE model with a mis-configured absorption coefficient (of -50% of its true value) and the true diffusion coefficient (a,b) and a 2D implementation of the BHTE model with the true absorption and diffusion values (c,d). Filtered temperature curves are shown in (a,c) and the time optimized Q values are reported in b and d.

The influence of a 2D implementation of the AEKF was then evaluated with the true absorption and diffusion coefficients. The filtered temperature curve and optimized Q value are plotted 11.6c,d. This configuration is thus identical to the experiment shown in figure 11.1c. Similar tendencies, as observed with the 3D implementation, were observed with the 2D implementation. However, the time optimized Q values show strong fluctuations of the optimal Q value. In this case, the bias introduced by a 2D implementation (with the true coefficients) is lower than the bias associated with a 3D implementation (using a mis-configured absorption coefficient of -50% of its true value). Therefore, the AEKF needs more times (more dynamic images) to accumulate an accuracy bias superior to the imposed upper bound (ε_t). Once detected, the AEKF adapts the value of Q (with a higher value) to improve the confidence in the measurements which in turn allows to reset, after few images, the baseline bias of the model. Therefore, the AEKF starts again to improve its confidence in the model. This effect can be observed several times which results in oscillations in the time optimized Q values. However, when needed, high Q values correctly belong to the optimum interval [log(-2), log(1)] shown in 11.4a (red curve).

11.3.2 Heating experiment on an agarose gel phantom

The method was evaluated on an agarose gel phantom during a HIFU heating experiment (see figure 11.7). Dynamic MR-temperature imaging of an agarose gel phantom was

obtained with a gradient recalled single-shot echo-planar sequence (300 images, single slice, TR=106 ms, TE=36 ms, flip angle=40°, voxel size=1.7×1.7×3 mm^3, matrix=64×64). The HIFU heating protocol employed 50 W of electrical power to the HIFU transducer over a period of 40 s in a fixed point P.

A second HIFU heating was performed 20 mn later (once heat evacuation of the first experiment was completed) using a modified heating protocol. Here, the focal point position was electronically updated each TR/4 ms in four different locations (± 0.5 mm on each axis from the point P). The AEKF was then applied, using the BHTE configuration obtained from the first fixed point experiment (which is thus not adapted to the present case), in order to observe its performance with a deliberately mis-configured BHTE model.

Physical filter parameters (absorption and diffusion) were estimated using [168]. Since only 2D temperature maps were available, a 2D implementation of the AEKF was employed and compared with a matched Kaiser Bessel FIR.

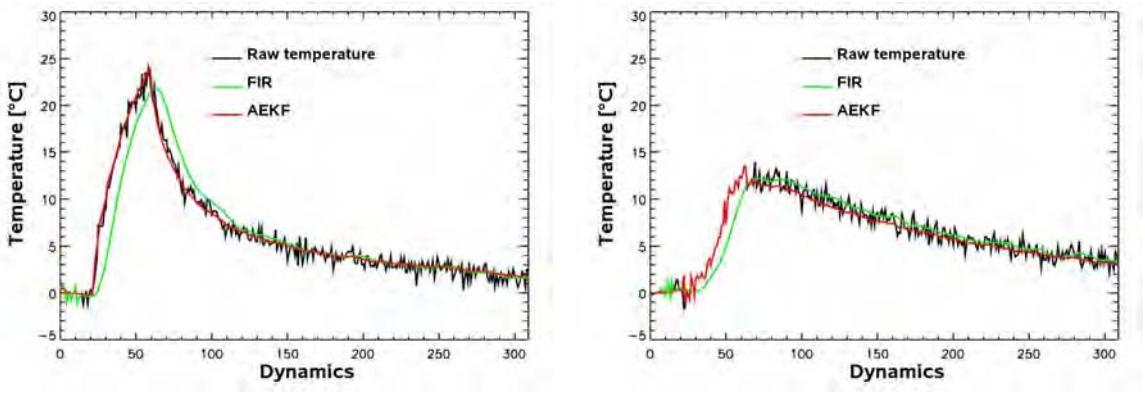

(a) (b)

Figure 11.7: Filtering performance of a FIR and the AEKF obtained on an agarose gel during heating experiments. (a) Temperature evolution obtained during the first heating experiment in the focal point using a properly configured BHTE based model. (b) Temperature evolution in the same point during the second heating experiment where four different locations where iteratively heated. The AEKF follows the measurements during the heat-up period since the model is incorrect but gains confidence during the cool-down period where the BHTE based model is correct.

The AEKF provided a better reduction of the temperature noise and did not introduce large latency as obtained with the FIR (see figure 11.7a). A second heating experiment was then realized with a different heating protocol where the focal point position was electronically updated on four different locations. The AEKF was run using the same configuration as in the fixed point experiment, which is thus expected to be incorrect for this experiment. The results are reported in figure 11.7b and show that the AEKF considers the model as incorrect during the heating period where the filter has a low confidence in the model. During the cooling period, the model is correct since only the heat diffusion is present (and is properly configured) and the filter strongly improves its confidence in the BHTE based model which results in a substantial reduction of the temperature noise. Again, the bias introduced by the latency of the FIR is avoided with the AEKF.

11.3.2.1 Heating experiment on an in-vivo porcine kidney

An MRI guided HIFU heating experiment was finally performed in vivo in the kidney of a pig under general anesthesia (see figure 11.8). MRI guided HIFU heating was performed

in vivo in the kidney of a pig under general anesthesia. Since the kidney was static during the experiment, no focal point position adjustment was required. Dynamic MR-temperature imaging employed the following sequence: 1500 dynamic sagittal images, one slice, TR=127 ms, TE=25 ms, flip angle=35°, FOV=142.5×285 mm^2, voxel size=3×3×6 mm^3. Heating was performed using 250 W of electrical power during a period of 19 s. After completion of the experiments the animal was euthanized by intravenous injection of Pentobarbital. The animal experiment was conducted in agreement with the French law on animal experimentation and in compliance with institution's rules for animal care and use.

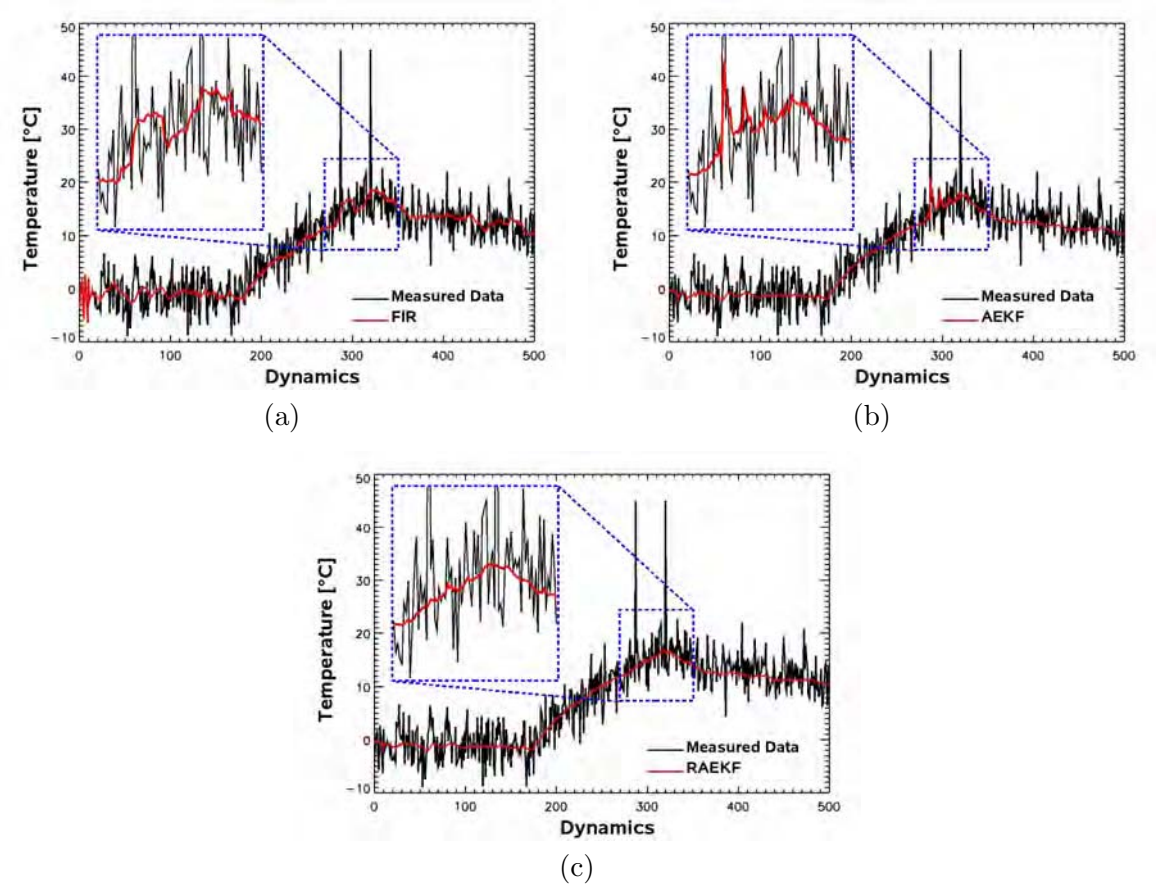

Figure 11.8: Temperature evolution of the HIFU experiment on an in-vivo porcine kidney using a (a) FIR filter, (b) the AEKF, (c) the robust AEKF. The robust AEKF allows to detect this strong temperature artifact as outlier and to replace it by the BHTE model prediction value.

A temperature elevation of 18°C was reached in the focal point. In order to evaluate the impact of large temperature artifacts on the filters, a second temperature dataset was derived from the initial temperature measurement including two large simulated temperature artifacts of 45 °C in the focal point. These types of artifact induced a strong perturbartion of both the FIR filter (figure 11.8a) and the AEKF (figure 11.8b). Note that the AEKF was much more influenced by the first temperature artifact since the adaptation of Q provided a higher value in the corresponding dynamic. The robust AEKF approach allowed to detect these two artifacted measures and the resulting filtered temperature was not affected (figure 11.8c). As a consequence, a variation of 75 % and 118 % of the measured thermal dose was observed between both experiments using the FIR and the AEKF respectively. The robust AEKF provided identical thermal dose values in both cases.

11.3.3 Real time benchmarking

The computation time of the EKF (using a dual processor, INTEL 3.1 GHz Penryn, two cores, 8 GB of RAM) was 0.71 ms for a 2D image of resolution 32×32 and 11.4 ms for a 3D image of resolution 32×32×16. In the AEKF, the additional time required for the autocalibration of the Q value is defined by the number of steps towards the optimum Q value. In our approach, an upper bound was imposed to the algorithm and was defined in order to fulfill the real time constraint.

11.4 Discussion and conclusions

11.4.1 BHTE model based temperature prediction

The performance of the BHTE model relies primarily on the accurate representation of the physical heating process. For this, it requires a priori knowledge of the exact form of the focal point $P_{(\vec{r},t)}$ and the local absorption and diffusion coefficients. In particular, the choice of the later two coefficients requires empirical data or a suitable calibration experiment. However, the spatial resolution of typical MR-sequences for interventional imaging is of the same order as the observed diffusion phenomena and focal point sizes leading to partial volume effects [169]. Therefore, a calibration results only in apparent absorption and diffusion coefficients, which will vary with increasing voxel sizes. Furthermore, although both apparent coefficients can be expected to be sufficiently homogeneous within large organs such as the liver, this assumption could break down in smaller heterogeneous tissues (e.g. tumors), or close to organ boundaries, where both become spatially variant. Another limitation of the predictor model arises from the negligence of the heat evacuation due to tissue perfusion. Although this is for the presented experiment on a gel of no consequence, future work on in-vivo tissue requires a careful assessment of the corresponding error bias and may have to take the perfusion term in equation (11.3) into account.

In addition, since the achievable MR-acquisition time severely limits the available volume coverage, the BHTE has to be in practice applied to 2D or severely undersampled 3D datasets. As shown in figure 11.5 the influence of a 2D implementation of the model is of little consequence as long as the spatial resolution in slice direction remains much larger than the characteristic diffusion length for the given temporal resolution of the MR-sequence.

Finally, the temperature prediction model is also directly influenced by the choice of the size (in mm) of the prediction area. A large area could prevent the real time use of the method (especially for the autocalibration that requires several temperature predictions to adjust the Q parameter). On the other hand, a small area may be insufficient to encompass the whole heated area introducing undesirable high frequencies in the Fourier domain that could be further reduced using apodization function. In the presented gel and in-vivo experiments being typical for clinical ablation, an area of 32×32 pixels with a pixel size in the range of a millimeter was found to be a good compromise.

11.4.2 Autocalibration performance of the EKF, dynamic evaluation of the BHTE model accuracy

Although the BHTE model is an efficient way to predict the temperature, the uncertainty of the model is a priori not known and was shown to vary over time (especially between heating and cooling). The autocalibration of the parameter Q allows to correctly handle the model accuracy of the proposed filter. Nevertheless, the autocalibration process is

influenced by two parameters: the spatial window size (M) and the temporal window size (N) employed to evaluate the filter accuracy (see equation (11.6)).

The spatial window size has to cover voxels contained in the ablation area and is thus subject to the influence of heat absorption and heat diffusion. In our experiment, 9 voxels around the focal point were selected for 2D experiments and 9 voxels of each of the two adjacent slices were included for 3D experiments (leading to a total of 27 voxels). Although the number of voxels prone to temperature increase can be limited in a fixed point heating experiment, this issue is expected to be clearly reduced for volumetric ablation (leading to a larger ablated area).

The temporal window size directly influences the frequency response of the proposed adaptation of Q. A large temporal window leads to stable convergence of the Q value, while introducing a latency on the Q adaptation. A small temporal window allows reactive adaptation of Q at the price of a reduced statistical sample contributing to equation (11.6). Consequently, this parameter has to be adjusted depending on the temporal dynamic of the temperature between two successive acquisitions. The auto-adaptation of Q allows to dynamically find the smallest Q value that maintains the introduced error bias of temperature below a predefined threshold defined by the ε parameter. This allows maximal measurement noise filtering under the condition of a guaranteed accuracy. For the case of a severely mis-configured filter, the auto-adaptation will give a higher emphasis on the measured data (high value of Q) in order to limit the introduced accuracy bias. In practice this means the filter will be less efficient for noise removal, however, a severely mis-configured filter will not introduce systematic errors in the filtered data.

11.4.3 Robust AEKF approach

In general, artifact detection is complicated by the requirement to find a robust criterion allowing to differentiate between a measurement artifact and changes due to the dynamic of the measured process. Since the proposed AEKF formalism employs the BHTE as a physical model for data prediction of the heating process, it is straightforward to seamlessly integrate a robust outlier detection without significant additional computational overhead. This is achieved by examining the innovation S_t for unphysical changes and to replace unphysical measurements by the predictor value T_t^-. Therefore, contrary to temporal filtering, where the amplitude of the artifacted datapoint still influences the amplitude of the filtered data (figure 11.8a,b), the proposed approach allows to replace the value entirely with a prediction based on the physical heating model (figure 11.8c). Furthermore, the proposed AEKF filter also accounts for the variations of the average model error during the heating process and thus conveniently allows to adjust the outlier rejection criterion by using the updated $\varepsilon(t-1)$ and $\sigma(S_{t-1})$ values.

11.4.4 Clinical aspects of temporal filtering of the temperature

The presented data have shown that due to the use of a physical model of the heating process, the AEKF performance surpasses the results of more simple filter designs. However, in order to evaluate the usefulness of the proposed AEKF for clinical applications, two other categories of requirements have to be considered: Patient safety aspects and real-world practicability. Since the proposed filter is intended for real-time MR-guidance of non-invasive HIFU ablations, additional latency and accuracy degradation can directly affect the success of the intervention and ultimately patient safety. Therefore, despite the fact that the BHTE model parameters are only available as coarse estimates prior to the intervention, the AEKF must be able to cope with a severe mis-configuration without impairing the accuracy of the filtered temperature values, as shown in figure 11.1c for the EKF. The AEKF filtering process was designed so that even a worst case scenario merely

results in an ineffective noise removal, without systematic errors introduced by the filter as shown in figures 11.6a and 11.7b. Furthermore, reliable temperature measurements are frequently hampered by the effects of occasional spontaneous motion events or instabilities/errors of the employed real-time data processing. As observed in figure 11.8a, a FIR filter can be severely disturbed by strong temperature artifact. This results in significant variation of the measured thermal dose (more than 75 % in the presented experiment) preventing its use as a reliable representation of the real delivered dose. On the contrary, the robust AEKF reliably identifies and removes such temperature artifacts by a model based estimate which avoid a systematic error bias of the final thermal dose value.

The proposed filter design is more complex than non-adaptive FIR or IIR filter designs, as a consequence the second important aspect is the practicability of its use. The main disadvantage of the proposed BHTE based AEKF is that the filter requires an approximate estimate of the absorption and the diffusion coefficients prior to the intervention. Both can be provided on an individual basis based on a low-power test shot as shown in [168]. Alternatively, since an adequate filter performance does not require the exact knowledge of either parameter, for standardized clinical scenarios such as uterine fibroid ablations, both values could be supplied based on averaged patient data. All other parameters of the filter are autocalibrated during the intervention, which reduces the risk of an arbitrary/empirical calibration by the user. Finally, although the AEKF implementation has a higher computational overhead than FIR or IIR designs, the benchmarking results show that the design is entirely compatible with the requirement of interventional guidance of high-framerate imaging associated with low processing latencies.

11.4.5 Conclusions

The proposed autocalibrated extended Kalman filter based on the bio-heat transfer equation was demonstrated to improve both precision and accuracy of MR-thermometry compared to simpler filter designs such as FIR-filters, without introducing undesired latency. Here, the maximal bias of accuracy introduced by the filter is defined by the choice of $\varepsilon_{threshold}$ and ensured by adapting the parameter Q. Therefore, with a severely misconfigured BHTE model, the AEKF will simply improve its confidence in the measure, resulting in a very little smoothing of the temperature, without giving rise to systematic errors.

In addition, the presence of large artifacts on temperature measurement is shown to strongly disturbs a FIR filter or an AEKF (especially if the Q optimization led to a non negligible confidence in the measurement). The resulting thermal dose is, in these cases, severely affected by a large bias preventing its use as a reliable criterion for the determination of tissue necrosis. Here, the robust AEKF allows the replacement of these sparse temperature measurement artifacts with BHTE prediction based estimates. This thus represents a promising approach to perform sustained MR-dosimetry over the whole intervention while ensuring and controlling patient safety.

Conclusion

Methodological developments have been proposed in this part to improve the performance of the processing steps employed for MR-thermometry and dosimetry calculations. Novel algorithms have been developed to address the problem of motion estimation with:

- The presence of structures appearing transient in the FOV, potentially occurring with reduced FOV imaging or out-of-plane motion.
- The presence of high intensity variations, potentially occurring during hyperthermia.

A solution was proposed for the correction of magnetic susceptibility variation in presence of spontaneous motion. Finally, the use of physical models (the linear model of phase variations with motion and the BHTE model) as an additional source of information allowed to propose:

- A novel criterion for motion estimation assessment.
- A novel temporal filter using the Kalman filtering formalism.

In this part, the limitations discussed in part II have been successfully addressed. However, to improve the reliability of the therapeutic intervention, further methodological developments should be carried out. Therefore, the potential perspectives of these researches and a summary of the contributions of this thesis are now discussed in the general conclusion of this manuscript.

Part IV

General conclusions and perspectives

11.5 Technical and methodological contributions

The objective of this thesis was to improve the existing methodology designed for MR-guided thermal ablation of mobile organs and to ensure the feasibility in using the new methods for real time applications. State-of-the-art motion compensated MR-thermometry and dosimetry strategies were generally limited to a framerate of 1 Hz. However, this framerate is insufficient to efficiently follow the displacement of an organ for a HIFU beam steering application. Therefore, prediction algorithms had to be employed for anticipation and interpolation, to increase the sampling of the displacement trajectory. Nevertheless, these algorithms show generally a poor prediction performance when applied over extended periods above a second. To overcome these limitations, a fast (subsecond) MR-thermometry and dosimetry pipeline has been developed in this thesis and existing methodology improvements have been proposed. A brief summary of the contributions of this thesis together with perspectives are presented in the following.

Real time implementation of state-of-the-art methodology for fast MR-thermometry and dosimetry

An efficient pipeline designed for very fast (10-15 Hz) motion compensated MR-thermometry and dosimetry of mobile organs has been proposed. The combination of fast MR-acquisition schemes to minimize intra-scan motion artifacts, together with an efficient processing pipeline designed to compensate for inter-scan motion and motion related magnetic susceptibility variations has been implemented for abdominal organs and the heart. In addition, the potential of GPU programming has been demonstrated to be well suited for the parallelization of image processing steps and represents a convenient way to ensure the real time condition and short latency with affordable commodity hardware. Finally, the potential of the proposed pipeline has been shown for several applications, such as target tracking for HIFU beam steering.

Novel approaches for motion estimation and compensation

Two main improvements have been proposed for the motion estimation process.

First, the presence of structures appearing transient (a situation occasionally encountered using reduced field of view imaging, for example) has been demonstrated to disturb optical flow algorithms. This problem has been addressed using a constrained motion estimation method. This method has been shown to improve the accuracy of motion estimates in both the kidney and the heart.

Second, the performance of the motion estimation process during hyperthermia was found biased by intensity variations induced by the heating process, and more precisely by the variation of the relaxation time T_1 and T_2 of the tissue. A solution has been proposed integrating the temperature, which is the physical cause of the intensity variation, into the formulation of the motion estimation problem. This method has been found to be well suited for motion estimation during hyperthermia and showed better performances than currently employed methods.

Novel hybrid approach for the correction of motion related magnetic susceptibility variations

Two approaches emerged recently for the correction of motion related magnetic susceptibility variations: the multi-baseline and the referenceless approaches. However, due to the duration of a typical intervention, spontaneous motion of the patient is likely to occur. This is problematic for the correction of motion related magnetic susceptibility variations using a multi-baseline approach. Therefore, a hybrid method, which takes advantage of

both multi-baseline and referenceless methods, was designed to handle such spontaneous motion events.

Novel criterion for motion estimation assessment

Automatic assessment of the accuracy of the estimated motion is for in-vivo data a challenging task. Existing criteria for such an assessment are generally based on the analysis of the magnitude images. These approaches exploit the similarity of both reference and registered magnitude images. In this thesis, these approaches have been demonstrated to be limited, especially for images suffering from low SNR. Therefore, a novel criterion has been proposed, based on phase image analysis. It relies on a physical model relating organ motion and magnetic susceptibility variations. Since in clinical practice, amplitude and complexity of organ motion or the SNR may vary between patients, an auto-calibration of the adjustable parameters of the motion estimation process has been presented using the proposed criterion. The resulting motion estimation was significantly improved when auto-calibrated with the proposed criterion compared to state-of-the-art criteria.

Temporal temperature filtering

With all temperature maps being registered in real time to a common reference position, the integration of a temporal filter has been proposed to reduce the measurement noise. However, non adaptive temporal filters such as IIR or FIR, generally introduce a latency which can generate a (not controlled) penalty of accuracy when a fast varying system is observed, and may, as a result, impair patient safety. Since this is not acceptable for clinical applications, a novel temporal filter has been proposed, exploiting the Kalman filtering theory. It combines temperature measurement and a prediction based on a physical model of the heat transfer in biological tissues. This filter was designed to improve the precision while controlling the potentially introduced accuracy penalty, using a dynamic adjustment of the confidence in the model. Consequently, in the case of a severely mis-configuration of the physical model, the filter simply follow the measurements without smoothing of the noise, preventing the introduction of large systematic errors. In addition, sparse artifacts on the temperature measurements of large amplitude are known to disturb typical FIR filters. Therefore an outlier detection was added to the filter to identify these artifacts and replace these values with model predictions. These artifacts were found to be correctly removed using this robust approach. Therefore, this filter represents an efficient way to improve the reliability of the thermal dose evaluation which is directly employed for the prediction of tissue necrosis, and thus to maintain patient safety.

11.6 Perspectives

Methodological aspects

In this thesis, we showed that MR-thermometry on mobile organs can be achieved with a precision of 1°C in abdominal organs and 2-3°C in the heart, which is well suited to control thermal therapies in the area of interest. However, several methodological aspects of the intervention may still be improved and are now presented.

Motion estimation improvement

Improvement of the spatial coverage in the third dimension may allow to perform real 3D motion estimation and compensation. This would be promising to address the problem of out of plane motion encountered when 2D imaging is used to observe complex 3D motions.

In addition, the presence of large vessels may also disturb the motion estimation process and especially local motion estimation algorithms. The proposed criterion designed to assess the quality of the motion estimation represents a promising way to detect such problematic areas. Then, the proposed optical flow formulation designed to discard pixels affected by intensity variation (induced by temperature elevation) could be adapted to reject such areas from the motion estimation process.

Moreover, in the presented works, the motion information is directly measured with help of MR-images, which limits the frequency of the measurements. The use of auxiliary information, that could be obtained for example using multi-modality imaging (such as MRI combined with ultrasound imaging), may allow to desynchronize the motion estimation process and the temperature mapping. This could allow for example to privilege the temporal resolution for motion estimation (required for beam steering application) and the spatial coverage for temperature mapping (required for volumetric control of the ablation). Auxiliary information could also be used to improve the employed slice tracking techniques.

Towards a 3D monitoring of the intervention

A 3D monitoring and control of the delivered energy should improve the patient safety during the intervention. This would allow to prevent undesired heating and to optimize the spatio-temporal energy delivery. Since MR-systems now allow to modify dynamically the sequence parameters, this offers new perspectives to achieve a 3D volume coverage using adaptive imaging methods such as a slice sweep methodology. However, this approach reduces the temporal resolution of the temperature measurement by the number of slices in the sweep direction. Results obtained with the proposed autocalibrated extended Kalman filter open great perspectives to overcome this limitation. The proposed formalism could be used to simultaneously remove measurement noise (in currently acquired slice) and predict the temperature at unmeasured locations (other slices). This would allow to achieve a full 3D temperature mapping using a sparse sampling technique.

Improvement of spatial and temporal resolutions

For thermal ablations of thin tissues such as in the heart or the use of high precision HIFU transducers, partial volume effects are expected to bias MR-thermometry accuracy. Therefore, the improvement of the spatial resolution appears mandatory and several strategies could be employed for this purpose.

Among those, reduced field of view imaging techniques can be used. However it imposes new challenges on the motion estimation process, due to the potential presence of structures appearing transient in the field of view. Nevertheless, this problem has been demonstrated to be efficiently addressed using the proposed constrained motion estimation.

High field MRI allows to improve the SNR. This gain can be invested to increase either the spatial and / or the temporal resolution while preserving image quality. However, both inhomogeneities of the magnetic field and distortions are also stronger at high field. Therefore, the balance between improved SNRs and additional artifacts has to be carefully evaluated in future studies.

Quality control of the intervention and patient safety

To guarantee patient safety and to improve the reliability of the treatment, quality control should be developed and integrated into the processing pipeline.

Prior modeling of the intervention could be used for this purpose. This represents a promising way to detect abnormal or unexpected situations during the therapeutic treatment. For example, unexpected or undesired spatial deposition of the energy can occur if secondary lobes are created along the HIFU beam path. This type of event, engaging the patient safety, could be detected by comparing measured data with model predictions.

The availability of independent measures for a given task and their degree of similarity may also be used as an indicator of the reliability of the result. Multi-modality imaging could provide such independent measures. Alternatively, simultaneous corrections of any processing step using several methods may also furnished such redundant information. Therefore, the methods developed in this thesis, may also be used for quality control purpose.

Clinical perspectives

MR-guided HIFU-ablation of abdominal organs

Nowadays, all main obstacles for MR-guided HIFU-ablation of abdominal organs have been addressed in in-vivo and ex-vivo studies. The main task of the integration of these isolated, and in some cases contradictory, approaches into a clinical package, now remains to be developed, including the methods developed in this thesis. For example, the treatment of the liver would require the integration of methods for inter-costal firing and volumetric monitoring as well as feedback control of the intervention.

MR-guided RF-ablation in the heart

MR-guided RF-ablation in the heart remains a much more challenging application. The presented study shows encouraging results of MR-thermometry and dosimetry in the heart with a precision in the range of 2-3 degrees. Although these experiments were carried out in the left ventricle, the final target is the atrium which is much more challenging since its thickness of 1 to 3 mm exceeds the voxel size of current employed sequences. Therefore, although the spatial resolution will have to be improved, the required spatial and temporal resolution needed for monitoring/guiding atrial wall interventions still remain to be investigated. Potential methodological solutions to improve spatial and temporal resolutions have been previously discussed in this conclusion. Furthermore, the feasibility of the presented methodology in presence of arrhythmia remains to be investigated before clinical studies can be anticipated.

Part V

Appendices

Appendix A

MR-image reconstruction

A.1 MR-acquisition in k-space

MRI is based on the interaction of nuclei magnetic spin with an external magnetic field. To allow the localization of a spin, magnetic field gradients are applied in each spatial dimension of the imaging plane/volume [170]. This renders the phase, of the recorded NMR-signal, spatially dependent. Therefore, the NMR-signal S of infinitesimal small sample at the point $\vec{r}$ in a MRI-system (referred to as magnetization) is a complex value that can be defined as follows:

$$S(\vec{r}) = \rho(\vec{r}) \cdot e^{-i2\pi\vec{k}\vec{r}} \tag{A.1}$$

where $\rho(\vec{r})$ is called the spin-density function, which describes the macroscopic object, and $e^{i\vec{k}\vec{r}}$ is the spatial dependent phase of the NMR signal. $\vec{k}$ represents the accumulated phase between excitation (at time $t' = 0$) and acquisition (at time $t' = t$) and is defined as follows:

$$\vec{k}(t) = \gamma \int_0^t \vec{G}(t')dt' \tag{A.2}$$

where γ is the gyromagnetic ratio and $\vec{G}(t')$ is the amplitude of the magnetic field gradient applied at time t$'$.

An NMR detection coil receives a signal $S(\vec{k})$, which corresponds to the ensemble of all signal sources $S(\vec{r})$ within the object as follows:

$$S(\vec{k}) = \int_{allspace} S(\vec{r})d\vec{r} \tag{A.3}$$

$$= \int_{allspace} \rho(\vec{r}) \cdot e^{-i2\pi\vec{k}\vec{r}}d\vec{r} \tag{A.4}$$

In order to obtain an image of the macroscopic object, we can perform a theoretical experiment where we repeat this measurement under the application of all possible magnetic field variations $\vec{G}$. This infinite amount of measurements would result in the complete description of $S(\vec{k})$, the so called k-space.

A.2 Reconstruction from k-space to spatial space

The k-space contains all necessary information for the reconstruction of an image of the original object. This can be shown by applying an inverse Fourier transformation (FT^{-1}):

$$FT^{-1}(S(\vec{k})) = \int_{\vec{k}} S(\vec{k}) \cdot e^{2\pi i \vec{k}\vec{r}} d\vec{k} \tag{A.5}$$

$$= \int_{\vec{k}} \int_{allspace} \rho(\vec{r'}) \cdot e^{-2\pi i \vec{k}\vec{r'}} \cdot e^{2\pi i \vec{k}\vec{r}} dr' d\vec{k} \tag{A.6}$$

$$= \int_{allspace} \rho(\vec{r'}) \left(\int_{\vec{k}} e^{-2\pi i \vec{k}(\vec{r'}-\vec{r})} d\vec{k} \right) dr' \tag{A.7}$$

$$\tag{A.8}$$

Using the definition of the Dirac delta function,

$$\delta(\vec{r'} - \vec{r}) = \int_{\vec{k}} e^{-2\pi i \vec{k}(\vec{r'}-\vec{r})} d\vec{k} \tag{A.9}$$

the Fourier transform of the acquired signal can be written as:

$$FT^{-1}(S(\vec{k})) = \int_{allspace} \rho(\vec{r'}) \delta(\vec{r'} - \vec{r}) dr' \tag{A.10}$$

$$= \rho(\vec{r}) \tag{A.11}$$

Therefore, the inverse Fourier transform of the acquired NRM-signal provides a spatial representation of the spin density, which is the mathematical representation of the macroscopic object.

Since in practice, an infinite amount of measurements is not possible, only a finite number of k-space points can be acquired. The resulting imperfect sampling of k-space $S_r(\vec{k})$ can be mathematically expressed with the help of the optical transfer function O:

$$S_r(\vec{k}) = O(\vec{k}) \cdot S(\vec{k}) \tag{A.12}$$

The inverse Fourier transform of $S_r(\vec{k})$ reads:

$$FT^{-1}(S(\vec{k})) = \int_{\vec{k}} O(\vec{k}) \cdot S(\vec{k}) \cdot e^{-i\vec{k}\vec{r}} d\vec{k} \tag{A.13}$$

$$= \int_{\vec{k}} \int_{allspace} O(\vec{k}) \cdot \rho(\vec{r'}) \cdot e^{i\vec{k}\vec{r}} \cdot e^{-i\vec{k}\vec{r}} dr' d\vec{k} \tag{A.14}$$

$$= \int_{allspace} \rho(\vec{r'}) \left(\int_{\vec{k}} O(\vec{k}) \cdot e^{i\vec{k}(\vec{r'}-\vec{r})} d\vec{k} \right) dr' \tag{A.15}$$

$$\equiv \int_{allspace} \rho(\vec{r'}) \cdot H(\vec{r'} - \vec{r}) dr' \tag{A.16}$$

$$\equiv \rho(\vec{r}) \otimes H(\vec{r}) \tag{A.17}$$

where $H(\vec{r'} - \vec{r})$ is defined as the pointspread function (PSF) and corresponds to the inverse Fourier transform of the optical transfer function. This means that in the case of a real imaging experiment, obtaining a limited amount of discrete sampling points, we do not obtain the true spin-density function anymore but instead the convolution of the spin density function with the PSF.

A.2.1 Finite continuous sampling of k-space

In practical case, one cannot acquire the signal for an infinity of values of k. Therefore, the k-space coverage is limited and the maximum k_{max} and minimum values k_{min} of k are defined by the maximum gradient amplitude $\|G_{max}\|$ and the application time t_{max} of the gradient as follows:

$$k_{max} = -k_{min} = \gamma \int_0^{t_{max}} \overrightarrow{G_{max}}(t')dt' \tag{A.18}$$

In such case, the optical transfer function O can be represented as a rectangular function of width $W = k_{max} - k_{min}$ and centered in $k = 0$ as illustrated in figure A.1a. The PSF function H is thus a sinc function with a full width at half maximum equal to $1/(W)$, which defines the real resolution of the MR-acquisition (see figure A.1b).

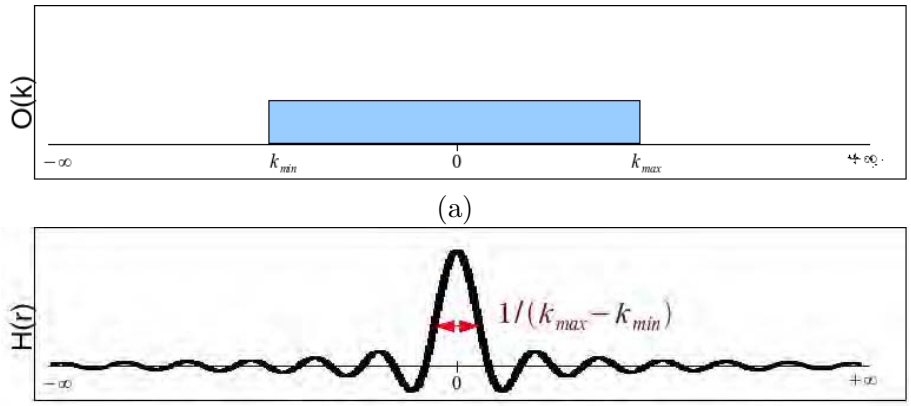

Figure A.1: Effect of a finite sampling of k-space: Optical transfer function O is shown in (a) and the corresponding PSF H is represented in (b).

A.2.2 Finite discrete sampling of k-space

In addition, in practical case a continuous sampling from k_{min} to k_{max} is not feasible and only a discrete sampling of this interval can be realized. This sampling pattern is illustrated in figure A.2 using Δk as the period between each k-space measurement and N as the number of measurements. Therefore, the sampling function can be seen as a collection of Dirac delta functions. The discrete Fourier transform of the sampling function thus provides N replications of the sinc function. In such conditions, the period of the sinc functions is equal to $(1/\Delta k)$ which in turn defines the field of view (FOV) of the imaging experiment. In our illustration, we assume Δk chosen to obtain a FOV equal to the object size. Therefore, during the convolution process, only one point contained in the object is used for each convolution kernel computation, which results in N repetitions of the object. The first period of the reconstructed signal is generally calculated as the reconstructed image.

A.3 Reconstruction from undersampled k-space to spatial space

In Chapter 4, we employed parallel imaging techniques for accelerating the MR-acquisition. These strategies rely on a partial acquisition of k-space. Since a direct reconstruction of the data would lead to fold-over artifacts, more sophisticated reconstruction methods are

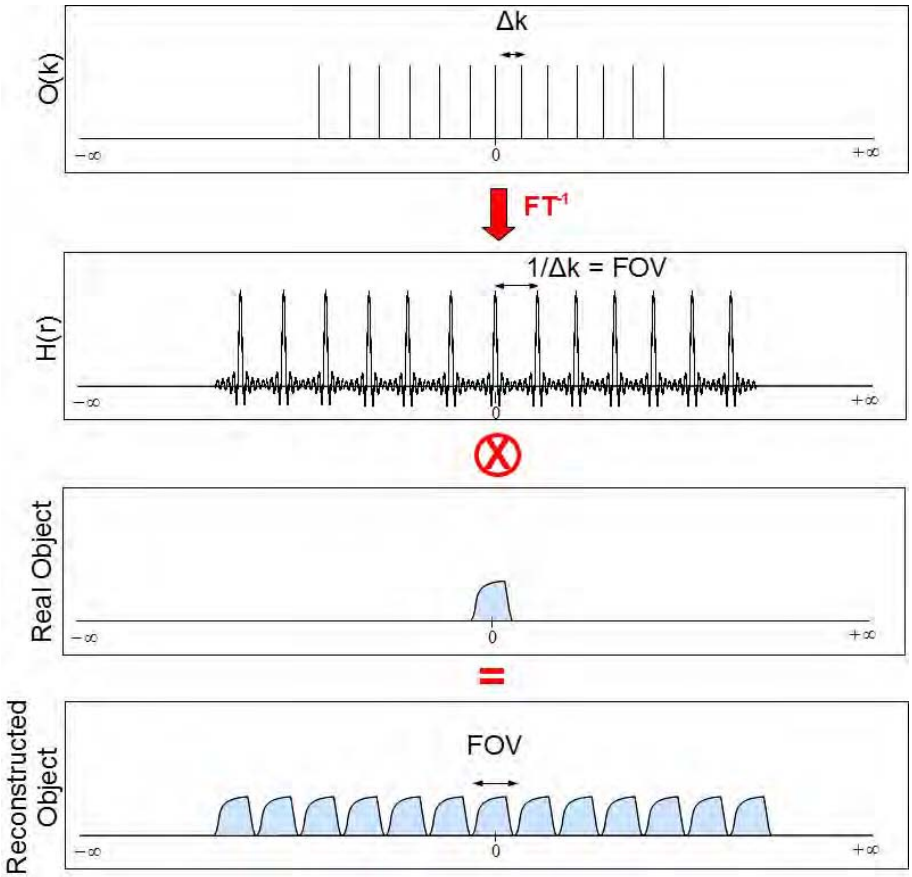

Figure A.2: Full sampling of k-space and reconstruction. Here $1/\Delta k$ is chosen as the object size, therefore, the distance between two delta peak in $H(\vec{r})$ is equal to the FOV.

employed that use several different receiver coils to acquire the signal simultaneously. Here, an explanation of the presence of fold-over artifacts in such conditions is explained using the mathematical formulation of the optical transfer function and the PSF.

The effect of a partial k-space acquisition is illustrated in the special case where only every other line is acquired (see figure A.3). Compared to figure A.2, the period of the Dirac delta functions in O is thus increased by a factor 2. Therefore, the resulting PSF contained a replication of the sinc function with a period reduced by a factor 2. Consequently, during the convolution process, two different points contained in the object are systematically averaged for each convolution kernel computation, which generates fold-over artifacts.

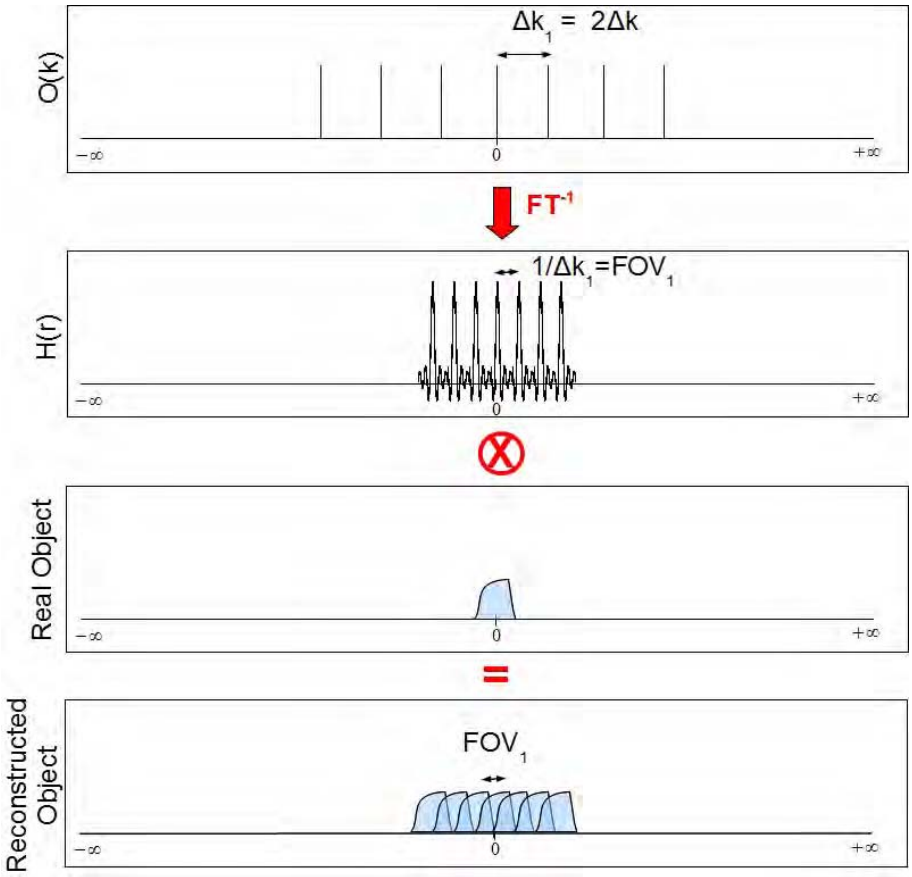

Figure A.3: Partial sampling of k-space and reconstruction. Since the sampling step of $O(\vec{k})$ is increased by a factor 2, the period of $H(\vec{r})$ is reduced by a factor 2, which leads after the convolution step to fold over artifacts.

Appendix B

Statistical hypothesis testing

As described in chapter 9, statistical tests have been employed to determine if the differences obtained with several experiments were statistically significant. In the presented works, means of measurement groups obtained from different experiments have been compared using ANOVA test and Student's t-test. These statistical tests are now described in detail in this appendix. They evaluate, with a level of significance p, the null hypothesis that can be formulated in our case as: "there is no significant difference between the means of the compared groups". However, these tests can typically lead to two different types of errors:

- type I error: The null hypothesis is rejected even though it is true.
- type II error: The null hypothesis is not rejected even though it is false.

These statistical tests are now described.

B.1 Student's t-test

For the specific case of comparing two different measurement groups, a Student's t-test can be employed [171]. This test differs if the two samples are dependent (paired) or independent. In our application described in chapter 9, we intended to compare the results of the motion estimation process with different methods over a group of volunteer. Therefore, there is every reason to suspect that the specific amplitude of the organ motion or the SNR associated to each volunteer experiment may influence the result. There, the results for a given volunteer can be considered as dependent, thus the dependent (paired) t-test has been employed and is now described.

The general form of a paired t-test is defined as follows:

$$t_{stat} = \frac{\overline{Y_d}}{\sigma_d \cdot \sqrt{(n)}} \tag{B.1}$$

where $\overline{Y_d}$ and σ_d are the average and the standard deviation of the differences between in each paired values and n is the number of samples of each group. Note that this statistic has a degree of freedom $d = n - 1$.

The probability density function of the Student's t-distribution is defined as follows:

$$f(t) = \frac{\Gamma\left(\frac{d+1}{2}\right)}{\sqrt{d\pi}\Gamma\left(\frac{d}{2}\right)} \left(1 + \frac{t^2}{d}\right)^{-(d+1)/2} \tag{B.2}$$

with Γ the gamma function defined as $\Gamma(x) = (x-1)!$.

The probability for the acceptance of the null hypothesis is thus given by:

$$p_{stat} = \int_{t_{stat}}^{\infty} f(t)dt \tag{B.3}$$

If $p_{stat} < p$, the null hypothesis is rejected and the difference between the two groups is considered as statistically significant. On the other hand, there is no significant difference between the means of the compared groups if $p_{stat} \geq p$.

B.2 ANOVA test

For the comparison of more than two groups of samples, an ANOVA test [172] can be employed. This test can be seen as a generalization of the t-test, which aims to differentiate the overall variance σ^2 of all measurements into two terms: The inter-group variance σ_I^2 and the within-group variance σ_W^2. Therefore, with K groups one can write:

$$\begin{aligned} \sigma^2 &= \sum_{i=1}^{K}\sum_{j=0}^{n_i} \frac{\left(Y_{ij} - \bar{Y}\right)^2}{N} \\ &= \sigma_I^2 + \sigma_W^2 \\ &= \sum_{i=1}^{K} \frac{n_i \left(\bar{Y}_i - \bar{Y}\right)^2}{N\,(K-1)} + \sum_{i=1}^{K}\sum_{j=0}^{n_i} \frac{\left(Y_{ij} - \bar{Y}_i\right)^2}{(N-K)} \end{aligned} \tag{B.4}$$

$$\tag{B.5}$$

where Y_{ij} is the j^{th} observation in i^{th} group, $\bar{Y}_i$ is the sample mean in i^{th} group ,$\bar{Y}$ is the sample mean in group, n_i is the number of samples in i^{th} group and N is the overall sample size.

The F-statistic is then defined as follows

$$F_{\text{stat}} = \frac{\sigma_I^2}{\sigma_W^2} \quad . \tag{B.6}$$

and the probability for the acceptance of the null hypothesis is given by:

$$p_{stat} = \int_{F_{stat}}^{\infty} f(x)dx \tag{B.7}$$

with f(x) the probability density function of the F-distribution defined as follows:

$$f(x) = \frac{\sqrt{\dfrac{(d_1 x)^{d_1}\, d_2^{d_2}}{(d_1 x + d_2)^{(}\, d_1 + d_2)}}}{x B\left(d_1/2, d_2/2\right)} \tag{B.8}$$

where $d_1 = K - 1$ and $d_2 = N - K$ are the degrees of freedom under the null hypothesis and B denotes the Beta function defined as $B(x, y) = \int_0^1 t^{x-1}(1-t)^{y-1}dt$.

The null hypothesis is thus rejected if $p_{stat} < p$ and additional t-tests between all pairs of groups have to be realized to determine which differences are statistically significant. If $p_{stat} \geq p$, no significant difference is present between all groups.

B.3 Bonferroni correction

The risk of committing a type I error increases with the number of tested hypothesis n. Therefore, correction methods have been developed to address the problem of multiple comparisons. The Bonferroni method correct this effect by testing each hypothesis with a significance level reduced by the factor $1/n$ [173, 174]. This method reduces the risk of a type I error but increases the probability of committing a type II error.

Appendix C

Minimization of a functional

The presented variational techniques for motion estimation purpose (as presented in chapter 2, section 2.1.3.2 and used in chapter 5, 7, 8 and 9) often rely in the minimization of a functional. In this appendix, an introduction to functional minimization based on the calculus of variation and Euler Lagrange equations [175] is given.

Let note F a functional defined on $C^2_{[a,b]}$ as follows:

$$F(g(x)) = \int_a^b f(x, g(x), g'(x))dx \tag{C.1}$$

where $g(x) : [a, b] \mapsto \mathbb{R}$ with $g(x) \in C^1_{[a,b]}$

Calculus of variation is a set of method that aims to find a function $g(x)$ that corresponds to extreme values of F.

C.1 Introduction to calculus of variation & Euler Lagrange equations

If $g(x)$ minimized F, therefore,

$$F(g(x)) \leq F(z(x)) \tag{C.2}$$

for any other function $z(x)$. The main idea of this approach consist in constructing a function $z(x)$ as follows:

$$z_\varepsilon(x) = g(x) + \varepsilon h(x) \tag{C.3}$$

where $h(x)$ is a real valued function and $h(x) \in C^2_{[a,b]}$ with $h(a) = h(b) = 0$.

Therefore, the derivative of $F_\varepsilon(z_\varepsilon(x))$ for $\varepsilon = 0$ has to be zero (since $F(g(x))$ is a minimum of F and has therefore a derivative equal to zero):

$$\frac{\partial F(z_\varepsilon(x))}{d\varepsilon}\Big|_{\varepsilon=0} = 0 \tag{C.4}$$

and is computed as follows:

$$\begin{aligned}\frac{d}{d\varepsilon}F(z_\varepsilon(x)) &= \frac{d}{d\varepsilon}\int_a^b f(x, z_\varepsilon(x), z'_\varepsilon(x))dx \\ &= \int_a^b \frac{\partial}{\partial\varepsilon} f(x, z_\varepsilon(x), z'_\varepsilon(x))dx\end{aligned}$$

By applying the chain rule law we obtain:

$$\frac{d}{d\varepsilon}F(z_\varepsilon(x)) = \int_a^b \frac{\partial f}{\partial x}\frac{\partial x}{\partial \varepsilon} + \frac{\partial f}{\partial z_\varepsilon}\frac{\partial z_\varepsilon}{\partial \varepsilon} + \frac{\partial f}{\partial z'_\varepsilon}\frac{\partial z'_\varepsilon}{\partial \varepsilon}dx \tag{C.5}$$

Since $\partial x/\partial \varepsilon = 0$, the equation can be reduced to

$$\frac{d}{d\varepsilon}F(z_\varepsilon(x)) = \int_a^b \frac{\partial f}{\partial z_\varepsilon}h(x) + \frac{\partial f}{\partial z'_\varepsilon}h'(x)dx \tag{C.6}$$

The integration by part rule says that if two function $l(x)$ and $m(x)$ are differentiable then:

$$\int_a^b l(x)m'(x) = [l(x)m(x)]_a^b - \int_a^b l'(x)m(x) \tag{C.7}$$

Therefore:

$$\frac{\partial f}{\partial z'_\varepsilon}h'(x) = [\frac{\partial f}{\partial z'_\varepsilon}h(x)]_a^b - \int_a^b \frac{d}{dx}\frac{\partial f}{\partial z'_\varepsilon}h(x)dx \tag{C.8}$$

Since $h(a) = h(b) = 0$, then, from equation (C.6) and (C.8), we obtain:

$$\frac{d}{d\varepsilon}F(z_\varepsilon(x)) = \int_a^b (\frac{\partial f}{\partial z_\varepsilon} - \frac{d}{dx}\frac{\partial f}{\partial z'_\varepsilon})h(x)dx \tag{C.9}$$

Based on equation (C.4) statement, equation (C.9) for ε=0 becomes:

$$\frac{\partial F(z_\varepsilon(x))}{d\varepsilon}\Big|_{\varepsilon=0} = \int_a^b (\frac{\partial f}{\partial g} - \frac{d}{dx}\frac{\partial f}{\partial g'})h(x)dx \tag{C.10}$$

Moreover, the fundamental lemma of calculus of variation states that, if a function $f(x)$ is a continuous in the interval $[a, b]$ and for every continuous function $h(x)$ with $h(a) = h(b) = 0$ we have:

$$\int_a^b f(x)h(x)dx = 0 \tag{C.11}$$

Then, $f(x)$ is identically zero on $[a, b]$. Therefore the fundamental lemma and equation (C.10) lead to

$$\frac{\partial f}{\partial g} - \frac{d}{dx}\frac{\partial f}{\partial g'} = 0 \tag{C.12}$$

C.2 Generalized form of Euler Lagrange equations

In the presented variational framework designed motion estimation purpose, the functional F generally has two function $u(x, y)$ and $v(x, y)$ and two variables x and y. $u(x, y)$ and $v(x, y)$ relates the horizontal and vertical displacement of each pixel of coordinate (x, y). Therefore, the presented Euler Lagrange has to be extended in this case two higher dimension. For this, a generalized version of Euler Lagrange equations has been developed [176] for a functional F defined by multiple functions $G = \{g1, g2, ..., gm\}$ with multiple variables $X = \{x_1, x_2, ..., x_N\}$.

The functional F is now defined as:

$$F(G(X))) = \tag{C.13}$$

$$\int ... \int_S f(x_1, ..., x_N, g1(x), ..., gm(x), g1_{x_0}, ..., g1_{x_N}, ..., gm_{x_0}, ..., gm_{x_N})dx_1...dx_N \tag{C.14}$$

where S relates the N dimensional region of the space defined by X and gi_{x_j} denotes the partial derivative of gi respect to x_j.

The generalized form of the Euler Lagrange equation is in such a case:

$$\begin{cases} \dfrac{\partial f}{\partial g1} - \displaystyle\sum_{k=0}^{m} \dfrac{\partial}{\partial x_k} \dfrac{\partial f}{\partial g1'_{x_k}} = 0 \\ \dfrac{\partial f}{\partial g2} - \displaystyle\sum_{k=0}^{m} \dfrac{\partial}{\partial x_k} \dfrac{\partial f}{\partial g2'_{x_k}} = 0 \\ \qquad\qquad \cdots \\ \dfrac{\partial f}{\partial gn} - \displaystyle\sum_{k=0}^{m} \dfrac{\partial}{\partial x_k} \dfrac{\partial f}{\partial gn'_{x_k}} = 0 \end{cases} \tag{C.15}$$

These equations are used for the minimization of the presented functionals with $M = 2$ (for u and v) and $N = 2$ (for x and y).

Appendix D

Optical flow derivation

This appendix describes the iterative scheme derivations of the employed and proposed variational techniques designed for motion estimation. In the first section, the initial derivation of the initial Horn & Schunck algorithm [70] (see chapter 2) is presented. In the last two sections, solution derivations for the motion estimation algorithms proposed in chapter 7 and chapter 8 of this thesis are developed.

D.1 Minimization of the Horn & Schunck functional

As described in chapter 2 (section 2.1.3.2), the general minimization problem proposed by Horn & Schunck is described with the following functional:

$$E = \iint_{xy} \left(\left[I_x u + I_y v + I_t \right]^2 + \alpha^2 \left[\|\nabla u\|_2^2 + \|\nabla v\|_2^2 \right] \right) dxdy \tag{D.1}$$

In this functional, we have two functions u and v with two variables x and y. Therefore, using the formalism developed in appendix C, this functional can be rewritten as follows:

$$E = \iint_{xy} f(x, y, u, v, u_x, u_y, v_x, v_y) dxdy \tag{D.2}$$

where $u_x = \partial u / \partial x$, $u_y = \partial u / \partial y$, $v_x = \partial v / \partial x$, $v_y = \partial v / \partial y$.

Its minimization can then be obtained using the calculus of variation and the Euler-Lagrange equations, as described in appendix C. The Euler Lagrange equations associated with the Horn & Schunck functional are thus:

$$\begin{cases} \dfrac{\partial f}{\partial u} - \dfrac{\partial}{\partial x}\dfrac{\partial f}{\partial u_x} - \dfrac{\partial}{\partial y}\dfrac{\partial f}{\partial u_y} = 0 \\ \dfrac{\partial f}{\partial v} - \dfrac{\partial}{\partial x}\dfrac{\partial f}{\partial v_x} - \dfrac{\partial}{\partial y}\dfrac{\partial f}{\partial v_y} = 0 \end{cases} \tag{D.3}$$

that gives the following system of equations:

$$\begin{cases} 2I_x(I_x u + I_y v + I_t) - 2\alpha^2 u_{xx} - 2\alpha^2 u_{yy} = 0 \\ 2I_y(I_x u + I_y v + I_t) - 2\alpha^2 v_{xx} - 2\alpha^2 v_{yy} = 0 \end{cases} \tag{D.4}$$

where $u_{xx} = \partial u_x / \partial x$, $u_{yy} = \partial u_y / \partial y$, $v_{xx} = \partial v_x / \partial x$ and $v_{xx} = \partial v_x / \partial x$.

The system can then rewritten as follows:

$$\begin{cases} I_x^2 u + I_x I_y v = \alpha^2 \Delta u - I_x I_t \\ I_x I_y u + \alpha^2 v = \alpha^2 \Delta v - I_y I_t \end{cases} \tag{D.5}$$

They proposed to approximate the Laplacian in the discrete domain with $\Delta u = \overline{u} - u$, with $\overline{u}$ the local average of u. This approximation allows to linearized the system as follows:

$$\begin{cases} (I_x^2 + \alpha^2)u + I_x I_y v = \alpha^2 \bar{u} - I_x I_t \\ I_x I_y u + (I_y^2 + \alpha^2)v = \alpha^2 \bar{v} - I_y I_t \end{cases} \tag{D.6}$$

The determinant D of the system is:

$$\Big\{ D = \alpha^2 (I_x^2 + I_y^2 + \alpha^2) \tag{D.7}$$

Solving this system for u and v using the Cramer's rule (which is described in appendix E) reads:

$$\begin{cases} u = \dfrac{(I_y^2 + \alpha^2)\bar{u} - I_x I_y \bar{v} - I_x I_t}{I_x^2 + I_y^2 + \alpha^2} \\ v = \dfrac{-I_x I_y \bar{u} + (I_x^2 + \alpha^2)\bar{v} - I_y I_t}{I_x^2 + I_y^2 + \alpha^2} \end{cases} \tag{D.8}$$

This equation holds for each pixel of the image and this equation for the i^{th} pixel can be rewritten as follows:

$$\begin{cases} u_i - \dfrac{(I_{y_i}^2 + \alpha^2)}{I_{x_i}^2 + I_{y_i}^2 + \alpha^2} \dfrac{1}{N_i} \displaystyle\sum_{j \in S_i} u_j + \dfrac{I_{x_i} I_{y_i}}{I_{x_i}^2 + I_{y_i}^2 + \alpha^2} \dfrac{1}{N_i} \sum_{j \in S_i} v_j &= -\dfrac{I_{x_i} I_{t_i}}{I_{x_i}^2 + I_{y_i}^2 + \alpha^2} \\ v_i + \dfrac{I_{x_i} I_{y_i}}{I_{x_i}^2 + I_{y_i}^2 + \alpha^2} \dfrac{1}{N_i} \displaystyle\sum_{j \in S_i} u_j - \dfrac{(I_{x_i}^2 + \alpha^2)}{I_{x_i}^2 + I_{y_i}^2 + \alpha^2} \dfrac{1}{N_i} \sum_{j \in S_i} v_j &= -\dfrac{I_{y_i} I_{t_i}}{I_{x_i}^2 + I_{y_i}^2 + \alpha^2} \end{cases} \tag{D.9}$$

where $\bar{u} = \frac{1}{N_i} \sum_{j \in S_i} u_j$, $\bar{v} = \frac{1}{N_i} \sum_{j \in S_i} v_j$ with $N_i = card(S_i)$ and S_i denotes the pixel area around the pixel i used to compute the average.

Therefore the calculation of u_i and v_i requires the calculation of all u_j and v_j and the general system to solve can be expressed as:

$$Ax = b \tag{D.10}$$

with

$$A = \begin{pmatrix}
1 & 0 & ... & & & & & & & & & \\
0 & 1 & ... & & & & & & & & & \\
 & & . & & & & & & & & & \\
 & & & . & & & & & & & & \\
 & & & & . & & & & & & & \\
0...0 & U_iV_i...U_iV_i & 0...0 & U_i & V_i & 1 & 0 & U_i & V_i & 0...0 & U_iV_i...U_iV_i & 0...0 \\
0...0 & U_iV_i...U_iV_i & 0...0 & U_i & V_i & 0 & 1 & U_i & V_i & 0...0 & U_iV_i...U_iV_i & 0...0 \\
 & & & & & & & . & & & & \\
 & & & & & & & & . & & & \\
 & & & & & & & & & . & & \\
 & & & & & & & & & ... & 1 & 0 \\
 & & & & & & & & & ... & 0 & 1
\end{pmatrix}$$

$$x = \begin{pmatrix} u_1 \\ v_1 \\ . \\ . \\ . \\ u_i \\ v_i \\ . \\ . \\ . \\ u_n \\ v_n \end{pmatrix} \text{ and } b = \begin{pmatrix} -I_{x_1}I_{t_1}/(I_{x_1}^2 + I_{y_1}^2 + \alpha^2) \\ -I_{y_1}I_{t_1}(I_{x_1}^2 + I_{y_1}^2 + \alpha^2) \\ . \\ . \\ . \\ -I_{x_i}I_{t_i}/(I_{x_i}^2 + I_{y_i}^2 + \alpha^2) \\ -I_{y_i}I_{t_i}/(I_{x_i}^2 + I_{y_i}^2 + \alpha^2) \\ . \\ . \\ . \\ -I_{x_n}I_{t_n}/(I_{x_n}^2 + I_{y_n}^2 + \alpha^2) \\ -I_{y_n}I_{t_n}/(I_{x_n}^2 + I_{y_n}^2 + \alpha^2) \end{pmatrix} \tag{D.11}$$

with $U_i = (I_y^2 + \alpha^2)/(I_x^2 + I_y^2 + \alpha^2)$ and $V_i = (I_x^2 + \alpha^2)/(I_x^2 + I_y^2 + \alpha^2)$

A is a very large and sparse matrix and Horn & Schunck proposed to use the Gauss Seidel method (which is described in detail in appendix E.1) in order to solve this system which is expected to be much more efficient than a Gauss elimination approach.

This approach provides an iteration scheme that leads to the solution as follows:

$$\begin{aligned}
u_i^{n+1} = \; & U_i \frac{1}{N_i}\Big(\sum_{j \in S_i, j<i} u_j^{n+1} + \sum_{j \in S_i, j>i} u_j^n\Big) \\
& - V_i \frac{1}{N_i}\Big(\sum_{j \in S_i} v_j^{n+1} + \sum_{j \in S_i} v_j^n\Big) \\
& - \frac{I_{x_i} I_{t_i}}{(I_{x_i}^2 + I_{y_i}^2 + \alpha^2)} \\
v_i^{n+1} = \; & V_i \frac{1}{N_i}\Big(\sum_{j \in S_i, j<i} v_j^{n+1} + \sum_{j \in S_i, j>i} v_j^n\Big) \\
& - U_i \frac{1}{N_i}\Big(\sum_{j \in S_i} u_j^{n+1} + \sum_{j \in S_i} u_j^n\Big) \\
& - \frac{I_{y_i} I_{t_i}}{(I_{x_i}^2 + I_{y_i}^2 + \alpha^2)}
\end{aligned} \tag{D.12}$$

Alternatively, one can also use the Jacobi approach (presented in appendix E.1) to solve the system. The only difference in the resulting iterative scheme will be the calculation of $\bar{u}$ and $\bar{v}$. In the Jacobi method, $\bar{u}^k$ and $\bar{v}^k$ are computed based only on values obtained at iteration $k-1$. In the Gauss Seidel approach, values of pixels of previous iteration (for pixels not yet treated at current iteration) and current iteration (for pixels already treated) are used to compute $\bar{u}$ and $\bar{v}$. This result in a faster convergence of the iterative scheme

and was privileged for CPU implementation. However, this approach is not parallelized and the Jacobi approach was employed for the GPU implementation. In order to simplify the notations, we consider $\bar{u}^n$ and $\bar{v}^n$ the average of u and v compute at iteration $n+1$ by any of these two methods. In such condition, the iterative numerical scheme can be rewritten as follows:

$$\begin{cases} u_i^{n+1} = \dfrac{(I_{y_i}^2 + \alpha^2)\overline{u_i}^n - I_{x_i} I_{y_i} \overline{v_i}^n - I_{x_i} I_{t_i}}{I_{x_i}^2 + I_{y_i}^2 + \alpha^2} \\ v_i^{n+1} = \dfrac{(I_{x_i}^2 + \alpha^2)\overline{v_i}^n - I_{x_i} I_{y_i} \overline{u_i}^n - I_{y_i} I_{t_i}}{I_{x_i}^2 + I_{y_i}^2 + \alpha^2} \end{cases} \tag{D.13}$$

that can be simplified into the famous solution:

$$\begin{cases} u^{n+1} = \overline{u}^n - I_x \dfrac{\overline{u}^n I_x + \overline{v}^n I_y + I_t}{I_x^2 + I_y^2 + \alpha^2} \\ v^{n+1} = \overline{v}^n - I_y \dfrac{\overline{u}^n I_x + \overline{v}^n I_y + I_t}{I_x^2 + I_y^2 + \alpha^2} \end{cases} \tag{D.14}$$

D.2 Minimization of the constrained optical flow functional

In this section, a detailed derivation of the iterative solution of the minimization of the functional proposed in chapter 7 is presented. As defined in equation (7.5), the functional E_c to minimize is defined as follows:

$$\begin{aligned} E_c(u,v) = &\iint \left(\left[I_x u + I_y v + I_t \right]^2 \right) dxdy \\ &+\alpha^2 \iint \left(\left[\|\nabla u\|_2^2 + \|\nabla v\|_2^2 \right] \right) dxdy \\ +\lambda^2 \iint &\left(\sum_{i=0}^{N} \left(\rho(d_i, R) \left[(u-u_i)^2 + (v-v_i)^2 \right] \right) \right) dxdy \end{aligned} \tag{D.15}$$

As presented for the derivation of the Horn & Schunck solution, the calculus of variation is employed in this case. Therefore, the Euler Lagrage equations provide the following system of equations:

$$\begin{cases} 2I_x(I_x u + I_y v + I_t) + 2\lambda^2 \sum_{i=0}^{N} \left(\rho(d_i, R) \left(u - u_i \right) \right) - 2\alpha^2 u_{xx} - 2\alpha^2 u_{yy} = 0 \\ 2I_y(I_x u + I_y v + I_t) + 2\lambda^2 \sum_{i=0}^{N} \left(\rho(d_i, R) \left(v - v_i \right) \right) - 2\alpha^2 v_{xx} - 2\alpha^2 v_{yy} = 0 \end{cases} \tag{D.16}$$

that can be simplified to:

$$\begin{cases} I_x^2 u + I_x I_y v = \alpha^2 \nabla u - I_x I_t - \lambda^2 \sum_{i=0}^{N} \left(\rho(d_i, R)(u - u_i) \right) \\ I_x I_y u + I_y^2 v = \alpha^2 \nabla v - I_y I_t - \lambda^2 \sum_{i=0}^{N} \left(\rho(d_i, R)(v - v_i) \right) \end{cases} \tag{D.17}$$

Using the approximation of the Laplacian as suggested by Horn and Schunck ($\nabla u = \overline{u} - u$) the system can be rewritten as:

$$\begin{cases} (I_x^2 + \alpha^2 + \lambda^2 \sum_{i=0}^{N} \left(\rho(d_i, R) \right))u + I_x I_y v = \alpha^2 \bar{u} - I_x I_t + \lambda^2 \sum_{i=0}^{N} \left(\rho(d_i, R)(u_i) \right) \\ I_x I_y u + (I_y^2 + \alpha^2 + \lambda^2 \sum_{i=0}^{N} \left(\rho(d_i, R) \right))v = \alpha^2 \bar{v} - I_y I_t + \lambda^2 \sum_{i=0}^{N} \left(\rho(d_i, R)(v_i) \right) \end{cases} \tag{D.18}$$

The determinant D of the system is:

$$\left\{ D = (\alpha^2 + \lambda^2 \sum_{i=0}^{N} \left(\rho(d_i, R) \right))(I_x^2 + I_y^2 + \alpha^2 + \lambda^2 \sum_{i=0}^{N} \left(\rho(d_i, R) \right)) \right. \tag{D.19}$$

Solving this system for u and v using the Cramer's rule reads:

$$\begin{cases} u = \frac{\alpha^2\left(I_y^2+\alpha^2+\lambda^2 S\right)\bar{u}-\alpha^2 I_x I_y \bar{v}-\alpha^2 I_x I_t+\lambda^2\left(\left(I_y^2+\alpha^2+S\right)S_{u_i}-I_x I_y S_{v_i}-I_x I_t S\right)}{(\alpha^2+\lambda^2 S)\left(I_x^2+I_y^2+\alpha^2+\lambda^2 S\right)} \\ v = \frac{\alpha^2\left(I_x^2+\alpha^2+\lambda^2 S\right)\bar{v}-\alpha^2 I_x I_y \bar{u}-\alpha^2 I_y I_t+\lambda^2\left(\left(I_x^2+\alpha^2+S\right)S_{v_i}-I_x I_y S_{u_i}-I_y I_t S\right)}{(\alpha^2+\lambda^2 S)\left(I_x^2+I_y^2+\alpha^2+\lambda^2 S\right)} \end{cases} \tag{D.20}$$

Again, this equations holds for each pixel of the image and leads to the same system as shown in equation (D.10) and (D.11) with:

$$\begin{cases} U_i = \frac{\alpha^2\left(I_y^2+\alpha^2+\lambda^2 S\right)}{(\alpha^2+\lambda^2 S)\left(I_x^2+I_y^2+\alpha^2+\lambda^2 S\right)} \\ V_i = \frac{\alpha^2\left(I_x^2+\alpha^2+\lambda^2 S\right)}{(\alpha^2+\lambda^2 S)\left(I_x^2+I_y^2+\alpha^2+\lambda^2 S\right)} \end{cases} \tag{D.21}$$

The resolution of this system is finally achieved using the Jacobi or the Gauss Seidel method (see appendix E.1) that provides the following iterative scheme:

$$\begin{cases} u^{n+1} = \frac{\alpha^2\left(I_y^2+\alpha^2+\lambda^2 S\right)\bar{u}^n-\alpha^2 I_x I_y \bar{v}^n-\alpha^2 I_x I_t+\lambda^2\left(\left(I_y^2+\alpha^2+S\right)S_{u_i}-I_x I_y S_{v_i}-I_x I_t S\right)}{(\alpha^2+\lambda^2 S)\left(I_x^2+I_y^2+\alpha^2+\lambda^2 S\right)} \\ v^{n+1} = \frac{\alpha^2\left(I_x^2+\alpha^2+\lambda^2 S\right)\bar{v}^n-\alpha^2 I_x I_y \bar{u}^n-\alpha^2 I_y I_t+\lambda^2\left(\left(I_x^2+\alpha^2+S\right)S_{v_i}-I_x I_y S_{u_i}-I_y I_t S\right)}{(\alpha^2+\lambda^2 S)\left(I_x^2+I_y^2+\alpha^2+\lambda^2 S\right)} \end{cases} \tag{D.22}$$

D.3 Minimization of the temperature regularized optical flow functional

In this section, the derivation of the solution to the minimization of the functional proposed in chapter 8 is detailed. In order to minimize the functional $E_{tr}(u, v)$ (see equation (8.1)) defined as:

$$E_{tr} = \iint \left(\beta(x,y)\left[I_x u + I_y v + I_t\right]^2 + \alpha^2\left[\|\nabla u\|_2^2 + \|\nabla v\|_2^2\right]\right) dxdy \tag{D.23}$$

we again use the calculus of variation where the associated Euler Lagrange equations reads:

$$\begin{cases} 2\beta(x,y)I_x(I_x u + I_y v + I_t) - 2\alpha^2 u_{xx} - 2\alpha^2 u_{yy} = 0 \\ 2\beta(x,y)I_y(I_x u + I_y v + I_t) - 2\alpha^2 v_{xx} - 2\alpha^2 v_{yy} = 0 \end{cases} \tag{D.24}$$

that can be simplified to:

$$\begin{cases} \beta(x,y)I_x^2 u + \beta(x,y)I_x I_y v = \alpha^2\nabla u - \beta(x,y)I_x I_t \\ \beta(x,y)I_x I_y u + \beta(x,y)I_y^2 v = \alpha^2\nabla v - \beta(x,y)I_y I_t \end{cases} \tag{D.25}$$

Using again the same approximation of the Laplacian as employed in the two previous sections, we obtain the following system:

$$\begin{cases} (\beta(x,y)I_x^2 + \alpha^2)u + \beta(x,y)I_x I_y v = \alpha^2\bar{u} - \beta(x,y)I_x I_t \\ \beta(x,y)I_x I_y u + (\beta(x,y)I_y^2 + \alpha^2)v = \alpha^2\bar{v} - \beta(x,y)I_y I_t \end{cases} \tag{D.26}$$

The determinant D of the system is:

$$\Big\{ D = \alpha^2(\beta(x,y)(I_x^2 + I_y^2) + \alpha^2) \tag{D.27}$$

Solving this system for u and v using the Cramer's rule and dividing equation by α^2 reads:

$$\begin{cases} u = \dfrac{(\beta(x,y)I_y^2 + \alpha^2)\bar{u} - \beta(x,y)I_xI_y\bar{v} - \beta(x,y)I_xI_t}{(\beta(x,y)(I_x^2 + I_y^2) + \alpha^2)} \\ v = \dfrac{-\beta(x,y)I_xI_y\bar{u} + (\beta(x,y)I_x^2 + \alpha^2)\bar{v} - \beta(x,y)I_yI_t}{(\beta(x,y)(I_x^2 + I_y^2) + \alpha^2)} \end{cases} \tag{D.28}$$

Here, U_i and V_i from equation (D.11) become:

$$\begin{cases} U_i = \dfrac{(\beta(x,y)I_y^2 + \alpha^2)}{(\beta(x,y)(I_x^2 + I_y^2) + \alpha^2)} \\ V_i = \dfrac{(\beta(x,y)I_x^2 + \alpha^2)}{(\beta(x,y)(I_x^2 + I_y^2) + \alpha^2)} \end{cases} \tag{D.29}$$

and the Jacobi or the Gauss Seidel method (see appendix E.1) provide the following iterative scheme:

$$\begin{cases} u^{n+1} = \dfrac{(\beta(x,y)I_y^2 + \alpha^2)\bar{u}^n - \beta(x,y)I_xI_y\bar{v}^n - \beta(x,y)I_xI_t}{(\beta(x,y)(I_x^2 + I_y^2) + \alpha^2)} \\ v^{n+1} = \dfrac{-\beta(x,y)I_xI_y\bar{u}^n + (\beta(x,y)I_x^2 + \alpha^2)\bar{v}^n - \beta(x,y)I_yI_t}{(\beta(x,y)(I_x^2 + I_y^2) + \alpha^2)} \end{cases} \tag{D.30}$$

that can simplified to:

$$\begin{cases} u^{n+1} = \overline{u}^n - \beta(x,y)I_x\dfrac{\overline{u}^nI_x + \overline{v}^nI_y + I_t}{\beta(x,y)(I_x^2 + I_y^2) + \alpha^2} \\ v^{n+1} = \overline{v}^n - I_y\dfrac{\overline{u}^nI_x + \overline{v}^nI_y + I_t}{\beta(x,y)(I_x^2 + I_y^2) + \alpha^2} \end{cases} \tag{D.31}$$

Appendix E

Solving large and sparse linear systems

As described in appendix D, the presented variational techniques designed for local motion estimation often rely in the minimization of a functional using the Euler Lagrange equations. This approach generally provides large and sparse linear systems to solve. In this appendix, a rapid presentation of general methods to solve linear systems is given, followed by specific methods adapted to our problem of spare and linear systems. Nevertheless, these adapted methods still require intensive computation and could takes advantage of a GPU implementation. Therefore, the feasibility and the potential of the parallelization of the solution computation are also presented and discussed.

Several strategies [177] have been proposed to solve a system of linear equations being of the form:

$$Ax = b \tag{E.1}$$

with

$$A = \begin{pmatrix} a_{1,1} & a_{1,2} & ... & a_{1,n} \\ a_{2,1} & a_{2,2} & ... & a_{2,n} \\ ... & & & \\ a_{m,1} & a_{m,2} & ... & a_{m,n} \end{pmatrix}, \; x = \begin{pmatrix} x_1 \\ x_2 \\ . \\ x_n \end{pmatrix} \text{ and } b = \begin{pmatrix} b_1 \\ b_2 \\ . \\ b_m \end{pmatrix} \tag{E.2}$$

where we suppose that A is composed by a set of independent lines.

This type of linear system generally have three type of behavior:

- $n = m$: The system is determined and there is a unique solution. A brief overview of the methods to solve these type of systems, especially in the case of a large and sparse matrix A, is given below.

- $n > m$: The system is under determined. There is more unknowns that equations. In such a case there is an infinity of solutions.

- $n < m$: The system is overdetermined. There is less unknowns that equations. This type of system has no solution and an approximate solution can be found by minimizing the function $f(x)$ defined as:

  $$f(x) = \|Ax - b\| \tag{E.3}$$

  Several approaches exist to minimize a given function f such as the gradient descent method, the Gauss-Newton method or the Marquardt Levenberg method.

In this appendix, we focus on methods to solve linear system where $n = m$. A number of methods have been proposed for this purpose such as:

- Elimination of variables: The principle is to express x_1 in function of the other variables as $f_1(x_2, x_3, ..., x_n)$ from the first equation and to replace x_1 by $f1(x_2, x_3, ..., x_n)$ in all other equations. The process is repeated for x_2 that is expressed in function of the remaining variable as $f_2(x_3, x_4, ..., x_n)$ and replaced in all remaining equations. This process is repeated until x_{n-1}. After that, A is an upper triangular matrix. One can directly get the solution of x_n from the last line of A and then replaced its values on the previous line to get the value of x_{n-1}, and so on until x_1. This is called a backward substitution. (Note that the same process for lower triangular matrix is called forward substitution).

- Row elimination: The objective is again to reduce the matrix A in a triangular matrix with all zero in its lower part. A set of matrix operation are allowed for that. The most famous algorithm is the Gauss Jordan elimination algorithm.

- The Cramer's rule: The solution is directly given by:

$$x_i = \frac{det(A_i)}{det(A)} \tag{E.4}$$

  where $det(A)$ is the determinant of the matrix A and A_i denotes the matrix A where the i^{th} column has been replaced by the the vector b.

A number of others approaches have been proposed for specific type of matrices. Now, we focus on large and sparse matrix that are for example encountered in the minimization of the variational approach of motion estimation such as the Horn & Schunck functional.

For large systems, iterative methods that start with an initial approximation of the solution and refine the solution at each iteration are generally preferred. These methods allow to reduce the computational time of the presented general methods.

E.1 Gauss Seidel method

The Gauss Seidel method [178] decomposes the matrix A into the following form:

$$A = L + U, \text{ with } L = \begin{pmatrix} a_{1,1} & 0 & ... & 0 \\ a_{2,1} & a_{2,2} & ... & 0 \\ ... & & & \\ a_{m,1} & a_{m,2} & ... & am,n \end{pmatrix}, \text{ and } R = \begin{pmatrix} 0 & a_{1,2} & ... & a1,n \\ 0 & 0 & ... & a2,n \\ ... & & & \\ 0 & 0 & ... & 0 \end{pmatrix} \tag{E.5}$$

that leads to the following relation:

$$Lx = b - Ux \tag{E.6}$$

The associated iterative scheme that solve again each diagonal element is of the form:

$$Lx^{k+1} = (b - Ux^k) \tag{E.7}$$

that provides the following system:

$$\begin{cases} a_{1,1}x_1^{k+1} = b_1 - \sum_{j>1}^{n} a_{1,j}x^k \\ a_{2,1}x_1^{k+1} + a_{2,2}x_2^{k+1} = b_2 - \sum_{j>2}^{n} a_{2,j}x^k \\ ... \\ a_{n,1}x_1^{k+1} + ... + a_{n,n}x_n^{k+1} = b_n \end{cases} \tag{E.8}$$

Since L is a lower triangular matrix, a forward substitution can be applied in order to obtain the solution of each x_i^{k+1} element as follows:

$$x_i^{k+1} = \frac{1}{a_{i,i}}(b_i - \sum_{j>i} a_{i,j}x_j^k - \sum_{j<i} a_{i,j}x_j^{k+1}) \tag{E.9}$$

At implementation level, each x_j^k can be overwritten as soon as updated. However, the computation of the solution of the i^{th} pixel requires the prior computation of the solution for each j^{th} pixel with $j < i$. Although this approach allows a fast convergence, the resolution is sequential and cannot be parallelized (at pixel level). Therefore, in our problem, this approach is not adapted for a GPU implementation.

E.2 Jacobi method

The Jacobi method [179] is very similar to the Gauss-Seidel method. Here, the matrix A is decomposed into the sum of a diagonal matrix D and a matrix R containing the remaining elements as follows:

$$A = D + R, \text{ with } D = \begin{pmatrix} a_{1,1} & 0 & ... & 0 \\ 0 & a_{2,2} & ... & 0 \\ ... & & & \\ 0 & 0 & ... & am,n \end{pmatrix}, \text{ and } R = \begin{pmatrix} 0 & a_{1,2} & ... & a_{1,n} \\ a_{2,1} & 0 & ... & a_{2,n} \\ ... & & & \\ a_{m,1} & a_{m,2} & ... & 0 \end{pmatrix} \tag{E.10}$$

In such condition, one can write:

$$Dx = b - Rx \tag{E.11}$$

The Jacobi method provide an iterative scheme that solves each diagonal element of A as follows:

$$x^{k+1} = D^{-1}(b - Rx^k) \tag{E.12}$$

Using a forward substitution (as described above in this appendix, this leads to the following iterative scheme for the i^{th} element of the diagonal:

$$x_i^{k+1} = \frac{1}{a_{i,i}}(b_i - \sum_{j\neq i} a_{i,j}x_j^k) \tag{E.13}$$

This approach requires to store all x_j^k from the previous step. Then, it uses two times more memory than the Gauss Seidel method. However, in our case, we typically deal with images of resolution of 128×128 and this point is thus negligible with current memory hardware. On the other hand, the resolution of the iterative scheme for one pixel do not require a priori knowledge of the solution of any neighboor at the current iteration. Therefore, each iteration of the numerical scheme can be done in parallel for each pixel which in turns represents a suitable solution for a GPU implementation [77, 122].

Appendix F

Digital filters

Since several digital filters are used in this thesis, a rapid presentation of the main principle of a digital filter is given.

A digital filter [180] transforms a discrete input time signal $x(t)$ to reduce or enhance certain aspects of that signal resulting in an output signal $y(t)$ (see figure F.1).

Figure F.1: General representation of a filter

A filter can be characterized by its impulse response $h(t)$ that corresponds to the filter response to an impulse signal that consists of a Dirac's delta.

$$y(t) = h(t) * x(t) \tag{F.1}$$

F.1 Frequency filters

Frequency basics filters can be divided into two classes: infinite impulse response (IIR) and finite impulse response (FIR) filters [180].

An FIR filter (which may only be implemented in discrete time) may be described as a weighted sum of delayed inputs. For such a filter, if the input becomes zero at any time, then the output will eventually become zero as well, as soon as enough time has passed so that all the delayed inputs are zero, too. Therefore, the impulse response lasts only a finite time, and this is the reason for the name finite impulse response.

For an IIR filter, by contrast, if the input is set to 0 and the initial conditions are non-zero, then the set of time where the output is non-zero will be unbounded; the filter's energy will decay but will be ever present. Therefore, the impulse response extends to infinity, and the filter is said to have an infinite impulse response.

Both of these filters are defined as follows:

$$y(t) = \sum_{i=0}^{N} a_i x(t-i) - \sum_{j=1}^{M} b_j y(t-j) \tag{F.2}$$

where $y(t)$ is the filter output, $x(t-i)$ are the filter inputs and $y_(t-j)$ are the previous filter outputs. a_i and b_j are the filter coefficients that defines the filter behavior. In a FIR filter, all b_j are set to zero.

A very efficient way to analyze the filter response is provided by the analysis of its associated transfer function H(z) that corresponds to the Z-transform of the impulse response h(t).

The z-transform of a signal s(n) is given by:

$$S(z) = \mathcal{Z}\left\{s[n]\right\} = \sum_{n=0}^{\infty} s(n) z^{-n} \tag{F.3}$$

with z a complex number. The z-transform is a generalized representation of the Fourier transform and allows to represent data into a frequency domain. Therefore, the analysis of the z-transform of the impulse response allows to determine the relation between the input and output of a linear time-invariant system in terms of frequency.

The transfer function $H(z)$ is then defined as:

$$H(z) = \frac{Y(z)}{X(z)} \tag{F.4}$$

where $X(z)$ and $Y(z)$ are the z-transform of the input signal and the output signal respectively.

Now, coming back to the general filter relation, shown in equation (F.2), one can re arrange this relation into:

$$\sum_{i=0}^{N} a_i x(t-i) = \sum_{j=0}^{M} b_j y(t-j) \tag{F.5}$$

with $b_0 = 1$.

Then the z-transform of this equation is:

$$\mathcal{Z}\left\{\sum_{i=0}^{N} a_i x(t-i)\right\} = \mathcal{Z}\left\{\sum_{j=0}^{M} b_j y(t-j)\right\} \tag{F.6}$$

Using the linearity property of the z-transform, equation (F.6) can be rewritten as:

$$\sum_{i=0}^{N} a_i \mathcal{Z}\left\{x(t-i)\right\} = \sum_{j=0}^{M} b_j \mathcal{Z}\left\{y(t-j)\right\} \tag{F.7}$$

Based on the shifting property of the z-transform, equation (F.7) becomes:

$$\sum_{i=0}^{N} a_i z^{-i} X(z) = \sum_{j=0}^{M} b_j z^{-j} Y(z) \tag{F.8}$$

The transfer function H is then derived from equation (F.4) and (F.8) as:

$$H(z) = \frac{\sum_{i=0}^{N} a_i z^{-i}}{\sum_{j=0}^{M} b_j z^{-j}} \tag{F.9}$$

with its most traditional form (as $b_0 = 1$) :

$$H(z) = \frac{\sum_{i=0}^{N} a_i z^{-i}}{1 + \sum_{j=1}^{M} b_j z^{-j}} \tag{F.10}$$

Given the transfer function $H(z)$, the frequency response is obtained by evaluating it on the unit circle in the complex plane, i.e., by setting $z = e^{j\omega T}$, where T is the sampling interval in seconds, and ω is radian frequency. This frequency response has a magnitude and a phase for each frequency.

The magnitude of the frequency response is called the amplitude response A and gives the filter gain at each frequency ω as follows:

$$A(\omega) = \|H(e^{j\omega T})\| \tag{F.11}$$

The magnitude response is generally described in decibel (Db). Note that a gain of 0 Db relates to no attenuation where -3 Db and -20 Db correspond to a gain of 0.707 and 0.1 respectively. Therefore, this gain defines how each signal frequency will be attenuated.

The second element of the frequency response is its phase response that corresponds to the delay introduced by the filter at each frequency and is defined as:

$$\Theta(\omega) = arctan(\frac{IMAG(H(e^{j\omega T}))}{REAL(H(e^{j\omega T}))}) \tag{F.12}$$

where REAL and IMAG denote the real part and the imaginary part of a complex number. A more intuitive representation of the effect is generally represented with the phase delay that correspond to the delay in second introduced for each frequency and is defined as:

$$P(\omega) = \frac{-\Theta(\omega)}{\omega} \tag{F.13}$$

A commonly encountered representation of filter phase response is called the group delay and refer to the average time delay imposed over the range of frequencies the filter is designed to pass through. The group delay is defined as follows:

$$D(\omega) = -\frac{\partial}{\partial\omega}\Theta(\omega) \tag{F.14}$$

F.2 State based filter

An important representation for discrete-time linear systems is the state-space formulation that aims to model the observations (measurements) (z_k) in function of the true state (x_k) of a model. The true state of the model at time k is obtained from the true state of the model at time $k-1$ and optional control input at time k. One of the most famous state based filter is the Kalman filter [161, 181] that is now detailed.

F.2.1 Kalman filter

In a Kalman filter, the observations z_k are related to the true state x_k of the model as follows:

$$z_k = Hx_k + v_k \tag{F.15}$$

where H is the observation matrix that maps the state space into the observed space and v_k is the measurement noise which is assumed to be white with a normal probability distribution and a covariance of R.

The true state of the model at time k is obtained from a linear stochastic equation:

$$x_k = Ax_{k-1} + Bu_{k-1} + w_{k-1} \tag{F.16}$$

where A is a matrix that defines the state model. B relates the optional control input u_k to the model state. w_k represents the process noise and is also assumed to be white with normal probability distribution and a covariance of Q. However, the true state of the model x_k cannot be directly computed since both v_k and w_k are unknown.

The Kalman filter proposes to combine both predicted data (based on filtered data obtained at time $k-1$) and measured data (z_k, obtained at time k) to obtain the filtered data at time k. In order to simplify the mathematical writing, we introduce the notation $\hat{T}_{i|j}$ that relates to an estimate of the variable T at time i obtained from observations up to (and including) at time j.

The predicted data($\hat{x}_{k|k-1}$) at time k, generally referred as a priori state estimate, is computed as follows:

$$\hat{x}_{k|k-1} = A\hat{x}_{k-1|k-1} + Bu_{k-1} \tag{F.17}$$

where $\hat{x}_{k-1|k-1}$ is called the a posteriori state estimate at time $k-1$ (that represents the filtered data obtained at time $k-1$).

The Kalman filter relies on the optimal combination (that makes the popularity of the Kalman filter) of both predicted data and measured data as follows:

$$\hat{x}_{k|k} = \hat{x}_{k|k-1} + K_k(z_k - H_k\hat{x}_{k|k-1}) \tag{F.18}$$

where K_k is weighting factor generally called the Kalman gain. In order to have an optimal combination , K_k is chosen to minimize the mean squared error (mse) of the a posteriori state estimate, respect to the true state x_k:

$$mse = E((x_k - \hat{x}_{k|k})^2) = \sum_{i=0}^{N}(cov(x_k(i) - \hat{x}_{k|k}(i))) = Tr(P_{k|k}) \tag{F.19}$$

where N is the size of the vector x_k, Tr is a function that computes the trace of a matrix, and $P_{k|k}$ is defined as:

$$P_{k|k} = cov(x_k - \hat{x}_{k|k}) \tag{F.20}$$

and is usually referred as the a posteriori estimate error covariance at time k. Therefore, this comes to find K_k that minimizes the trace of $P_{k|k}$.

F.2.1.1 Derivation of the Kalman gain

The a posteriori estimate error covariance $P_{k|k}$ depends also on the true state x_k of the model and is therefore unknown. Therefore, further mathematical manipulations are required in order to be able to compute $P_{k|k}$.

From equation (F.18), one can do a substitution of $\hat{x}_{k|k}$ that reads:

$$P_{k|k} = cov(x_k - (\hat{x}_{k|k-1} + K_k(z_k - H\hat{x}_{k|k-1}))) \tag{F.21}$$

From equation (F.15), a further substitution of z_k gives:

$$P_{k|k} = cov(x_k - (\hat{x}_{k|k-1} + K_k(Hx_k + v_k - H\hat{x}_{k|k-1}))) \tag{F.22}$$

that can be simplified into

$$P_{k|k} = cov((I - K_kH)(x_k - \hat{x}_{k|k-1}) - K_kv_k) \tag{F.23}$$

Since the measurement noise v_k is uncorrelated from the other terms, equation (F.23) can be re-written as:

$$P_{k|k} = cov((I - K_kH)(x_k - \hat{x}_{k|k-1})) + cov(K_kv_k) \tag{F.24}$$

A property of covariance matrix says that $cov(AX) = Acov(X)A^T$ with X a random variable matrix and A a given matrix. Therefore, the a posteriori estimate error covariance can be formulated as:

$$P_{k|k} = (I - K_kH)cov(x_k - \hat{x}_{k|k-1})(I - K_kH)^T + K_kcov(v_k)K_k^T \tag{F.25}$$

that leads to the recursive following form:

$$P_{k|k} = (I - K_kH)P_{k|k-1}(I - K_kH)^T + K_kRK_k^T \tag{F.26}$$

that can be re-written (with $(I - K_kH)^T = (I - H^TK_k^T)$ as:

$$P_{k|k} = P_{k|k-1} - K_kHP_{k|k-1} - P_{k|k-1}H^TK_k^T + K_k(HP_{k|k-1}H^T + R)K_k^T \tag{F.27}$$

As $P_{k|k}$ is now computable in a recursive way, the selection of the optimal Kalman gain is feasible. As previously mentioned, K_k is chosen to minimize the trace of $P_{k|k}$ which is obtained when:

$$\frac{\partial Tr(P_{k|k})}{\partial K_k} = 0 \tag{F.28}$$

Based on the following properties of the derivatives of the trace of a matrix [182] (with A and X two matrices):

$$\begin{array}{lcl} \dfrac{\partial Tr(XA)}{\partial X} & = & A^T \\ \dfrac{\partial Tr(AX^T)}{\partial X} & = & A \\ \dfrac{\partial Tr(XAX^T)}{\partial X} & = & XA^T + XA \end{array} \tag{F.29}$$

the derivation of $Tr(P_{k|k})$ gives:

$$(HP_{k|k-1})^T + P_{k|k-1}H^T + K_k(HP_{k|k-1}H^T + R)^T + K_k(HP_{k|k-1}H^T + R) = 0 \tag{F.30}$$

Since $P_{k|k-1}$ is a symmetric matrix, $P_{k|k-1}H^T = P_{k|k-1}^T H^T = (HP_{k|k-1})^T$ and $HP_{k|k-1}H^T$ is then also a symmetric matrix. R is also a symmetric matrix, therefore, $(HP_{k|k-1}H^T + R)^T = (HP_{k|k-1}H^T + R)$. This thus leads to the following simplifications:

$$-2(HP_{k|k-1})^T + 2K_k(HP_{k|k-1}H^T + R) = 0 \tag{F.31}$$

and can be rearraged to the following equation:

$$(HP_{k|k-1})^T = K_k(HP_{k|k-1}H^T + R) \tag{F.32}$$

By the symmetry of $P_{k|k-1}$ we have:

$$(HP_{k|k-1})^T = P_{k|k-1}^T H^T = P_{k|k-1}H^T \tag{F.33}$$

The optimal Kalman gain can be finally computed as follows:

$$K_k = P_{k|k-1}H^T(HP_{k|k-1}H^T + R)^{-1} \tag{F.34}$$

Note that in the condition of an optimal Kalman gain, by multiplying equation (F.34) with $(HP_{k-1}H^T + R)K_k^T$, we obtain the following equality:

$$P_{k|k-1}H^T K_k^T = K_k(HP_{k|k-1}H^T + R)K_k^T \tag{F.35}$$

which then leads to a simplification of the recursive form of the a posteriori estimate error covariance defined in equation (F.27) as:

$$P_{k|k} = P_{k|k-1} - K_k HP_{k|k-1} = (I - K_k H)P_{k|k-1} \tag{F.36}$$

The final calculation of $P_{k|k}$ requires the calculation of $P_{k|k-1}$ often referred in the literature as the a priori estimate error covariance which is defined as:

$$P_{k|k-1} = cov(x_k - \hat{x}_{k|k-1}) \tag{F.37}$$

and can be re-written by substituting x_k and $\hat{x}_{k|k-1}$ from equation (F.16) and (F.17) as:

$$P_{k|k-1} = cov(Ax_{k-1} + Bu_{k-1} + w_{k-1} - A\hat{x}_{k-1|k-1} - Bu_{k-1}) \tag{F.38}$$

that can be simplified to

$$P_{k|k-1} = cov(A(x_{k-1} - \hat{x}_{k-1|k-1}) + w_{k-1}) \tag{F.39}$$

and leads to the general recursive form of the a priori estimate error covariance computation:

$$P_{k|k-1} = AP_{k-1|k-1}A^T + Q \tag{F.40}$$

F.2.1.2 The discrete Kalman filter algorithm

Although this filter can be written in one equation, this algorithm is generally divided into two steps called the "prediction step" and the "update step".

The prediction step provides estimate of the a priori state and the a priori error covariance as follows:

$$\begin{aligned} \hat{x}_{k|k-1} &= A\hat{x}_{k-1|k-1} + Bu_{k-1} \\ P_{k|k-1} &= AP_{k-1|k-1}A^T + Q \end{aligned} \tag{F.41}$$

The update step provides estimate of the a posteriori state and the a posteriori error covariance as follows:

$$\begin{aligned} K_k &= P_{k|k-1}H^T(HP_{k|k-1}H^T + R)^{-1} \\ \hat{x}_{k|k} &= \hat{x}_{k|k-1} + K_k(z_k - H\hat{x}_{k|k-1}) \\ P_{k|k} &= (I - K_kH)P_{k|k-1} \end{aligned} \tag{F.42}$$

F.2.2 Extended Kalman filter

The extended Kalman filter (EKF) was proposed to handle non linear models [183]. In this case the state based model is defined as:

$$z_k = g(x_k) + v_k \tag{F.43}$$

and

$$x_k = f(x_{k-1}, u_{k-1}) + w_{k-1} \tag{F.44}$$

where g and f are non linear functions.

The a posteriori state estimate is then defined as:

$$\hat{x}_{k|k} = \hat{x}_{k|k-1} + K_k(z_k - g(\hat{x}_{k|k-1})) \tag{F.45}$$

and the a priori state estimate as:

$$\hat{x}_{k|k-1} = f(\hat{x}_{k-1|k-1}, u_{k-1}) \tag{F.46}$$

The a posteriori error estimate covariance $P_{k|k}$ is computed with the same substitution scheme used for the Kalman filter derivation with the linearization of $g(x_k)$ around $\hat{x}_{k|k-1}$ that is:

$$g(x_k) \approx g(\hat{x}_{k|k-1}) + G_k(x_k - \hat{x}_{k|k-1}) \tag{F.47}$$

where G_k is a matrix of the partial derivative of g with respect to x in $\hat{x}_{k|k-1}$. In this condition, we can write:

$$\begin{aligned} P_{k|k} &= cov(x_k - \hat{x}_{k|k}) && \text{(F.48)} \\ &= cov(x_k - (\hat{x}_{k|k-1} + K_k(z_k - g(\hat{x}_{k|k-1})))) && \text{(F.49)} \\ &= cov(x_k - (\hat{x}_{k|k-1} + K_k(g(\hat{x}_{k|k-1}) + G_k(x_k - (\hat{x}_{k|k-1}) + v_k - g(\hat{x}_{k|k-1}))))) && \text{(F.50)} \\ &= cov((I - K_kG_k)(x_k - \hat{x}_{k|k-1}) + v_k) && \text{(F.51)} \\ &= (I - K_kG_k)P_{k|k-1}(I - K_kG_k)^T - K_kRK_k^T && \text{(F.52)} \\ & && \text{(F.53)} \end{aligned}$$

The a priori error estimate covariance $P_{k|k-1}$ is computed using a linearization of $f(x_{k-1}, u_{k-1})$ around $\hat{x}_{k-1|k-1}$ as follows:

$$f(x_{k-1}, u_{k-1}) \approx f(\hat{x}_{k-1|k-1}, u_{k-1}) + F_{k-1}(x_{k-1} - \hat{x}_{k-1|k-1}) \tag{F.54}$$

where F_{k-1} is a matrix of the partial derivative of f with respect to x in $\hat{x}_{k-1|k-1}$. Therefore, $P_{k|k-1}$ is obtained as follows:

$$
\begin{aligned}
P_{k|k-1} &= cov(x_k - \hat{x}_{k|k-1}) && \text{(F.55)}\\
&= cov(f(x_{k-1}, u_{k-1}) + w_{k-1} - f(\hat{x}_{k-1|k-1}, u_{k-1})) && \text{(F.56)}\\
&= cov(f(\hat{x}_{k-1|k-1}, u_{k-1}) + F_{k-1}(x_{k-1} - \hat{x}_{k-1|k-1}) + w_{k-1} - f(\hat{x}_{k-1|k-1}, u_{k-1})) && \text{(F.57)}\\
&= cov(F_{k-1}(x_{k-1} - \hat{x}_{k-1|k-1}) + w_{k-1}) && \text{(F.58)}\\
&= F_{k-1}P_{k-1|k-1}F_{k-1} + Q && \text{(F.59)}\\
& && \text{(F.60)}
\end{aligned}
$$

Note that final equation of $P_{k|k}$ and $P_{k|k-1}$ have the same form that in the Kalman filter except that matrices A and H are replaced by the matrices F_{k-1} and G_k respectively. The optimal gain which minimizes the trace of $P_{k|k}$ is obtained with the same mathematical scheme as for the regular Kalman filter. Therefore, the final discrete EKF algorithm can be sum up identically into two steps:

- prediction step:

$$
\begin{aligned}
\hat{x}_{k|k-1} &= f(\hat{x}_{k-1|k-1}, u_{k-1})\\
P_{k|k-1} &= F_{k-1}P_{k-1|k-1}F_{k-1}^T + Q
\end{aligned}
\qquad \text{(F.61)}
$$

- update step:

$$
\begin{aligned}
K_k &= P_{k|k-1}G_k^T(G_kP_{k|k-1}G_k^T + R)^{-1}\\
\hat{x}_{k|k} &= \hat{x}_{k|k-1} + K_k(z_k - g(\hat{x}_{k|k-1}))\\
P_{k|k} &= (I - K_kG_k)P_{k|k-1}
\end{aligned}
\qquad \text{(F.62)}
$$

Résumé

Introduction

Cette thèse porte sur le développement de nouveaux outils pour le traitement du cancer et des arythmies cardiaques par ablation thermique guidée par IRM.

Hyperthermie locale en médecine

Cette section présente les traitements thérapeutiques existants, leurs limites et l'intéret potentiel d'un traitements par hyperthermie locale.

Traitement du cancer : Plusieurs approches thérapeutiques sont actuellement utilisées et souvent combinées pour le traitement du cancer, comme la chimiothérapie, la chirurgie ou la radiothérapie [1]. Cependant, ces techniques ne sont pas toujours utilisables suivant le type de cancer et peuvent générer de nombreux effets secondaires. Ainsi, le développement de nouvelles approches visant à améliorer l'efficacité du traitement tout en diminuant ces effets secondaires est désirable. Dans ce contexte, l'hyperthermie locale apparaît comme une alternative thérapeutique très prometteuse. Elle peut être utilisée pour l'ablation directe des tissus tumoraux [2, 3, 4] mais aussi pour le dépôt local de médicaments [5]. Dans cette thèse, les travaux ont porté sur l'ablation thermique directe utilisant des élévations de température autour de 50-80°C pendant une période de courte durée (plusieurs dizaines de secondes) afin de générer une nécrose des tissus tumoraux [6].

L'hyperthermie locale peut être réalisée avec différents outils de chauffage mini ou non invasifs comme le laser [2], la radio fréquences [3] ou les ultrasons focalisés (UF) [4]. Ces trois modalités sont en cours d'évaluation pour le traitement du cancer du sein [7, 8, 9, 10], de la prostate [11], des organes abdominaux [12] et du cerveau [13]. Afin d'améliorer l'efficacité de l'intervention, l'IRM a été suggérée pour contrôler et guider le processus thérapeutique [18, 19, 20, 21, 22, 23] et a déjà été intégrée en routine clinique comme par exemple pour le traitement des fibromes utérins [24, 25]. En revanche, l'application aux organes mobiles n'est pas directe puisque de nouveaux challenges doivent être abordés, notamment celui du mouvement des organes. Dans cette thèse, des développements techniques et méthodologiques sont proposés pour améliorer le guidage par IRM en temps réel d'ablations thermiques par ultrasons focalisés sur les organes abdominaux (rein et foie).

Traitement des arythmies cardiaques : Les arythmies cardiaques sont causées par une ou des stimulations électriques anormales du coeur, entraînant des contractions inefficaces du muscle cardiaque. Les deux principaux traitements thérapeutiques reposent sur l'utilisation de drogues anti-arythmiques et la cardioversion (souvent appelée défibrillation). Cependant, une rechute est observée avec ces traitements dans 77% des cas après un an [29]. Ainsi, de nouvelles stratégies ont été développées afin d'améliorer le taux de succès du traitement. L'ablation tissulaire par hyperthermie locale permet de changer l'impédance électrique des tissus responsables de la pathologie [30, 31] et de rétablir une contraction cardiaque efficace. Le chauffage par radio fréquences est privilégié pour cette intervention et est déjà utilisé en routine clinique [32, 33, 34, 35]. Cependant, un échec thérapeutique est observé dans 30 % des cas, probablement dû à un chauffage insuffisant ou excessif. Dans cette thèse, la possibilité de guider cette intervention par IRM est évaluée afin de contrôler le chauffage réalisé.

Contrôle de l'ablation thermique par IRM

L'IRM permet l'obtention d'images avec un excellent contraste tissulaire mais aussi avec une résolution spatialle et temporelle élevée. Ainsi elle apparaît comme une modalité d'imagerie très prometteuse pour le guidage des interventions ciblées.

Imagerie IRM : L'IRM acquiert les données dans l'espace K, qui peut être vu comme une extension de l'espace de Fourier. Une transformée de Fourier inverse permet d'obtenir une image complexe dont le module correspond à l'information anatomique (position et constitution des tissus) et où la phase est directement proportionnelle à la fréquence de résonance des protons (pour des séquences IRM en écho de gradient).

Thermométrie par IRM : L'IRM permet aussi l'obtention d'une information de température pour chaque pixel puisque plusieurs propriétés magnétiques des tissus, comme la fréquence de résonance des protons de l'eau, sont dépendantes de la température. Ainsi une variation de température est directement proportionelle à une variation de phase [37].

Dosimétrie IRM : La relation entre l'élévation de température appliquée dans les tissus et la mort cellulaire résultante a été évaluée et modélisée à travers le concept de la dose thermique [38], défini comme suit :

$$DT = \begin{cases} \int_0^t 2^{T(t)-43}, \text{ si } T < 43°C \\ \int_0^t 4^{T(t)-43}, \text{ si } T \geq 43°C \end{cases} \tag{F.63}$$

La destruction cellulaire est obtenue lorsque la dose thermique excède la dose thermique létale qui est définie comme une élévation de température à 43°C pendant 240mn (avec une température basale de 37°C). Ainsi, la dose thermique représente un outil intéressant pour la prédiction de la nécrose induite et pour la détermination de la fin de la thérapie.

Ablations thermiques guidées par IRM sur organes mobiles : Les challenges

Le ciblage thérapeutique des organes mobiles comporte de nombreux challenges, dont la principale source est liée à l'influence du mouvement des organes. Les organes ciblés, le rein, le foie et le coeur, ont des mouvements spécifiques propres. Le mouvement du rein et du foie est principalement causé par l'activité respiratoire. Bien que le rein ait un mouvement rigide linéaire, le foie admet un mouvement plus complexe, composé d'un déplacement linéaire ainsi que d'une déformation élastique. Enfin, le mouvement du coeur est sujet à un déplacement linéaire lié à l'activité respiratoire combiné avec une forte contraction induite par l'activité cardiaque. Les contraintes induites par le déplacement de ces organes sur les modalités de l'intervention sont maintenant présentées.

Mouvement intra-scan : Il correspond au mouvement des organes durant l'acquisition d'une image et génère des effets de flou sur les images reconstruites. Les séquences synchronisées sur le cycle respiratoire ou cardiaque (à l'aide d'un capteur externe) permettent de s'abstraire de ce problème mais diminuent substantiellement la résolution temporelle de l'acquisition. Ainsi, des acquisitions ultra-rapides sont généralement privilégiées afin de minimiser les mouvements intra-scan.

Bruit de mesure : L'utilisation de séquences rapides introduit généralement un bruit de mesure élevé. Le bruit présent sur les images de magnitude reconstruites, peut être quantifié avec le SNR. Ce dernier définit directement la précision maximale pouvant être obtenue pour le calcul de la thermométrie [84]. Or, plusieurs traitements durant l'intervention utilisent les informations de thermométrie comme le calcul de la dose thermique, le contrôle automatique de la température [89, 90] ou des stratégies avancées d'ablations volumétriques [93]. Par conséquent, ces algorithmes sont susceptibles d'être biaisés ou de devenir instables à cause de la présence de bruit sur les mesures de thermométrie.

Mouvement inter-scan : Il correspond au mouvement d'un organe entre deux images. Il est particulièrement problématique pour l'évaluation de la dose thermique qui requiert une analyse temporelle pixel par pixel. Ce mouvement peut être dans le plan d'imagerie (mouvement dans le plan) ou dans la direction perpendiculaire à ce plan (mouvement hors plan de coupe).

Mouvement hors plan de coupe : L'imagerie 3D qui pourrait permettre de s'abstraire des mouvements hors plan de coupe est difficilement envisageable sur des organes mobiles, notamment à cause des mouvements intra-scan. Une solution alternative consiste à ajuster la position du plan de coupe dans la troisième dimension à l'aide d'informations sur le mouvement obtenu par un écho navigateur [40] ou un écho ultra sonore [41].

Mouvement dans le plan : Pour résoudre le problème lié au déplacement des organes entre les images, des algorithmes d'estimation et de compensation du mouvement sont généralement utilisés. De nombreux algorithmes ont été proposés dans ce but. Denis de Senneville et al. [58] ont montré qu'un algorithme estimant un modèle global du mouvement, suivi par un raffinement local du champ de déplacements obtenu par estimation du flot optique était une solution satisfaisante. L'estimation du flot optique repose sur l'hypothèse de conservation de l'énergie (ici l'intensité) entre deux images. L'approche la plus populaire a été proposée par Horn & Schunck [70], qui cherche le champ de déplacements (u, v) minimisant la fonctionnelle suivante:

$$E = \iint \left(\left[I_x u + I_y v + I_t \right]^2 + \alpha^2 \left[\|\nabla u\|_2^2 + \|\nabla v\|_2^2 \right] \right) dxdy \tag{F.64}$$

où I_x,I_y,I_t sont les gradients spatio temporels sur l'intensité et α est une constante permettant la pondération des deux métriques (variation d'intensité et régularité du mouvement).

Modification de la susceptibilité magnétique locale : Cet effet entraîne une variation de signal sur les images de phase qui se superpose à la variation de phase induite par l'hyperthermie. Afin de corriger cet effet avant le calcul de température, plusieurs méthodes ont été proposées comme les techniques "referenceless" ou "multi-baseline". La première extrapole l'information de phase dans la zone chauffée à partir du signal de phase des tissus non chauffés situés en périphérie. Cette phase synthétique non perturbée par l'effet du chauffage peut alors être soustraite à la phase courante pour obtenir la température. La méthode "multi-baseline" requiert une étape de pré-traitement où une modélisation des variations de phase en fonction du mouvement. Ainsi, durant l'hyperthermie, à partir de l'information de mouvement, une image de phase peut être obtenue par ce modèle et soustraite à la phase courante pour en déduire la température.

Ajustement du point focal en temps réel : Dans le cadre d'un chauffages UF, la position du point focal doit être dynamiquement ajustée (électroniquement) avec le mouvement de l'organe afin d'optimiser le dépôt d'énergie dans la zone souhaitée. De plus, pour l'obtention d'une ablation volumétrique, le point focal peut aussi être déplacé afin de chauffer une région plus importante. Ces deux mécanismes de contrôle automatique de la position du point focal requièrent par conséquent des informations de mouvement et de thermométrie en temps réel, avec une faible latence.

Aspects cliniques : La sécurité du patient doit être garantie. De plus, la procédure interventionelle doit être simple et automatique de façon à pouvoir être intégrée en routine clinique. Enfin, le temps total de l'intervention doit être optimisé afin de minimiser le coût de l'intervention.

Développements techniques et métodologiques

Les principaux développements réalisés durant cette thése sont maintenant présentés.

Reconstruction des images IRM en temps réel

Introduction : La réduction du temps d'acquisition apparaît nécessaire pour la minimisation des mouvements intra-scan. L'imagerie parallèle permet une réduction du temps d'acquisition en réalisant une acquisition partielle de l'espace K (par exemple uniquement chaque k^{ieme} ligne, où k est appelé le facteur d'accélération). Dans ce cas, le signal IRM est acquis par plusieurs canaux (éléments d'antenne) en parallèle. Le signal obtenu par un élément d'antenne se trouve alors pondéré par sa sensibilité et les méthodes de reconstruction exploitent la différence de sensibilité spatiale entre chaque élément d'antenne afin de compenser l'effet du sous échantillonnage de l'espace K. De plus, comme les mouvements des antennes sont fréquents durant l'intervention, la mise à jour des cartes de sensibilité apparaît nécessaire. La reconstruction TSENSE [103] permet cela mais est associée à un temps de calcul élevé, limitant son utilisabilité en temps réel pour l'IRM interventionelle. Dans cette étude, une implémentation est proposée, visant à satisfaire les contraintes temps réel de l'intervention thérapeutique et assurer une latence faible [107, 108].

Matériel et méthode : Une implémentation *multi-thread* est proposée dans l'objectif de paralléliser le transport des données, la reconstruction générale des données et la reconstruction spécifique liée à la méthode TSENSE. La reconstruction TSENSE a été portée sur carte graphique (GPU) et a nécessité une attention particulière sur la gestion et la disposition des données en mémoire. Les performances d'une implémentation GPU augmentent fortement si les accès mémoire de chaque thread se font de manière continue. Ainsi, les données ont été réorganisées en mémoire à plusieurs reprises de façon à optimiser les temps d'exécution. Les échanges de données entre CPU et GPU se font via un bus PCI-express qui ont un débit limité. Ainsi, Ils ont été minimisés dans l'implémentation proposée.

Le reconstructeur utilisé était un double processeur (INTEL, 3.1 GHz Penryn, quatre noyaux) avec 8 Gb de RAM et une carte réseau de bande passante 1Gb/s. Le GPU était une carte NVIDIA 8800 GTX avec 756 MB de DRAM.

Résultats : La reconstruction seule de la méthode TSENSE combinant CPU et GPU permet de réduire le temps d'exécution, pour une image de résolution 128×128, par un facteur 8 comparé à une implémentation utilisant uniquement un CPU. Dans ces conditions, la reconstruction seule de la méthode TSENSE a un pic théorique de performance entre 75 images/s (facteur d'accélération 4, 16 canaux) et 330 images/s (facteur d'accélération 2, 4 canaux). Cependant, en pratique, le pic de performance est limité par la bande passante du système d'acquisition (2.1 MB/s) qui correspond à une fréquence d'imagerie de 20 images/s (facteur d'accélération de 2 et 16 canaux) et 40 images/s (facteur d'accélération de 4 et 16 canaux). Le temps de transport varie entre 17 ms (facteur d'accélération de 4, 4 canaux, $\approx$135 KB par image) et 76 ms (facteur d'accélération de 2, 16 canaux, $\approx$1 MB par image). La latence totale de la reconstruction ainsi obtenue varie de 20 ms (facteur d'accélération de 4 et 4 canaux) à 85 ms (facteur d'accélération de 2 et 16 canaux).

Discussion et conclusion : L'implémentation proposée de la méthode de reconstruction TSENSE permet une fréquence de reconstruction supérieure à la fréquence d'acquisition IRM, assurant ainsi la condition temps réel avec une latence faible. La vitesse de l'imagerie est par conséquent limitée par la limite imposée par la séquence IRM utilisée.

Thermométrie et dosimétrie en temps réel sur organes mobiles

Introduction : Le calcul de la thermométrie et de la dosimétrie requiert une chaîne de traitements complexes afin de corriger les artefacts liés notamment aux mouvements ou au bruit. Dans cette étude, une extension de la méthode présentée par Denis de Senneville et al. [58] est proposée et une implémentation combinant CPU et GPU a été ajoutée afin de garantir la condition temps réel et assurer une latence faible [121, 122].

Matériel et méthode : La chaîne de traitement est composée de plusieurs étapes visant à corriger l'influence du mouvement, les variations de susceptibilité magnétique induites par le mouvement et la dérive temporelle du signal de phase (lié à l'échauffement des gradients du scanner IRM). Par la suite, la thermométrie est calculée et le bruit associé est réduit en utilisant un filtre temporel. Finalement, la dose thermique est évaluée.

La correction du mouvement se compose de deux étapes : Le mouvement global (modèle affine) est estimé par minimisation d'un critère qualité sur le recalage (inter-corrélation). Afin de raffiner localement l'estimation, un algorithme d'estimation du flot optique est appliqué. La correction de la variation de susceptibilité magnétique est réalisée avec la méthode "multi-baseline". La dérive temporelle sur l'image de phase est corrigée en soustrayant un offset global de température (calculé sur une région extérieure à la zone chauffée). Un filtre temporel à réponse impulsionnelle infinie (RII) est utilisé pour réduire le bruit sur la température. Enfin, pour permettre la faisabilité de ces traitements en temps réel, une implémentation combinant CPU et GPU a été réalisée.

Résultats : La méthode proposée a été évaluée dans les organes abdominaux (rein et foie) de 11 volontaires sains en condition de respiration libre. La précision initiale de la mesure de thermométrie (de 8°C) à été réduite à 0.79°C (dans le rein) et à 0.98 °C (dans le foie). La méthode a également été validée in-vivo dans le rein d'un cochon durant une ablation par UF. La précision de la température dans l'ensemble du rein était de 0.65°C et une élévation de température de 12 °C a été mesurée, correspondant à une dose thermique égale à 10% de la dose létale.

Cette méthode a été par la suite évaluée dans le coeur et plus précisement dans le ventricule gauche de 9 volontaires sains en respiration libre. Une précision moyenne de 3.6 °C sur la mesure de thermométrie a été obtenue. Une ablation par chauffage RF (puissance RF de 10 W pendant 60 s) a également été réalisée dans le ventricule gauche d'un mouton où une précision de 1 °C et une élévation de 16 °C ont été mesurées.

L'implémentation combinant CPU et GPU a permis une réduction du temps total d'excécution de 81 ms à 13 ms, réduisant la latence totale (qui inclut 13 ms de transport de données et 1 ms de reconstruction) de 95 ms à 27 ms.

Discussion et conclusion : La chaîne de traitements proposée pour la thermométrie et la dosimétrie sur organes mobiles permet de satisfaire la contrainte temps réel. En revanche, même si la précision des mesures obtenues apparaît prometteuse en vue d'une application clinique, plusieurs questions doivent être encore adressées afin de garantir la sécurité du patient. Ainsi des développements sont proposés dans cete thèse afin d'améliorer l'estimation du mouvement en présence de mouvements hors plan de coupe (entraînant la présence de structures non persistantes dans les images) ainsi que pendant l'hyperthermie (où des variations d'intensité sur les images peuvent être observées). Un nouveau critère qualité sur l'estimation du mouvement est présenté et utilisé pour auto-calibrer l'algorithme d'estimation du mouvement. De plus, l'utilisation d'un filtre RII (ou RIF) introduit géréralement une latence additionnelle sur le signal filtré, générant un biais systématique. Ainsi, un nouveau filtre a été mis au point, afin de réduire le bruit tout en contrôlant le biais introduit par le filtre.

Estimation du mouvement en présence de structures non persistantes

Introduction : Afin de réduire le temps d'acquisition et permettre une amélioration de la résolution spatiale et ou temporelle, l'acquisition d'un champ de vue restreint autour de l'organe apparaît comme une alternative intéressante [139, 141]. En revanche, ces techniques, comme les mouvements hors plan de coupe, généralement engendrent la présence de structures non persistantes dans les images (induite de l'activité respiratoire) et entraînent la violation de l'hypothèse de conservation d'énergie faite par les algorithmes d'estimation du flot optique. Ainsi, une nouvelle approche variationnelle est proposée pour l'estimation du flot optique qui intègre le mouvement de points caractéristiques comme terme de régularisation de la fonctionnelle d'erreur [145, 146].

Matériel et méthode : L'algorithme d'estimation du mouvement proposé est composé de deux étapes. Premièrement, les points caractéristiques sont choisis. Pour cela, un masque est manuellement dessiné autour de l'organe sur l'image de référence. Son contour est extrait puis régulièrement sous-échantillonné. Pour affiner le positionnement de chaque point échantillonné, le point caractéristique [52] le plus proche est choisi. Durant la deuxième étape, le mouvement est estimé pour chaque image de la manière suivante. Une estimation du mouvement global est réalisée puis utilisée comme initialisation de l'estimation du déplacement (u_i, v_i) de chacun des N points caractéristiques $(1 < i \leq N)$. Les déplacements (u_i, v_i) considérés comme aberrants, sont automatiquement rejetés. Le mouvement des points caractéristiques est alors intégré à une nouvelle fonctionnelle d'erreur E_c :

$$\begin{aligned} E_c(u,v) = &\iint \left(\left[I_x u + I_y v + I_t \right]^2 + \alpha^2 \left[\|\nabla u\|_2^2 + \|\nabla v\|_2^2 \right] \right) dxdy \\ &+\lambda^2 \iint \left(\sum_{i=0}^{N} \left(\rho(d_i, R) \left[(u-u_i)^2 + (v-v_i)^2 \right] \right) \right) dxdy \end{aligned} \tag{F.65}$$

où $\rho(d_i, R) = \exp\left(-d_i^2/R^2\right)$ pondère l'influence de chaque point caractéristique en fonction de sa distance d_i au pixel de coordonnées (x, y) (avec R une constante). Une approche multi-résolution a été rajouté et une implémentation GPU a été réalisée.

Résultats : Cet algorithme a été évalué in-vivo dans le coeur et dans le rein de 13 volontaires sains en condition de respiration libre. La séquence cardiaque utilisée était synchronisée avec le cycle cardiaque afin s'abstraire du phénomène de contraction. Pour quantifier la qualité du recalage, le contour de l'organe sur les images recalées a été manuellement dessiné et le recouvrement avec la position originale a été calculée. L'algorithme proposé présente des performances similaires à celles de l'algorithme de Horn & Schunck sur les images conservant les même structures que l'image de référence. En revanche, en présence des structures non persistantes, les performances de l'algorithme proposé garantissent un recouvrement minimal de 91% dans le coeur et 88% dans le rein. Ces résultats surpassent ceux obtenus avec l'algorithme de Horn & Schunck (72% dans le coeur et 83% dans le rein). Enfin, l'implémentation GPU a permis la réduction du temps total d'exécution de 85 ms à 22 ms assurant sa faisabilité en temps réel avec une latence faible.

Discussion et conclusion : Dans cette étude, une fonctionnelle d'erreur est proposée pour l'estimation du flot optique, intégrant le déplacement de points caractéristiques comme terme de régularisation. Les performances obtenues en présence de structures non persistentes améliorent nettement celles de la méthode de Horn & Schunck.

Estimation du mouvement pendant l'hyperthermie

Introduction : Durant l'hyperthermie, le chauffage induit une modification des propriétés tissulaires (temps de relaxation T_1, T_2 et T_2^*) générant des variations locales d'intensité dans les images de magnitude. Les algorithmes de flot optique, attribuant une variation d'intensité à un mouvement, sont alors susceptibles d'être perturbés. Dans cette étude, la cause physique de la perturbation (le changement local de température) est intégrée à la fonctionnelle d'erreur de Horn & Schunck [70] pour ajuster la confiance locale sur l'utilisation des variations d'intensités pour l'estimation du flot optique [152].

Matériel et méthode : Une fonction de pondération $\beta(x, y)$, dépendant directement de la température, a été introduite dans la formulation de le fonctionnelle d'erreur. Cette fonction permet d'attribuer à chaque pixel de coordonnées (x, y) un niveau de confiance dans l'hypothèse de conservation de l'énergie (une valeur de 1 dénote une forte confiance et une valeur de 0 représente une confiance nulle). La formulation de la fonctionnelle est exprimée de la manière suivante :

$$E(u, v) = \iint \left(\beta(x, y) \left[I_x u + I_y v + I_t \right]^2 + \alpha^2 \left[\|\nabla u\|_2^2 + \|\nabla v\|_2^2 \right] \right) dxdy \tag{F.66}$$

où la fonction $\beta(x, y)$ est mise à jour en temps réel en utilisant la dernière carte de température $T(x, y)$ comme suit :

$$\beta(x, y) = \begin{cases} 1 & , \text{ si } T(x, y) < T_{seuil} \\ \exp \frac{-(T(x,y)-T_{seuil})^2}{k^2} & , \text{ si } T(x, y) \geq T_{seuil} \end{cases} \tag{F.67}$$

où k^2 permet de définir la vitesse de convergence vers 0. Enfin, une approche multi-résolution a été rajouté pour l'estimation de grand déplacement. Une implémentation GPU de la méthode a également été réalisée.

Résultats : L'algorithme a été évalué et comparé avec la méthode de Horn & Schunck sur des données simulées et durant une expérience de chauffage sur un muscle porcin ex-vivo. Sur la simulation, un objet avec un mouvement vertical complexe (amplitude maximale de 4 pixels) a été généré sur 200 images et une décroissance de signal sur une région de taille 5×5 pixels a été ajoutée sur les 100 dernières images. Sur les 100 premières images, l'erreur quadratique moyenne (EQM) entre le mouvement estimé et le mouvement réel avec les deux algorithmes était de l'ordre de 0.3 pixels. Durant les 100 dernières images, l'algorithme de Horn & Schunck a vu ses performances diminuer (EQM $\approx$ 1-2 pixels) alors que la méthode proposée a permis de maintenir une précision de 0.3 pixels.

Une seconde expérience a été conduite où un muscle porcin ex-vivo a été positionné dans l'IRM sur une plateforme générant un mouvement périodique translationnel (amplitude maximale=10 pixels). Le mouvement était estimé en parallèle avec un écho navigateur servant ainsi de mesure de référence. L'EQM entre le mouvement estimé et le mouvement de référence était de l'ordre de 0.4 pixels. Durant le chauffage RF, cette erreur a augmenté au dessus de 2 pixels pour l'algorithme de Horn & Schunck et est restée constante autour de 0.4 pixels avec la méthode proposée.

Discussion et conclusion : La méthode de Horn & Schunck est très sensible aux variations d'intensité liées à l'hyperthermie. L'intégration de la cause physique de la variation d'intensité (la température) a permis d'améliorer nettement les performances de l'estimation du mouvement. Cette approche pourrait également être adaptée pour le rejet de régions problématiques comme des artères, où dans le cas d'IRM de contraste utilisant des passages de bolus.

Auto-calibration de l'algorithme d'estimation du mouvement

Introduction : Les algorithmes d'estimation du mouvement ont généralement plusieurs paramètres libres. Leur calibration optimale dépend de plusieurs éléments comme la complexité de la déformation, l'amplitude du mouvement, le bruit sur les images, etc. Cependant une calibration manuelle apparaît difficile car elle serait sujette aux approximations de l'utilisateur et serait très coûteuse en temps. Pour ces raisons, une méthode automatique de calibration est proposée dans cette étude [154, 155].

Matériel et méthode : Afin d'auto-calibrer un tel algorithme, la définition d'un critère qualité sur l'estimation du mouvement est nécessaire. Généralement, des critères basés sur la comparaison des images de magnitude (référence et recalée) sont utilisés mais sont généralement biaisés par la présence du bruit sur les images, puisque le "recalage du bruit" améliore ces critères. Dans cette étude, un nouveau critère, basé sur la comparaison des images de phase est proposé. Cependant, deux effets entraînent une variation du signal des images de phase : le déplacement des organes et la variation de susceptibilité magnétique induite par le mouvement. Ce dernier effet doit donc être enlevé avant le calcul de similarité. Pour cela une modélisation (relation linéaire [79]) de la variation de la phase recalée φ avec le mouvement D est réalisée comme suit :

$$\varphi(x, y, k) = a(x, y).D(x, y, k) + b(x, y) \tag{F.68}$$

pour chaque dynamique k (ici $k = 50$ pour couvrir plusieurs cycles respiratoires). $D(x, y, k)$ est la composante principale du mouvement estimée à la dynamique k au pixel de coordonnées (x, y) et a et b sont les coefficients du modèle linéaire, estimés par une régression linéaire. Une fois a et b estimés, le critère qualité sur l'estimation du mouvement est calculé comme suit. Pour chaque image de la phase de calibration, la composante du mouvement est extraite et une phase synthétique est obtenue à partir de l'équation (F.68). L'erreur quadratique moyenne (EQM) est calculée entre chaque image de phase et sa phase synthétique associée. Ces valeurs sont alors moyennées temporellement et le résultat peut alors être utilisé comme critère de qualité sur l'estimation du mouvement.

Résultats : Le critère de qualité basé sur la phase a été comparé avec un critère basé sur la magnitude pour l'auto-calibration de l'algorithme de Horn & Schunck et plus particulièrement le paramètre α^2 (voir équation (F.64)). Dans une première expérience, un muscle porcin ex-vivo a été positionné dans l'IRM sur une plateforme générant un mouvement périodique translationnel (amplitude maximale 12 mm). Le mouvement était estimé simultanément avec un écho navigateur servant ainsi de mesure de référence. L'EQM entre le mouvement estimé et le mouvement de référence était de l'ordre de 1 pixel et de 0.5 pixel avec une auto-calibration utilisant le critère basé sur la magnitude et sur la phase, prespectivement. Une étude a été réalisée sur des données in-vivo dans le rein et le foie de 12 volontaires en condition de respiration libre. Pour chaque expérience, 10 points dans chacun des organes ont été recalés manuellement et utilisés comme mouvement de référence. L'auto-calibration utilisant le critère de magnitude et celle utilisant le critère sur la phase ont respectivement généré des EQM (sur le mouvement estimé sur les 10 points) de 1.5 mm et de 0.8 mm.

Discussion et conclusion : Le mouvement étant estimé sur les images de magnitude et le bruit entre les images de magnitude et de phase étant indépendant, le critère proposé n'est par conséquent pas amélioré par le "recalage du bruit". Il permet ainsi de surpasser les performances des critères basés sur la magnitude. Enfin, son utilisation pour l'auto-calibration d'un algorithme d'estimation du mouvement a également été démontrée.

Réduction du bruit et contrôle de la précision

Introduction : Les algorithmes utilisant la température peuvent être biaisés par la présence de bruit sur les mesures de thermométrie (comme par exemple pour le calcul de la dose thermique ou la rétroaction sur l'outil de chauffage dans le cadre de stratégies d'ablations volumétriques [93]). Le filtrage temporel de la température a été proposé comme solution, en utilisant un filtre à réponse impulsionnelle infinie (RII) [122]. En revanche ces filtres génèrent généralement une latence qui entraîne un biais sur le signal filtré. Dans cette étude, un filtre est proposé basé sur le formalisme du filtre de Kalman, combinant les mesures de température avec des prédictions obtenues par un modèle physique décrivant le transfert de chaleur dans les tissus biologiques [165, 166].

Matériel et Méthode : Un filtre de Kalman étendu (FKE) combine efficacement les mesures et les prédiction obtenues à partir d'un modèle (non linéaire), connaissant la précision du modèle et des mesures. Le modèle utilisé est basée sur la résolution de l'équation de transfert de chaleur [163] qui permet une prédiction de la température correspondant à l'instant t à partir de la température à l'instant $t-1$. Il intègre la puissance émise et les coefficients d'absorption, de diffusion et de perfusion des tissus. Ainsi la précision du modèle dépend directement de la précision des coefficients d'absorption et de diffusion utilisés. Or, ces paramètres ne sont généralement disponibles qu'avec une certaine incertitude. Par conséquent, la précision du modèle n'est a priori pas connue et peut varier dans le temps (puisque le phénomène d'absorption n'intervient pas durant la période de refroidissement). Ainsi un ajustement dynamique de la précision du modèle, notée Q, a été rajouté. En utilisant l'hypothèse que le bruit des mesures est blanc autour des vrais valeurs, le modèle peut être considéré comme juste si la somme ϵ entre les prédictions et les mesures est proche de zéro. Ce critère a été utilisé pour contrôler le biais introduit par le modèle en ajustant dynamiquement la précision Q du modèle. Pour cela, la plus petite valeur de Q permettant d'obtenir une valeur $\epsilon < \epsilon_{seuil}$ (avec ϵ_{seuil} la tolérance maximale du biais introduit par le filtre) est sélectionnée. Une approche robuste (basée sur le critère de Chauvenet appliqué sur la différence entre la mesure et la prédiction) a été rajouté afin de remplacer des mesures considérées comme aberrantes, par les prédictions du modèle.

Résultats : Le filtre a été évalué sur des données simulées auxquelles un bruit gaussien a été ajouté. L'erreur quadratique moyenne (EQM) entre le signal filtré et le signal non bruité a été évalué avec un filtre à réponse impulsionelle finie (RIF) et le FKE. Le RIF n'a apporté aucune amélioration de l'EQM durant la chauffage dû au biais généré par la latence introduite. Durant le refroidissement, une amélioration de l'EQM d'un facteur 3 a été obtenue. Le FKE a permis de réduire l'EQM dans le pire cas (avec des paramètres d'absorption et de diffusion délibérément mal configurés de $\pm$ 50%) par un facteur 3 et 15 pour les périodes de chauffage et de refroidissement, respectivement. Le filtre a également été évalué in-vivo durant le chauffage d'un rein porcin. Le RIF et le FKE ont été appliqué sur les mesures initiales de thermométrie, ainsi que sur une copie de ces mesures où un artefact de 45°C a été simulé sur deux images. Sur la seconde expérience, contrairement au RIF qui a été fortement perturbé, l'approche robuste du FKE a permis la corrections des deux artefacts. La dose thermique calculée pour chacune des deux expériences était identique avec le FKE alors qu'une variation de 75 % a été observé avec le RIF.

Discussion et conclusions : Le filtre proposé permet la réduction du bruit tout en garantissant un biais maximal de ϵ_{seuil} autour des mesures. Ainsi, si le modèle s'avère très mal paramétré, le filtre se contentera de suivre les mesures. Enfin l'approche robuste du filtre permet d'enlever des artefacts qui pourraient rendre instable ou inutilisable les résultats des algorithmes utilisant la température (comme le calcul de la dose thermique).

Conclusions générales

L'objectif de cette thèse était d'améliorer la méthodologie existante pour la guidage par IRM des ablations thermiques sur organes mobiles et d'en assurer la faisabilité en temps réel.

Développements méthodologiques et techniques:

La méthodologie existante était généralement limitée à une fréquence d'imagerie de 1 Hz [58]. Cependant, une intervention par UF sur organes mobiles nécessite une mise à jour dynamique de la position du point focal avec le mouvement de l'organe. Dans ces conditions, une fréquence de 1 Hz est insuffisante pour suivre efficacement le déplacement d'un organe. Ainsi des algorithmes de prédiction du mouvement devaient être utilisés pour augmenter la résolution temporelle de l'information de mouvement. Cependant, ces algorithmes voient généralement leur performances se dégrader rapidement pour des prédictions sur des périodes de plusieurs centaines de millisecondes.

Dans cette thèse, une chaîne de traitements est présentée pour obtenir une information de thermométrie et de dosimétrie en temps réel avec une fréquence élevée de l'ordre de 10-15 Hz. La combinaison d'une acquisition IRM rapide (pour minimiser les mouvements intra-scan) avec une chaîne de traitements pour la correction des mouvements inter-scan et des variations de susceptibilité magnétique a été évaluée avec succès dans les organes abdominaux et dans le coeur. Son potentiel pour l'ajustement dynamique de la position de point focal du transducteur HIFU avec le mouvement de l'organe a été démontrée.

Des développements méthodologiques ont été réalisés sur plusieurs aspects de la chaîne de traitements. Ainsi, plusieurs solutions ont été proposées pour améliorer l'estimation du mouvement. Une nouvelle fonctionnelle d'erreur pour l'estimation du flot optique a été proposée afin d'améliorer l'estimation du mouvement en présence de structures non persistantes dans les images. Une seconde amélioration a été proposé afin d'améliorer la robustesse de l'algorithme contre les variations d'intensité induites par l'hyperthermie. Pour cela, une extension de la fonctionnelle d'erreur a été proposée afin d'integrer directement la température comme coefficient d'ajustement de la confiance dans l'intensité. Enfin, comme le choix des paramètres libres des algorithmes d'estimation du mouvement sont directement dépendant de l'amplitude du mouvement des organes ou du SNR (qui varient d'un patient à un autre), une méthode d'auto-calibration de ces algorithmes a été proposée. Un nouveau critère pour l'évaluation in-vivo de la qualité du mouvement estimé a été développé et a été utilisé pour effectuer cette auto-calibration.

De plus, comme les cartographies de température sont recalées sur une même position de référence, l'intégration d'un filtre temporel a permis d'améliorer la précision des mesures. Cependant, les filtres temporels comme les RIF ou RII introduisent généralement une latence qui, avec des systèmes variant rapidement, se traduit par un biais systématique (non contrôlé) qui peut menacer la sécurité du patient. Cela n'étant pas acceptable pour une application clinique, un nouveau filtre a été proposé, visant à améliorer la précision tout en garantissant un biais maximal (défini par l'utilisateur).

Enfin, l'utilisation du GPU, pour la parallélisation des algorithmes de traitement d'images, s'est avérée efficace et représente un moyen peu onéreux pour assurer la compatibilité des algorithmes utilisés avec la condition temps réel.

Perspectives

Perspectives méthodologiques: Bien que la thermométrie par IRM permette d'obtenir une précision de l'ordre du degré dans les organes abdominaux et de l'ordre de 2-3°C dans le coeur, plusieurs aspects méthodologiques pourraient encore être améliorés.

L'estimation du mouvement dans le foie peut être perturbée par la présence de certains vaisseaux sanguins. Le critère proposé pour l'évaluation de la qualité du mouvement pourrait être utilisé pour détecter automatiquement ces zones. L'analyse de la carte d'erreur du fit obtenue lors de la création du modèle linénaire entre variation de phase et déplacement pourrait permettre de discriminer de telles regions. Enfin la méthode proposée pour rejeter des pixels lors de l'estimation du flot optique durant l'hyperthermie pourrait être étendue afin de rejeter également les pixels appartenant aux zones problématiques. De plus, l'estimation du mouvement est directement réalisée sur les images IRM. L'utilisation d'informations auxiliaires (pouvant être obtenues par exemple avec l'imagerie multi-modale) pourrait permettre de découpler l'estimation du mouvement du calcul de thermométrie. Cela permettrait de pouvoir choisir des stratégies d'imagerie différentes (en terme de résolution spatio-temporelle par exemple) pour chacun des deux processus.

L'amélioration de la couverture spatiale de la thermométrie (vers la 3D) devrait également permettre d'optimiser les stratégies d'ablations volumétriques. Comme les IRM récentes permettent maintenant de modifier dynamiquement les paramètres des séquences, le déplacement dynamique du plan d'imagerie représente une solution prometteuse pour balayer un volume 3D. Cependant ce type de solution réduit la résolution temporelle de la thermométrie. Le formalisme du filtre de Kalman proposé repésente ainsi une solution interessante pour augmenter cette résolution temporelle. Il pourrait être utilisé sur la coupe acquise comme un filtre (et comme présenté dans notre étude) mais pourrait également être employé comme prédicteur dans le reste du volume 3D. Cela permettrait d'obtenir une thermométrie 3D avec une haute résolution temporelle avec un échantillonage réduit de mesures. D'autres stratégies peuvent être considérées afin d'améliorer la couverture spatialle et temporelle. L'imagerie avec un champ de vue restreint est une solution interessante mais peut génerer la présence de structures non persistentes dans les images, pouvant être problématique pour les algorithmes d'estimation du mouvement. Néamoins, ce problème a été efficament adressé en intégrant le mouvement de points caractéristiques comme paramètre de régularisation dans l'estimation du flot optique.

Enfin le développement de méthodes pour contrôler le déroulement de l'intervention thérapeutique devra être réalisé. La modélisation *a priori* de l'intervention représente une piste intéressante. De plus, l'utilisation simultanée de différentes méthodes d'acquisition (image multi-modale) ou de correction pourrait fournir des mesures indépendantes pour une même tâche et ainsi augmenter la fiabilité des résultats. Par conséquent, les méthodes développées dans cette thése pourraient être utilisées également à de fins de contrôle.

Perspectives cliniques: L'ablation par UF guidée par IRM sur les organes abdominaux peut être réalisée avec une précision de l'ordre du degré. Des solutions efficaces ont été developées pour traiter les principaux problèmes liés à cette intervention thérapeutique. Cependant le développement d'une chaîne incluant l'ensemble des solutions reste à développer. L'ablation par UF guidée par IRM ayant maintenant gagné en maturité, son transfert vers la clinique devra également être abordé.

L'ablation par RF guidée par IRM dans le coeur reste encore un challenge, même si les études présentées montrent des résultats encourageants avec une précision de thermométrie de l'ordre de 2-3 degrés. Bien que ces études aient été réalisées dans le ventricule gauche, la cible finale est l'atrium qui a une épaisseur de 1-3 mm correspondant à la taille des voxels des séquences IRM utilisées. Ainsi, des stratégies pour améliorer la résolution spatiale devront être développées afin de réduire les effets de volume partiel. De plus, les expériences présentées ont été réalisées sur des volontaires sains et des animaux sains. Par conséquent, la faisabilité de la méthodologie de thermométrie et de dosimétrie en présence d'arythmies devra être également évaluée.

Publications

Peer reviewed journal papers

- S. Roujol, J.Benois-Pineau, B. Denis de Senneville, M. Ries, B. Quesson, C. Moonen, Robust real time constrained motion estimation for interventional MRI on mobile organs, *IEEE trans Inf. Tech. Biomed.*, Submitted
- S. Roujol, B. Denis de Senneville, S. Hey, C.T.W. Moonen, M. Ries, Robust adaptive extended Kalman filtering for real time MR-thermometry guided HIFU interventions, *IEEE trans Med Imaging*, In press
- B. Denis de Senneville, S. Roujol, P. Jaïs, C.T.W. Moonen, G. Herigault, B. Quesson, Feasibility of fast MR-thermometry during cardiac RF ablation, *NMR Biomed*, In press
- S. Roujol, M. Ries, C. Moonen, B. Denis de Senneville, Automatic registration calibration for real time MR-interventional applications, *IEEE trans Med Im*, In press
- S. Hey, A. Cernicanu, B. Denis de Senneville, S. Roujol, M. Ries, C.T.W. Moonen, P. Jaïs, B. Quesson, Towards Optimized MR Thermometry of the Human Heart at 3T, *NMR Biomed*, In press
- M. Ries, B. Denis de Senneville, S. Roujol, Y. Berber, B. Quesson, C.T.W. Moonen, Real-Time 3D Target Tracking in MRI guided Focused Ultrasound Ablations in moving Tissues, *Magn Reson Med*, 2010, 64(6):1704-12
- B. Denis de Senneville, S. Roujol, C.T.W. Moonen, M. Ries, Motion Correction in MR Thermometry of Abdominal Organs: A Comparison of the Referenceless vs the Multi-baseline Approach, *Magn Reson Med*, 2010, 64(5):1373-81
- B. Quesson, M. Merle, M. Kohler, C. Mougenot, S. Roujol, B. Denis de Senneville, C.T.W. Moonen, A method for MRI guidance of intercostal high intensity focused ultrasound ablation in the liver, *Medical Physics*, 2010, 37(6):2533-40
- S. Roujol, M. Ries, B. Quesson, C. Moonen, and B. Denis de Senneville, Real time thermometry and dosimetry for interventional guidance in abdominal organs, *Magn Reson Med*, 2010, 63(4):1080-7.
- S. Roujol, B. De Senneville, E. Vahala, T. Sorensen, C.T.W. Moonen, M. Ries, Online real-time reconstruction of adaptive TSENSE with commodity CPU/GPU hardware, *Magn Reson Med*, 2009 Dec;62(6):1658-64.
- B. Quesson, F. Cornelis, S. Hey, S. Roujol, B. Denis De Senneville, M. Ries, N. Grenier, H. Trillaud, C. Moonen, IRM et ultrasons focalises, *Journal de Radiologie*, 2009, 90(10):1255
- N. Grenier, I. Mendichovszky, B. Denis de Senneville, S. Roujol, P. Desbarats, M. Pedersen, K. Wells, J. Frokiaer, I. Gordon, Measurement of Glomerular Filtration Rate With Magnetic Resonance Imaging: Principles, Limitations, and Expectations, *Semin Nucl Med* 38(1), 47-55/2008.
- B. Denis de Senneville, I. Mendichovszky, S. Roujol, I. Gordon, C.T.W. Moonen, N. Grenier, Improvement of MRI-Functional measurement with automatic movement correction in native and transplanted kidneys, *J Magn Reson Imaging.* 2008, 28(4):970-8.

Peer reviewed conference papers

- S. Roujol, B. Denis de Senneville, S. Hey, C. Moonen, M. Ries, Extended Kalman filtering for MR-thermometry guided high intensity focused ultrasound using the bio heat transfer equation, *IEEE International Conference on Image Processing (ICIP)*, 2011, In press.

- S. Roujol, M. Ries, C. Moonen, B. Denis de Senneville, Robust real time motion estimation for MR-thermometry, *IEEE International Symposium on Biomedical Imaging (ISBI)*, 508-511, 2011.

- S. Roujol, J. Benois-Pineau, B. Denis de Senneville, B. Quesson, M. Ries, C. Moonen, Real time constrained motion estimation for ecg-gated cardiac MRI, *IEEE International Conference on Image Processing (ICIP)*, 757-760, 2010.

- S. Roujol, M. Ries, B. Quesson, J. Benois-Pineau , C. Moonen,B. Denis de Senneville , A new criterion for motion estimation assessment for MR-thermometry, *IEEE International Symposium on Biomedical Imaging (ISBI)*, 1241-1244, 2010.

- B. Quesson, M. Merle, M. Khler, C. Mougenot, S. Roujol, B. Denis de Senneville, C.T.W. Moonen, Inter-costal Liver Ablation Under Real Time MR-Thermometry With Partial Activation Of A HIFU Phased Array Transducer, *9th International Symposium on Therapeutic Ultrasound (ISTU). AIP Conference Proceedings*, Volume 1215, pp. 243-246, 2010.

- M. Ries, B. Denis de Senneville, S. Roujol, S. Hey, G. Maclair, M. Khler, B. Quesson, C.T.W. Moonen, Three Dimensional Motion Compensation for Real-Time MRI Guided Focused Ultrasound Treatment of Abdominal Organs, *9th International Symposium on Therapeutic Ultrasound (ISTU). AIP Conference Proceedings*, Volume 1215, pp. 239-242, 2010.

Abstracts, short papers

- B. Denis de Senneville, S. Roujol, P. Jaïs, C.T.W. Moonen, G. Herigault, B. Quesson, Feasibility of fast MR-thermometry during cardiac RF ablation, *Proceedings 19th Scientific Meeting, International Society of Magnetic Resonance in Medicine*, Montreal, Canada, 2011, p. 1765.

- S. Roujol, M. Ries, B. Quesson, C. Moonen, and B. Denis de Senneville, Real-time MR-Thermometry and Dosimetry for interventional guidance on abdominal organs, *Proceedings 18th Scientific Meeting, International Society for Magnetic Resonance in Medicine*, Stockholm, Sweden, 2010, p. 1830.

- M. Ries, B. Denis de Senneville, S. Roujol, and C. Moonen, Latency compensation for real-time 3D HIFU beam-steering on moving targets, *Proceedings 18th Scientific Meeting, International Society for Magnetic Resonance in Medicine*, Stockholm, Sweden, 2010, p. 1807.

- B. Denis de Senneville, S. Roujol, C. Moonen, and M. Ries, PRF based MR-Thermometry on Abdominal Organs: A pragmatic comparison of referenceless vs multi-baseline, *Proceedings 18th Scientific Meeting, International Society for Magnetic Resonance in Medicine*, Stockholm, Sweden, 2010, p. 251.

- S. Hey, A. Cernicanu, B. D. de Senneville, S. Roujol, M. Ries, C. T. W. Moonen, and B. Quesson, Feasibility of MR-thermometry with blood suppression on the human heart at 3T, *Proceedings 18th Scientific Meeting, International Society for Magnetic Resonance in Medicine*, Stockholm, Sweden, 2010, p. 289.

- B. Quesson, M. Merle, M. Khler, C. Mougenot, S. Roujol, B. Denis de Senneville, and C. T. Moonen, inter-costal liver ablation under real-time MR-thermometry with partial activation of a HIFU phased array transducer, *Proceedings 18th Scientific Meeting, International Society for Magnetic Resonance in Medicine*, Stockholm, Sweden, 2010, p. 4139.

- S. Roujol, B. De Senneville, E. Vahala, T. Sorensen, C.T.W. Moonen, M. Ries, Online real-time reconstruction of adaptive TSENSE with commodity CPU/GPU hardware, *Proceedings 17th Scientific Meeting, International Society for Magnetic Resonance in Medicine*, Honolulu, USA, 2009, p. 2839.

- S. Roujol, B. denis de Senneville, G. Maclair, S. Hey, P. Jaïs, C.T.W. Moonen, B. Quesson, Advances in real-time MR temperature mapping of the human heart, *Proceedings 17th Scientific Meeting, International Society for Magnetic Resonance in Medicine*, Honolulu, USA, 2009, p. 444.

- B. Denis de Senneville, I. Mendichovszky, S. Roujol, I. Gordon, C.T.W. Moonen, N. Grenier, Improvement of Functional MRI measurement with automatic movement correction in native and transplanted kidneys, *Proceedings 16th Scientific Meeting, International Society of Magnetic Resonance in Medicine*, Toronto, Canada, 2008, p. 2602.

Bibliography

[1] D.M. Hartl, A. Ferlito, D.F. Brasnu, J.A. Langendijk, A. Rinaldo, C.E. Silver, and G.T. Wolf. Evidence-based review of treatment options for patients with glottic cancer. *Head Neck*, Jan 2011.

[2] A.L. Gough-Palmer and W.M.W. Gedroyc. Laser ablation of hepatocellular carcinoma - A review. *World J. Gastroenterol*, 14(47):7170–4, 2008.

[3] A.R. Gillams. The use of radiofrequency in cancer. *Brit. J. Cancer*, 92(10):18259, 2005.

[4] F.J. Fry. Precision high intensity focusing ultrasonic machines for surgery. *Am. J. Phys. Med*, 37:152–156, 1958.

[5] J.N. Weinstein, Magin R.L., M.B. Yatvin, and D.S. Zaharko. Liposomes and local hyperthermia: selective delivery of methotrexate to heated tumors. *Science*, 204(4389):188–191, 1979.

[6] C. Streffer. Metabolic changes during and after hyperthermia. *Int. J. Hyperthermia*, 1(4):305–19, 1985.

[7] W.E. Burak, D.M. Agnese, S.P. Povoski, T.L. Yanssens, K.J. Bloom, P.E. Wakely, and D.G. Spigos. Radiofrequency ablation of invasive breast carcinoma followed by delayed surgical excision. *Cancer*, 98(7):1369–76, 2003.

[8] F. Izzo, R. Thomas, P. Delrio, M. Rinaldo, P. Vallone, A. Dechiara, G. Botti, G. D'Aiuto, P. Cortino, and S.A. Curley. Radiofrequency ablation in patients with primary breast carcinoma : a pilot study in 26 patients. *Cancer*, 92(8):2036–44, 2001.

[9] D.S. Dowlatshahi, K.and Francescatti and K.J. Bloom. Laser therapy for small breast cancers. *Am. J. Surgery*, 184(4):359–63, 2002.

[10] G. Orgera, G. Curigliano, M. Krokidis, G. Bonomo, L. Monfardini, P. Della Vigna, M.G. Zampino, and F.. Orsi. High-intensity focused ultrasound effect in breast cancer nodal metastasis. *Cardiovasc Intervent Radiol*, 33(2):447–9, 2010.

[11] A. Blana, F.J. Murat, B. Walter, S. Thuroff, W.F. Wieland, C. Chaussy, and A. Gelet. First analysis of the long-term results with transrectal HIFU in patients with localised prostate cancer. *Europ. Urology*, 53:119403, 2008.

[12] R.O. Illing, J.E. Kennedy, F. Wu, G.R. ter Haar, A.S. Protheroe, P.J. Friend, F.V. Gleeson, D.W. Cranston, R.R. Phillips, and M.R. Middleton. The safety and feasibility of extracorporeal high-intensity focused ultrasound (HIFU) for the treatment of liver and kidney tumours in a western population. *Brit. J. Cancer*, 93(8):8905, 2005.

[13] K. Hynynen and G. Clement. Clinical applications of focused ultrasound - the brain. *Int. J. Hyperthermia*, 23(2):19302, 2007.

[14] H. Mumtaz, M.A. Hall-Craggs, A. Wotherspoon, M. Paley, G. Buonaccorsi, Z. Amin, I. Wilkinson, M.W. Kissin, T.I. Davidson, I. Taylor, and S.G. Bown. Laser therapy for breast cancer: MR imaging and histopathologic correlation. *Radiology*, 200:651–8, 1996.

[15] T.J. Vogl, R. Straub, K. Eichler, D. Woitaschek, and M.G. Mack. Malignant Liver Tumors Treated with MR Imaging - guided Laser-induced Thermotherapy: Experience with Complications in 899 Patients (2,520 lesions). *Radiology*, 225:367–77, 2002.

[16] M. Lepetit-Coiffè, H. Laumonier, O. Seror, B. Quesson, M.B. Sesay, C.T.W. Moonen, N. Grenier, and H. Trillaud. Real-time monitoring of radiofrequency ablation of liver tumors using thermal-dose calculation by MR temperature imaging: initial results in nine patients, including follow-up. *Eur. Radiol.*, 20(1):193–01, 2010.

[17] S. Clasen and P.L. Pereira. Magnetic resonance guidance for radiofrequency ablation of liver tumors. *J. Magn. Res. Im.*, 27(2):421–33, 2008.

[18] H.E. Cline, J.F. Schenck, K. Hynynen, R.D. Watkins, S.P. Souza, and F.A. Jolesz. MR-guided focused ultrasound surgery. *J Comput. Assist. Tomogr.*, 16(6):956–965, 1992.

[19] K. Hynynen, O. Pomeroy, D.N. Smith, P.E. Huber, N.J. McDannold, J. Kettenbach, J. Baum, S. Singer, and F.A. Jolesz. MR imaging-guided focused ultrasound surgery of fibroadenomas in the breast: A feasibility study. *Radiology*, 219:176–85, 2001.

[20] D.B. Zippel and M.Z. Papa. The use of MR imaging guided focused ultrasound in breast cancer patients: A preliminary phase one study and review. *Bull. Cancer*, 12:21–38, 2005.

[21] H. Furusawa, K. Namba, S. Thomson, F. Akiyama, A. Bendet, C. Tanaka, Y. Yasuda, and H. Nakahara. Magnetic resonance-guided focused ultrasound surgery of breast cancer: Reliability and effectiveness. *J. Am. Coll. Surg.*, 203:54–63, 2006.

[22] B. Quesson, M. Merle, S. Roujol, B. Denis de Senneville, M.O. Köhler, C. Mougenot, and C.T.W. Moonen. A method for MRI guidance of intercostal high intensity focused ultrasound ablation in the liver. *Med. Phys.*, 37(6):2533–41, 2010.

[23] A.B. Holbrook, J.M. Santos, E. kaye, V. Rieke, and K. Butts-Pauly. Real-time MR thermometry for monitoring HIFU ablations of the liver. *Magn. Res. Med.*, 63(2):365–73, 2010.

[24] C.M. Tempany, E.A. Stewart, N.J. McDannold, B.J. Quade, F.A. Jolesz, and K. Hynynen. MR imaging-guided focused ultrasound surgery of uterine leiomyoma: A feasibility study. *Radiology*, 226:89705, 2003.

[25] F.M. Fennessy, C.M. Tempany, N.J. McDannold, M.J. So, G. Hesley, B. Gostout, H.S. Kim, G.A. Holland, D.A. Sarti, K. Hynynen, F.A. Jolesz, and E.A. Stewart. Uterine leiomyomas: MR imaging-guided focused ultrasound surgery - results of different treatment protocols. *Radiology*, 243:885893, 2007.

[26] K. Butts-Pauly, C.J. Diederich, V. Rieke, D. Bouley, J. Chen, W. Nau, A.B. Ross, A. Kinsey, and G. Sommer. Magnetic resonance-guided high-intensity ultrasound ablation of the prostate. *Magn Res Imaging.*, 17(3):19507, 2006.

[27] D. Gianfelice, C. Gupta, W. Kucharczyk, P. Bret, D. Havill, and M. Clemons. Palliative treatment of painful bone metastases with MR imaging - guided focused ultrasound. *Radiology*, 249(1):355363, 2008.

[28] B. Larrat, M. Pernot, J.-F. Aubry, E. Dervishi, R. Sinkus, D. Seilhean, Y. Marie, A.-L. Boch, M. Fink, and M. Tanter. MR-guided transcranial brain HIFU in small animal models. *Phys. Med. Biol.*, 55(2):365–88, 2010.

[29] V. Fuster, L.E. Ryden, D.S. Cannom, H.J. Crijns, A.B. Curtis, K.A. Ellenbogen, J.L. Halperin, J.Y. Le Heuzey, G.N. Kay, J.E. Lowe, S.B. Olsson, E.N. Prystowsky, J.L. Tamargo, S. Wann, S.G. Priori, J.J. Blanc, A. Budaj, J. Camm, V. Dean, J.W. Deckers, C. Despres, K. Dickstein, J. Lekakis, K. McGregor, M. Metra, J. Morais, A. Qsterspey, J.L. Tamargo, J.L. Zamorano, S.C. Smith, A.K. Jacobs, C.D. Adams, J.L. Anderson, E.M. Antman, J.L. Halperin, S.A. Hunt, R. Nishimura, J.P. Ornato, R.L. Page, and B. Riegel. ACC/AHA/ESC 2006 guidelines for the management of patients with atrial fibrillation-executive summary: a report of the American College of Cardiology/American Heart Association Task Force on Practice Guidelines and the European Society of Cardiology Committee for Practice Guidelines (Writing Committee to Revise the 2001 Guidelines for the Management of Patients with Atrial Fibrillation). *Eur. Heart J.*, 27:1979–2030, Aug 2006.

[30] A. Chugh and F. Morady. Atrial brillation: Catheter ablation. *J. Interv. Card. Electrophysiol*, 16:1526, 2006.

[31] P. Jaïs, B. Cauchemez, L. Macle, E. Daoud, P. Khairy, R. Subbiah, M. Hocini, F. Extramiana, F. Sacher, P. Bordachar, G. Klein, R. Weerasooriya, J. Clémenty, and M. Haïssaguerre. Catheter ablation versus antiarrhythmic drugs for atrial fibrillation: The A4 study. *Circulation*, 118(24):24982505, 2008.

[32] D. Traub, J.P. Daubert, S. McNitt, W. Zareba, and B. Hall. Catheter ablation of atrial fibrillation in the elderly: where do we stand? *Cardiol J*, 16(2):113–20, 2009.

[33] A. Dolara. Short-term versus long-term outcomes after catheter ablation for atrial fibrillation: impact on clinical practice. *J Cardiovasc Med (Hagerstown)*, 2010.

[34] O. Voroshilovsky and J.N. Schapira. Management of atrial fibrillation: focus on catheter-based ablation. *Rev Cardiovasc Med*, 11(2):74–83, 2010.

[35] A. Verma. The techniques for catheter ablation of paroxysmal and persistent atrial fibrillation: a systematic review. *Current opinion in cardiology*, 2010.

[36] V. Rieke and K. Butts Pauly. MR thermometry. *J. Magn Res Imaging.*, 27(2):376–90, 2008.

[37] Y. Ishihara, A. Calderon, H. Watanabe, K. Okamoto, Y Suzuki, K. Kuroda, and Y. Suzuki. A precise and fast temperature mapping using water proton chemical shift. *Magn. Res. Med.*, 34:814–823, 1995.

[38] S.A. Sapareto and W.C.L. Dewey. Thermal dose determination in cancer therapy. *Int. J. Radiation Oncology Biol. Phys.*, 10:787–800, 1984.

[39] L. Qin, P. van Gelderen, J.A. Derbyshire, F. Jin, J. Lee, J.A. de Zwart, Y. Tao, and J.H. Duyn. Prospective head-movement correction for high-resolution MRI using an in-bore optical tracking system. *Magn. Res. Med.*, 62(4):924–934, 2009.

[40] M. Ries, B. Denis de Senneville, S. Roujol, S. Hey, G. Maclair, M. Kohler, B. Quesson, and C.T.W. Moonen. Three dimensional motion compensation for real-time MRI guided focused ultrasound treatment of abdomainal organs. In *In Proceedings of the 9th International symposium on therapeutic ultrasound (ISTU). AIP Conference Proceedings*, volume 1215, pages 239–42, 2010.

[41] D. A. Feinberg, D. Giese, D. A. Bongers, S. Ramanna, M. Zaitsev, M. Markl, and M. Gunther. Hybrid ultrasound MRI for improved cardiac imaging and real-time respiration control. *Magn Reson Med*, 63:290–296, 2010.

[42] J.B. Maintz and M.A. Viergever. A survey of medical image registration. *Medical Image Analysis*, 2(1):1–36, 1998.

[43] P. Markelj, D. Tomazevic, B. Likar, and F. Pernus. A review of 3D/2D registration methods for image-guided interventions. *Medical Image Analysis*, 2010.

[44] J.A. de Zwart, F.C. Vimeux, J. Palussière, R. Salomir, B. Quesson, C. Delalande, and C.T. Moonen. On-line correction and visualization of motion during MRI-controlled hyperthermia. *Magn. Res. Med.*, 45(1):128–37, 2001.

[45] M. Pernot, M. Tanter, and M. Fink. 3D real-time motion correction in high intensity focused ultrasound therapy. *Magnetic Resonance in Medicine*, 30(2004):1239–1249, Ultrasound Med Biol.

[46] H. Shirato, S. Shimizu, K. Kitamura, T. Nishioka, K. Kagei, S. Hashimoto, H. Aoyama, T. Kunieda, N. Shinohara, H. Dosaka-Akita, et al. Four-dimensional treatment planning and fluoroscopic real-time tumor tracking radiotherapy for moving tumor. *International Journal of Radiation Oncology Biology Physics*, 48(2):435–442, 2000.

[47] K.P. Gall, A.F. Thornton, J. Munzenrider, and S. Rosenthal. Experience using radiopaque fiducial points for patient alignment during radiotherapy. *International Journal of Radiation Oncology Biology Physics*, 27:161–162, 1993.

[48] J.Y. Jin, S. Ryu, K. Faber, T. Mikkelsen, Q. Chen, S. Li, and B. Movsas. 2D/3D image fusion for accurate target localization and evaluation of a mask based stereotactic system in fractionated stereotactic radiotherapy of cranial lesions. *Medical physics*, 33:4557, 2006.

[49] M. Bock, S. Müller, S. Zuehlsdorff, P. Speier, C. Fink, P. Hallscheidt, R. Umathum, and W. Semmler. Active catheter tracking using parallel MRI and real-time image reconstruction. *Magnetic resonance in medicine*, 55(6):1454–1459, 2006.

[50] P.H.S. Torr and A. Zisserman. Feature based methods for structure and motion estimation. In *Proceedings of the International Workshop on Vision Algorithms*, ICCV, pages 278–294, 2000.

[51] K. Mikolajczyk and C. Schmid. Scale and affine invariant interest point detectors. *International Journal of Computer Vision*, 60(1):63–86, 2004.

[52] C. Harris and M. Stephens. A combined corner and edge detector. In *In Proceedings of The Fourth Alvey Vision Conference*, pages 147–151, 1988.

[53] D.G. Lowe. Object recognition from local scale-invariant features. In *Computer Vision, 1999. The Proceedings of the Seventh IEEE International Conference on*, volume 2, pages 1150–1157 vol.2, 1999.

[54] M.A. Fischler and R.C. Bolles. Random sample consensus: a paradigm for model fitting with applications to image analysis and automated cartography. *Commun. ACM*, 24(6):381–395, 1981.

[55] D.N. Levin, CA Pelizzari, GT Chen, CT Chen, and MD Cooper. Retrospective geometric correlation of MR, CT, and PET images. *Radiology*, 169(3):817, 1988.

[56] M. Irani and P. Anandan. About direct methods. In *Proceedings of the International Workshop on Vision Algorithms*, ICCV, pages 267–277, 2000.

[57] L. Junck, J.G. Moen, G.D. Hutchins, M.B. Brown, and D.E. Kuhl. Correlation methods for the centering, rotation, and alignment of functional brain images. *Journal of nuclear medicine*, 31(7):1220, 1990.

[58] B. Denis de Senneville, C. Mougenot, and C.T.W. Moonen. Real time adaptive methods for treatment of mobile organs by MRI controlled high intensity focused ultrasound. *Magn. Res. Med.*, 57(2):319–30, 2007.

[59] I. Pratikakis, C. Barillot, P. Hellier, and E. Mmin. Robust multiscale deformable registration of 3D ultrasound images. *International Journal of Image and Graphics*, 3(4):547–566, 2003.

[60] N. Alperin, D.N. Levin, and C.A. Pelizzari. Retrospective registration of X-ray angiograms with MR images by using vessels as intrinsic landmarks. *Journal of Magnetic Resonance Imaging*, 4(2):139–144, 1994.

[61] P. Markelj, D. Tomazevic, F. Pernus, and B. Likar. Robust gradient-based 3-D/2-D registration of CT and MR to X-ray images. *Medical Imaging, IEEE Transactions on*, 27(12):1704–1714, 2008.

[62] E. De Castro and C. Morandi. Registration of translated and rotated images using finite fourier transforms. *IEEE Trans. Pattern Anal. Mach. Intell.*, 9(5):700–703, 1987.

[63] B.S. Reddy and B.N. Chatterji. An FFT-based technique for translation, rotation, and scale-invariant image registration. *IEEE Transactions on Image Processing*, 5(8):1266–1271, 1996.

[64] C.K. Cheong, K. Alizawa, T. Saito, and M. Hatori. Motion estimation with wavelet transform and the application to motion compensated interpolation. *Acoustics, Speech, and Signal Processing, IEEE International Conference on*, 5:217–220, 1993.

[65] J. Illingworth and J. Kittler. A survey of the hough transform. *Computer Vision Graphics and Image Processing*, 44(1):87–116, 1988.

[66] H. Kälviäinen. Motion estimation and the randomized hough transform (rht): New methods with gradient information. In Dmitry Chetverikov and Walter Kropatsch, editors, *Computer Analysis of Images and Patterns*, volume 719 of *Lecture Notes in Computer Science*, pages 191–198. Springer Berlin / Heidelberg, 1993.

[67] N. Carranza, G. Cristobal, M.J. Ledesma-Carbayo, and A. Santos. A new cardiac motion estimation method based on a spatio-temporal frequency approach and Hough transform. In *Computers in Cardiology*, pages 805 – 808. 2006.

[68] A.N. Netravali and J.D. Robbins. Motion compensated television coding part I. *Bell System Technical Journal*, 58(3):631–670, 1979.

[69] C. Cafforio and R. Rocca. The differential method for motion estimation. *Image Sequence Processing and Dynamic Scene Analysis, T.S.Huang, Ed., New York, Springer-Verlag*, pages 104–124, 1983.

[70] B.K.P. Horn and B.G. Schunck. Determining optical flow. *Artificial intelligence*, 17:185–203, 1981.

[71] N. Cornelius and T. Kanade. Adapting optical-flow to measure object motion in reflectance and X-ray image sequences. In *Proc. of the ACM SIGGRAPH/SIGART*, pages 145–153, New York, NY, USA, 1986.

[72] M.A. Gennert and S. Negahdaripour. Relaxing the brightness constancy assumption in computing optical flow. Technical report, Cambridge, MA, USA, 1987.

[73] H.H. Nagel and W. Enkelmann. An investigation of smoothness constraints for the estimation of displacement vector fields from image sequences. *Pattern Analysis and Machine Intelligence*, 8:565–593, 1986.

[74] F.R. Hampel, E.M. Ronchetti, P.J. Rousseeuw, and W.A. Stahel. *Robust Statistics: The Approach Based on Influence Functions*. Wiley, 1st edition edition, 1986.

[75] M.J. Black and P. Anandan. A framework for the robust estimation of optical flow. In *Computer Vision, 1993. Proceedings., Fourth International Conference on*, pages 231–236, 1993.

[76] Y. Kim, A.M. Martínez, and A.C. Kak. Robust motion estimation under varying illumination. *Image and Vision Computing*, 23:365–375, 2005.

[77] B. Denis de Senneville, K.O. Noe, M. Ries, M. Pedersen, C.T.W. Moonen, and T.S. Sorensen. An optimised multi-baseline approach for on-line MR-temperature monitoring on commodity graphics hardware. In *Fifth IEEE International Symposium on Biomedical Imaging*, pages 1513–1516, 2008.

[78] K.K. Vigen, B.L. Daniel, J.M. Pauly, and K. Butts. Triggered, navigated, multi-baseline method for proton resonance frequency temperature mapping with respiratory motion. *Magn. Res. Med.*, 50(5):1003–10, 2003.

[79] G Maclair, B Denis de Senneville, M Ries, B Quesson, P Desbarats, J Benois-Pineau, and C T W Moonen. PCA-based magnetic field modeling: application for on-line mr temperature monitoring. *Med Image Comput Comput Assist Interv*, 10(2):411–9, 2007.

[80] S. Hey, G. Maclair, B.D. de Senneville, M. Lepetit-Coiffe, Y. Berber, M.O. Kohler, B. Quesson, C.T. Moonen, and M. Ries. Online correction of respiratory-induced field disturbances for continuous MR-thermometry in the breast. *Magn. Res. Med.*, 61(6):1494–9, 2009.

[81] V. Rieke, K.K. Vigen, G. Sommer, B.L. Daniel, Pauly J.M., and Butts K. Referenceless PRF shift thermometry. *Magn. Res. Med.*, 51(6):1223–31, 2004.

[82] R.D. Peters and R.M. Henkelman. Proton-resonance frequency shift MR thermometry is affected by changes in the electrical conductivity of tissue. *Magn. Res. Med.*, 43:62–71, 2000.

[83] S.J. Riederer. Recent technical advances in MR imaging of the abdomen. *J. Magn Res Imaging.*, 6:822–832, 1996.

[84] T.E. Conturo and G.D. Smith. Signal to noise in phase angle reconstruction : Dynamic range extension using phase reference offsets. *Magn. Res. Med.*, 15:420–437, 1990.

[85] S. Bobkova, L. Gavrilov, V. Khokhlova, A. Shaw, and J. Hand. Focusing of high-intensity ultrasound through the rib cage using a therapeutic random phased array. *Ultrasound Med Biol*, 36(6):888–906, 2010.

[86] Y.Y. Botros, E.S. Ebbini, and J.L. Volakis. Two-step hybrid virtual array ray (VAR) technique for focusing through the rib cage. *IEEE Trans Ultrason Ferroelectr Freq Contr*, 45(4):989–1000, 1998.

[87] F. Ernst, A. Schlaefer, and A. Schweikard. Prediction of respiratory motion with wavelet-based multiscale autoregression. In *MICCAI 2007*, pages 668–675, 2007.

[88] L. Ramrath, A. Schlaefer, F. Ernst, S. Dieterich, and A. Schweikard. Prediction of respiratory motion with a multi-frequency based Extended Kalman Filter. In *Proceedings of the 21st International Conference and Exhibition on Computer Assisted Radiology and Surgery (CARS'07)*, volume 2 of *International Journal of CARS*, pages 56–58. CARS, 2007.

[89] D. Arora, D. Cooley, T. Perry, M. Skliar, and R.B. Roemer. Direct thermal dose control of constrained focused ultrasound treatments: phantom and in vivo evaluation. *Phys. Med. Biol.*, 50(8):1919–35, 2005.

[90] D. Arora, M.A. Minor, M. Skliar, and R.B. Roemer. Control of thermal therapies with moving power deposition field. *Phys. Med. Biol.*, 51(5):1201, 2006.

[91] R. Salomir, F.C. Vimeux, J.A. de Zwart, N. Grenier, and C.T. Moonen. Hyperthermia by MR-guided focused ultrasound: accurate temperature control based on fast MRI and a physical model of local energy deposition and heat conduction. *Magn. Res. Med.*, 43(3):342–7, 2000.

[92] C. Mougenot, R. Salomir, J. Palussire, N. Grenier, and C.T.W. Moonen. Automatic spatial and temporal temperature control for MR-guided focused ultrasound using fast 3D MR thermometry and multispiral trajectory of the focal point. *Magn. Res. Med.*, 52(5):1005–15, 2004.

[93] C. Mougenot, R. Salomir, J. Palussière, N. Grenier, and C.T.W. Moonen. Automatic spatial and temporal temperature control for MR-guided focused ultrasound using fast 3D MR thermometry and multispiral trajectory of the focal point. *Magn. Res. Med.*, 52:1005–1015, 2004.

[94] C.R. Hill, I. Rivens, M.G. Vaughan, and G.R. ter Haar. Lesion development in focused ultrasound surgery: a general model. *Ultrasound Med Biol*, 20(3):259–69, 1994.

[95] C. Damianou, K. Hynynen, and X. Fan. Evaluation of accuracy of a theoretical model for predicting the necrosed tissue volume during focused ultrasound surgery. *IEEE Trans Ultrason Ferroelectr Freq Contr*, 42(2):1827, 1995.

[96] F. Chavrier, J.Y. Chapelon, A. Gelet, and D. Cathignol. Modeling of high-intensity focused ultrasound-induced lesions in the presence of cavitation bubbles. *J Acoust Soc Am*, 108(1):432–40, 2000.

[97] F.P. Curra and P.D. Mourad. Numerical simulations of heating patterns and tissue temperature response due to high-intensity focused ultrasound. *IEEE Trans Ultrason Ferroelectr Freq Contr*, 47(4):107789, 2000.

[98] A. Pulkkinen and K. Hynynen. Computational aspects in high intensity ultrasonic surgery planning. *Computerized Medical Imaging and Graphics*, 34(1):69–78, 2010.

[99] M. Ries, B. Denis de Senneville, S. Roujol, Y. Berber, B. Quesson, and C.T.W. Moonen. Real-time 3D target tracking in MRI guided focused ultrasound ablations in moving tissues. *Magn. Res. Med.*, 64(6):1704–12, 2010.

[100] D.K. Sodickson and W.J. Manning. Simultaneous acquisition of spatial harmonics (SMASH): Fast imaging with radiofrequency coil arrays. *Magn. Res. Med.*, 38:591–603, 1997.

[101] M.A. Griswold, P.M. Jakob, R.M. Heidemann, M. Nittka, V. Jellus, J. Wang, B. Kiefer, and A. Haase. Generalized autocalibrating partially parallel acquisitions (GRAPPA). *Magn. Res. Med.*, 47:1202–1210, 2002.

[102] M. Pruessmann, K.P.and Weiger, M.B. Scheidegger, and P. Boesiger. SENSE: Sensitivity encoding for fast MRI. *Magn. Res. Med.*, 42(5):952–62, Nov 1999.

[103] P. Kellman, F.H. Epstein, and E.R. McVeigh. Adaptive sensitivity encoding incorporating temporal filtering (TSENSE). *Magn. Res. Med.*, 45:846–852, 2001.

[104] M.A. Guttman, P. Kellman, A.J. Dick, R.J. Lederman, and E.R. McVeigh. Real-time accelerated interactive MRI with adaptive TSENSE and UNFOLD. *Magn. Res. Med.*, 50(2):315–321, 2003.

[105] M.S. Hansen, D. Atkinson, and T.S. Sorensen. Cartesian SENSE and k-t SENSE reconstruction using commodity graphics hardware. *Magn. Res. Med.*, 59(3):463–8, 2008.

[106] *NVIDIA CUDA Compute Unified Device Architecture - Programming Guide*, 2007.

[107] S. Roujol, B.D. de Senneville, E. Vahala, T.S. Sorensen, C. Moonen, and M. Ries. Online real-time reconstruction of adaptive TSENSE with commodity CPU/GPU hardware. *Magn. Res. Med.*, 62(6):1658–64, 2009.

[108] S. Roujol, B.D. de Senneville, E. Vahala, T.S. Sorensen, C. Moonen, and M. Ries. Online real-time reconstruction of adaptive TSENSE with commodity CPU/GPU hardware. In *Proceedings 16th Scientific Meeting, International Society for Magnetic Resonance in Medicine*, 2009.

[109] H. Bruder, H. Fisher, H.E. Reinfelder, and Schmitt F. Image reconstruction for EPI with non- equidistant k-space sampling. *Magn. Res. Med.*, 23:311–323, 1992.

[110] D.C. Schmidt, D.L. Levine, and S. Mungee. The design and performance of real-time object request brokers. *Computer Communications*, 21:294–324, 1998.

[111] I Pyrali, D.C. Schmidt, and R. Cytron. Techniques for enhancing real-time CORBA quality of service. In *IEEE Proceedings Special Issue on Real-time Systems*, 2002.

[112] Numerical Algorithms Group Ltd. *AMD Core Math Library User Guide*. 2006.

[113] J.J. Dongarra, J. DuCroz, I. Duff, and S. Hammarling. A set of level 3 basic linear algebra subprograms: Model implementation and test programs. *ACM Trans. Math. Softw.*, 16(1):18–28, 1990.

[114] E. Anderson, Z. Bai, C. Bischof, J. Demmel, J. Dongarra, J. DuCroz, A. Greenbaum, S. Hammarling, A. McKenny, S. Ostrrouchov, and D. Sorensen. *LAPACK Users Guide*. SIAM Publications, Philadelphia, 1992.

[115] W.H. Press, S.T. Teukolsky, W.A. Vetterling, and B.P. Flannery. *Numerical recipes in C++: The art of scientific computing*. Cambridge University Press, Cambridge, 2002.

[116] G. Maclair, M. Ries, and C.T.W. Moonen. Low latency vs. non-linear phase: A balanced approach for UNFOLD filter design in quantitative real-time MRI. In *Proceedings of International Society of Magnetic Resonance in Medicine, Seattle, USA*, 2006.

[117] K.P. Pruessmann, M. Weiger, P. Bornert, and P. Boesiger. Advances in sensitivity encoding with arbitrary k-space trajectories. *Magn. Res. Med.*, 46:638–651, 2001.

[118] S. Kozerke, C. Baltes, J. Tsao, M.S. Hansen, K.P. Pruessman, and P. Boesiger. Comparison of SENSE and k-t SENSE in dynamic imaging. In *Proceedings of the 13th Annual Meeting ISMRM, Miami, USA*, 2005.

[119] W. Press, S. Teukolsky, W. Vetterling, and B. Flannery. *Numerical Recipes in C*. Cambridge University Press., Cambridge, 1992.

[120] M. Deimling and O. Heid. Magnetization prepared true FISP imaging. In *Proceedings of the 2nd Annual Meeting of SMRM, San Francisco, USA*, 1994.

[121] S. Roujol, M. Ries, B. Quesson, C. Moonen, and B. Denis de Senneville. Real-time MR-thermometry and dosimetry for interventional guidance on abdominal organs. In *Proceedings 18th Scientific Meeting, International Society for Magnetic Resonance in Medicine*, 2010.

[122] S. Roujol, M. Ries, B. Quesson, C.T.W. Moonen, and B. Denis de Senneville. Real-time MR-thermometry and dosimetry for interventional guidance on abdominal organs. *Magn. Res. Med.*, 63(4):1080–1087, 2010.

[123] J.B.A. Maintz and M.A. Viergever. A survey of medical image registration. *Medical Image Analysis*, 2(1):1–36, 1998.

[124] Regalia. *Adaptive IIR (infinite impulse response) filtering in signal processing and control (Electrical engineering and electronics series/90)*. Lavoisier, 1995.

[125] K.J. Friston, J. Ashburner, C.D. Frith, J.B. Poline, J.D. Heather, and R.S.J. Frackowiak. Spatial registration and normalisation of images. *Human Brain Mapping*, 2:165–189, 1995.

[126] S.K Mitra. *Digital Signal Processing, second edition*. McGraw-Hill, 2001.

[127] S. Roujol, B. denis de Senneville, G. Maclair, S. Hey, P. Jaïs, C.T.W. Moonen, and B. Quesson. Advances in real-time MR temperature mapping of the human heart. In *Proceedings 18th Scientific Meeting, International Society for Magnetic Resonance in Medicine*, 2010.

[128] B. Denis de Senneville, S. Roujol, Jaïs P., C.T.W. Moonen, G. Herigault, and B. Quesson. Feasibility of fast MR-thermometry during cardiac RF ablation. *NMR BioMed.*, In press.

[129] S. Hey, A. Cernicanu, B.D. de Senneville, S. Roujol, M. Ries, C.T.W. Moonen, and B. Quesson. Feasibility of MR-thermometry with blood suppression on the human heart at 3T. In *Proceedings 18th Scientific Meeting, International Society for Magnetic Resonance in Medicine*, 2010.

[130] M.D. Cerqueira, N.J. Weissman, V. Dilsizian, A.K. Jacobs, S. Kaul, W.K. Laskey, D.J. Pennell, J.A. Rumberger, T. Ryan, and M.S. Verani. Standardized myocardial segmentation and nomenclature for tomographic imaging of the heart: a statement for healthcare professionals from the Cardiac Imaging Committee of the Council on Clinical Cardiology of the American Heart Association. *Circulation*, 105(4):539–542, 2002.

[131] A. Kolandaivelu, M.M. Zviman, V. Castro, A.C. Lardo, R.D. Berger, and H.R. Halperin. Noninvasive assessment of tissue heating during cardiac radiofrequency ablation using MRI thermography. *Circ Arrhythm Electrophysiol*, 3(5):521–9, 2010.

[132] W. A. Grissom, V. Rieke, A. B. Holbrook, Y. Medan, M. Lustig, J. Santos, M. V. McConnell, and K. B. Pauly. Hybrid referenceless and multibaseline subtraction MR thermometry for monitoring thermal therapies in moving organs. *Med. Phys.*, 37:5014–26, 2010.

[133] S. Chavez, Q.S. Xiang, and L. An. Understanding phase maps in MRI: a new cutline phase unwrapping method. *IEEE Trans Med Imaging*, 21(8):966–77, 2002.

[134] M. Ries, B. Denis de Senneville, S. Roujol, and C. Moonen. Latency compensation for real-time 3D HIFU beam-steering on moving targets. In *Proceedings 18th Scientific Meeting, International Society for Magnetic Resonance in Medicine*, 2010.

[135] C.J. Hardy, J.D. Pearlman, J.R. Moore, P.B. Roemer, and H.E. Cline. Rapid NMR cardiography with a half-echo M-mode method. *J Comput Assist Tomogr*, 15(5):868–74, 1991.

[136] K. Nehrke, P. Bornert, J. Groen, J. Smink, and J.C. Bock. On the performance and accuracy of 2D navigator pulses. *Magn Res Imaging.*, 17(8):1173–1181, 1999.

[137] H. Greenspan, G. Oz, N. Kiryati, and S. Peled. MRI inter-slice reconstruction using super-resolution. *Magn Res Imaging.*, 20(5):437–46, 2002.

[138] B. Denis de Senneville, S. Roujol, Jaïs P., C.T.W. Moonen, G. Herigault, and B. Quesson. Feasibility of fast MR-thermometry during cardiac RF ablation. In *Proceedings 19th Scientific Meeting, International Society of Magnetic Resonance in Medicine*, 2011.

[139] B.J. Wilm, J. Svensson, A. Henning, K.P. Pruessmann, P. Boesiger, and S.S. Kollias. Reduced field-of-view MRI using outer volume suppression for spinal cord diffusion imaging. *Magn. Res. Med.*, 57(3):625–630, 2007.

[140] U. Katscher, Bornert P., C. Leussler, and van den Brink J.S. Transmit SENSE. *Magn. Res. Med.*, 49:144–155, 2003.

[141] T. Schaeffter, V. Raschea, P. Brnerta, and G. Mensb. Interactive reduced FOV imaging for projection reconstruction and spiral acquisition. *Magn Res Imaging.*, 19(5):677–684, 2001.

[142] S. Loncarič and T. Macan. Point constrained optical flow for LV motion detection. In *SPIE Proceedings of Medical Imaging*, volume 3978, pages 521–529, 2000.

[143] A. Becciu, H. van Assen, L.M.J. Florack, S. Kozerke, V. Roode, and B.M. ter Haar Romeny. A multi-scale feature based optic flow method for 3D cardiac motion estimation. In *SSVN*, 2009.

[144] T. Brox, C. Bregler, and J. Malik. Large displacement optical flow. *CVPR*, 0:41–48, 2009.

[145] S. Roujol, J. Benois-Pineau, B. Denis de Senneville, M. Ries, B. Quesson, and C. Moonen. Robust real time constrained motion estimation for interventional MRI on mobile organs. *IEEE trans Inf. Tech. Biomed.*, submitted.

[146] S. Roujol, J. Benois-Pineau, B. Denis de Senneville, B. Quesson, M. Ries, and C.T.W. Moonen. Real time constrained motion estimation for ECG-gated cardiac MRI. In *IEEE International Conference on Image Processing (ICIP)*, pages 757–760, 2010.

[147] D.L. Pham, C. Xu, and J.L. Prince. A survey of current methods in medical image segmentation. In *Annual Review of Biomedical Engineering*, volume 2, pages 315–338. 2000.

[148] A. Murat Tekalp. *Digital video processing.* Prentice-Hall, Inc., Upper Saddle River, NJ, USA, 1995.

[149] S. Baker, D. Scharstein, J.P. Lewis, S. Roth, M.J. Black, and R. Szeliski. A database and evaluation methodology for optical flow. In *In Proceedings of the IEEE International Conference on Computer Vision (ICCV)*, pages 1–8. IEEE, 2007.

[150] J.M. Odobez and Bouthemy P. Robust multiresolution estimation of parametric motion models. *Journal of Visual Communication and Image Representation*, 6(4):348–365, Dec 1995.

[151] G. Maclair, B. Denis de Senneville, M. Ries, B. Quesson, P. Desbarats, J. Benois-Pineau, and C.T.W. Moonen. PCA-based image registration : Application to on-line MR temperature monitoring of moving tissues. In *ICIP*, pages 141–144, 2007.

[152] S. Roujol, M. Ries, C. Moonen, and B. Denis de Senneville. Robust real tiem motion estimation for mr-thermometry. In *IEEE International Symposium on Biomedical Imaging (ISBI)*, pages 508–511, 2011.

[153] J.L. Barron, D.J. Fleet, and S.S. Beauchemin. Performance of optical flow techniques. *International Journal of Computer Vision*, 12(1):43–77, Feb 1992.

[154] S. Roujol, M. Ries, B. Quesson, C. Benois-Pineau, J. Moonen, and B. Denis de Senneville. A new criterion for motion estimation assessment for MR-thermometry. In *IEEE International Symposium on Biomedical Imaging (ISBI)*, pages 1241–1244, 2010.

[155] S. Roujol, M. Ries, C. Moonen, and B. Denis de Senneville. Automatic registration calibration for real time MR-interventional applications. *IEEE trans Med Imaging*, In press.

[156] J. De Poorter, C. De Wagter, Y. De Deene, C. Thomson, F. Stahlberg, and E. Achten. The proton resonance frequency shift method compared with molecular diffusion for quantitative measurement of two dimensional time dependent temperature distribution in phantom. *Journal of Magnetic Resonance. Series B*, 103:234–241, 1994.

[157] S.J. Wharton and R. Bowtell. Dipole-based filtering for improved removal of background field effects from 3D phase data. In *19th Annual Meeting of ISMRM*, 2010.

[158] F. Schweser, B.W. Lehr, and J.R. Deistung, A.and Reichenbach. A novel approach for separation of background phase in swi phase data utilizing the harmonic function mean value property. In *19th Annual Meeting of ISMRM*, 200.

[159] B. Denis de Senneville, S. Roujol, C. Moonen, and M. Ries. PRF based MR-thermometry on abdominal organs: A pragmatic comparison of referenceless vs multi-baseline. In *Proceedings 18th Scientific Meeting, International Society for Magnetic Resonance in Medicine*, 2010.

[160] B. Denis de Senneville, S. Roujol, C.T.W. Moonen, and M. Ries. Motion correction in MR thermometry of abdominal organs: A comparison of the referenceless vs the multi-baseline approach. *Magn. Res. Med.*, 64(5):1373–81, 2010.

[161] R.E. Kalman. A new approach to linear filtering and prediction problems. *Journal of Basic Engineering*, 82(1):35–45, 1960.

[162] J.K. Potocki and H.S. Tharp. Concurrent hyperthermia estimation schemes based on extended Kalman filtering and reduced-order modelling. *Int. J. Hyperthermia*, 9(6):849–65, 1993.

[163] H.H. Pennes. Analysis of tissue and arterial blood temperatures in the resting human forearm. *Journal of applied physiology*, 1(2):93–122, 1948.

[164] G. Ye, P.P. Smith, and J.A. Noble. Model-based ultrasound temperature visualization during and following HIFU exposure. *Ultrasound Med Biol*, 36(2):234–49, 2010.

[165] S. Roujol, B. Denis de Senneville, S. Hey, C.T.W. Moonen, and M. Ries. Robust adaptive extended Kalman filtering for real time MR-thermometry guided HIFU interventions. *IEEE trans Med Imaging*, In press.

[166] S. Roujol, B. Denis de Senneville, S. Hey, C. Moonen, and M. Ries. Extended Kalman filtering for MR-thermometry guided high intensity focused ultrasound using the bio heat transfer equation. In *IEEE International Conference on Image Processing (ICIP)*, In press.

[167] A. Chauvenet. *A manual of spherical and practical astronomy.* Lippincottt, Philadelphia, 1^{st} edition, 1863.

[168] I. Dragonu, P.L. de Oliveira, C. Laurent, C. Mougenot, N. Grenier, C.T.W. Moonen, and B. Quesson. Non-invasive determination of tissue thermal parameters from high intensity focused ultrasound treatment monitored by volumetric MRI thermometry. *NMR Biomed.*, 22(8):843–51, 2009.

[169] N. Todd, U. Vyas, J. de Bever, A. Payne, and D.L. Parker. The effects of spatial sampling choices on MR temperature measurements. *Magnetic Resonance in Medicine*, 65:515–21, 2011.

[170] E.M. Haacke, R.W. Brown, M.R. Thompson, and R. Venkatesan. *Magnetic resonance imaging: physical principles and sequence design.* Wiley New York:, 1999.

[171] Student. The Probable Error of a Mean. *Biometrika*, 6(1):1–25, 1908.

[172] G. Rupert and J. Miller. Beyond ANOVA, basics of applied statistics, 1985.

[173] C.E. Bonferroni. Il calcolo delle assicurazioni su gruppi di teste. In *In Studi in Onore del Professore Salvatore Ortu Carboni, Rome, Italy*, pages 13–60, 1935.

[174] J.P. Shaffer. Multiple Hypothesis Testing. *Ann. Rev. Psych.*, 46:561–84, 1995.

[175] C. Fox. *An introduction to the calculus of variations*. Dover Pubns, 1987.

[176] R. Courant and D. Hilbert. *Methods of mathematical physics*. Wiley-Interscience, 1989.

[177] S.J. Axler. *Linear algebra done right*. Springer Verlag, 1997.

[178] H. Jeffreys and B.S. Jeffreys. *Methods of mathematical physics*. Cambridge Univ Pr, 1999.

[179] I.N. Bronshtein, K.A. Semendyayev, and K.A. Hirsch. *Handbook of mathematics*. Springer Berlin:, 2007.

[180] S.K. Mitra and Y. Kuo. *Digital signal processing: a computer-based approach*, volume 128. McGraw-Hill, 1998.

[181] G. Welch and G. Bishop. An introduction to the Kalman filter. *University of North Carolina at Chapel Hill, Chapel Hill, NC*, 7(1), 1995.

[182] K.B. Petersen and M.S. Pedersen. The matrix cookbook. Technical report, 2008.

[183] P. Zarchan and H. Musoff. *Fundamentals of kalman filtering: A practical approach*. Aiaa, 2005.

Résumé

L'ablation des tissus par hyperthermie locale guidée par IRM est une technique prometteuse pour le traitement du cancer et des arythmies cardiaques. L'IRM permet d'extraire en temps réel des informations anatomiques et thermiques des tissus. Cette thèse a pour objectif d'améliorer et d'étendre la méthodologie existante pour des interventions sur des organes mobiles comme le rein, le foie et le coeur. La première partie a été consacrée à l'introduction de l'imagerie rapide (jusqu'à 10-15 Hz) pour le guidage de l'intervention par IRM en temps réel. L'utilisation de cartes graphiques (GPGPU) a permis une accélération des calculs afin de satisfaire la contrainte de temps réel. Une précision, de l'ordre de 1°C dans les organes abdominaux et de 2-3°C dans le coeur, a été obtenue. Basé sur ces avancées, de nouveaux développements méthodologiques ont été proposés dans une seconde partie de cette thèse. L'estimation du mouvement basée sur une approche variationnelle a été améliorée pour gérer la présence de structures non persistantes et de fortes variations d'intensité dans les images. Un critère pour évaluer la qualité du mouvement estimé a été proposé et utilisé pour auto-calibrer notre algorithme d'estimation du mouvement. La méthode de correction des artefacts de thermométrie liés au mouvement, jusqu'ici restreinte aux mouvements périodiques, a été étendue à la gestion de mouvements spontanés. Enfin, un nouveau filtre temporel a été développé pour la réduction du bruit sur les cartographies de température. La procédure interventionnelle apparaît maintenant suffisamment mature pour le traitement des organes abdominaux et pour le transfert vers la clinique. Concernant le traitement des arythmies cardiaques, les méthodes ont été évaluées sur des sujets sains et dans le ventricule gauche. Par conséquent, la faisabilité de l'intervention dans les oreillettes mais aussi en présence d'arythmie devra être abordée.

Mots-clés: IRM interventionnelle, thermométrie, système temps réel, estimation du mouvement, filtrage du signal

Summary

MR-guided thermal ablation is a promising technique for the treatment of cancer and atrial fibrillation. MRI provides both anatomical and temperature information. The objective of this thesis is to extend and improve existing techniques for such interventions in mobile organs such as the kidney, the liver and the heart. A first part of this work focuses on the use of fast MRI (up to 10-15 Hz) for guiding the intervention in real time. This study demonstrated the potential of GPGPU programming as a solution to guarantee the real time condition for both MR-reconstruction and MR-thermometry. A precision in the range of 1°C and 2-3°C was obtained in abdominal organs and in the heart, respectively. Based on these advances, new methodological developments have been carried out in a second part of this thesis. New variational approaches have proposed to address the problem of motion estimation in presence of structures appearing transient and high intensity variations in images. A novel quality criterion to assess the motion estimation is proposed and used to autocalibrate our motion estimation algorithm. The correction of motion related magnetic susceptibility variation was extended to treat the special case of spontaneous motion. Finally, a novel temporal filter is proposed to reduce the noise of MR-thermometry measurements while controlling the bias introduced by the filtering process. As a conclusion, all main obstacles for MR-guided HIFU-ablation of abdominal organs have been addressed in in-vivo and ex-vivo studies, therefore clinical studies will now be realized. However, although promising results have been obtained for MR-guided RF-ablation in the heart, its feasibility in the atrium and in presence of arrhythmia still remains to be investigated.

Key words: Interventional MRI, thermometry, real time system, motion estimation, signal filtering